

Czech Technical University in Prague
Faculty of Electrical Engineering

Doctoral Thesis

February 2024

Hadi Hematian

Czech Technical University in Prague

Faculty of Electrical Engineering

Department of Physics

***STUDY OF MOLECULAR
INTERACTIONS ON
SEMICONDUCTOR SURFACES BY
COMPUTATIONAL METHODS***

Doctoral Thesis

Hadi Hematian

Prague, February 2024

Ph.D. Programme: Applied Physics (code: P0533D110030)

Supervisor: *prof. RNDr. Bohuslav Rezek, Ph.D.*

Acknowledgment

I would like to express my gratitude to my supervisor, professor RNDr. Bohuslav Rezek, Ph.D., for his invaluable guidance, exceptional planning abilities, and readiness to help. Next, I am thankful to prof. Stuart Parkin for supervising and facilitating my six-month internship at the Max Planck Institute of Microstructure Physics in Halle, Germany. Additionally, I want to thank dr. Egor Ukraintsev, dr. David Rutherford, and dr. Jaroslav Kuliček for being supportive colleagues. Last but not least, I would like to thank my wife and my family for their support.

Annotation

Interactions of molecules with semiconductor surfaces have always been a crucial topic in physics, chemistry, and materials science due to the novel and interesting structural, chemical, electronic, and optical properties of such interfaces. However, there are still large gaps in the literature, especially in understanding the interfaces between metal oxide semiconductors and biological components (from proteins, and peptides to single amino acids). Especially theoretical work can provide new insights and interpretation approaches. In this work, at first, the non-idealities in the ZnO lattice of real materials (oxygen and zinc vacancies or impurity erbium atoms) are theoretically studied, showing noticeable effects on the electronic and optical properties of ZnO. We then focus on computational study of interactions between the ZnO surfaces and two well-known and biologically important molecules, bovine serum albumin (BSA) and thiorphan. The classical force field method and quantum-based density functional tight binding (DFTB) approaches are employed in a complementary manner. The computational findings are also supported by atomic force microscopy (AFM) experimental results. We compare the adsorption of these selected biomolecules on different ZnO polar and non-polar surfaces. BSA adsorbs on all the studied ZnO surfaces, while interactions are found to be considerably affected by the atomic scale surface structure chemistry of ZnO. In the case of thiorphan, molecular dynamics simulations using CO dipole arrays to mimic ZnO surface polarity show that the surface polarity, giving rise to different electric field orientation and distance dependence, has the key role in the interactions and molecular assembly rather than the surface chemistry. Finally, study of biomolecules interacting with magnetized surfaces shows interesting dependency on the type of enantiomers and direction of magnetic dipole of the surface.

Keywords

density functional theory, molecular dynamics, semiconductors, biomolecules

Anotace

Interakce molekul s povrchy polovodičů byly vždy zásadním tématem ve fyzice, chemii a vědě o materiálech kvůli novým a zajímavým strukturním, chemickým, elektronickým a optickým vlastnostem takových rozhraní. V literatuře však stále existují velké mezery, zejména v pochopení rozhraní mezi polovodiči na bázi oxidů kovů a biologickými složkami (od proteinů a peptidů po jednotlivé aminokyseliny). Zejména teoretická práce může poskytnout nové poznatky a interpretační přístupy. V této práci jsou nejprve teoreticky studovány neidealities v mřížce ZnO reálných materiálů (kyslíková a zinková vakancie nebo příměsi atomů erbia), které vykazují znatelný vliv na elektronické a optické vlastnosti ZnO. Poté se zaměříme na výpočetní studium interakcí mezi povrchy ZnO a dvěma dobře známými a biologicky důležitými molekulami, bovinním sérovým albuminem (BSA) a thiorfanem. Klasická metoda silového pole a metoda těsné vazby založená na funkcionálu hustoty (DFTB) jsou využívány komplementárním způsobem. Výsledky výpočtů jsou také podpořeny experimentálními výsledky mikroskopie atomárních sil (AFM). Porovnáváme adsorpci daných vybraných biomolekul na různých polárních a nepolárních površích ZnO. BSA se adsorbuje na všech studovaných typech povrchů ZnO, přičemž bylo zjištěno, že interakce jsou značně ovlivněny chemií povrchové struktury ZnO v atomárním měřítku. V případě thiorfanu simulace molekulární dynamiky využívající CO dipólová pole k napodobení povrchové polarizace ZnO ukazují, že povrchová polarita, která vede k odlišné orientaci elektrického pole a závislosti na vzdálenosti, má klíčovou roli v interakcích a molekulárním sestavování spíše než povrchová chemie. Studium biomolekul interagujících s magnetizovanými povrchy ukazuje zajímavou závislost na typu enantiomerů a směru magnetického dipólu povrchu.

Klíčová slova

teorie funkcionálu hustoty, molekulární dynamika, polovodiče, biomolekuly

Contents

Aims of the thesis.....	8
1. Introduction.....	9
2. Zinc oxide as material.....	16
2.1. Zinc oxide principal low index surfaces.....	17
2.2. Common adsorbates on ZnO surfaces.....	18
3. Theoretical methods.....	20
3.1. Force Field.....	20
3.1.1. Definition of force field.....	20
3.1.2. Simple pair and bond-order potentials.....	21
3.1.3. Multi-body reactive force fields (ReaxFF).....	22
3.2. Quantum mechanics methods.....	23
3.2.1. Basic aspects of quantum mechanics.....	24
3.2.2. Born-Oppenheimer approximations.....	25
3.2.3. Basis set.....	25
3.2.4. Hartree-Fock method.....	25
3.2.5. Density functional theory (DFT).....	27
3.2.6. Density functional tight binding (DFTB).....	29
3.3. Molecular dynamics.....	32
3.3.1. Basic MD concepts.....	32
3.3.2. Considering environment conditions.....	33
3.3.3. Numerical integration.....	34
4. RESULTS - Defects in ZnO crystal structures.....	35
4.1. Computational details.....	35
4.2. Zinc and oxygen vacancies.....	36
4.3. Adding a dopant: erbium doped ZnO.....	38
5. RESULTS - Bovine serum albumin (BSA) adsorption on ZnO surfaces....	45
5.1. Orientation preference of BSA on ZnO surfaces.....	46
5.1.1. Computational details.....	46
5.1.2. The most favourable orientations of BSA on ZnO.....	47

5.2. Binding of BSA amino acids to ZnO surfaces	52
5.2.1. Computational details	52
5.2.2. Structural and electronic properties	54
5.2.3. Binding energy and charge transfer	58
6. RESULTS - Thiorphan adsorption on ZnO surfaces.....	63
6.1. Surface atomic structure effects on adsorption of thiorphan.....	64
6.1.1. Computational details	64
6.1.2. Binding of thiorphan to ZnO surface atoms.....	65
6.2. Surface polarity effects on adsorption of thiorphan	66
6.2.1. Computational details	66
6.2.2. Thiorphan molecules on polar and non-polar surfaces	67
7. RESULTS - Interaction of chiral molecules with magnetized surfaces.....	74
7.1. Computational details	76
7.2. Cysteine enantiomers on magnetized nickel surfaces	77
8. Conclusion	80
References	82
APPENDIX	89
A. Atomic force microscopy and further computational data.....	89
B. Own contribution of the author.....	98
C. List of co-authored publications.....	98
D. Conference presentations	99
E. Awards and honours.....	100
F. Publications reprints.....	101

Aims of the thesis

The purpose of this thesis is to use computational methods to study the nature and viability of the bonding between biomolecules and semiconductor surfaces in order to improve our understanding of the characteristics and functionality of these systems. The thesis specifically aims to explore density functional tight binding (DFTB), force field, and molecular dynamics simulations to investigate the interactions of selected large and small biomolecules with material surfaces of different polarity and chemistry as the model systems. To define basis of the study the thesis also aims to provide analysis of the existing knowledge and state-of-the-art about the employed materials and methods. Analysing structural, chemical and electronic characteristics that indicate viability and possible advantages for biosensing is the aim with regard to potential applications.

1. Introduction

As the fundamental component of contemporary electronics, semiconductors are used to power a wide range of electronic devices thanks to their special conductivity qualities. The surfaces of semiconductors play a crucial role in their behavior and functionality in electronic applications. This significance of the semiconductor surface also reaches the domain of molecular interfaces, where the interactions between semiconductors and molecules are yet relatively unknown territory. Comprehending and modifying these interfaces provides opportunities for innovative uses, resulting in the creation of semiconductor-molecule hybrid systems possessing a variety of functions. Computational approaches are essential in this intricate context because they provide a virtual laboratory for simulating and analyzing the complex interactions among semiconductors and molecules at both the molecular and atomic levels. The convergence of semiconductors, semiconductor surfaces, molecular interfaces, and computational techniques not only drives the development of electronic technologies but also creates new opportunities for creative applications that push the limits of what is feasible in the field of semiconductor-molecule interfaces, from energy devices to sensors. For the current research on semiconductor-molecule interactions, zinc oxide (ZnO) has been selected as the semiconductor due to its unique characteristics that allow for a thorough investigation. ZnO is a popular candidate for many electronic applications due to its broad bandgap and superior semiconducting properties. Moreover, its distinct surface characteristics and chemical stability make it a perfect platform for studying molecular interactions at the atomic and molecular levels. ZnO's availability and transparency increase its applicability in real-world situations. From the computational point of view, accuracy and efficiency are the driving forces behind the decision to use density functional tight binding (DFTB) and force field molecular dynamics (FFMD) techniques for simulations. DFTB is an excellent tool for exploring the complex electronic structures and characteristics of semiconductor-molecule interfaces because it strikes a compromise between computational cost and accuracy. In the meanwhile, FFMD

simulations provide an in-depth understanding of the system's evolution over time by demonstrating the dynamic behavior and mobility of molecules on the semiconductor surface. By strategically combining DFTB and FFMD simulation techniques using ZnO as the semiconductor material, the goal is to accurately and computationally efficiently investigate the intricacies of semiconductor-molecule interactions.

Beyond its traditional applications, due to their distinct properties and biological functions, nanostructured ZnO-based materials have recently caught the interest of biomaterial scientists. The interest in implementing ZnO's beneficial properties for biological applications, ranging from drug delivery ^[1,2] and biosensing ^[3,4] to tissue regeneration ^[5], has been rapidly growing during the last decades. Due to their superior electronic characteristics, ZnO nanostructures are good candidates for fabricating biosensors. ZnO-based quantum dots are intriguing options as bio-probes for cell and tissue imaging because of their distinctive photoluminescent features, including an adjustable emission wavelength, good water stability, and high quantum yield. ZnO nanostructures are also interesting materials for tissue regeneration, bacterial resistance, and wound treatment due to their high catalytic and antibacterial capabilities as well as their biocompatibility. For instance, the Zn²⁺ ions produced by ZnO nanostructures have the capacity to boost keratinocyte migration toward a wound site and promote the healing process ^[6]. The bacterial cell membrane may be fatally damaged as a result of the production of reaction oxygen species (ROS) and the release of Zn²⁺ ions from ZnO nanoparticles ^[7,8]. In addition, ZnO can be used as a drug carrier since it is a type of pH-responsive system. ZnO nanowire protein sensors enhanced by the piezotronic effect ^[9], ZnO films synthesized using spray pyrolysis with antibacterial activity ^[10], flexible and microporous chitosan hydrogel/nano ZnO composite bandages for wound dressing ^[11], and a new generation of chitosan-encapsulated ZnO quantum dots for drug delivery ^[12], are some further examples of successful implementation of ZnO materials for biological purposes.

Regarding the ever-growing utilization of ZnO-based materials and nanostructures for biological purposes, such as the abovementioned examples, the research on ZnO interactions with different biomolecules such as proteins, peptides, and amino acids is becoming more and more critical. Some of the biomolecules are even used in ZnO synthesis, such as DNA ^[13], albumin, urease ^[14], amino acids ^[15–17], peptides, polyamines, cyclodextrin ^[18], bacteria ^[19,20], and viruses ^[21]. These biomolecules not only interact with ZnO and form hybrid materials but also, in some cases, impact ZnO forming systems ^[22] and even modify ZnO surface

morphology ^[14,23,24]. Multiple experimental studies investigated the interactions between ZnO surfaces and peptides for ZnO morphology modification ^[25–27]. It is evident from the numerous reports on the formation of innovative and varied ZnO structures employing biomolecules that biomolecules are important instruments to control, reproduce, and modify the physical, chemical, and even electronic properties of ZnO. For instance, the increased green photoluminescence for materials created in the presence of spider silk peptides is an illustration of how biomolecules may be employed to change the optical characteristics of ZnO and potentially be used as biosensors or in optoelectronic devices ^[22].

The hybrid ZnO-biomolecules interfacial system cannot be completely understood based purely on experimental techniques. Therefore, theoretical and computational approaches, including molecular dynamics (MD) simulations, DFTB, and density functional theory (DFT) have so far been used to comprehend how biomolecules are able to attach to ZnO surfaces.

For instance, MD simulations were able to provide a justification for the experimentally observed strong binding of IgG to the ZnO (10 $\bar{1}$ 0) plane ^[28]. In that study, using AFM imaging, immunoglobulin G (IgG) was seen to attach to the (10 $\bar{1}$ 0) plane more frequently than the other three crystallographic planes. The spatial positioning and distribution of the amino acids in the protein that interact strongly with ZnO, and therefore their availability for contact, were shown to be the cause of this behaviour, which was then explained by using Monte Carlo MD simulations ^[28]. An earlier MD simulation analysis of interactions between the ZnO planes and twenty-two different amino acids led to the identification of the specific amino acids interacting significantly with ZnO planes ^[29]. Tyrosine and tryptophan were found to have high binding energies (BEs) on the Zn-terminated (0001) surface there, but asparagine, tryptophan, and histidine had the greatest BEs on the (10 $\bar{1}$ 0) surface ^[29]. A different theoretical model based on effective interfacial energies was also suggested to comprehend how the GT-16 peptide alters the ZnO morphology ^[30]. The relative growth rates of ZnO crystal planes in the presence of GT-16 were predicted by using an adsorption-nucleation model. This theoretical strategy was thought to be a less complicated and computationally less expensive alternative to molecular modelling. The variations in the adsorption behaviour of G-12 and GT-16 peptides to ZnO facets were further studied in later research using Monte Carlo MD simulations ^[26]. The goal was to compute the adsorption energy and anticipate potential G-12 and GT-16 binding moieties to the ZnO planes

[(0001) and (10 $\bar{1}$ 0)]. Both peptides were shown to adhere well to ZnO planes while a lower adsorption energy was seen for the (0001) ZnO plane for both peptides compared to the (10 $\bar{1}$ 0) plane ^[26].

In other works, interactions of the nucleotide bases of deoxyribonucleic acid (DNA) and ribonucleic acid (RNA) with a ZnO cluster were investigated by the DFT method ^[31]. It was found that ZnO site preference towards the nucleobases is identical to that of the metal clusters, suggesting that the metal clusters maintain their site preference even in their oxidized condition ^[31]. The geometry and energy associated with various adsorption configurations of four distinct amino acids on the zinc oxide (10 $\bar{1}$ 0) surface were also studied by DFT and DFTB-based molecular dynamics simulations ^[32]. The advantages and limitations of DFTB compared to conventional DFT were emphasized, showing the DFT adsorption geometries to be accurately reproduced by the DFTB approach ^[32]. Another study employed *ab initio* calculations based on DFT to investigate the adsorption of selected amino acids on the ZnO (10 $\bar{1}$ 0) surface ^[33]. It was found that for some amino acids the most energetically favourable configurations involve the deprotonation of the molecule if the water screening is ineffective ^[33].

Despite such valuable theoretical studies of the interactions between biomolecules and ZnO surfaces, there is still a lack of systematic studies comparing the behaviour of other important biomolecules on different ZnO surfaces and addressing the electronic properties of such systems. Most of the abovementioned studies focused on one particular ZnO surface, without comparing various possible ZnO facets or studying the electronic and optical aspects of the ZnO-biomolecules compounds. It is also worth mentioning that based on our comprehensive literature review, the theoretical research on interactions of ZnO polar surfaces with biomolecules has been noticeably limited, especially when it comes to ZnO (000 $\bar{1}$) surface. The situation is even worse for ZnO nonpolar (11 $\bar{2}$ 0) surface for which there is a lack of available studies of ZnO-biomolecular systems.

The main goal of this thesis has been thus to explore the interactions of biomolecules with various low-index surfaces of ZnO on a theoretical basis using suitable computational methods. In this study, we have always included all important ZnO low-index surfaces in all simulations to provide a systematic comparison between them and the effects of their properties on the behaviour of ZnO-biomolecular interfaces. In most parts, we also try to study the ZnO-biomolecular systems under the study from an electronic standpoint. Among diverse biomolecules, serum

albumin (SA) and thiorphan have been selected as biologically relevant molecules for the case studies in this work.

Serum albumin (SA) is the most plentiful protein in blood plasma. It has been investigated intensively for its numerous vital functions, such as maintaining the oncotic pressure, transporting drugs as well as contributing to the functionality of the immune system. Numerous experimental studies commonly use BSA. BSA is a stable and non-reactive protein. It is inexpensive and has analogous functions and similar physicochemical properties to human serum albumin. It comprises about 583 amino acids and no carbohydrates. Figure 1.1 shows a schematic representation of the BSA molecule with some highlighted amino acids.

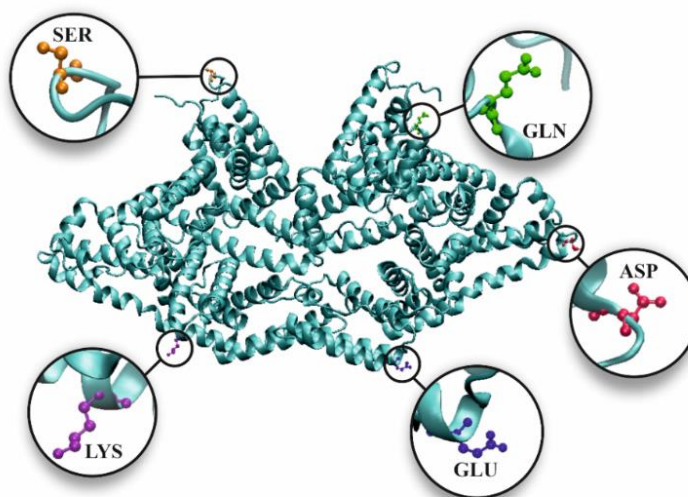


Figure 1.1. Schematic representation of BSA molecule with some amino acids highlighted

Interactions of ZnO materials with serum albumin as the most abundant plasma protein in mammals' blood have been studied in a limited number of studies and, in most cases, merely experimentally [34–37]. Chapter 5 of this thesis, in which the adsorption of BSA on different ZnO low index surfaces is studied, consists of two Sections with two different computational settings. In Section 4.1, orientation preference of a whole BSA molecule on different ZnO surfaces is investigated. The study in this part is based on a comparison of the total energy of the ZnO-BSA system at different orientations of BSA. Here, a question may arise why is the information about the orientation preference of BSA on ZnO surfaces important. This question is answered in Section 4.1, where it is shown that the orientation of BSA is a crucial factor affecting the

thickness and roughness of adsorbed BSA layers on ZnO surfaces. This finding is supported also by experimental microscopic data. Due to the enormous size (numbers and types of atoms) of the ZnO-BSA system and the fact that the system's total energy is the main parameter of interest, the classical force field approach was employed in this part. The ReaxFF potential (described in Chapter 3) was selected to describe interactions between atoms to achieve some initial perspective from the chemical point of view, in addition to the total energy. This initial perspective leads the research to select the proper parts of the large ZnO-BSA system for more precise calculations in Section 4.2, in which the electronic and binding properties of the system are studied by using DFT-based calculations.

Following our comprehensive investigations with BSA, thiorphan was selected as the next molecule for our computational investigation into the interactions between ZnO and biomolecules. In contrast to BSA, thiorphan's smaller size enables the possibility to employ more complicated precise, and computationally costly simulations, including molecular dynamics simulations involving a huge number of molecules. This strategic choice aims to enhance our understanding of how surface ZnO dipoles impact molecular assembly, utilizing both experimental and computational approaches. Thiorphan is a well-known, easily available biomolecule and its relevance as a small, zinc-related molecule makes it a fitting candidate for our study. By integrating experimental data and computational insights, we intend to obtain a full understanding of how ZnO affects molecule assembly, with thiorphan performing a crucial role in this research.

Thiorphan is a small bioactive molecule that was first introduced in 1980^[38]. Thiorphan, opposite to BSA which was a huge molecule, is small. It has many proven applications in medicine, such as being an enkephalinase inhibitor with a strong affinity for membrane metallo-endopeptidase^[39,40] and blocking the degradation of the luteinizing hormone-releasing hormone^[41]. Especially, it is mainly used as a selective inhibitor of neutral endopeptidase (NEP)^[41] and metalloproteinase^[42]. NEP is a zinc-ectoenzyme involved in the metabolism of some important regulatory peptides in both the central nervous system and the periphery^[43]. The zinc atom in NEP and both the thiol group and benzene ring in thiorphan play a crucial role in molecular interactions and forming tertiary structure^[43]. Zinc, sulfur, and nitrogen atoms are important in the processes in which biomolecules act as inhibitors of matrix metalloproteinases^[44]. In Figure 1.2, the atomic representation of a thiorphan molecule has been illustrated.

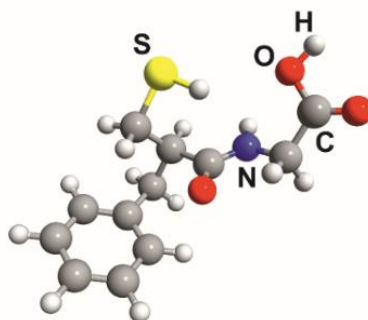


Figure 1.2. Atomic representation of a thiorphan molecule

Despite its biological importance, thiorphan adsorption on surfaces (including surfaces with zinc atoms) has not been studied yet, not even from a mere semiconductor-molecule interface point of view. In Chapter 6, for the first time, the adsorption of thiorphan on various ZnO low-index facets has been studied. Generally speaking, the ZnO surface can influence thiorphan adsorption due to the presence of Zn and O atoms on the surface or the presence of dipoles on the ZnO surface. Both possibilities are studied in Chapter 6 by DFTB and classical MD methods, in Sections 5.1 and 5.2, respectively.

In the pursuit of understanding interactions between ZnO and biomolecules, a significant development emerged during the author's internship at the Max Planck Institute of Microstructure Physics (MPI). The focus shifted to exploring the influence of magnetized surfaces on interactions with molecules. Recognizing our proficiency in simulating molecular adsorption on surfaces, MPI introduced this captivating field of study with a specific emphasis on the role of molecule chirality in these surface interactions. The effect of magnetized surfaces on chiral biomolecules has thus been studied in Chapter 7 of the thesis. Since executing costly spin-polarized simulations is required for the computational investigation of chirality, an attempt was made to choose a straightforward and simple structure for the calculations, consisting of the chiral biomolecule cysteine on a magnetized nickel (111) surface. The binding energy and structural characteristics of the final optimized system were examined in order to comprehend the interactions between molecules and surfaces after both enantiomers of cysteine were placed on differently magnetized nickel surfaces.

2. Zinc oxide as material

Zinc oxide (ZnO) is an inorganic compound classified in materials science as a metal-oxide semiconductor in the II-VI group with a covalency at the boundary between ionic and covalent semiconductors. ZnO crystal forms are wurtzite, zinc blende, and rocksalt, depending on the pressure. The wurtzite phase is the most stable phase in ambient circumstances. The wurtzite structure of ZnO has been illustrated in Figure 2.1, in which each cation (Zn^{+2}) is surrounded by four anions (O^{-2}) and vice versa. The arrangement of zinc and oxygen atoms in this way culminates in a polar symmetry along the hexagonal axis. A hexagonal unit cell is required to construct the ZnO crystal since the wurtzite crystal is based on the hexagonal crystal system. The lattice constants measured by X-ray diffraction are $a=3.250$ and $c=5.207$ [45], with tetrahedral coordination and an sp^3 hybridization nature.

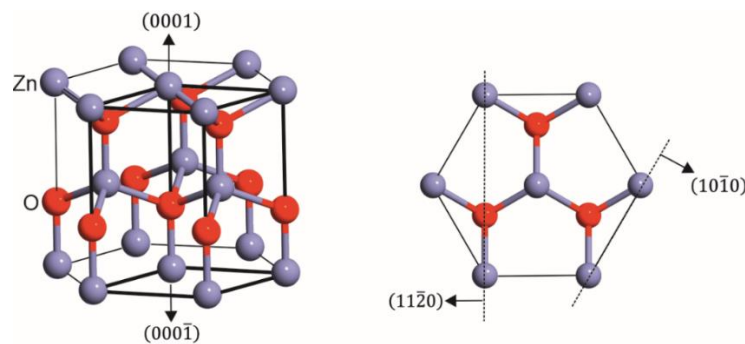


Figure 2.1. The hexagonal wurtzite structure model of ZnO.

From the electronic point of view, zinc oxide is an ionic n-type semiconductor with a wide band gap of 3.37 eV at room temperature [46]. ZnO is considered a multifunctional material due to its unique set of physical and chemical properties, such as high chemical stability, high electrochemical coupling coefficient, wide direct bandgap, broad light

absorption spectrum, photoluminescence, photocatalytic properties and high photostability^[47]. That is why ZnO has gained significant importance in optical, electrical, optoelectronic as well as biomedical research and applications. Towards these applications, ZnO has already been synthesized and used in a range of forms such as nanorod, nanowire, and two-dimensional (2D) forms in a variety of applications, namely photonic devices, lasers, and photovoltaics^[48–52].

2.1. Zinc oxide principal low-index surfaces

In terms of surface morphology, the following four surfaces are the principal low-index facets of a wurtzite ZnO crystal: the Zn-terminated (0001) surface, the O-terminated (000 $\bar{1}$) surface and the two mixed-terminated surfaces. As can be seen in Figure 2.2, the Zn-faced (0001) and the O-faced (000 $\bar{1}$) surfaces that are constructed with only zinc and oxygen atoms respectively are polar, while the mixed-terminated (10 $\bar{1}$ 0) and (11 $\bar{2}$ 0) facets are non-polar.

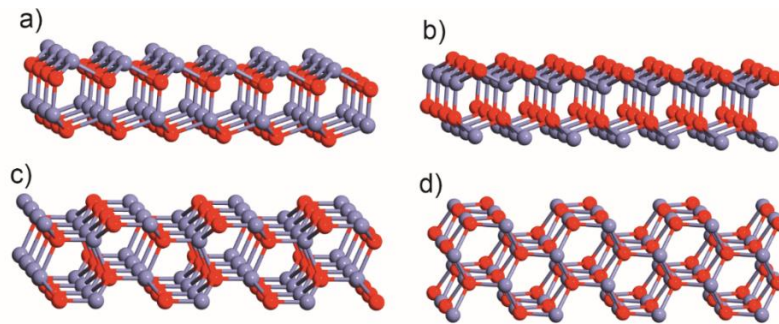


Figure 2.2. ZnO polar and non-polar surfaces; **a)** polar (0001) known also as Zn-faced, **b)** polar (000 $\bar{1}$) known also as O-faced, **c)** non-polar (10 $\bar{1}$ 0), and **d)** non-polar (11 $\bar{2}$ 0) surfaces. Note that the four surfaces are shown as cleaved from bulk and are not relaxed. As-cleaved polar surfaces are not electrostatically stable because of the formation of a dipole moment between two polar surfaces.

Among the surfaces, the mixed-terminated (10 $\bar{1}$ 0) facet is the most energetically favourable and often observed as dominant based on SEM morphology images^[53]. The structure of the (10 $\bar{1}$ 0) surface should resemble a bulk truncation since it is a non-polar surface, meaning there are no electrostatic instabilities as on polar surfaces^[54–58]. Since this non-polar surface has no electrostatic instability, theoretical calculations are simple and several theoretical findings have been reported for this surface^[59–62]. Only a few investigations have been conducted on (11 $\bar{2}$ 0) nonpolar

surface with few works published compared to the other low-index ZnO surfaces. Low energy electron diffraction (LEED) and scanning tunneling microscopy (STM) experiments carried out on $(11\bar{2}0)$ surface agreed with a surface termination that was bulk-like ^[63,64]. It was concluded that this surface orientation was rather unstable based on observing a high background in LEED and significant surface roughness in STM.

As mentioned above, ZnO hexagonal wurtzite structure has a polar c axis and is therefore non-centrosymmetric. Existence of polar (0001) and $(000\bar{1})$ surfaces (and observed pyroelectric and piezoelectric effects) are attributed to this characteristic of the material ^[65]. It is common to consider the projection of the bulk unit cell dipole to define the polar surfaces. The term "polar surface" is used if this projection is not zero for a specific surface orientation. The dipole moment in the instance of ZnO is pointed in the crystallographic (0001) direction, resulting in an electrostatic field in this direction. This electrostatic field is the reason for the instability of ideal ZnO polar surfaces, which are formed by simply truncating the bulk structure with the same ions with the same charge ^[66]. Even though ZnO polar surfaces appear unstable and thus theoretically unfeasible, they have been proved to exist, and their stability has been subject to many studies ^[67]. Unlike other polar surfaces of metal oxides, no evidence of reconstruction on (0001) has been seen in the literature ^[56,68]. Experimental work has also failed to show any proof of reconstruction on $(000\bar{1})$ polar ZnO surface using either LEED ^[54,58,69] or X-ray ^[67]. However, other explanations have been proposed for the stability of ZnO polar surfaces, such as surface vacancies and surface functional groups ^[70].

2.2. Common adsorbates on ZnO surfaces

In recent years, several theoretical and experimental research on various kinds of adsorbates on ZnO substrates have been conducted. Thermal desorption spectroscopy (TDS), X-ray photoelectron spectroscopy (XPS), and ultraviolet photoelectron spectroscopy (UPS) are the principal experimentally used methods. The fewest number of investigations are on the adsorbates on the polar O-faced surface ^[71,72], while the majority of information is available for adsorbates on the $(10\bar{1}0)$ surface ^[59,72–74]. Besides water, the majority of the focus on adsorbates on ZnO surfaces has been on molecules important for the production of methanol from synthesis gas, namely H_2 , CO , and CO_2 .

Figure 2.3 shows some examples of adsorption of such adsorbates on different ZnO surfaces. Figure 2.3a illustrates the adsorption of water

molecules on $(10\bar{1}0)$ surface. The initial investigation of water adsorption on this surface was conducted using TDS and XPS to examine the adsorption and condensation of water ^[75]. According to their findings, the water molecules chemisorb at the co-ordinately unsaturated Zn site. The existence of a stable (2×1) structure with each unit cell containing one intact and one dissociated water molecule was discovered by a theoretical study using Car-Parrinello *ab-initio* molecular dynamics simulations ^[60]. Another example is the adsorption of hydrogen atoms on the (0001) surface. The interaction of H atoms with this surface is weaker than on other surfaces because Zn-H bonds should have lower binding energy than O-H bonds. As may be predicted, exposure of this surface to atomic hydrogen results in the creation of a (1×1) overlayer made up of Zn-hydride species (Figure 2.3b), according to experimental research utilizing He atom scattering ^[76].

Adsorption of CO and CO₂ on O-faced and $(10\bar{1}0)$ surfaces are shown in Figure 2.3c and 2.3d, respectively. When the O-faced surface is exposed to CO, an ordered adlayer of CO forms, which is positioned in the surface's O-vacancies and bonded to the O-atom nearest to the surface ^[77,78]. The O-atom in CO is nearly where the O-atom of the substrate was before it was removed to make the vacancy. It has been suggested that exposure of ZnO $(10\bar{1}0)$ surface to CO₂ causes the development of a surface carbonate species ^[79]. However, the new theoretical results show that the structure is more stable when the second O-atom also makes a covalent bond with the substrate, resulting in a tridentate (Figure 2.3d) ^[74].

These examples are only some illustrative instances of common adsorbates on ZnO surfaces. A variety of other cases with the same adsorbates or other adsorbates have been reported in the literature. One can read a review paper ^[53] for more detailed information about adsorbates on ZnO surfaces.

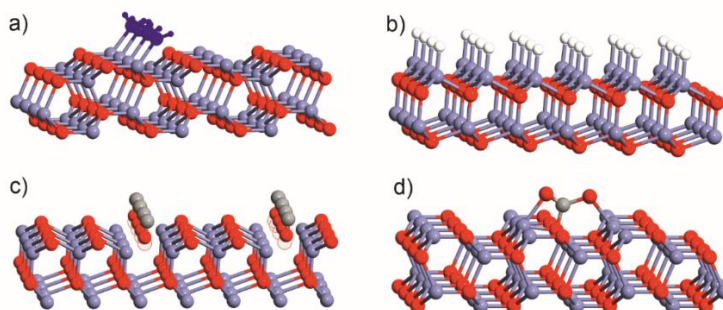


Figure 2.3. Examples of the structures of common adsorbates on ZnO surfaces; **a)** water molecules on $(10\bar{1}0)$ surface, **b)** hydrogen atoms on (0001) , **c)** CO molecules on $(000\bar{1})$, and **d)** CO₂ on $(10\bar{1}0)$ surfaces.

3. Theoretical methods

This Chapter focuses on a brief yet comprehensive description of the theoretical background and approximations this work is based on. It starts with an introduction to the classical approaches that use empirical force fields in computational simulations, also known as the force field methods. It continues by introducing the basic principles of quantum mechanical methods. Subsequently, more sophisticated simulation methods based on quantum theory, such as density functional theory (DFT) and density functional tight binding (DFTB) are introduced. The Chapter finishes with a short introduction to molecular dynamics methods.

3.1. Force Field

3.1.1. Definition of force field

A force field is a mathematical expression that describes how the energy of a system depends on the positions of its constituent components. In classical simulations, the inter-particle interactions are modelled by the so-called effective potentials between particles. These potentials enable classical simulations for a large number of particles and often solely rely on the distance between particles, R . The corresponding potential has two components: an attracting (negative) part and a repulsive (positive) part. This composition defines the particles being attracted when they are sufficiently close and repelling when they are too close. In equilibrium, the particles are at a distance of R_{\min} , equal to the minimum of their interaction potential (Figure 3.1). The sum of all inter-particle interactions in the simulations is used to calculate the system's total interaction. Pair potentials have the benefit of enabling relatively quick calculations, although they don't provide an accurate picture of the actual interactions. For example, chemical reactions cannot be described by simple classical potentials since bond breaking/forming is an electronic phenomenon.

Generally, the total energy of a system of N interacting particles defined by classical (empirical) potentials is given by equation 3.1 ^[80]:

$$\begin{aligned}
 U(\vec{r}_1, \dots, \vec{r}_N) = & \sum_i U_1(\vec{r}_i) + \sum_i \sum_{j>i} U_2(\vec{r}_i, \vec{r}_j) \\
 & + \sum_i \sum_{j>i} \sum_{k>j} U_3(\vec{r}_i, \vec{r}_j, \vec{r}_k) + \dots
 \end{aligned}
 \tag{3.1}$$

where U_1 is a one-body term caused by an external field, U_2 is a two-body term, also known as a pair potential, where the interaction is dependent on the distance between two atoms and is unaffected by the presence of other atoms, and U_3 is a three-body term that depicts the altered interaction between two atoms as a result of the presence of a third atom and so on. The more terms one includes, the more details of the system will be included, of course at the cost of more calculation load.

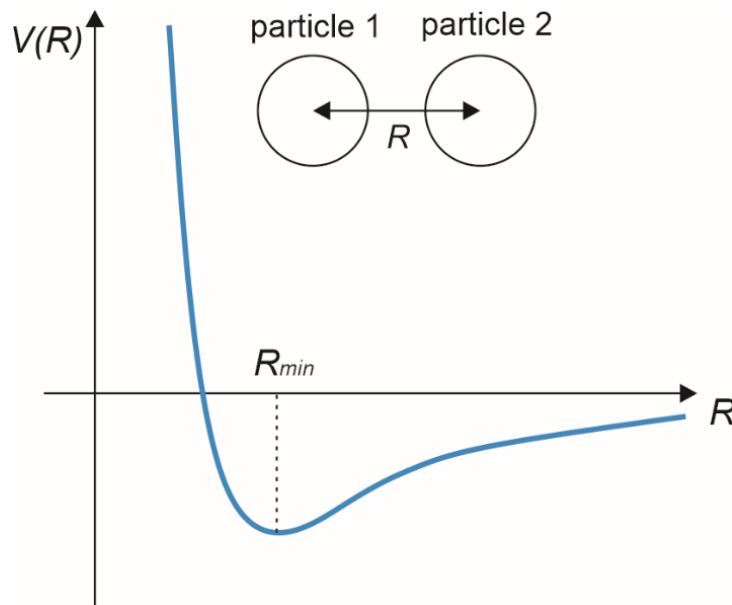


Figure 3.1. Two particles at distance R and the corresponding potential

3.1.2. Simple pair and bond-order potentials

In very simple systems like an ideal gas system in which particles do not interact with each other or in a real gas system, simple potential models could be suitable options to describe long-range van der Waals interactions. Some well-known examples of these potentials are ^[80]:

- the sphere potential: $V(r_{ij}) = \begin{cases} \infty & r_{ij} < \sigma \\ 0 & r_{ij} \geq \sigma \end{cases}$
- the square-well potential: $V(r_{ij}) = \begin{cases} 0 & r_{ij} < \sigma_1 \\ -\varepsilon & \sigma_1 \leq r_{ij} \leq \sigma_2 \\ 0 & r_{ij} > \sigma_2 \end{cases}$
- the harmonic potential: $V(r_{ij}) = a_0 + \frac{1}{2}k(r_{ij} - r_0)^2$
- the Buckingham potential: $V(r_{ij}) = C\left(\frac{\sigma}{r_{ij}}\right)^6 - Ae^{-\sigma r_{ij}}$
- the Lennard-Jones potential: $V(r_{ij}) = 4\varepsilon\left[\left(\frac{\sigma}{r_{ij}}\right)^{12} - \left(\frac{\sigma}{r_{ij}}\right)^6\right]$

It is worth bearing in mind that every unknown parameter in the equations above, except the distance between particles (r_{ij}), is a parameter that needs to be adjusted for different chemical elements. As a result, there are limitations in using basic pair potentials defined for a specific system for other systems. One way to cope with this issue to some extent is using bond-order potentials. The bond order is the number of chemical bonds between a pair of atoms and is not necessarily an integer. In conventional potentials such as Lennard-Jones, the bond length solely defines their interaction energy. In contrast, in bond-order potentials, the bond length is related to the bond-order by Pauling principle, and therefore the total energy is described by both. Tersoff^[81] and the Brenner potentials^[82], and the environment-dependent interatomic potential (EDIP)^[83] are some well-known bond-order potentials.

3.1.3. Multi-body reactive force fields (ReaxFF)

The potentials discussed up to this point are simple to apply in a computational code, but they are highly system-dependent. In other words, there are always limitations to using the force field set of a specific system for other systems. They also are unable to provide an accurate description of chemical reactions and bond-breaking phenomena. The reactive force field (ReaxFF)^[84] is a molecular model to address chemical reactions in classical calculations. Due to the inclusion of finite range interactions, ReaxFF can handle huge systems and make the potential computationally efficient. The total energy of a system in the ReaxFF force field can be represented as^[80]:

$$E_{total} = E_{2-body} + E_{3-body} + E_{4-body} + E_{multi-body} + E_{other} \quad (3.2)$$

$$E_{2-body} = E_{bond} + E_{VanderWaals} + E_{Coulombic}$$

$$E_{3-body} = E_{angle\ strain}, \quad E_{4-body} = E_{torsional},$$

$$E_{multi-body} = E_{over-coordination}$$

$$E_{other} = E_{under-coordination} + E_{penalty} + E_{conj}$$

The bond energy, or E_{bond} , depends on the bond order. $E_{Coulombic}$ are the electronic interactions, $E_{VanderWaals}$ is the non-bonded van der Waals interactions, $E_{angle\ strain}$ and $E_{torsional}$ consider the angle strain and torsional energy, respectively. The over-coordination energy term imposes a penalty for over-coordinated atoms. The undercoordination energy term takes into account the energy contribution for resonances of n electrons between connected under-coordinated atomic centers. $E_{penalty}$ is the penalty for molecules of the "allene"-type ($H_2C=C=CH_2$), and E_{conj} is a term that considers the effects of conjugation on molecular energy. Every term in equation 3.2 expresses the bond order and refers to a specific chemical bond. Only the element type is considered, and no atom type, such as hybridization, is accounted for. The bond order between a pair of atoms is derived directly from the interatomic distance and includes contributions from σ , π , and $\pi-\pi$ bonds. Due to the geometry-dependent charge calculation technique in reactive force fields, polarization effects can be taken into consideration. ReaxFF's ability to accurately explain bond dissociation and effectively mimic chemical processes is one of its key advantages.

3.2. Quantum mechanics methods

Quantum theory was introduced at the beginning of the 20th century and succeeded in properly describing the atomistic structure of matter. To study the electronic properties of materials, such as bonding phenomenon and charge transfer, quantum mechanics theory needs to be applied instead of classical descriptions. Classical approaches are especially not adequately reliable to describe the phenomena in chemical interactions, e.g., bonding formation. The quantum theory is in principle, an exact theory, but different approximations are applied to make use of it in practical applications. In the following sub-sections, firstly, a brief review has been provided on the basic concepts of the quantum theory.

Afterward, the necessary approximations to make this theory applicable and affordable for computer simulations are presented. The review papers, such as ^[85], can be referred to as comprehensive studies on quantum theory.

3.2.1. Basic aspects of quantum mechanics

The foundation of quantum mechanics is the concept of “wave function”, or $\Psi(\mathbf{x}, t)$, which describes the state of a particular system. The Schrödinger equation may be solved to get the wave function $\Psi(\mathbf{x}, t)$. The time-dependent Schrödinger equation is:

$$i\hbar \frac{d\Psi(\mathbf{x}, t)}{dt} = \hat{H}(\mathbf{x}, t)\Psi(\mathbf{x}, t) \quad (3.3)$$

where $\hat{H}(\mathbf{x}, t)$ is time-dependent Hamiltonian of the system, and \hbar is the reduced Planck's constant. In the time-independent Schrödinger equation, we can divide the wave function into two spatial and time parts ($\Psi(\mathbf{x}, t) = \psi(\mathbf{x})\varphi(t)$), and we can write:

$$\hat{H}(\mathbf{x})\psi(\mathbf{x}) = E\psi(\mathbf{x}) \quad (3.4)$$

The Hamiltonian of a system is then:

$$\begin{aligned} \hat{H} = & - \sum_i \frac{\hbar^2 \nabla_r^2}{2m_e} - \sum_I \frac{\hbar^2 \nabla_r^2}{2M_I} - \sum_{i,I} \frac{Z_I \mathbf{e}^2}{|\vec{R}_I - \vec{r}_i|} + \frac{1}{2} \sum_{i \neq j} \frac{\mathbf{e}^2}{|\vec{r}_i - \vec{r}_j|} \\ & + \sum_{I,J} \frac{Z_I Z_J \mathbf{e}^2}{|\vec{R}_I - \vec{R}_J|} \end{aligned} \quad (3.5)$$

It is a sum of quantum operators defining kinetic energy of nuclei, kinetic energy of electrons, electron-nuclei attraction, electron-electron repulsion, and nucleus-nucleus repulsion. In this equation, the indices i and j run over the total number of electrons, and I and J run over nuclei. The mass of electrons and nuclei are represented by m_e and M_I respectively. The positions of the electrons and the atoms in space are given by \vec{r}_i and \vec{R}_I . The atomic number of the nuclei is Z_I and \mathbf{e} is the electron charge.

3.2.2. Born-Oppenheimer approximations

As the system size grows, calculating equation 3.3 with a Hamiltonian of equation 3.5 becomes highly challenging or even impossible for a many-body system. The Born-Oppenheimer approximation (BO) is hence one of the key approximations used. According to this assumption, ions travel slowly in space, while electrons react immediately to any ionic motion. As a result, the wavefunction Ψ depends only on the electronic degrees of freedom and the potential between the nuclei and the kinetic energy of the nuclei are treated as constants. Therefore, equation 3.5 is simplified to:

$$\hat{H} = -\sum_i \frac{\hbar^2}{2m_e} - \sum_{i,I} \frac{Z_I e^2}{|\vec{R}_I - \vec{r}_i|} + \frac{1}{2} \sum_{i \neq j} \frac{e^2}{|\vec{r}_i - \vec{r}_j|} \quad (3.6)$$
$$V_{ion}(\vec{r}_i) = \sum_{i,I} \frac{Z_I e^2}{|\vec{R}_I - \vec{r}_i|}$$

3.2.3. Basis set

Basis set are a proper set of basis functions that are used to represent $\psi(\mathbf{x})$, to make the solution of the time-independent Schrödinger equation straightforward. For instance, by using a set of atomic orbitals $\phi_i(\mathbf{x})$ which are practical for molecular systems, the wave function $\psi(\mathbf{x})$ could be written as a Linear Combination of Atomic Orbitals (LCAO):

$$\psi(\mathbf{x}) = \sum_{i=1}^K c_i \phi_i(\mathbf{x}) \quad (3.7)$$

Now, one can consider the Schrödinger equation solved only by finding expansion coefficients c_i . The atomic orbitals $\phi_i(\mathbf{x})$ could be approximated by Slater-type orbitals, which are a series of Gaussian-type orbitals with analytical atomic integrals.

3.2.4. Hartree-Fock method

Hartree-Fock (HF) approaches are the origins of contemporary quantum mechanics modelling techniques^[86,87]. The HF method assumes that each electron moves independently of the others in the field generated by the solid nuclei (BO approximation) and the mean field of the other electrons. The HF technique approximates a solution to the Schrödinger equation. It requires that the final field calculated from the charge distribution be

"self-consistent" with the assumed initial field (self-consistent field method, SCF).

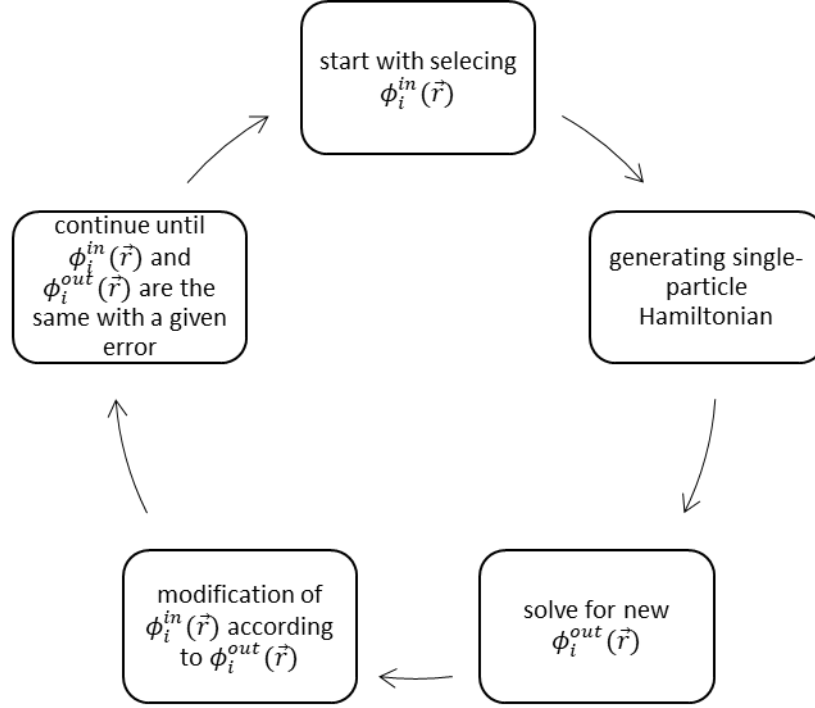


Figure 3.2. Scheme of the self-consistent field (SCF) algorithm. ^[80]

A single Slater determinant maps the electrical wavefunction. The following Slater determinant may thus be used to represent the many-body wavefunction Ψ^{HF} for N electron in the HF framework, supposing that $\phi_i(\vec{r}_i)$ are the normalized single-particle states, and that i is the index running over the single particles, i.e., electrons:

$$\Psi^{HF}(\{\vec{r}_i\}) = \frac{1}{\sqrt{N!}} \det\{\phi_i(\vec{r}_i)\} \quad (3.8)$$

The expectation value of the Hamiltonian of the many-body systems with respect to Ψ^{HF} is then the total energy of the system.

$$\begin{aligned}
 E^{HF} &= \langle \Psi^{HF} | H | \Psi^{HF} \rangle \\
 &= \sum_i \left\langle \phi_i \left| -\frac{\hbar^2 \nabla_r^2}{2m_e} + V_{ion}(\vec{r}^i) \right| \phi_i \right\rangle \\
 &\quad + \frac{e^2}{2} \sum_{i \neq j} \left\langle \phi_i \phi_j \left| \frac{1}{|\vec{r}^i - \vec{r}^j|} \right| \phi_i \phi_j \right\rangle
 \end{aligned} \quad (3.9)$$

The kinetic energy and the ionic potential (the interactions between the electrons and nuclei) are included in the initial summation of this

equation. The interactions between electrons are taken into consideration in the second summation. The single-particle HF equation then can be written as ^[80]:

$$\begin{aligned} \varepsilon_i \phi_i(\vec{r}^i) = & \left[-\frac{\hbar^2 \nabla_r^2}{2m_e} + V_{ion}(\vec{r}^i) + V_i^H(\vec{r}^i) \right] \phi_i(\vec{r}^i) \\ & - e^2 \delta_{s_i, s_j} \sum_{i \neq j} \left\langle \phi_j \left| \frac{1}{|\vec{r}^i - \vec{r}^j|} \right| \phi_i \right\rangle \phi_j(\vec{r}^i) \end{aligned} \quad (3.10)$$

where the second term is the “exchange” term between electrons. The Hartree potential, which varies for each electron and takes into account repulsion from neighbouring electrons, is represented by $V_i^H(\vec{r})$, and the spin of the particles i and j are labelled by $s_{i/j}$. The self-consistent solution of equation 3.10 using the iterative approach, shown in Figure 3.2, is usually implemented for HF simulations.

3.2.5. Density functional theory (DFT)

In order to solve the Schrödinger equation, the HF (and post-HF approaches) are all dependent on efforts to employ adequate approximations to the many-body wavefunctions. In 1964 Hohenberg and Kohn formulated a theory that made a new path to approach the problem. According to Hohenberg and Kohn’s theory, a system’s ground state electron density uniquely identifies the acting single-electron potential ^[88]. This density controls the Hamiltonian and all the properties of the ground state. An energy functional $E[\rho]$ then can be defined that provides the exact ground state energy for the exact ground state density. The energy is minimized for this exact density.

The fundamental idea behind DFT is that the overall density of electrons of the system n is considered rather than the many-body wavefunction Ψ so it is not necessary to define Ψ . In theory, DFT builds single-particle equations and then applies approximations. If $\Psi(\vec{r}_1, \dots, \vec{r}_N)$ is the total wavefunction of an electronic system, the electronic density of the ground state can be written as:

$$n(\vec{r}) = N \int \Psi^*(\vec{r}_1, \dots, \vec{r}_N) \Psi(\vec{r}_1, \dots, \vec{r}_N) d\vec{r}_2 \dots d\vec{r}_N \quad (3.11)$$

where \vec{r}_i represents the location of electron i . The universal operators for every N-electron system, the kinetic energy T , the electron-electron interaction W , and the external potential V , all determine the Hamiltonian. The following can be represented as a density universal functional:

$$F[n(\vec{r})] = \langle \Psi(n) | (T + W) | \Psi(n) \rangle \quad (3.12)$$

and the total energy of the system may be stated as:

$$E[n(\vec{r})] = \langle \Psi | H | \Psi \rangle = F[n(\vec{r})] + \int V(\vec{r})n(\vec{r})d\vec{r} \quad (3.13)$$

The functional may be further stated as follows by using the basic functions ($\phi_i(\vec{r})$) and one- and two-particle densities:

$$F[n(\vec{r})] = T^S[n(\vec{r})] + \frac{e^2}{2} \iint \frac{n(\vec{r}')n(\vec{r}'')}{|\vec{r}' - \vec{r}''|} d\vec{r}' d\vec{r}'' + E^{XC}[n(\vec{r})] \quad (3.14)$$

where $E^{XC}[n(\vec{r})]$ refers to all exchange and correlation effects and is often broken down into an exchange term and a correlation term in the most widely used models:

$$E^{XC}[n(\vec{r})] = \int [\varepsilon^x[n(\vec{r})] + \varepsilon^{cor}[n(\vec{r})]]n(\vec{r}) d\vec{r} \quad (3.15)$$

The single-particle potential energy equation, known as Kohn-Sham equation, is produced by applying the variational principle to density and also Langrange multipliers:

$$\left[-\frac{\hbar^2}{2m_e} \nabla^2 + V_{eff}(\vec{r}, n(\vec{r})) \right] \phi_i(\vec{r}) = \varepsilon_i \phi_i(\vec{r}) \quad (3.16)$$

The effective potential (which is again a function of density) can also be stated as:

$$V_{eff}(\vec{r}, n(\vec{r})) = V(\vec{r}) + e^2 \int \frac{n(\vec{r}')}{|\vec{r}' - \vec{r}|} d\vec{r}' + \frac{\delta E^{XC}[n(\vec{r})]}{\delta n(\vec{r})} \quad (3.17)$$

Equation 3.17 has three terms: the external potential, the kinetic energy, and the variational functional derivative of the exchange-correlation interaction, respectively. The system's solution may be calculated by iteratively solving the Kohn-Sham equations in equation 3.16 until self-consistency is obtained. The DFT algorithm is quite similar to the computer approach for solving the HF equations shown in Figure 3.2. Following a guess for the initial electron density, the corresponding Kohn-Sham equations are solved. Every SCF step compares the new electron density to the original estimate after applying the solution. This process is repeated until the input and output electron densities converge within a predetermined tolerance.

3.2.6. Density functional tight binding (DFTB)

DFT is a reliable and popular electronic structure approach. However, DFT is too expensive (in terms of simulation time) to handle complex systems with a large number of atoms/electrons. There are conventional force fields that can handle millions of atoms. Still, they are only helpful when there are no chemical events, such as bond creation or bond breaking, or when the underlying electronic structure is not of interest. An approach that bridges this gap is known as the tight-binding method. In conventional tight binding, the eigenstates of the Hamiltonian are extended on a basis made of a linear combination of atomic orbitals, which describes tightly bonded electrons to an atom or in a solid:

$$\phi_i(\vec{r}) = \sum_A \sum_{\mu \in A} c_{\mu i} \phi_{\mu}(\vec{r} - \vec{R}_A) \quad (3.18)$$

The eigenstates are expanded using one basis function $\phi_{\mu}(\vec{r} - \vec{R}_A)$ for each orbital at atom A , known as a minimum basis. Equation 3.18 converts the solution of the Kohn-Sham equations from a non-linear problem to a set of linear equations for the coefficients $c_{\mu i}$:

$$\sum_A \sum_{\nu \in A} c_{\nu i} (H_{\mu\nu} - \varepsilon_i S_{\mu\nu}) = 0 \quad (3.19)$$

where $S_{\mu\nu}$ and $H_{\mu\nu}$ are the overlap and Hamilton matrix, respectively, and are given as:

$$H_{\mu\nu} = \langle \phi_{\mu} | \hat{H} | \phi_{\nu} \rangle \quad S_{\mu\nu} = \langle \phi_{\mu} | \phi_{\nu} \rangle \quad (3.20)$$

The more recent and efficient method in the tight-binding scheme is DFT-based tight binding or density functional tight binding (DFTB) formalism^[89–91] which has been developed over the two-three decades and is comprehensively described in several review articles^[92–94]. In Figure 3.3, one can see the position of DFTB among the other three typical simulation approaches.

The fundamental concept of DFTB is an expansion of the density $\rho(r) = \rho_0(r) + \Delta\rho(r)$ around a reference density $\rho_0(r)$. By substitution of this into the total DFT energy and also accounting for the nucleus-nucleus interaction, the total DFTB energy is given by:

$$\begin{aligned}
E_{DFTB}[\rho_0 + \Delta\rho] &= \sum_i n_i \int \phi_i^* \left(-\frac{\nabla^2}{2} + V^{ne} + \int' \frac{\rho'_0}{|\vec{r}' - \vec{r}'|} + V^{XC}[\rho_0] \right) \phi_i \\
&+ E_{rep} \\
&+ \frac{1}{2} \int' \int \left(\frac{1}{|\vec{r}' - \vec{r}'|} + \frac{\delta^2 E^{XC}[\rho]}{\delta\rho\delta\rho'} \Big|_{\rho_0, \rho'_0} \right) \Delta\rho\Delta\rho' \quad (3.21) \\
&+ \frac{1}{6} \int'' \int' \int \frac{\delta^3 E^{XC}[\rho]}{\delta\rho\delta\rho'\delta\rho''} \Big|_{\rho_0, \rho'_0, \rho''_0} \Delta\rho\Delta\rho'\Delta\rho'' + \dots
\end{aligned}$$

All of the energy from the reference density ρ_0 is provided in the first line of equation 3.21. The nucleus-nucleus interaction and exchange-correlation contributions, as well as the portions of the energy that occur from double counting in the first line, are all represented by the term E_{rep} in the second line.

$$E_{rep} = \frac{1}{2} \sum_{A,B} V_{AB}^{rep} [\rho_{0A}, \rho_{0B}, r_{AB}] \quad (3.22)$$

where ρ_{0A} and ρ_{0B} are the reference densities of atoms A and B, respectively and $r_{AB} = |\vec{R}_B - \vec{R}_A|$. The pair potentials V_{AB}^{rep} are obtained from DFT calculations for the corresponding reference system.

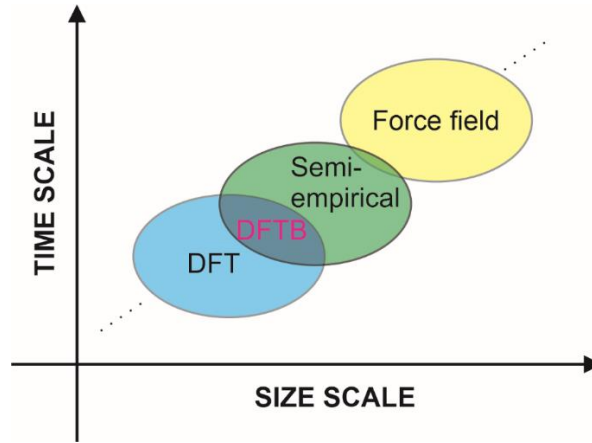


Figure 3.3. DFTB position in simulation methods used in materials science, based on time and size scales.

Lines two and three of Equation 3.21 provide details on density changes up to the second and third orders, respectively. Depending on where the energy is truncated, a certain degree of DFTB is employed. The method relates to a non-self-consistent DFTB technique if the total energy is only approximated using the first two lines. This level of approximation

cannot appropriately model materials such as ZnO; hence the second order estimate of the energy is employed (first three lines in Equation 3.21). Finally, the total DFTB energy can be written as:

$$E_{DFTB}[\rho_0 + \Delta\rho] = \sum_{iAB} \sum_{v \in A} \sum_{\mu \in B} n_i c_{vi} c_{\mu i} H_{v\mu}^0 + E_{rep} + E^{2nd}[\rho_0, \Delta\rho] \quad (3.23)$$

The atom-centered pseudoatomic wave functions are expressed as spherical harmonics and Slater-type orbitals as:

$$\phi_{\mu}(\vec{r}) = \sum_{n,\alpha,l_{\mu},m_{\mu}} a_{n\alpha} r^{l_{\mu}+n} \exp(-\alpha r) Y_{l_{\mu},m_{\mu}}\left(\frac{\vec{r}}{r}\right) \quad (3.24)$$

l and m are the azimuthal and magnetic quantum numbers. Five different values for α and $n = 0, 1, 2, \text{ and } 3$ form a converged basis set^[95] for elements up to the third row. Through the self-consistent solution of the atomic Kohn-Sham equations, the coefficients, $a_{n\alpha}$, are found:

$$\left[-\frac{1}{2} \nabla^2 + V^{psat}(\vec{r}) \right] \phi_{\mu}(\vec{r}) = \varepsilon_{\mu}^{psat} \phi_{\mu}(\vec{r}) \quad (3.25)$$

where V^{psat} is expanded by a term $\left(\frac{r}{r_c}\right)^2$ to consider the compression of the potential due to interatomic interaction. The Hamilton matrix elements are approximated by using density overlap of the form:

$$H_{\mu\nu}^0 = \begin{cases} \varepsilon^{free\ atom} & \mu = \nu \\ \langle \phi_{\mu} | \hat{T} + V[\rho_{0A}, \rho_{0B},] | \phi_{\nu} \rangle & A \neq B \\ 0 & A = B, \mu \neq \nu \end{cases} \quad (3.26)$$

in which the potential $V[\rho_{0A}, \rho_{0B},]$ is without the compression term $\left(\frac{r}{r_c}\right)$.

The only remaining term in equation 3.23 that needs to be determined is the second order energy term E^{2nd} . Here, the density fluctuations are considered to be a superposition of atomic contributions determined by Mulliken analysis:

$$E^{2nd} \approx \frac{1}{2} \sum_{AB} \Delta q_A \Delta q_B \gamma_{AB} \quad (3.27)$$

where γ_{AB} is an analytic function^[91] representing the interaction between the charge density fluctuations. In^[91], a more thorough explanation of the approximation in the second order term and the precise formula for γ_{AB} are provided. Now the corresponding Kohn-Sham equations should be

solved self-consistently to calculate the coefficients of the LCAO expansion. The well-known Slater-Koster files are fundamental to any DFTB computation in which for different types of atom pair at different interatomic distances, the overlap matrix element $S_{\mu\nu}$ and the Hamilton matrix element $H_{\mu\nu}^0$ are listed.

3.3. Molecular dynamics

Molecular dynamics (MD) can be considered a virtual laboratory method by which one can study the behaviour of atoms as a function of time. This technique makes it possible to relate the macroscopic features of a system to its microscopic structure. It can be implemented in various scales and fields, from studying surfaces and hybrid interfaces to complex systems such as proteins. In the following sub-sections, the fundamental aspects and some essential concepts of MD which are necessary to understand our results (the parts in which MD has been employed) are briefly reviewed.

3.3.1. Basic MD concepts

MD classically describes the motion of N atoms in a physical system. It is believed that the particles interact, and Newton's equations of motion ($\vec{F}_i = m_i \vec{a}_i$) may be quantitatively solved to determine these interactions. The total potential energy $E(\{\vec{r}_j\})$, which is derived from the inter-particle potentials, clearly relates the forces acting on the particles to the inter-particle interactions:

$$\vec{F}_i = -\nabla E(\{\vec{r}_j\}) \quad (3.28)$$

In so-called Hamilton's description, a Hamiltonian for the system is defined as:

$$H(\{\vec{r}_j\}, \{\vec{p}_j\}) = V(\{\vec{r}_j\}(t)) + \sum_{i=1}^{3N} \frac{p_i^2(t)}{2m_i} \quad (3.29)$$

where p_i is the momentum of particle i . Potential energy is presented in the first term, followed by kinetic energy. The motion equations then can be derived from the Hamiltonian:

$$\vec{r}_i = \frac{\partial H}{\partial p_i}, \quad \vec{p}_i = -\frac{\partial H}{\partial r_i} \quad (3.30)$$

which connects the microscopic states to macroscopic properties. Statistical ensembles and statistical mechanics methods are then employed to make this connection possible. The often employed ensembles are the micro-canonical, canonical, and isobaric/isothermal ensembles (NPT). For instance, in an MD simulation at a constant volume V and temperature T (the NVT canonical ensemble), the average kinetic energy relates to the set temperature.

3.3.2. Considering environment conditions

In MD simulations, setting the environment conditions may be done directly by utilizing thermostats (for applying a fixed temperature) or barostats (for applying pressure). A thermostat's basic operation is to produce a statistical ensemble at a set temperature (in NVT simulations) and adjust the system's temperature by altering Newtonian dynamics. A barostat has a manner similar to thermostats but for controlling the pressure (in NPT simulations). In the absence of any of these, the microcanonical (NVE) ensemble is sampled by the MD simulations since it is the ensemble that results from Newtonian dynamics, which preserves the total energy. There are several thermostats and barostats available in the literature. One can find a lengthy and detailed analysis of various thermostats and barostats in ^[96] and ^[97], respectively. Here, we introduce the Berendsen barostat by which the MD simulations in this work have been performed in the NPT ensemble.

Berendsen Barostat

The Berendsen barostat introduces a new term into the equations of motion, resulting in a change in pressure of:

$$\left(\frac{dp}{dt}\right)_{bath} = \frac{p_0 - p}{\tau_p} \quad (3.31)$$

where the system's goal and actual pressures are, respectively, p_0 and p (at the current time step). The coupling is controlled by the time constant τ_p , which also regulates pressure variations. The positions and velocities are rescaled by $\dot{r} = v + \alpha r$, where α is a parameter related to the isothermal compressibility.

3.3.3. Numerical integration

If the number of particles in a system exceeds three, Newton's equations of motion can be solved only numerically by numerical integration. A Taylor expansion is often used to get the integration of the motion equations. The Taylor expansion of the equations of motion, up to orders of three and two, would be provided through:

$$\vec{r}_i(t + \Delta t) = \vec{r}_i(t) + \Delta t \cdot \vec{v}_i(t) + \frac{(\Delta t)^2}{2m_i} \vec{F}_i(t) + \mathcal{O}((\Delta t)^3) \quad (3.32)$$

$$\vec{v}_i(t + \Delta t) = \vec{v}_i(t) + \frac{\Delta t}{m_i} \vec{F}_i(t) + \mathcal{O}((\Delta t)^2)$$

where \vec{r}_i , \vec{v}_i , and \vec{F}_i are the position, velocity, and force acting on particle i , and Δt is the time-step in the simulations, and t is the time. Although integration strategies are highly effective, they are not the best for simulating physical systems. One must consider the following criteria for selecting a method of integration: accuracy, energy conservation, time-reversibility, and preservation of the phase-space in the simulations. Euler ^[98], Verlet ^[99], Leap-frog ^[100], and Velocity-Verlet ^[101] are some examples of the well-known integration schemes frequently used in MD simulations. Readers are referred to ^[80] to read a well-structured review of the integration schemes in MD.

4. RESULTS - Defects in ZnO crystal structures

There are several non-ideal features in the structure of real ZnO materials, such as surface and subsurface defects, existence of common dopants such as rare earth elements, and surface chemistry including the hydroxylation phenomenon. To provide a deeper insight into the properties of ZnO materials in reality, in this Chapter we summarize our computational study of some of the most common and important non-idealities in the structure of ZnO lattice and their effects on the material electronic and optical characteristics. More details can be found in the enclosed paper *J. Phys. Chem. C* 127 (2023) 22177, doi:[10.1021/acs.jpcc.3c05471](https://doi.org/10.1021/acs.jpcc.3c05471), and its supplementary materials in Appendix F. Computational study of interactions between ZnO structures with biomolecules will be then presented in subsequent Chapters.

4.1. Computational details

We performed density functional theory calculations to investigate the impacts of vacancies and dopant atoms in ZnO lattice on atomic and electronic scales. All the structures have been optimized using the DFT method, The generalized gradient approximation (GGA) exchange-correlation, and the Perdew–Burke–Ernzerhof (PBE) functional. Afterward, the structures' electronic and optical properties were calculated using the DFT-1/2 method and the same exchange-correlation and functional. By creating an atomic self-energy potential that cancels the electron-hole self-interaction energy, the DFT-1/2 technique corrects the DFT self-interaction error. This potential is determined for atomic sites in the system and is defined as the difference between the neutral atom's potential and a charged ion's potential after removing a fraction of the atom's charge. The sum of these atomic potentials is the overall self-energy potential. The DFT Hamiltonian with added DFT-1/2 self-energy

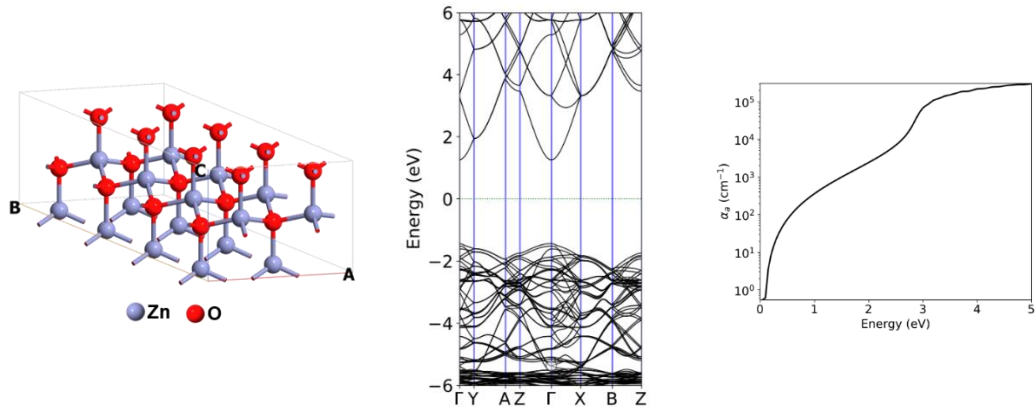
potential has been found to considerably enhance band gaps for various semiconducting and insulating systems ^[102,103]. We used a supercell of Wurtzite structure with a total of 32 atoms inside. The supercells were allowed to relax to the minimum energy with periodic boundary conditions and criteria of force tolerance of 0.01 eV/Å and stress error tolerance of 0.001 eV/Å³.

4.2. Zinc and oxygen vacancies

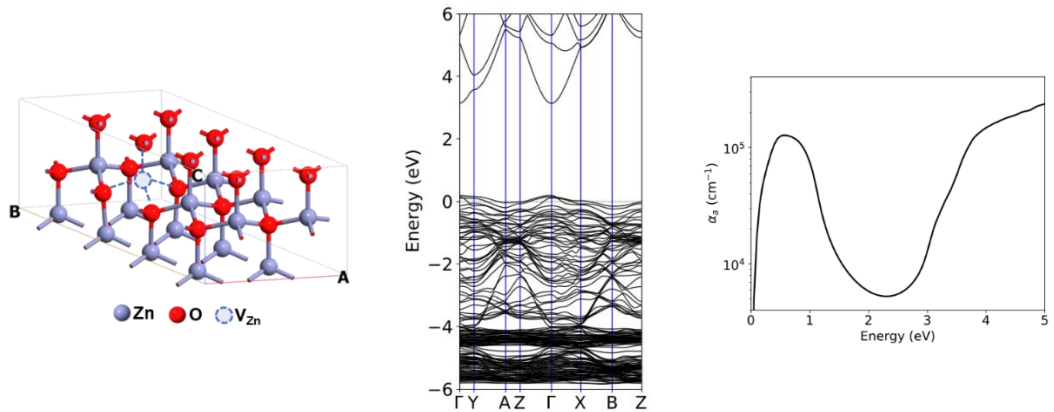
The oxygen (V_O) and zinc (V_{Zn}) vacancies, among other defects found in ZnO, are important for several reasons. Firstly, because they are thought to be the ZnO defects with the lowest formation energies, their presence in undoped ZnO is extremely likely ^[104]. Secondly, these vacancies have one of the most noticeable and significant effects on the modification of ZnO, supported by both experimental research and theoretical studies ^[46,105]. For instance, it has been suggested that the presence of oxygen vacancies enhances the use of UV light and stretches the absorption edge into the visible light spectrum, resulting in a rise in the efficiency of different photocatalytic and photoelectrochemical processes ^[106]. Furthermore, it was shown that zinc vacancies result in the emergence of room-temperature ferromagnetism ^[107], which may be used in innovative spintronic devices, such as magnetoresistive sensors or memory.

Based on the DFT-1/2 simulations we found that these vacancies have also substantial effects on the ZnO band structure and optical properties such as absorbance spectrum. In Figure 4.1, one can see the structural properties, the electronic band structure, and the absorbance coefficient of the ZnO with zinc and oxygen vacancies. A Zn vacancy pushes the system towards a p-type semiconductor. While zinc vacancy results in p-type behaviour in the bandstructure, oxygen vacancy does not cause n-type behaviour, but it is a potential source of compensation in p-type ZnO.

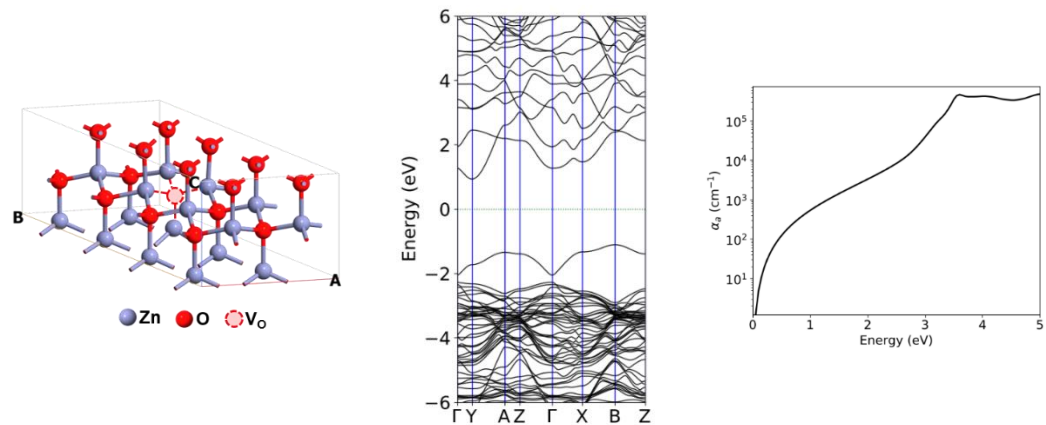
1. ZnO pristine



2. ZnO with single Zn vacancy



3. ZnO with single O vacancy



4. ZnO with single Zn and O vacancies

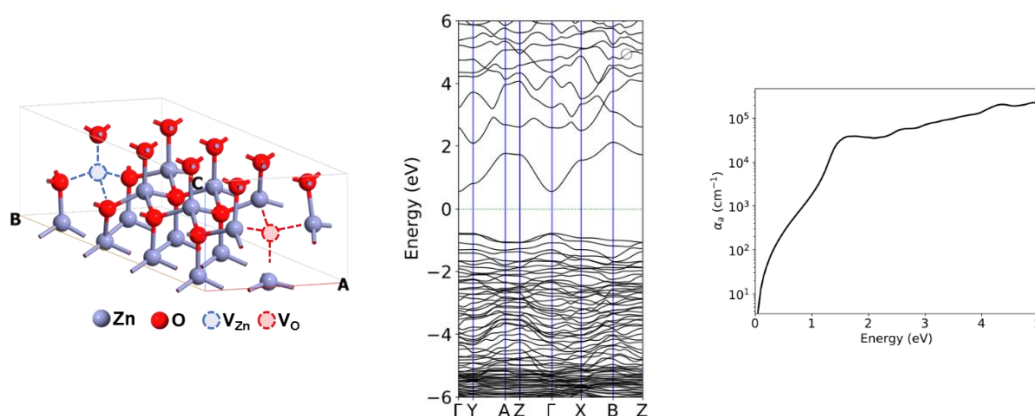


Figure 4.1. Atomic scheme of relaxed structure, band structure diagram, and optical absorbance coefficient of 1. pristine ZnO and 2.-4. ZnO with zinc and oxygen vacancies as obtained by DFT-1/2 simulations.

4.3. Adding a dopant: erbium doped ZnO

The electronic/optical and structural characteristics of the semiconductor materials may be changed and controlled by the doping process. For example, doping and co-doping ZnO with metals including In, Ga, Al, Co, Fe, and Ni is a popular practice. It was discovered that doping with such metals altered the optical, electrical, and structural characteristics of ZnO and led to new uses for the material. In the case of ZnO, there has also been a lot of interest in rare earth elements in the ZnO matrix, which enhance and modify the optical properties. Erbium is the most common rare earth dopant in ZnO among other rare earths, and this is due to its favourable energy level transition, which improves its optical and electrical properties and allows for new applications like waveguides and up-down-shifting solar cells. Most studies on Er-doped ZnO have concentrated on the photoemission at 1.54 μm , but little attention has been devoted to how Er affects the structure, microstructure, and optical characteristics of ZnO. Since such properties need to be studied theoretically, too, there are also some theoretical studies on erbium-doped ZnO in the literature^[108,109]. However, only a few possible scenarios of Er doping have been investigated in these studies.

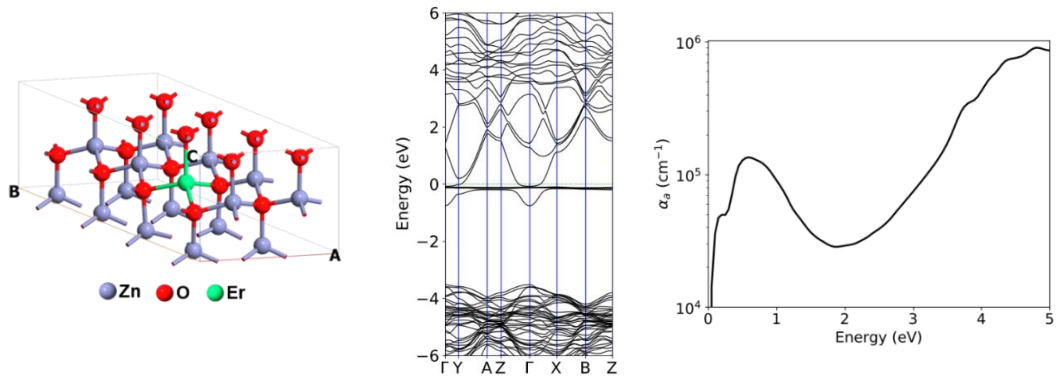
In this work, we thus implemented the DFT-1/2 method to comprehensively study the effects of Er doping in different possible sites

along with varying kinds of defects on ZnO electronic and optical properties.

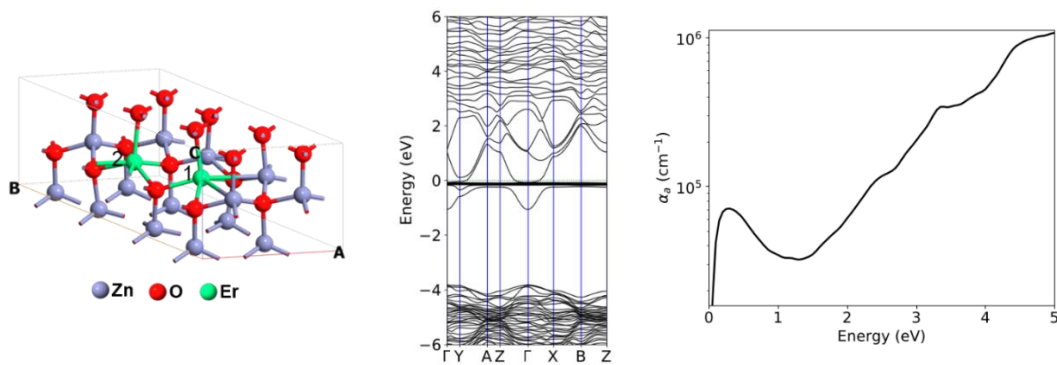
Figure 4.2 shows the structure, absorption coefficient, and bandstructure for different possible scenarios of erbium doping in the ZnO structure. One can see that ZnO preserves its crystalline structure for all erbium-doped systems with substitutional erbium defects. In contrast, the interstitial erbium dopant agitates the ZnO crystal, resulting in an amorphous structure around the doping agent. This is in good agreement with the hydrogen and oxygen plasma treatment of free-standing ZnO:Er nano- and microrods [ZnO_Er H_O], where the presence of an amorphous phase was detected in the hydrogen plasma treated ZnO:Er(1%) sample [110]. However, interestingly, as soon as the V_{Zn} appears in the close vicinity of the Er (model 13), the erbium ion moves and fills in the zinc vacancy during the optimization process. The final relaxed system again exhibits a crystalline structure.

In the bandstructure shown in Figure 4.2, one can see the localized states near the Fermi level (zero) attributed to the f-orbital of the doped erbium atom. From Figure 4.1 and Figure 4.2, we can compare the bandstructure of pristine ZnO with the bandstructures of all studied systems. The following results could be found from the bandstructure comparison: i) Erbium-doped systems generally have more condensed bands, especially valance bands, and ii) in erbium-doped systems, 4f orbital of erbium localizes around the Fermi level. With 4f orbital of erbium atoms, the Fermi level has been shifted upward and into the conduction band. A Zn vacancy has an opposite effect and pushes the system towards a p-type semiconductor. For all the models, the absorption spectra were calculated as well as shown in Figure 4.2. By qualitatively (considering only the shape) comparing them with the experimentally obtained absorptance spectra in Figure A1 in the Appendix, one may infer that the theoretically predicted model 2 from the previous Section and models (5-9, 12, 13) are the closest to the experimentally observed absorptance of the undoped ZnO NRA (Figure A1a) and ZnO:Er(1%) NRA (Figure A1b), respectively. They exhibit one relatively broad band peaking at about 0.75 eV, and the other band strongly overlapped with the absorption edge covering the about 1-2 eV range (starting from approximately 1.5-1.8 eV) of visible light. The position of the first band correlates very well with the position of the experimentally observed A0 band. The position of the second band is in good agreement with the localization of the experimental A1,2 bands.

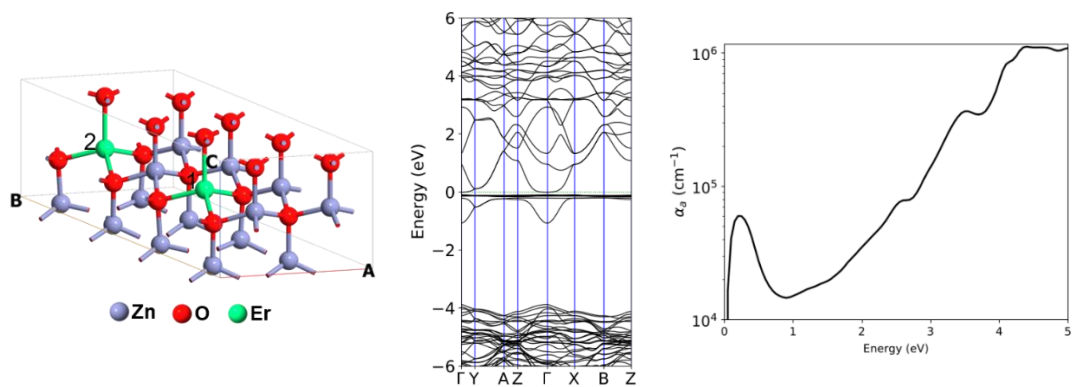
5. ZnO:Er, single Er atom



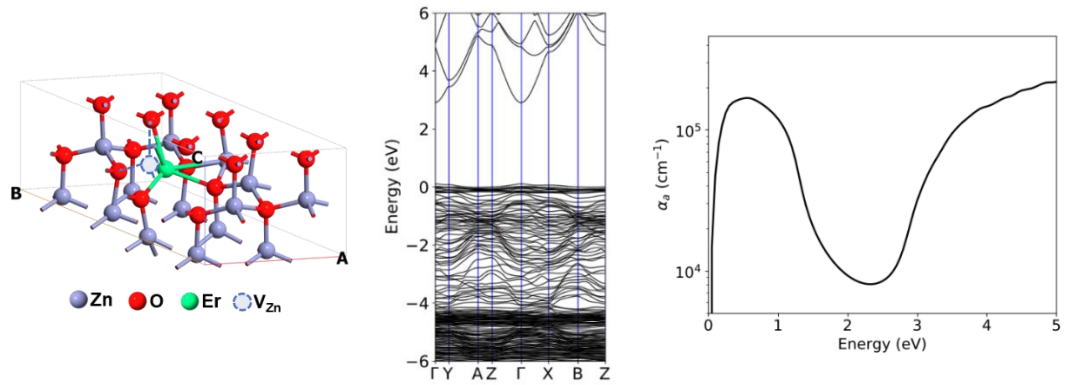
6. ZnO:Er, two Er atoms next to each other



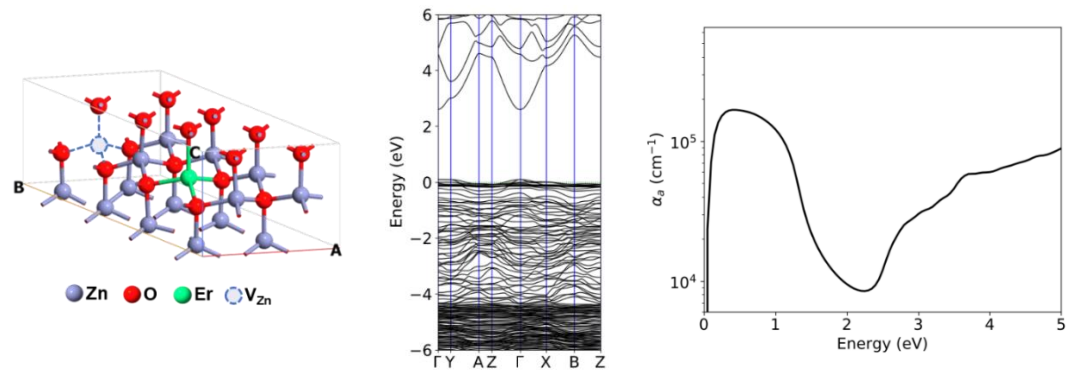
7. ZnO:Er, two Er atoms far from each other



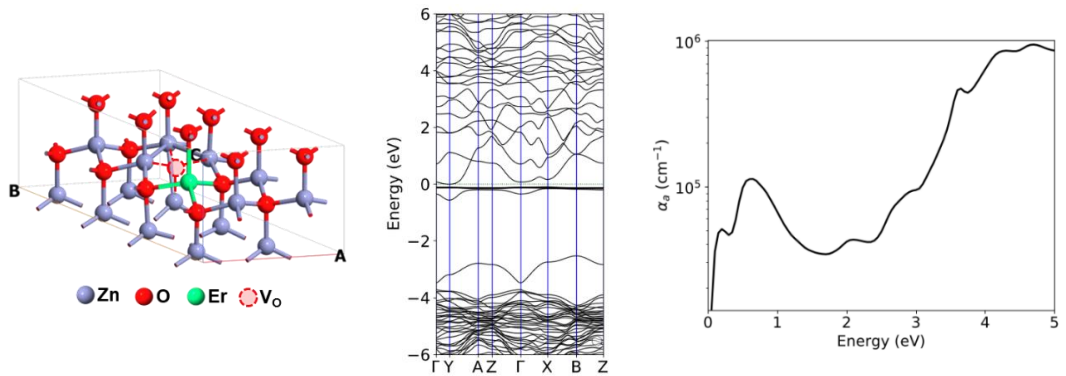
8. ZnO:Er, single Er atom next to single Zn vacancy



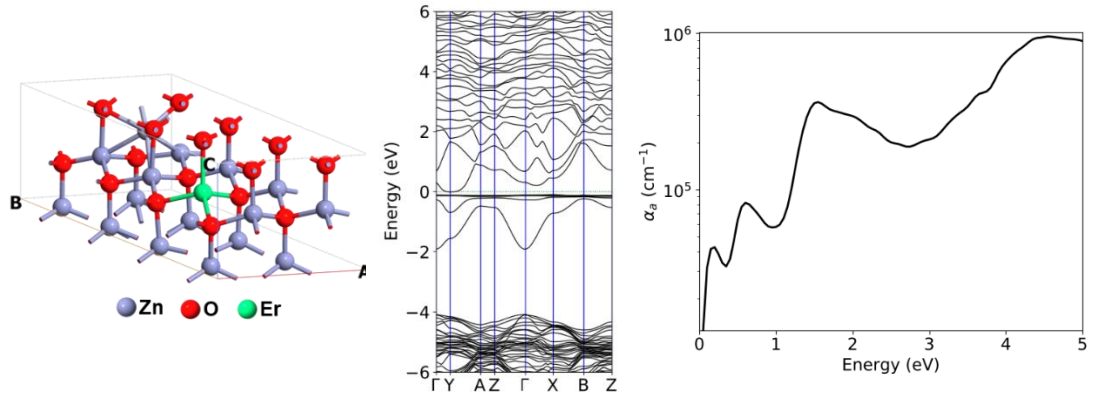
9. ZnO:Er, single Er atom far from Zn vacancy



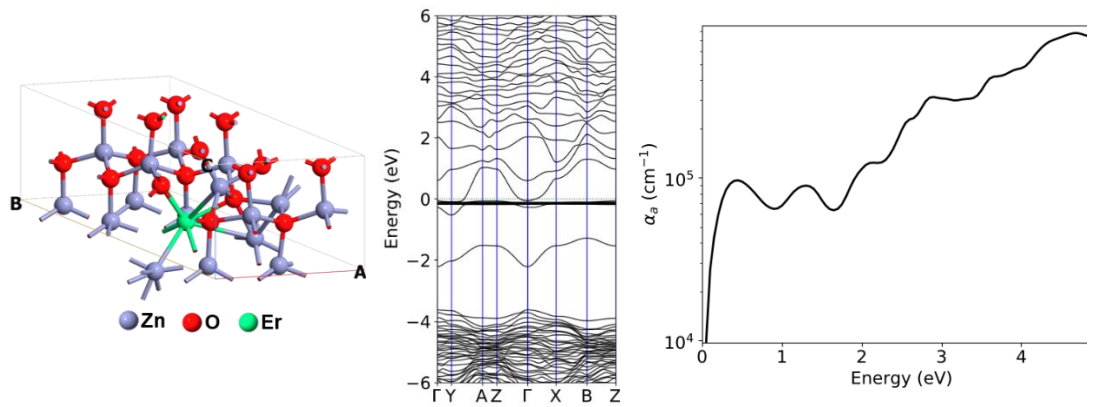
10. ZnO:Er, single Er atom along with O vacancy



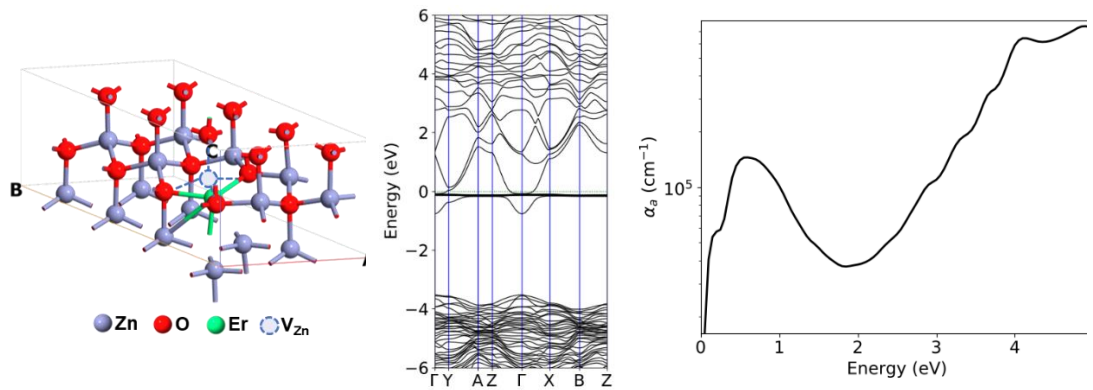
11. ZnO:Er, single Er along with interstitial Zn defect



12. ZnO:Er, single interstitial Er atom



13. ZnO:Er, single interstitial Er atom along with Zn vacancy



14. ZnO:Er, single interstitial Er atom along with O vacancy

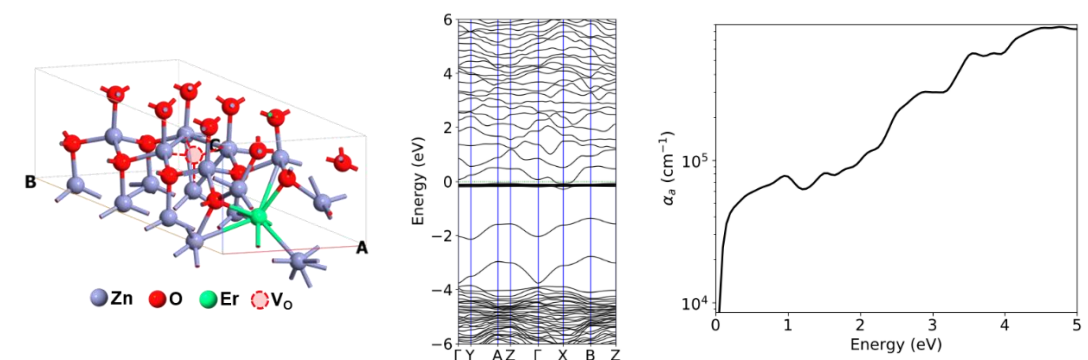


Figure 4.2. Atomic scheme of relaxed structure, bandstructure diagram, and optical absorbance coefficient of erbium doped ZnO with zinc and oxygen vacancies as obtained by DFT-1/2 simulations.

The result of the Bader charge analysis for the doped erbium atom is shown in Table 4.1. The valence configuration of erbium atom is [6s² 4f¹²], representing 14 valence electrons. Bader charge analysis shows almost 12 valence electrons for the doped erbium atom(s) in all optimized systems. It means that the erbium atom loses nearly two electrons, becoming Er²⁺ in all studied configurations, including the ZnO doped by one erbium atom in an interstitial site. All these considerations led to the conclusion that, in principle, Er²⁺ may substitute for the regular Zn with and without V_{Zn} or V_O in the local surroundings or be interstitial in ZnO host.

We believe that these significant modifications in the electronic and optical characteristics of ZnO can affect the interactions of these materials with molecules such as biomolecules studied in this work, which opens a new horizon to the current research. The study of biomolecules interfaces with ZnO structures with vacancies and dopants such as erbium can lead us to ZnO-based structures with new electronic and optoelectronic properties, which can be useful for a variety of applications from biosensing to photovoltaics.

Table 4.1. Summary of Bader charge analysis results. Number of calculated valence electrons after relaxation for erbium atoms in the erbium-doped ZnO structures. The original number of valence electrons of free erbium is 14.

Structures	Erbium 1	Erbium 2
5	12.00	-
6	12.02	11.97
7	12.02	12.02
8	11.59	-
9	11.75	-
10	12.01	-
11	12.04	-
12	11.98	-
13	12.00	-
14	11.98	-

5. RESULTS - Bovine serum albumin (BSA) adsorption on ZnO surfaces

The orientation preference of a whole BSA molecule on different ZnO surfaces is investigated in Section 5.1. The study is based on a comparison of the total energy of the ZnO-BSA system at different orientations of BSA. The ReaxFF potential was selected to describe interactions between atoms. As mentioned in Chapter 3, force field calculations cannot give reliable information about a system's chemical bonding and electronic properties. Although in force field simulations of this work, ReaxFF has been employed, which is a well-known force field in describing chemical interactions such as chemical bonding to some extent, any information on binding (and electronic) phenomena needs to be validated by an electronic simulation method. Nevertheless, the ReaxFF force field not only provided the results about the total energy of the system but also guided us in selecting the proper parts of the system for more precise simulations. This is especially crucial because performing higher-level calculations is too costly and even impossible for ZnO-BSA system with a whole BSA molecule. Smaller parts of the system must be selected for any further electronic calculations.

DFT popular and efficient approaches, such as local and gradient density approximations (LDA and GGA) are known to be unable to give a good description of ZnO (and generally metal-oxides) electronic properties ^[111–114]. For example, these methods significantly underestimate the bandgap of ZnO and other metal-oxide systems ^[115]. This problem can be solved by implementing DFT+U or hybrid techniques, which are even more computationally costly than GGA and LDA methods. The other option is the DFTB method which is especially a good candidate due to the large number of systems that need to be studied in this work. DFTB provides a precise band structure of ZnO with a bandgap close to the experimental value. Furthermore, its reliability for

describing ZnO-biomolecule systems has also been tested in multiple research ^[32,116].

Therefore, in Section 5.2, the DFTB calculations were employed for some specific parts of the system where the chemical reactions were observed in force field calculations in Section 5.1. These selected parts include particular amino acids (AAs) of BSA (see Figure 1.1) interacting with the surface atoms of ZnO. Results of the ZnO-AAs interactions not only help us understand the ZnO-BSA interactions at the electronic level but also can be important and interesting independently as they provide information about ZnO-AAs interactions. Totally, the binding and electronic properties of 20 selected ZnO-AAs structures are studied in detail using DFTB simulations. Finally, it is worth mentioning that the simulation results are supported by complementary experimental AFM study data for both the force field and DFTB calculations.

The main results and computational setting are briefly summarized below. More details can be found in the enclosed papers IOP Conference Series: Materials Science and Engineering 2021, 1050, 012006. doi:[10.1088/1757-899x/1050/1/012006](https://doi.org/10.1088/1757-899x/1050/1/012006), Physica Status Solidi (a) 2021, 218 (6), 2000558. doi: [10.1002/pssa.202000558](https://doi.org/10.1002/pssa.202000558), and ChemPhysChem 2022, 23 (2), e202100639. doi: [10.1002/cphc.202100639](https://doi.org/10.1002/cphc.202100639) including their supplementary materials in Appendix F.

5.1. Orientation preference of BSA on ZnO surfaces

5.1.1. Computational details

The systems under the study consist of a BSA molecule on four ZnO slabs. BSA molecules are available from the RCSB Protein Data Bank website (PDB ID of 4F5S), and ZO slabs were cleaved from a bulk ZnO structure in the QuantumATK software database. Since hydrogen atoms are generally not observed in X-ray crystal structures, the BSA structure from the Protein Data Bank lacks hydrogen atoms. Mol Probitry has been employed to add hydrogens to the BSA molecule. Some approximations were also considered to provide the feasibility of using predefined force field potential sets as there are no sets of force fields defined for all types of atoms in the ZnO-BSA system. Sulfur atoms have been excluded from the structure of the BSA molecule to enable ReaxFF potential for force field simulations. This seems a reasonable simplification as sulfur atoms in BSA are not situated at or near the locations where the molecule interacts with ZnO. The reliability of ReaxFF potential for describing interactions between ZnO surfaces with biomolecules has been shown in

multiple studies such as ^[117]. To deduce the volume and duration of the calculations, different orientations of BSA molecules have been manually adjusted over ZnO surfaces in the distance range of 3-20 Å. The systems were relaxed to stable configurations with criteria of force tolerance of 0.01 eV/Å and stress error tolerance of 0.001 eV/Å³. The optimization trajectory and total energy of the system then have been observed to discuss the interactions of the BSA molecule with ZnO planes.

The simulations were carried out for different orientations of BSA over nonpolar and polar ZnO planes. Figure 5.1 depicts five non-equivalent configurations used for forcefield simulations based on the direction of BSA molecule versus ZnO surface: Head, Side, Flat, Legs, and Tip. The distance between the nearest atom of the BSA molecule and the surface of ZnO slab was set manually at around 3 Å for all configurations. The simulations were also performed for the distance of 20 Å, where there was no interaction between the BSA molecule and ZnO surface detected regardless of the orientation of BSA.

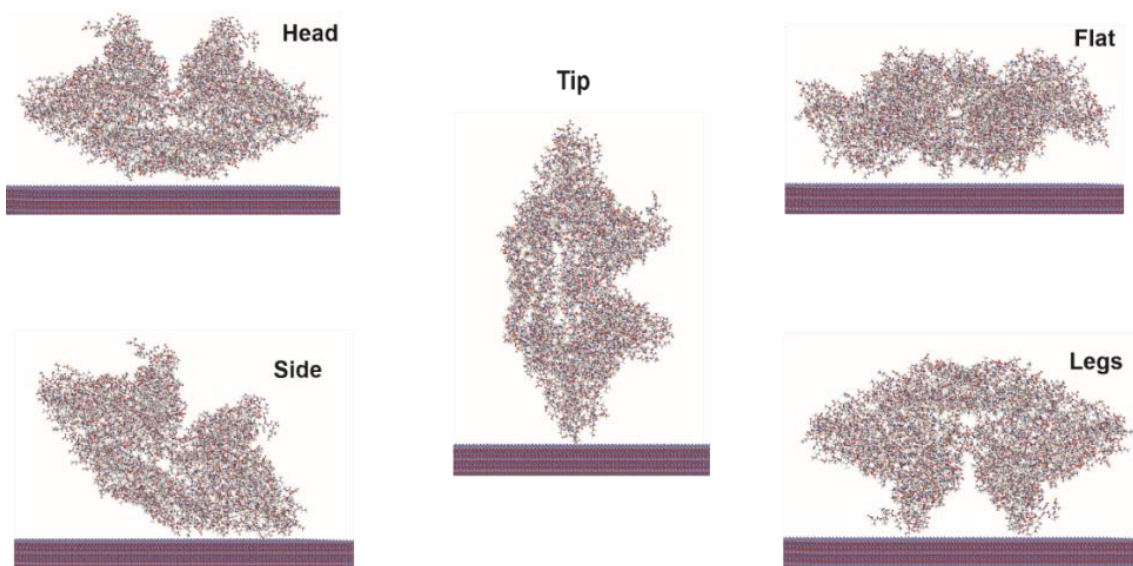


Figure 5.1. Different orientations of BSA molecule versus ZnO surface

5.1.2. The most favourable orientations of BSA on ZnO

To compare different orientations of BSA and determine the most likely one over each ZnO plane, total energy of the system is displayed via bar graphs in Figure 5.2. Since the orientation of the BSA molecule is the only varying aspect and other characteristics of the systems remain entirely

unaffected, the total energy of the systems can be observed to deduce the favourable position. According to the total energy graphs in Figure 5.2, the tendency of the BSA molecule to be adsorbed on ZnO nonpolar and polar Zn-faced surfaces is noticeably different for different orientations. The Head orientation has the lowest energy in the BSA-ZnO (0001) system, and thus it is the most likely orientation over ZnO (0001) surface. The Side orientation has been observed as the most favourable for BSA-ZnO (10 $\bar{1}$ 0) and BSA-ZnO (11 $\bar{2}$ 0) systems. For the O-faced ZnO surface, the situation is slightly different. The system's total energy is almost the same for all orientations except for the Tip orientation, which has the minimum value. This means that the Tip orientation is expected to be the most favourable orientation on the O-faced surface.

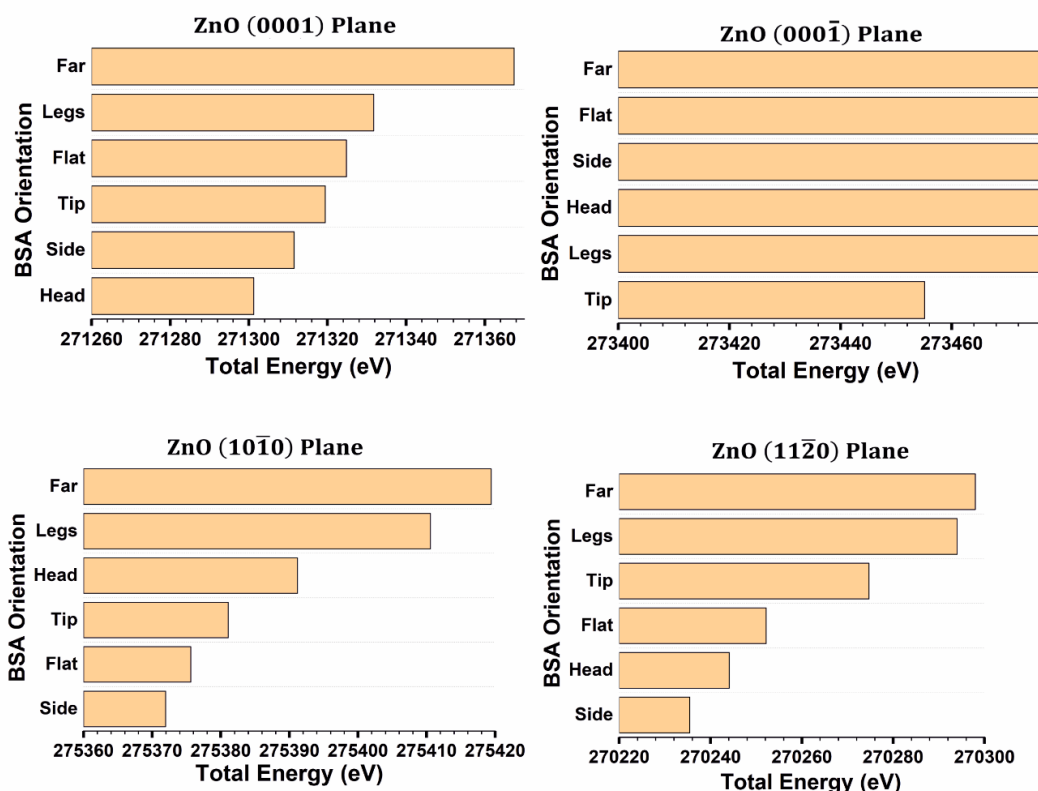


Figure 5.2. Total energies of the ZnO-BSA system for different orientations of BSA on different ZnO surfaces

The different orientation preferences of BSA can directly affect the roughness and thickness of adsorbed BSA molecules on different ZnO surfaces. Table 5.1 shows the root mean square (RMS) roughness and average height of the BSA molecule on various ZnO facets. These values are calculated based on the ZnO-BSA relaxed structures in which the BSA is oriented in the most favourable position on each surface.

Table 5.1. RMS roughness and the average height of BSA molecule on ZnO surfaces determined in force field calculations

ZnO-BSA system	RMS roughness of BSA molecule in force field simulations (Å)	The average height of BSA molecule in force field simulations (Å)
polar Zn-faced (0001)	15.4	45.7
polar O-faced (000 $\bar{1}$)	26.4	103.0
non-polar (10 $\bar{1}$ 0)	20.4	53.3
non-polar (11 $\bar{2}$ 0)	20.1	52.9

To support the calculation results, the results have been compared with experimental atomic force microscopy (AFM) morphology results. Figure 5.3a compares the BSA layer thickness defined by AFM and average height of the BSA molecule obtained in the simulation. Figure 5.3b compares the RMS roughness of the BSA layer obtained by AFM and force field simulations (See Table A1 in the appendix for exact AFM values). Both dependencies show good agreement between experimental and theoretical results. We consider only the relative difference between different ZnO surfaces in experiments and computing. Two to three times observed differences in absolute values for experiment and computing could be due to the deformation of molecules by the AFM tip. Readers are encouraged to see the appendix (Table A1 and Figure A2) for more information on AFM morphology results.

The key finding is the high thickness of the BSA layer on the polar O-face (000 $\bar{1}$) ZnO surface. This is clearly explained by force field simulations showing that the BSA molecule adopts a vertical orientation on polar O-faced (000 $\bar{1}$) plane. On the other hand, lower values of BSA layer thickness on the other three surfaces might be because the BSA molecules are attracted to all other ZnO surfaces with more horizontal orientations. RMS roughness values of BSA layers measured in AFM also correspond well to RMS roughness values of BSA molecules defined by

force field simulations. The only discrepancy is the non-polar $(11\bar{2}0)$ facet. The reason could be the slightly higher aggregation of BSA molecules on non-polar $(11\bar{2}0)$ ZnO surface compared to the other three ZnO surfaces.

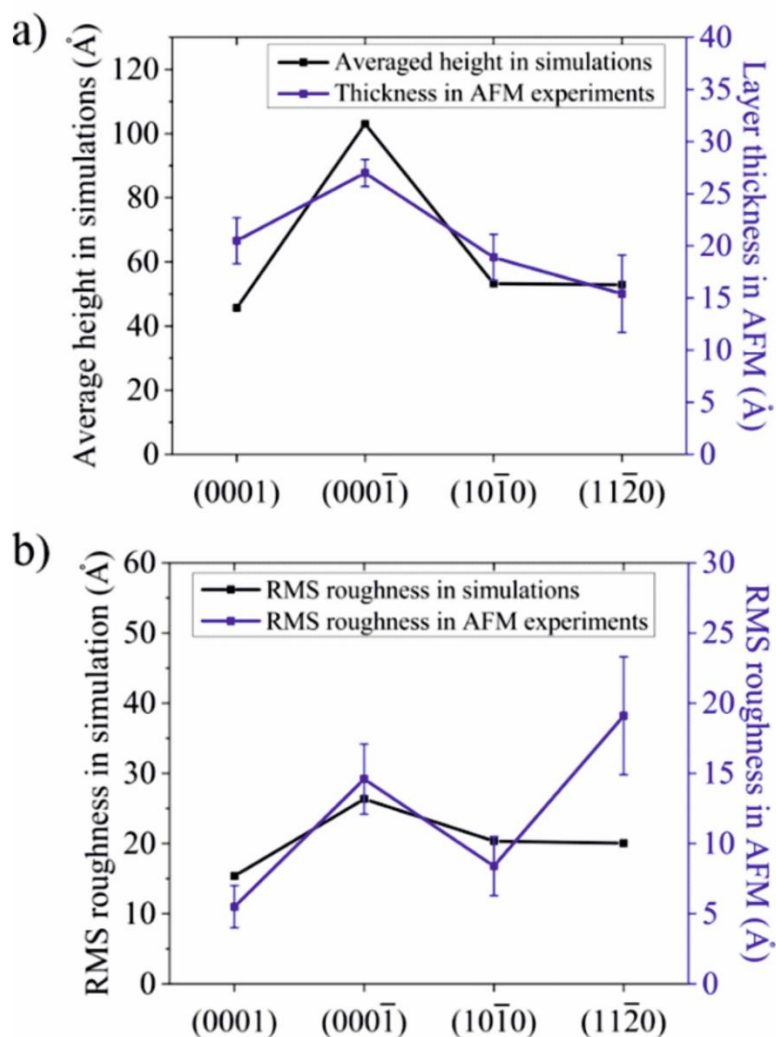


Figure 5.3. Comparison between *a)* RMS roughness of BSA layer obtained by AFM and force field simulations, *b)* BSA layer thickness defined by AFM and averaged height of BSA molecule obtained by force field simulations.

The further important observation in force field simulation is different interaction mechanisms. The mechanism of interactions is not identical in the most favourable positions over different planes and depends on the different groups of atoms from the BSA molecule and the type of the ZnO plane. Atoms are differently re-arranged, and the adsorption might occur through either physisorption or chemisorption. Figure 5.4 shows examples of observed interactions in forcefield

simulations for BSA molecule over ZnO non-polar and polar planes (See Figure A4 in the appendix for all images).

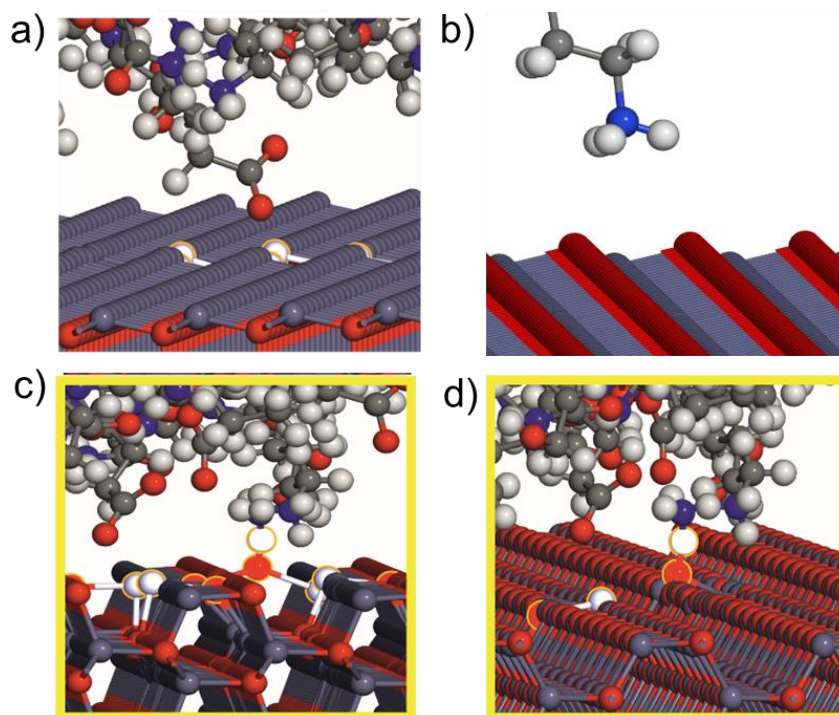


Figure 5.4. Magnified images of BSA-ZnO interaction sites for different orientations of BSA over ZnO **a)** (0001), **b)** (000 $\bar{1}$), **c)** (10 $\bar{1}$ 0), and **d)** (11 $\bar{2}$ 0) planes. The structures are results of force field simulations. Yellow frames denote the configurations in which chemical bonding happens in the calculations.

In all cases, the proximity of BSA molecule amino acid residues (AAs) to the ZnO surface has culminated in mutual attraction, followed by re-arrangement of surface atoms on the ZnO slab. The exception is the O-faced surface that repelled the BSA in all orientations. In addition to these displacements, chemical bonding of atoms from the BSA molecule with atoms on the ZnO surface can also be seen at interaction sites in Side and Tip orientations over (10 $\bar{1}$ 0) plane, as well as Side and Flat orientations over (11 $\bar{2}$ 0) plane. In these cases, highlighted by yellow frames in Figure 5.4, chemical bonding happens between hydrogen atoms of the BSA molecule and surface oxygen atoms of ZnO. For (0001) surface, no chemical bonding has been observed since it contains only Zn atoms, compared to nonpolar surfaces, which include both Zn and O atoms. It must be mentioned here that more accurate electron-based calculations must be employed to investigate the chemical bonding phenomena and validate the observed chemical bonds. Nevertheless, the

results obtained from the current force field simulations will be helpful for the selection of relevant parts of the system for more expensive calculations. Validating the chemical bonding phenomena observed in force field simulations by employing the DFTB method is going to be done in the next Section.

In summary, in this part, we employed force field simulations to investigate the interactions of BSA molecule with ZnO nonpolar and polar surfaces. The total energy indicates that the BSA molecule is likely to adsorb in different orientation on different ZnO surfaces. The way how BSA molecule interacts with ZnO surfaces depends on the type of ZnO surface as well as the orientation of the BSA molecule. The computational results demonstrate that the vicinity of BSA molecule with ZnO surfaces results in re-arrangement of atoms on ZnO surfaces that lowers the total energy and gives rise to physical binding. Furthermore, chemical bonding between BSA atoms and ZnO surface has also been observed in several configurations, which needs to be validated by more accurate (but more costly) electron-based simulation methods. This may have important implications for interaction of ZnO with biological environment as well as impact its optical and electronic properties.

5.2. Binding of BSA amino acids to ZnO surfaces

5.2.1. Computational details

In this Section, DFTB calculations were done for some selected segments of our large BSA-ZnO systems to verify and understand the results of our study in the force field Section and the binding and electronic properties of the structures. DFTB calculations were done for various ZnO surfaces, and specific AAs (ASP, GLU, GLN, LYS, and SER) were selected based on the interacting sites of BSA with ZnO surfaces in force field calculations. The directions of AAs were also selected based on their exposure to ZnO surfaces in force field calculations. Figure 5.5 depicts the transition from force field to DFTB calculations.

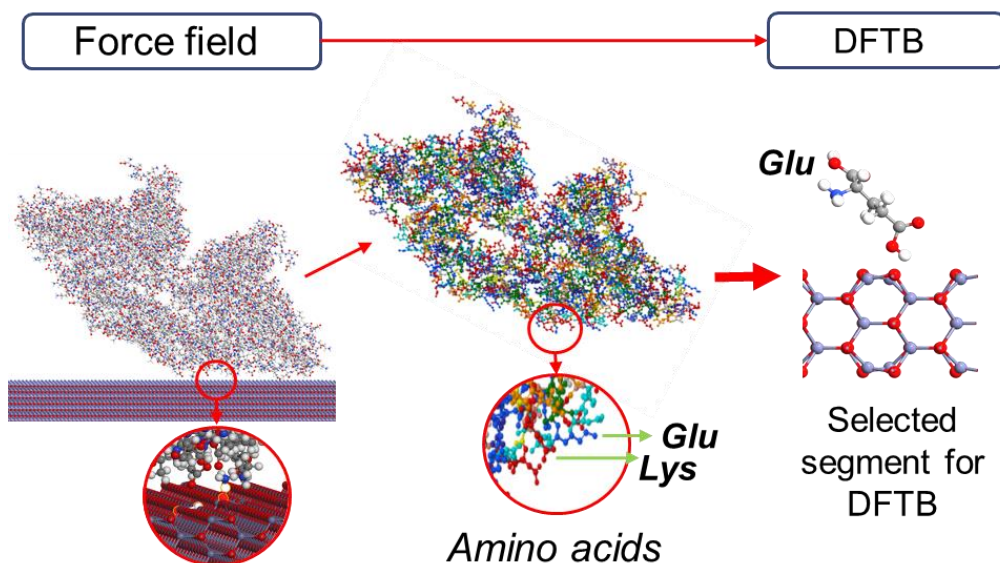


Figure 5.5. From force field to DFTB calculations

The DFTB calculations, therefore, were carried out for 20 structures: five amino acids selected based on force field calculation results over four ZnO surfaces. A self-consistent tight-binding model based on the Slater-Koster model using *znorg-0-1* parameter set, built for calculations on Zn bulk, ZnO bulk, ZnO surfaces, and ZnO interactions with organic molecules ^[118], has been implemented. The ZnO surfaces have been prepared by cleaving the ZnO bulk in four orientations of interest with the cell dimensions of $10 \times 10 \times 30 \text{ \AA}^3$. The surfaces and the molecules were allowed to relax to the minimum energy separately before running the final optimization process for molecule-on-surface systems. The molecules were then adjusted on the surfaces in similar orientations they showed favourable in force field simulations, and the whole structures were allowed to relax to the stable configurations with criteria of force tolerance of 0.01 eV/\AA and stress error tolerance of 0.001 eV/\AA^3 . The following boundary conditions have been considered in the simulations: periodic in A and B directions, Neumann under the slab, and Dirichlet above the slab.

The final relaxed ZnO polar and non-polar surfaces are illustrated in Figure 5.6. The relaxation process was relatively straightforward for two non-polar surfaces, comprising cleaving the bulk in defined directions and allowing the surfaces to relax. In contrast, doing the same process for polar surfaces would create instability due to establishing an internal dipole moment. Even though ZnO polar surfaces appear unstable and thus theoretically unfeasible, they have been proved to exist, and their stability has been subject to many studies ^[67]. Several explanations have been

proposed for their stability, such as surface vacancies and surface functional groups ^[70]. This study used surface zinc and oxygen vacancies offered in ^[119] to compensate for the internal dipole and stabilize ZnO polar surfaces for further calculations.

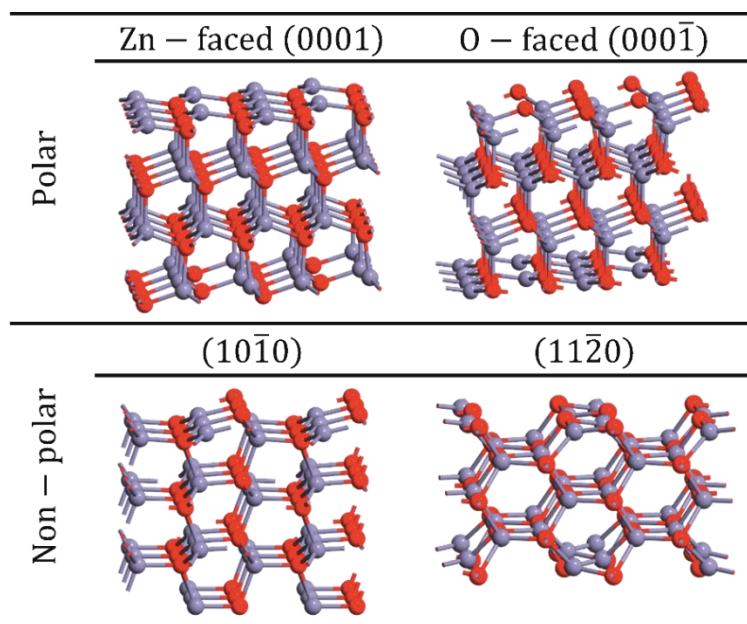


Figure 5.6. Schemes of atomic structure of ZnO polar and non-polar surfaces, as relaxed by using DFTB method.

For the 20 structures, the following characteristics have been calculated and discussed: post-contact optimized systems, the binding energy between the adsorbed amino acids and ZnO surfaces, charge transfer between the adsorbed amino acids and ZnO surfaces, and HOMO-LUMO energy levels for the post-contact structures.

5.2.2. Structural and electronic properties

Figure 5.7 shows different configurations of chemisorption of AAs on four ZnO surfaces. One can see that amino acids have been chemisorbed vertically or horizontally on non-polar and polar Zn-face surfaces through either one or two oxygen-zinc and nitrogen-zinc bonds. The same depiction for all structures can be found in Figure A5 in the appendix. For Zn-faceted (0001), (000 $\bar{1}$), and (11 $\bar{2}$ 0) surfaces, DFTB calculations confirm the formation of the covalent bonds (O-Zn and N-Zn) between the amino acids and ZnO surfaces. Through the optimization process, the amino acids approached and made bonds with the surfaces without noticeable deviation from the initially set alignments. The exception is for

($10\bar{1}0$) systems in which most amino acids deviated considerably from their commencing orientations and lay on the surface, which probably cannot be the case when one considers the amino acids connected to the BSA.

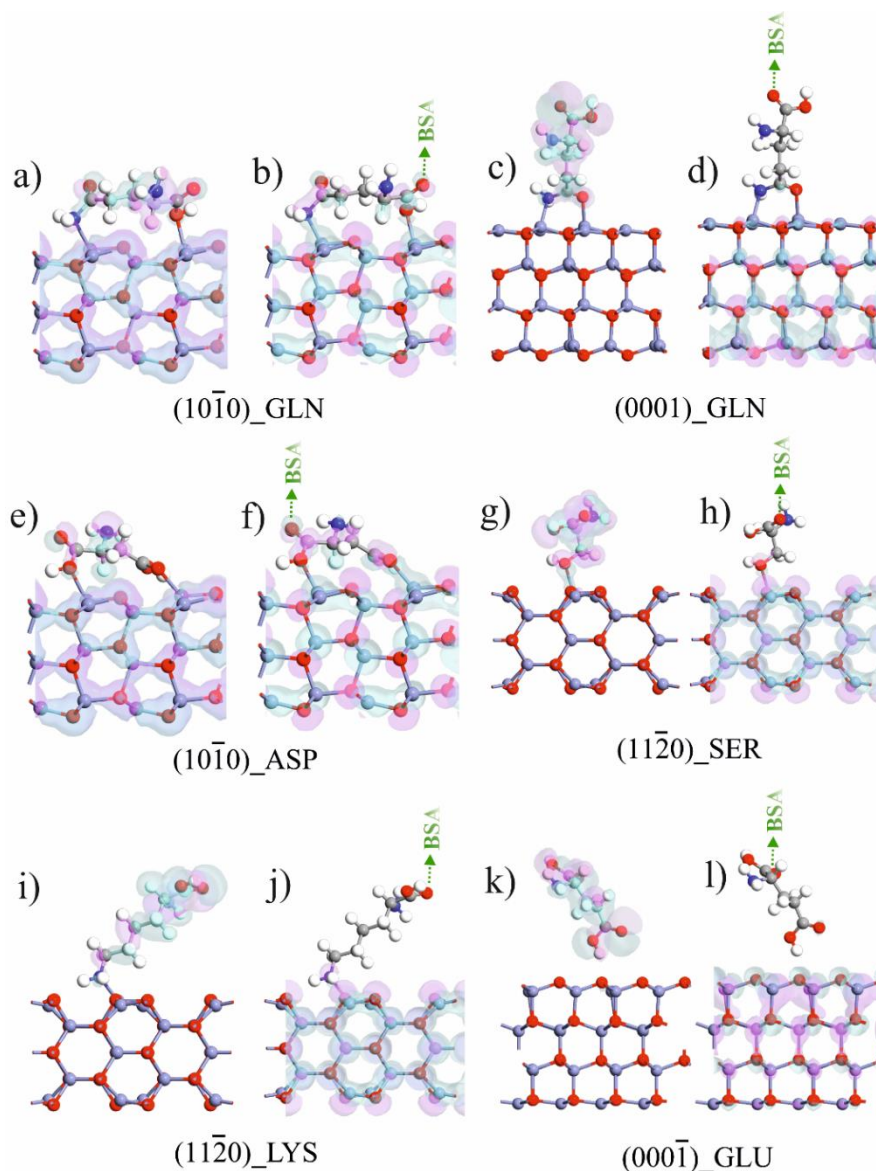


Figure 5.7. Different configurations of chemisorption of amino acids on ZnO surfaces and HOMO-LUMO distributions. Standing double O-Zn and N-Zn bonds **a)** HOMO and **b)** LUMO, lying double O-Zn and N-Zn bonds **c)** HOMO and **d)** LUMO, double O-Zn bonds **e)** HOMO and **f)** LUMO, single O-Zn bond **g)** HOMO and **h)** LUMO, single N-Zn bond **i)** HOMO and **j)** LUMO, and no bonds **k)** HOMO and **l)** LUMO.

On the other hand, the surface repelled the amino acids on the O-faced polar surface, and the systems relaxed for the distance between the surface and the molecule in the range of 2-3 Å. DFTB simulations are

done for different single amino acids on different ZnO surfaces. We believe this is reasonable since in each interaction site in our FF calculations, one specific amino acid interacts with the surface. Single amino acids are generally freer to move and can adopt different orientations compared to AAs bound in BSA. Some observed orientations of amino acids in DFTB calculations may thus not be structurally likely for the whole BSA. Yet both force field of the whole BSA molecule and DFTB with individual AAs agree well on the way of bonding to different ZnO facets. It is also worth mentioning that in our DFTB simulations, we tried to use the implicit solvent model in a few cases, such as $(11\bar{2}0)$ _GLN system (Figure 5.8). As one can see, no qualitative differences were observed in the structures and properties with and without the implicit solvent, while the calculations were several times more costly with the solvent. Therefore, the present study as a whole was conducted without the solvent.

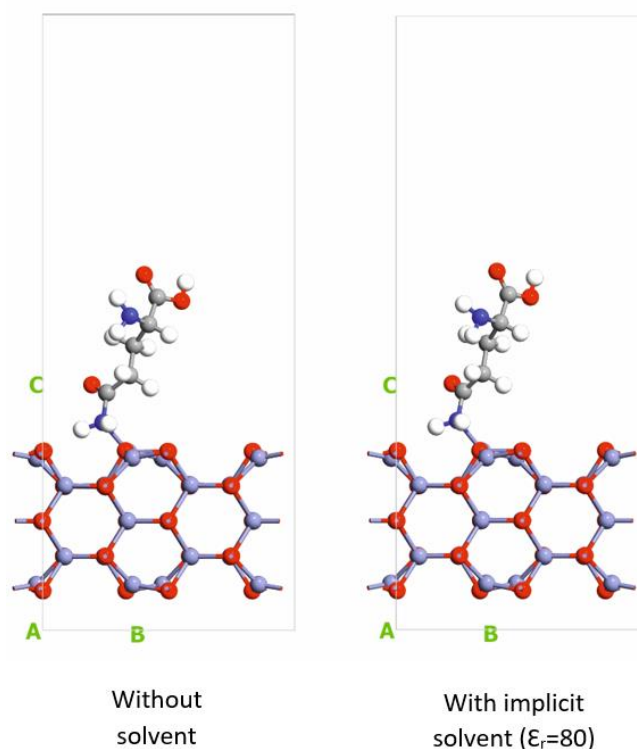


Figure 5.8. Optimized $(11\bar{2}0)$ _GLN system by DFTB, without solvent and by implicit solvent ($\epsilon_r=80$)

In addition to the optimized AA-ZnO configurations, Figure 5.7 also displays the highest occupied molecular orbital (HOMO) and lowest unoccupied molecular orbital (LUMO) for the representative structures.

All the computed structures are presented in the appendix in Figure A5. Spatially separated HOMO-LUMO levels were observed for all complexes related to $(11\bar{2}0)$ and (0001) surfaces, but for the $(10\bar{1}0)$ surface, HOMO-LUMO separation only occurred for LYS. For the O-faced surface, the HOMO-LUMO separation was seen for all amino acids except GLN. It is also worth mentioning that HOMO is placed on the amino acid for most structures with spatially separated HOMO-LUMO, while LUMO is placed on the ZnO slab. The observed spatial separation of the HOMO and LUMO can affect the separation of excitons and charge carrier transport, which could be highly interesting for sensing applications and optoelectronics.

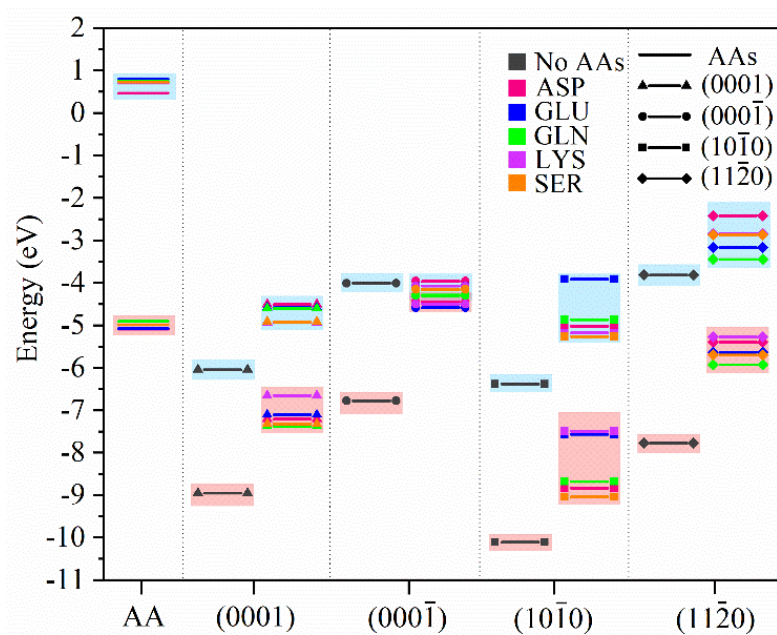


Figure 5.9. HOMO-LUMO levels for all structures, including amino acids, ZnO slabs, and all post-contact structures. (HOMOs in red and LUMOs in blue boxes)

Figure 5.9 presents HOMO-LUMO energetic levels for all structures, including amino acids, ZnO slabs, and all post-contact structures. The values of HOMO-LUMO energy gaps for all systems are listed in Table 5.2. The HOMO-LUMO gaps for ZnO slabs are 2.91 eV, 2.77 eV, 3.72 eV, and 3.96 eV for (0001) , $(000\bar{1})$, $(10\bar{1}0)$, and $(11\bar{2}0)$ respectively. Compared to the gap in bulk ZnO (3.37 eV), the HOMO-LUMO gaps in $(10\bar{1}0)$ and $(11\bar{2}0)$ slabs are higher probably because of the well-known electron confinement phenomenon that occurs in finite slabs. However, in (0001) and $(000\bar{1})$ slabs, the gaps are lower than the bulk gap, probably because of the vacancies imposed on these surfaces for the aforementioned stabilization purposes. For amino acids, the calculated

HOMO-LUMO gaps range from 5.55 to 5.87 eV. After the optimization process, the calculated HOMO-LUMO gaps for almost all (10 $\bar{1}$ 0), (11 $\bar{2}$ 0), (0001) systems decreased to the range between 1.72 eV and 3.65 eV. The exceptions are ASP, GLN, and SER over (10 $\bar{1}$ 0) surface, in which a slight increase was detected. For O-faced surface structures, HOMO-LUMO gaps decreased drastically in the AA-ZnO complexes, indicating a semi-metallic behaviour that may be interesting for some applications.

5.2.3. Binding energy and charge transfer

Binding energy (E_b) represents the energy preference of the related interaction. It can be understood as the difference in the total energies of the relaxed structures after and before contact. In this work, it is calculated according to Equation 4.1:

$$E_b = E_{sm}^t - E_s^t - E_m^t \quad (4.1)$$

where E_{sm}^t corresponds to the total energy of the structure, including molecule adsorbed on the slab surface while E_s^t and E_m^t stands for the total energies of the solo slab and solo molecule, respectively. Charge transfer between the molecules and zinc oxide surfaces was studied by calculating the atomic charge on the intrinsic and adsorbed systems.

Table 5.2 and Figure 5.10 show the calculated values for binding energy and charge transfer for all the structures. The striking result is the clear linear correlation of binding energy with the charge transfer in the AA-ZnO complexes. To our best knowledge, such trend has not been observed before, yet it is in clear agreement with other computational and AFM results. It may explain various reported photoluminescence results and opens prospects for tuning the optical and electronic properties of ZnO in biological environments ^[120,121]. The binding energies are overall negative and, therefore, exothermic (thermodynamically favourable) for all amino acids adsorbed on non-polar and Zn-faced polar surfaces, suggesting they are likely to form in real systems spontaneously. Spontaneous interactions between ZnO nanoparticles and BSA have been already reported experimentally ^[35] and it is thus supported by our simulation results. The exception is the O-faced surface, where the binding energies are close to zero.

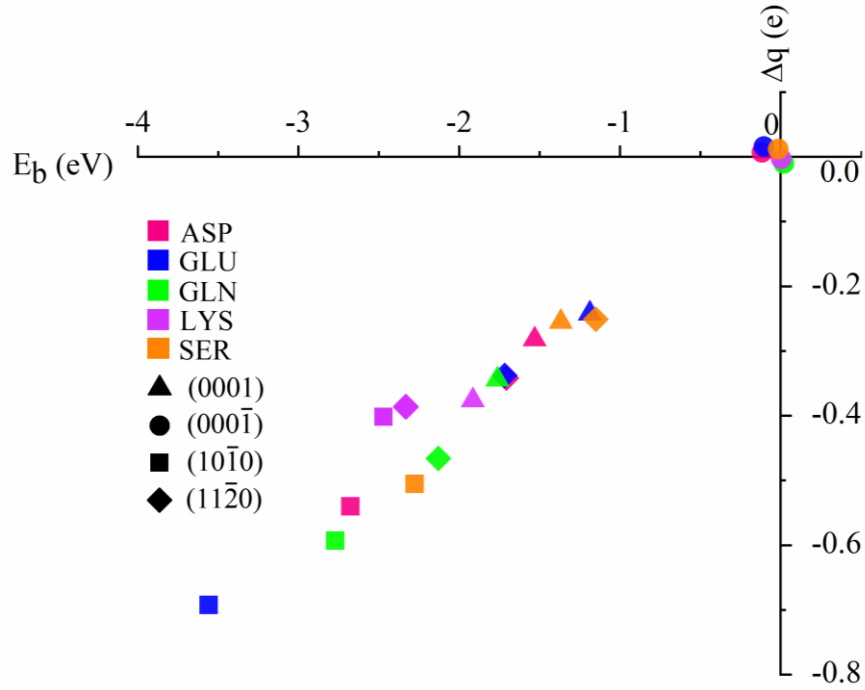


Figure 5.10. Binding energy and charge transfer for all post-contact structures

Table 5.2. Binding energy, transferred charge, and HOMO-LUMO gaps for all configurations

AAs	ZnO surface	BE (eV)	Δq (e)	H-L gap (eV)
ASP	(0001)	-1.706	-0.342	2.700
	(000 $\bar{1}$)	-0.116	0.007	0.488
	(10 $\bar{1}$ 0)	-2.676	-0.540	3.815
	(11 $\bar{2}$ 0)	-1.529	-0.282	2.979
GLU	(0001)	-1.716	-0.338	2.524
	(000 $\bar{1}$)	-0.103	0.016	0.508
	(10 $\bar{1}$ 0)	-3.557	-0.692	3.654
	(11 $\bar{2}$ 0)	-1.186	-0.242	2.463
GLN	(0001)	-2.129	-0.466	2.766
	(000 $\bar{1}$)	0.020	-0.010	0.012
	(10 $\bar{1}$ 0)	-2.772	-0.593	3.812
	(11 $\bar{2}$ 0)	-1.761	-0.344	2.480

LYS	(0001)	-1.914	-0.376	1.717
	(000 $\bar{1}$)	0.003	-0.003	0.424
	(10 $\bar{1}$ 0)	-2.470	-0.402	2.320
	(11 $\bar{2}$ 0)	-2.332	-0.386	2.430
SER	(0001)	-1.366	-0.255	2.405
	(000 $\bar{1}$)	-0.014	0.012	0.001
	(10 $\bar{1}$ 0)	-2.277	-0.505	3.774
	(11 $\bar{2}$ 0)	-1.149	-0.251	2.832

An apparent surface morphology dependency is observed. Generally, non-polar surfaces, compared to polar surfaces, show higher values for both binding energy and charge transfer. Therefore, the tendency of amino acids to be adsorbed on these surfaces seems to be higher. To be more specific, (10 $\bar{1}$ 0) surface is likely to make the most potent binding with amino acids. In contrast, the O-face (000 $\bar{1}$) surface with negligible values for both binding energy and charge transfer had the weakest interactions with ZnO surfaces.

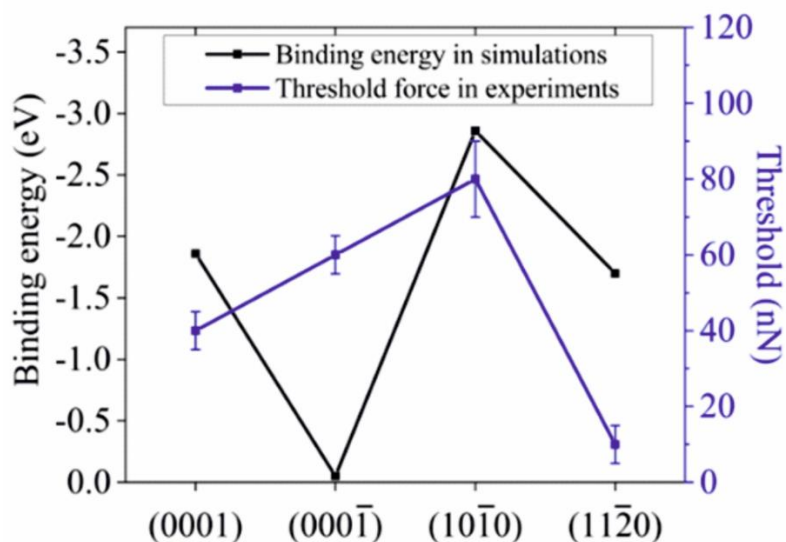


Figure 5.11. Comparison between force threshold required to remove BSA layer from ZnO surfaces by AFM tip and binding energy in DFTB simulations

To support the DFTB calculation results, they have been compared with experimental atomic force microscopy (AFM) nanoshaving experiments. The nanoshaving experiments use contact and tapping regime of AFM to determine the binding or adhesion strength of adsorbed molecules on the surface (see Table A1 and Figure A3 in the appendix for more details on nanoshaving results). Figure 5.11 compares the force threshold required to remove the BSA layer from ZnO surfaces by AFM tip and binding energy averaged values for five amino acids obtained by DFTB simulations.

The key point here is the high force threshold required to remove the BSA layer from the non-polar $(10\bar{1}0)$ ZnO surface, clearly explained by DFTB simulations indicating high binding energies and covalent bonds to Zn surface atoms for all five amino acids on non-polar $(10\bar{1}0)$ ZnO surface. Covalent bonds between organic molecules and $(10\bar{1}0)$ ZnO surface are not unprecedented. Zn-S covalent bonds are already reported experimentally for octadecanethiols on $(10\bar{1}0)$ ZnO surface ^[122]. Our results indicate that the spontaneous formation of covalent bonds between organic molecules and ZnO is a far more general effect. Extensively more adhesion of proteins on $(10\bar{1}0)$ than other ZnO surfaces has also been reported in another AFM study of ZnO surfaces ^[28] which can be appropriately justified with our DFTB calculation. The force threshold is lower for the other three surfaces because BSA molecules have lower binding energy to all other ZnO surfaces. The only discrepancy here is the O-faced $(000\bar{1})$ surface for which the BSA removal force cannot be explained based on the binding energy. This could be because the main part of the removal force on $(000\bar{1})$ surface is the force needed to penetrate the mutually tightly bound BSA layer rather than to break the binding between BSA molecules and the ZnO surface.

In this Chapter, the adsorption of BSA on various ZnO surfaces was studied experimentally and theoretically. We employed AFM topography measurements and nanoshaving method to determine the roughness, thickness, and adhesion strength of BSA on four dominant low-index ZnO surface facets. FF and DFTB calculations were also carried out to study the physics behind the interactions on atomic and electronic level. BSA layers were formed on all the studied ZnO facets. AFM measurements and FF calculations are in good agreement showing higher roughness and layer thickness for the $(000\bar{1})$ surface due to BSA particular upright orientation preference on this surface. The nanoshaving experiments indicate the strongest binding of BSA to the $(10\bar{1}0)$ plane. This is corroborated by the DFTB simulations that show the most potent binding

of BSA AAs on the $(10\bar{1}0)$ facet. DFTB simulations also reveal that the interaction between BSA AAs and ZnO surfaces affects the electronic properties of the complexes, such as charge transfer, which has a linear dependence on the binding energy, and HOMOLUMO energy levels and spatial localization (including spatial separation in many cases). The results of this study are thus highly relevant for designing ZnO-based materials and for understanding their function in various applications ranging from biomedicine and biosensing to optoelectronics.

6. RESULTS - Thiorphan adsorption on ZnO surfaces

The intriguing behavior of BSA as a biomolecule on ZnO surfaces in the previous chapter, particularly its distinct responses on various ZnO surfaces, has motivated the exploration of how biomolecules might assemble differently on different ZnO surfaces. However, such study needs performing molecular dynamics simulations for a large number of molecules on different ZnO surfaces. Performing such costly calculations for large molecules such as BSA is not possible. Thiorphan was selected as the molecule for our computational investigation into modelling of the assembly of biomolecules on ZnO surfaces. In contrast to BSA, thiorphan's smaller size enables the possibility to employ more complicated precise and computationally costly simulations, including molecular dynamics simulations involving a huge number of molecules. Thiorphan is a well-known, easily available biomolecule and its relevance as a small, zinc-related molecule makes it a fitting candidate for our study. This strategic choice aims to enhance our understanding of how surface ZnO dipoles impact molecular assembly, utilizing both experimental and computational approaches. By integrating experimental data and computational insights, we intend to obtain a full understanding of how ZnO affects molecule assembly, with thiorphan performing a crucial role in this Chapter.

Generally speaking, the ZnO surface can influence biomolecule adsorption due to the presence of Zn and O atoms on the surface or due to the presence of dipoles on the ZnO surface.

Both possibilities will be considered in the following Sections of this Chapter. Firstly, in Section 6.1, the binding structure of thiorphan to ZnO surfaces has been studied by the same simulation method and settings used for ZnO-AAs systems in the previous Chapter (DFTB/ *znorg-0-1*) to consider the impact of surface Zn and O atoms on the adsorption of one thiorphan molecule on different ZnO facets. The potential of this method

to describe binding properties between ZnO surfaces and biomolecules was proved in the previous Chapter, where it was employed for ZnO-AAs systems. To investigate the adsorption and possible aggregation of thiorphan molecules, the behaviour of many molecules should be simulated. DFTB calculations are computationally very costly, and the necessity to compensate dipole moment of ZnO surfaces in DFTB simulations leads to loss of interaction. To speed up calculations and make a more realistic analysis, the force field model has been used in Section 6.2.

In Section 6.2, the effects of surface polarity on the adsorption of thiorphan on ZnO surfaces have been investigated on a larger scale for many thiorphan molecules by using classical isothermal-isobaric ensemble (NPT) molecular dynamics simulations to resemble an actual experimental situation. The interactions between the atoms were described by the ReaxFF force field in these MD simulations. To model the surface polarity, the well-known validated C=O model dipole layer was used instead of ZnO surfaces. This approach is helpful from two aspects: firstly, the approved/validated force field parameter for the interaction of Zn atom with C, H, O, S, and N atoms is unavailable. Secondly, by using C=O dipole layer in simulations, the main parameter under the study would be merely polarity (not also ZnO surface chemistry). This is valuable because the results then could be valid and useful in a more general and wider perspective, to understand the adsorption behaviour of the biomolecules on materials with polar and non-polar surfaces generally. It is worth mentioning that the results of these calculations were in very good agreement with AFM measurements on thiorphan adsorbed on various ZnO crystal facets. The simulation results help successfully interpret the findings of the experiments.

The main results and computational settings are briefly summarized below. More details can be found in the enclosed paper Langmuir 2023, 39 (5), 1764–1774. doi: [10.1021/acs.langmuir.2c02393](https://doi.org/10.1021/acs.langmuir.2c02393), including its supplementary materials in the Appendix F.

6.1. Surface atomic structure effects on adsorption of thiorphan

6.1.1. Computational details

The method and computational settings are the same as those used in the previous Chapter in the sub-Section 5.2.1. A self-consistent tight-binding

model based on the Slater-Koster model using *znorg-0-1* parameter set, built for calculations on Zn bulk, ZnO bulk, ZnO surfaces, and ZnO interactions with organic molecules^[118], has been implemented. The ZnO surfaces have been prepared by cleaving the ZnO bulk in four orientations of interest with the settings that ensure the slabs can host thiorphan molecule with no interaction between adjacent slabs and between the surfaces at the top and bottom of the slab. The polar surfaces were cleaved by surface lattice definition vectors of 4 and 6 times in A and B directions, resulting in a slab of $13.1 \times 17 \times 40 \text{ \AA}^3$. The nonpolar surfaces were cleaved by surface lattice definition vectors three times in both directions, providing a slab of $9.8 \times 16 \times 40 \text{ \AA}^3$. The surfaces and the molecules were allowed to relax to the minimum energy separately before running the final optimization process for molecule-on-surface systems in a vacuum. The relaxation process for ZnO polar surfaces is the same as in the sub-Section 5.2.1.

6.1.2. Binding of thiorphan to ZnO surface atoms

Figure 6.1 shows the result of DFTB simulations with one thiorphan molecule placed into a vacuum above four different ZnO facets. Covalent bonding between the S atom in thiorphan molecule and Zn atom in ZnO slab was observed in the case of (0001), $(10\bar{1}0)$ and $(11\bar{2}0)$ ZnO surfaces. Contrary, thiorphan molecule was repelled by the O-faced $(000\bar{1})$ ZnO surface.

This behaviour is similar to the adsorption of amino acids on different ZnO surface facets. In those simulations, covalent bonding between N and/or O atoms in amino acids and Zn atom in ZnO slab was observed in the case of (0001), $(10\bar{1}0)$ and $(11\bar{2}0)$ ZnO surfaces. Repelling of amino acids from O-faced $(000\bar{1})$ ZnO surface was observed (see the Section 5.3).

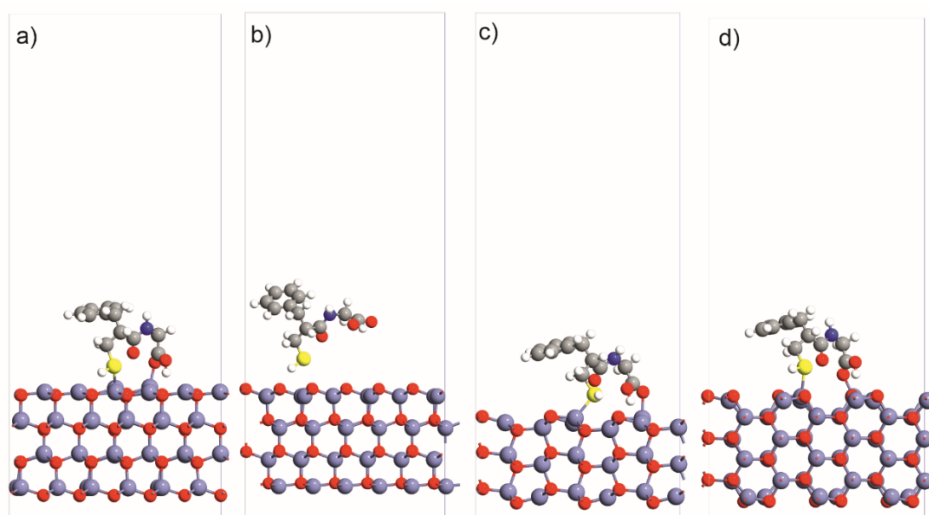


Figure 6.1. Final stages of DFTB simulations for one thiorphan molecules adsorption process on a) (0001), b) (000 $\bar{1}$), c) (10 $\bar{1}$ 0) and d) (11 $\bar{2}$ 0) ZnO facets.

6.2. Surface polarity effects on adsorption of thiorphan

6.2.1. Computational details

For further insight into the adsorption mechanisms and different effects of particular ZnO surface facets, we employed force field molecular dynamics (FFMD) simulations to analyze the adsorption of thiorphan molecules. NPT molecular dynamics simulations were used to investigate the effects of surface polarity on the adsorption of thiorphan molecules on different ZnO surfaces. Berendsen barostat was implemented to describe and control the simulation environmental conditions at the ambient conditions. The ReaxFF empirical force field method was used for optimizing the systems to the lowest energy (0.05 eV/Å) prior to molecular dynamics simulations. The same force field was also employed to describe the interactions between atoms in all molecular dynamics simulations.

To investigate the polarity effects, we used well-established C=O dipoles as a model to mimic the ZnO polar and non-polar surface polarity. Dipole surfaces were constructed with 324 C=O dipoles with the same orientation, fixed next to each other at a 0.5 nm distance in a 9×9×9 nm³ cell. The direction of the C=O dipoles was changed to mimic the ZnO polar and non-polar surface dipoles. C=O dipoles with the oxygen atoms

at the top and C=O dipoles with the carbon atoms at the top represent the ZnO polar (000 $\bar{1}$) and (0001) surfaces, respectively. ZnO non-polar (10 $\bar{1}$ 0) and (11 $\bar{2}$ 0) surfaces were represented by lateral C=O dipoles. Ten layers of 20 randomly distributed thiorphan molecules were then exposed to the three dipole surfaces in a layer-by-layer process. Enough time was given to each layer to develop changes upon each dipole surface. We found the 1 to 2 million steps with 0.1 to 0.5 femtosecond settings optimal for the molecular dynamics simulations. Shorter time did not cover the complete development of the systems, while longer one did not show any further useful changes. The adsorbed thiorphan molecules were then fixed, and remaining floating molecules in the solution were removed from the system before doing the same process for the next layer.

We also did multilayer simulations for three C=O dipole surfaces to study the effects of layer distance on the adsorption of thiorphan molecules. The same above-mentioned dipole surfaces were used in a 9×9×15 nm³ cell along with six layers of 20 randomly distributed thiorphan molecules (120 molecules) in 6 layers with distances between 1 to 6 nm. The simulation settings are the same as mentioned in the former paragraph. All the molecular dynamics simulations in this work were done with periodic boundary conditions and at room temperature. It is also worth noting that all the MD simulations were done in the ethanol solvent to make the simulation environment similar to the experimental conditions where thiorphan solution in ethanol was used for adsorption on ZnO. To speed up the calculations, instead of individual ethanol molecules, we used an implicit solvent with $\epsilon=24.3$ [123].

6.2.2. Thiorphan molecules on polar and non-polar surfaces

The adsorption kinetic of thiorphan on different dipoles was investigated by a method in which new portions of molecules arrive after the previous portion has its time to interact with the surface. The technique is described in detail in the Section 6.2.1. Figure 6.2a, b, and c show the results of adsorption for C-top dipole (mimicking Zn-face ZnO), O-top dipole (mimicking O-face ZnO), and horizontally oriented C=O dipole (mimicking non-polar ZnO facets) respectively. For each set of simulations final 3D image, side view, and top view are shown.

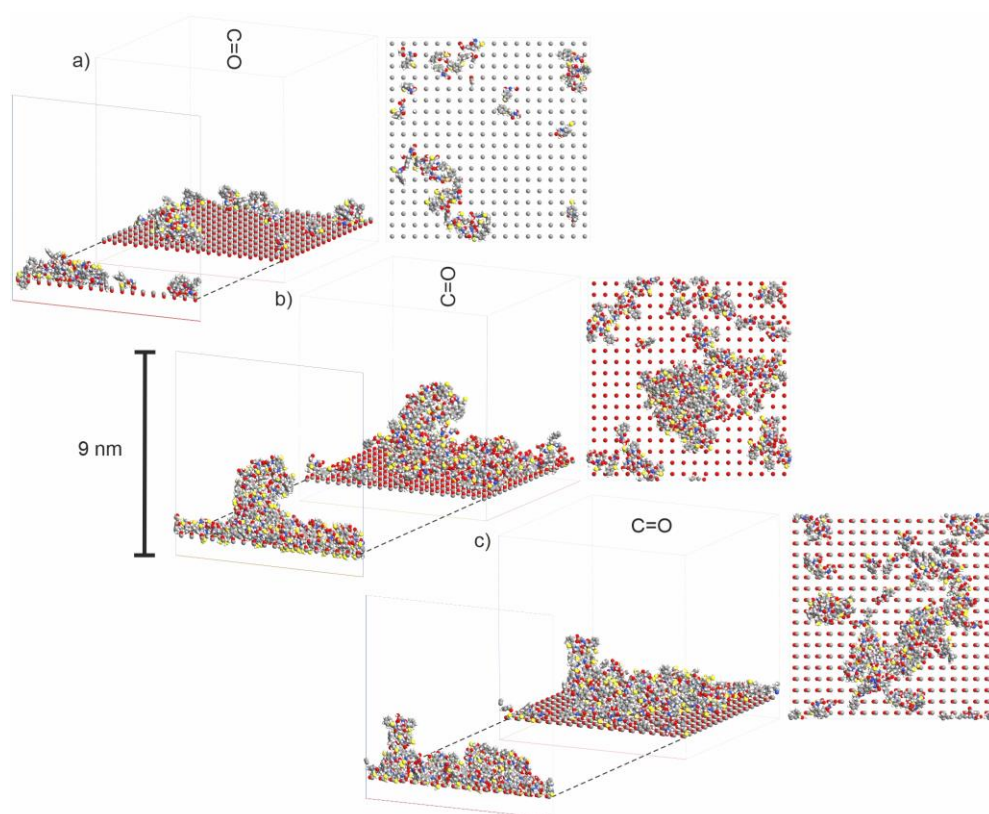


Figure 6.2. Final stage of MD simulations for 10×20 thiorphan molecules adsorption process on **a)** C-top, **b)** O-top, and **c)** horizontally oriented C=O dipole layers

The number of adsorbed molecules is the smallest for C-top dipole (this result is in line with experimental AFM results in Figure A6). About 50 %, 10%, and 30% of total adsorbed molecules were adsorbed single on C-top, O-top, and horizontally oriented dipoles, respectively. In addition, aggregations that were formed to be adsorbed on the non-polar surface were mostly smaller, i.e., consisted of fewer molecules than the ones for the O-top surface. Therefore, we can say that single adsorption (and small aggregations) happens on the non-polar surface more than it does on the O-top surface. This result is in line with experimental AFM results (Figure A6) and with simulation results (Figure 6.3), too.

To address the reason behind the formation of nanodots with different sizes on polar surfaces and the formation of 4 nm thick nanoislands on nonpolar surfaces, six layers with 1 nm thickness were filled with 6×20 thiorphan molecules and placed above three different dipole layers. The results of FFMD simulations are shown in Figure 6.3. Figure 6.3a shows the initial placement of thiorphan molecules. Molecules with different initial heights are marked with different colors. Figure 6b–d shows the results of adsorption for the C-top, O-top dipole,

and horizontally oriented C=O dipole, respectively. Those simulations were performed three times to increase the reliability of the observed results. In Figure 6.3, one can also see the total dipole of the surfaces and adsorbed molecules calculated and visualized by VMD. It is important to note that the total dipoles of the adsorbed molecules were calculated separately and independently from the surface dipole arrays, merely based on the orientation and arrangement of the molecules on each surface. The arrangement and orientation of the molecules on each surface are in a way that the total dipole of the adsorbed molecules aligns along the corresponding surface total dipole. Figure 6.3 confirms that the molecule orientation and adsorption process is governed by electric field lines and not by polarization effects (that would turn it in the opposite direction).

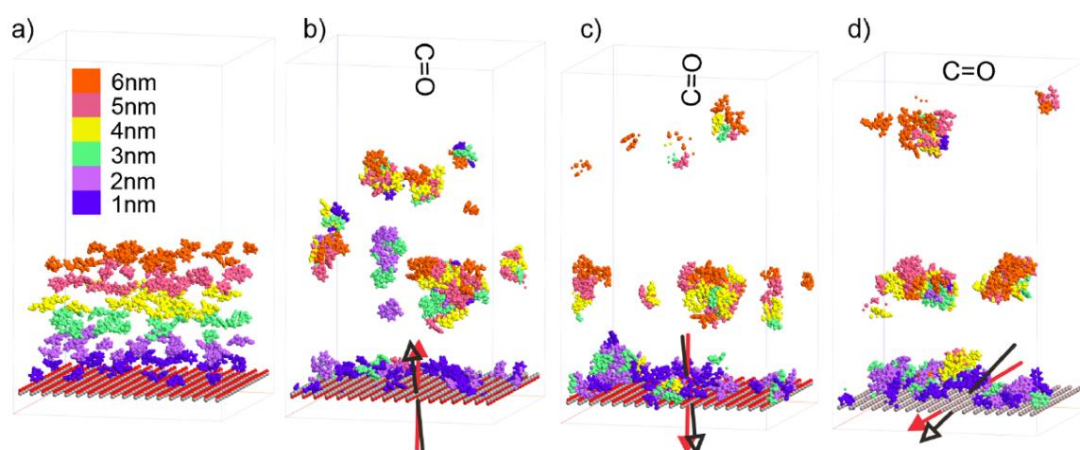


Figure 6.3. *a) Initial stage of the adsorption process of six layers, consisting of 20 thiorphan molecules each. The final stage of the adsorption process on b) C-top, c) O-top, and d) horizontally oriented C=O dipole array, respectively*

Figure 6.4a summarizes the results of FFMD simulations and shows the probability of adsorption for molecules, placed at a certain height above the surface. In all cases, the larger distance from the surface causes a smaller probability of adsorption. Analysis of these data reveals a distance at which the probability of adsorption is 50%. The height values are 1.74, 3.08, and 2.65 nm for the C-top dipole, O-top dipole, and horizontally oriented C=O dipole, respectively. Figure 6.4b shows the dependences of the electric field magnitude vs distance from a single dipole. It proves that the reason for such adsorption behavior is solely the impact of the electric field created by ZnO dipoles. Such data correlate well with the results of experiments. On average, a thiorphan molecule should approach a twice closer distance to the C-top dipole (represents

Zn-faced ZnO facet) than to all other dipoles. Thus, the smallest coverage can be expected for the C-top dipole surface (Figures 6.2a and 6.3b) and for the Zn-faced ZnO facet (Figure 1) due to the interaction of the molecule with the surface dipole. This result clearly shows that thiorphan molecules behave differently depending on the surface dipole orientation.

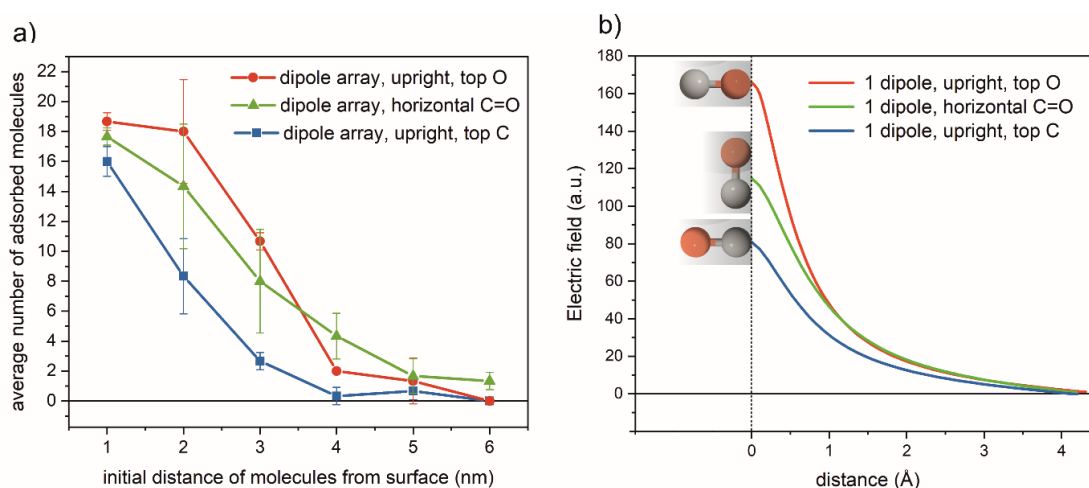


Figure 6.4. *a) Dependences of the average number of adsorbed molecules vs. initial distance of molecules from dipole array surface. b) Dependences of the electric field vs. distance from a single dipole*

The orientation of the dipole on the different ZnO surfaces is not identical. The surface dipole in the ZnO crystal is in the [0001] direction, from the O-face facet to Zn-face facet. This results in pointing up and pointing down surface dipoles on Zn-face and O-face surfaces, respectively. In FFMD simulations, we modeled these orientations by using C=O dipole arrays.

The results of similar MD simulations with two other solvents, namely, water ($\epsilon \approx 80$) and chloroform ($\epsilon = 4.8$) are shown in Figure A7. Chloroform has the lowest ϵ value for all solvents, in which thiorphan can be dissolved. Water has a higher ϵ value than any solvent, in which thiorphan can be dissolved. As one can see, the surface polarity-dependent adsorption behavior is observed for these two solvents, too. This behavior is the same in all three solvents, indicating negligible influence of the solvent on adsorption behavior.

On the Zn-faced surface, as shown in Figure A6d, the presence of surface dipoles pointing up creates an electric field with electric field lines pointing up. In the FFMD simulations in Figure 6.3b and 6.4a, it

corresponds to the weakest field intensity. Accordingly, only a few thiorphan molecules from a close surface vicinity (0–1.74 nm) tend to adsorb on the C-top surface which mimics the polarity of the Zn-face ZnO surface. Therefore, the coverage of thiorphan molecules in FFMD simulations is low and scattered on this surface (50% of the molecules adsorbed individually). This is in agreement with the formation of small nanodots (<4 nm) observed on the Zn-faced ZnO facet by AFM experiments in Figure A6.

On the other hand, on the O-faced surface in Figure A6d, the presence of surface dipoles pointing down creates an electric field with electric field lines pointing down. In the FFMD simulations in Figures 6.3c and 6.4a, it corresponds to the strongest field intensity. Accordingly, a larger amount of thiorphan molecules from a farther distance (0–3.08 nm) tends to adsorb on the O-top surface which represents the O-face ZnO surface. Therefore, the coverage of thiorphan molecules in FFMD simulations is high and most of the molecules adsorb in the form of large aggregations. These observations from simulations correlate well with the AFM experiments in Figure 1 in which large nanodots (~25 nm) are observed on the Oface ZnO facet after 48 h deposition.

On the nonpolar surfaces, as shown in Figure A6d, the presence of horizontally oriented surface dipoles creates an electric field with electric field lines aligned horizontally. In the FFMD simulations in Figures 6.3d and 6.4a, it still corresponds to a decaying electrical field in the perpendicular direction from the surface with an intensity that is between the upward and downward oriented dipoles. Therefore, the coverage of thiorphan molecules is relatively high in FFMD simulations on the horizontal C=O dipoles surface which mimics the polarity of ZnO nonpolar surfaces. It is also noteworthy that more molecules tend to adsorb individually (30%) on the horizontal C=O dipoles surface, compared to the O-top surface (10%). Opposite to aggregation, the individually adsorbed molecules can join each other to form layers. The laterally oriented electric dipole can thus explain the formation of the first 4 nm thick layer and subsequent formation of larger nanoislands on (1010) and (1120) ZnO facets as observed by AFM in Figure 1.

The inability of the AFM tip even with a high load (2400nN) to penetrate and completely remove thiorphan nanoislands and large nanodots shows that the thiorphan structures are quite rigid (Figure A8). This may indicate strong intermolecular interactions between the molecules within the nanoislands and large nanodots. Based on DLS measurements (Figure A9), thiorphan molecules do not aggregate in

solution; however, according to MD simulations, bigger aggregations and clusters of thiorphan molecules have been observed on the O-faced ZnO surface compared to the other surfaces. Thus, even despite the absence of covalent bonds between thiorphan molecules and O-faced ZnO (Figure 6.1b), mutual interactions of molecules are stronger on this surface compared to other surfaces, leading to the formation of large nanodots and to the inability of the AFM tip to remove nanoislands and large nanodots from O-faced ZnO (Figure A8b and f). On the other hand, the formation of covalent bonds between thiorphan molecules and Zn-faced ZnO surface (Figure 6.1a) together with the formation of only small nanodots (Figure A6a) and weak aggregation (Figure 6.3b) does not create sufficiently strong interactions and allow the AFM tip to remove small nanodots (Figure A8e). The orientation of the electric field on nonpolar surfaces, which is lateral, applies lateral forces to the molecules (see the dipole direction in Figure 6.3d) and thus can spread the molecules more uniformly on the nonpolar surfaces. This can aid the formation of more uniform layers all over the surface compared to the nanodots on the polar surfaces with vertical dipoles (see the dipole directions in Figure 6.3b and c).

Moreover, simulations show that a large amount of molecules are adsorbed on the surface individually, not as aggregates. These individually placed molecules can then more easily merge to form layers. Figure A8 shows that the thickness of each layer within nanoislands is 3.4–3.6 nm. Therefore, the thiorphan layer can be considered a new example of an ultrathin nanostructured nanomaterial and thus open a new field of research for such molecular materials.

In this Chapter, the covalent bonding of individual thiorphan molecules to all ZnO facets, except the O-face ZnO, was theoretically observed by DFTB. FFMD was also carried out for the C-top dipole (mimicking Zn-face ZnO), O-top dipole (mimicking O-face ZnO), and horizontally oriented C=O dipole (mimicking nonpolar ZnO facets) to study the physics behind the thiorphan–ZnO interactions. FFMD explains experimentally observed results solely by the impact of the surface dipoles orientation and electric field magnitude. The characteristic distance, at which the thiorphan molecule has a 50% chance to adhere, is the lowest (1.74 nm) for the C-top dipole layer, mimicking the Zn-face ZnO facet (i.e., the surface with upright dipole and minimal thiorphan coverage) and is the highest (3.08 nm) for the O-top dipole layer, mimicking the O-face ZnO facet (i.e., the surface with downward dipole and maximum thiorphan coverage).

According to the results of this work, different ZnO surfaces can be good candidates for different applications based on the desired purpose. For instance, the O-face ZnO surface can be the most useful for biosensing, biointerfaces, or drug delivery when the purpose is maximizing the number of engaged molecules but without affecting the chemistry of the sensor surface and the structure of the molecule. On the other hand, the (1010) ZnO surface may be the best choice when oriented molecules with oriented dipoles and maximum chemical interactions with the sensor surface are necessary to enhance the sensor response.

The controlled self-assembly of thiorphan molecules by ZnO surface dipole orientation and magnitude can be a rather general effect applicable also for other molecules and surfaces. Moreover, the well-defined self-limited nanometer thicknesses of the observed dense molecular layers can be considered as an example of the formation of novel ultrathin nanostructured two-dimensional (2D) molecular nanomaterials. Thereby, the present study can open a new field of research for such materials.

7. RESULTS - Interaction of chiral molecules with magnetized surfaces

Following the investigations of interactions between ZnO and biomolecules, specifically BSA and thiorphan, the author pursued an internship at the Max Planck Institute of Microstructure Physics (MPI). During this internship, a novel and relevant area of study emerged, focusing on the impact of magnetized surfaces on interactions with chiral molecules. MPI, acknowledging our expertise in the simulation of molecular adsorption and assembly on surfaces, introduced this intriguing field of study, with a particular emphasis on the role of chirality in surface interactions. The topic of chiral molecules and magnetized surfaces interaction offers a wide range of applications, particularly in the field of spintronics. Comprehending the interaction between chiral molecules and magnetized surfaces is essential for the advancement of spintronic devices. Chiral molecules possess spin-dependent characteristics that may be utilized for spin manipulation and control and therefore advancing the creation of spin-based electrical devices. Beyond the field of spintronics, chiral molecules' interactions with magnetic surfaces have applications in chemical and biological sensing, where they may lead to the development of extremely sensitive and focused detection methods. This multidisciplinary study has the potential to advance basic science as well as real-world applications in emerging technology.

The particular emphasis of the internship was on using magnetic surfaces, which was in line with MPI's research interests. Despite the divergence from ZnO surfaces during the internship, it is noteworthy that ZnO has been identified to possess tunable magnetic characteristics as well ^[124]. This interlink broadens the scope of our study and raises the

possibility that the results of the internship might be used also in the field of ZnO-molecule interactions.

The intriguing interaction between magnetized surfaces and chiral molecules is a captivating area of study in the world of molecular science. Chiral molecules are unique because they come in two different forms (enantiomers), such as left and right hands (see Figure 7.1). This uniqueness affects how they react in chemical processes.

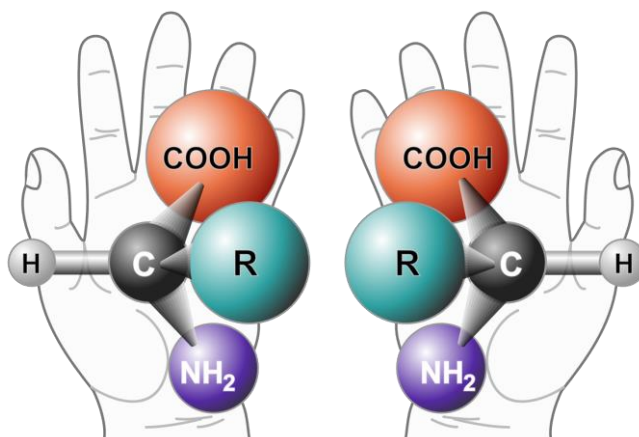


Figure 7.1. Two enantiomers of a chiral molecule (an amino acid).
(source: Wikipedia Commons)

Simultaneously, magnetism, a natural force evident in everyday occurrences such as the attachment of magnets to metallic surfaces, has constantly captivated the scientific community's imagination. Its influence extended to diverse facets of human life, from compasses guiding explorers to the functioning of magnetic resonance imaging (MRI) machines unveiling the secrets of the human body.

When we bring these two interesting ideas together, magnetized surfaces and chiral molecules, we discover a world of fascinating phenomena. It can be considered as putting together pieces of a puzzle because the direction of magnetism on the surface is like the key that unlocks how chiral molecules react.

Different studies have concentrated on this topic for a long time. They have developed theories to explain it and carried out experiments to observe it in action. Some of these experiments use special microscopes to closely examine tiny particles ^[125].

The significance of such property lies in its potential applications. It turns out that these interactions between magnetized surfaces and chiral molecules can have practical applications. For instance, they could lead to more effective methods of delivering medicines precisely to specific

parts of the body, ensuring that the right amount reaches the right place. Additionally, they could help improve how we perform certain chemical reactions, which is vital for creating new materials or enhancing existing ones.

Thus, this Chapter reports the results of the author's internship at the Max Planck Institute of Microstructure Physics in Halle, Germany, under the supervision of prof. Stuart Parkin. MPI in Halle is the leading research centre in the field of spintronics and chirality. Prospects for completing this research and publication of the results in an impacted journal are being discussed.

7.1. Computational details

For the method, Density Functional Theory (DFT) calculations would be the best option for our purposes as it could accurately capture both magnetic properties as well as molecular structures, allowing to compare different systems more effectively. In order to accurately capture the behaviour of the systems of interest, spin-polarized DFT (GGA and PBE) calculations were implemented. A series of DFT calculations were conducted to examine the effects of magnetization on the behaviour of chiral molecules adsorbed onto surfaces.

The most proper structure for studying the interactions between magnetized surfaces and chiral molecules is an optimized surface with strong magnetic properties and an appropriate molecular geometry that would allow us to observe how its structure is affected by the presence of a magnetic field. This method has been proved to work very well experimentally in ^[126], where it has been shown experimentally that the interaction of chiral molecules with a perpendicularly magnetized substrate is enantiospecific. Here, we intend to assess this idea theoretically by using DFT method.

The selected structure comprised nickel surfaces magnetized in two opposite directions interacting with two cysteine enantiomers as the chiral molecule (Figure 7.2). There are two main reasons for selecting this structure: it is computationally efficient and the selected chiral molecule is a biomolecule that is relevant to the other studied molecules in previous Chapters. The simulations were mainly run on FEL clusters due to their extreme computing power, but some parts were also run on MPI clusters for better accuracy.

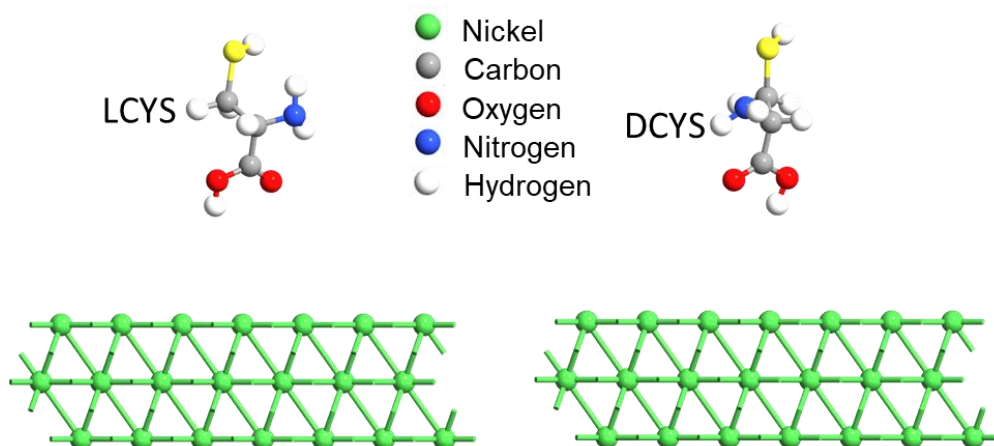


Figure 7.2. Two enantiomers of a chiral molecule (Cysteine) on a magnetized nickel (111) surface.

7.2. Cysteine enantiomers on magnetized nickel surfaces

In Figure 7.3, the final stages of DFT optimization of two enantiomers of a chiral molecule (Cysteine) on a spin-down and spin-up magnetized nickel (111) surface are shown.

In Figure 7.3a, one can see two enantiomers of the chiral molecule (Cysteine) on the spin-down magnetized nickel (111) surface after relaxation by DFT calculations. Figure 7.3b shows the same enantiomers of the same chiral molecule (Cysteine) on the spin-up magnetized nickel (111) surface after relaxation by DFT calculations.

The behaviour of the chiral molecule (CYS) on the magnetized surfaces (nickel) shows a clear dependency on the direction of the magnetization of the surface as well as on the type of molecule (LCYS or DCYS). Another interesting point is the dependency of the bonding of the molecules to the surfaces on the magnetization of the surface. The orientation of the adsorbed molecules and also the chemical interactions of the molecules on oppositely magnetized surfaces are obviously different.

Figure 7.4 presents the computed binding energies corresponding to the systems depicted in Figure 7.3. Within Figure 7.4, the binding energy values for the two enantiomers of a chiral molecule, Cysteine, on a (111) nickel surface magnetized in opposing directions are provided. Specifically, for the LCYS molecule, the binding energy on the spin-down magnetized nickel (111) surface is 2.38 eV, contrasting with the

value of 1.22 eV on the spin-up surface, indicating a more robust adsorption on the spin-down surface. Conversely, for the DCYS molecule, the binding energy on the spin-down surface is 1.16 eV, while on the spin-up surface, it is 3.4 eV, illustrating a more substantial adsorption. These results confirm the selective behaviour of molecules on magnetized surfaces shown in Figure 7.3. We can see that magnetization may act as a kind of driving force and polarization force on molecules that gives rise to such reactions selectively.

In conclusion, the analysis of Figures 7.3 and 7.4 reveals distinct behaviors of enantiomers of the chiral molecule Cysteine (CYS) on spin-down and spin-up magnetized nickel (111) surfaces. The dependency of the chiral molecule's behavior on both the direction of magnetization and the molecule type (LCYS or DCYS) is evident. Notably, the bonding of molecules to the magnetized surfaces displays a clear correlation with the magnetization direction, influencing the orientation and chemical interactions of the adsorbed molecules.

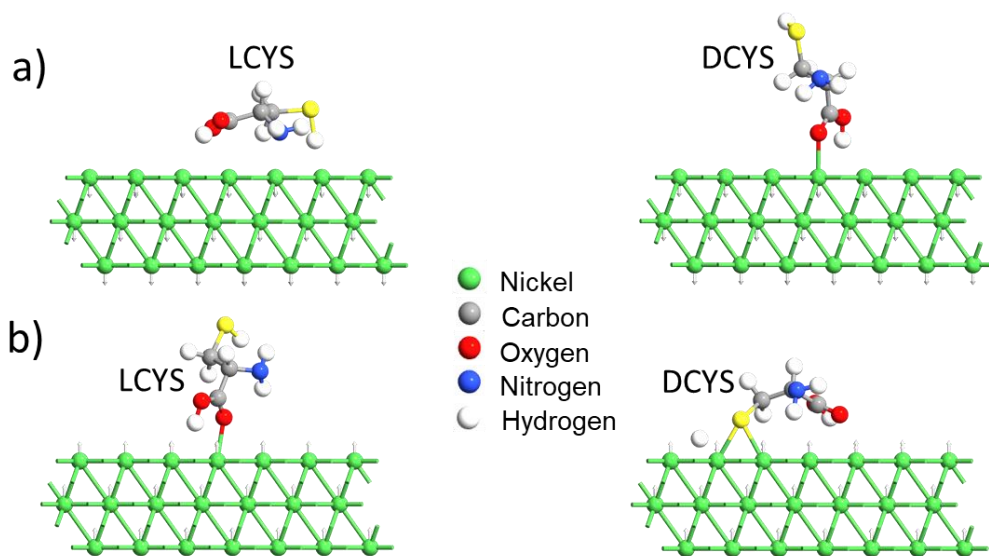


Figure 7.3. Two enantiomers of a chiral molecule (Cysteine) on **a)** spin-down and **b)** spin-up magnetized nickel (111) surface after relaxation by DFT calculations.

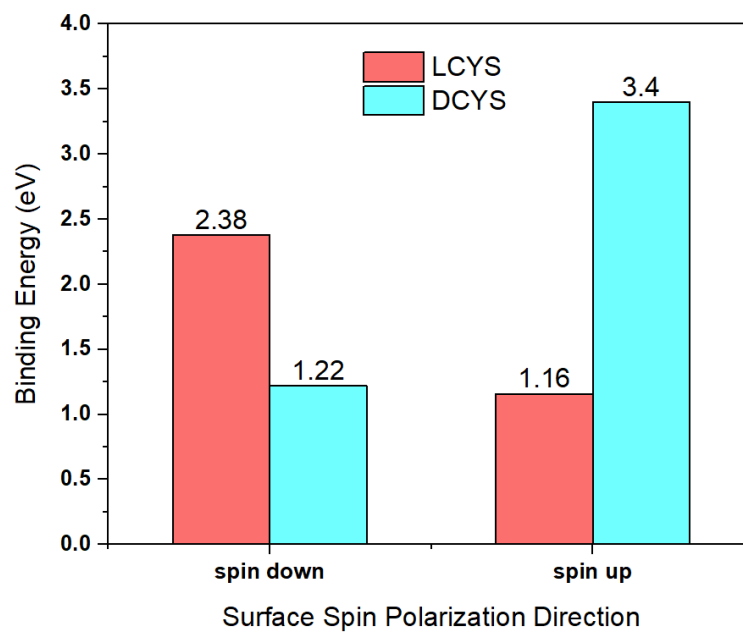


Figure 7.4. Binding energy of the two enantiomers of a chiral molecule (Cysteine) on (111) nickel surface magnetized in opposite directions

8. Conclusion

Classical and quantum-based calculations were employed to understand the interactions between ZnO dominant low-index polar and nonpolar surfaces and two important biomolecules, BSA and thiorphan. The results of classical force field and quantum-based density functional tight binding (DFTB) calculations provided key details on ZnO-BSA and ZnO-thiorphan interfaces at both atomic and electronic level.

The ZnO-BSA interactions are substantially affected by the surface chemistry of ZnO surfaces. According to the total energy analysis, the BSA molecule on the $(000\bar{1})$ surface has the highest roughness and average height, hinting at a specific upright BSA arrangement. Binding energies reveal that the BSA molecule on $(10\bar{1}0)$ surface has the most robust binding with atomic rearrangement and bonding between specific amino acids (AAs) and ZnO. Besides the structural properties, the ZnO interaction with these AAs also controls charge transfer and HOMO-LUMO energy positions in the BSA-ZnO complexes. These results are in a good agreement with the AFM morphology measurements and nanoshaving experiments performed with BSA layers adsorbed on various ZnO surfaces.

In terms of thiorphan, even though the covalent bonding of individual thiorphan molecules to all ZnO facets, except O-faced ZnO, was observed in DFTB simulations, MD simulations by using CO dipole arrays to mimic ZnO surface polarity, show that the ZnO surface polarity has the role key in the interactions rather than surface chemistry. On the C-top dipole array (mimicking Zn-faced surface), the coverage of thiorphan molecules is low, while around half of the molecules are placed single and scattered. On the O-top dipole array (mimicking the O-faced surface), many thiorphan molecules (placed in a larger distance range of 0–3.08 nm from the surface) tend to adsorb in large aggregates on the surface. On the horizontally oriented array, a lot of thiorphan molecules (placed in a distance range of 0 – 2.65 nm) were adsorbed, but individually or in small aggregates. These polarity-dependent results were corroborated also experimentally by AFM, showing small nanodots, large

nanodots, and nanoislands on Zn-faced, O-faced, and ZnO nonpolar surfaces, respectively.

These models, simulation methodology, obtained knowledge and expertise enabled us to initiate the study of the interactions of magnetic surfaces with chiral molecules as a current research hot topic. Our calculations revealed an intriguing dependence of these interactions on the enantiomer type and surface magnetization orientation. This dependency can be seen in both the properties of chemical bonds and the binding energies of the molecules on the surfaces. For instance, it was shown that the D-enantiomer of Cysteine has stronger interactions with spin-up magnetized nickel surface while on the spin-down magnetized surface, the L-enantiomer is the molecule with stronger binding and interactions. These preliminary results open interesting prospects for further studies and applications.

Regarding the prospects of this study, our investigation focused on understanding the interactions between ideal ZnO surfaces and biomolecules. While one chapter explored the non-idealities in the ZnO lattice and their impact on electronic and optical characteristics, the examination of how these non-idealities influence the interactions of ZnO with biomolecules was not explicitly addressed. This represents an intriguing direction for potential research as exploring the effects of non-idealities on ZnO-biomolecule interfaces could yield more realistic outcomes and interesting applications.

Considering the significance of these non-idealities in the ZnO lattice, further research in this direction has the potential to provide a more comprehensive understanding of the dynamics involved in ZnO-biomolecule interactions. This exploration could not only refine theoretical models but also offer practical insights for applications in biomedicine and related fields where the interactions between ZnO and biomolecules are of critical importance.

Furthermore, our preliminary theoretical examination revealed that these interactions depend also on the magnetization direction of the surface. Due to time constraints and the alignment with MPI interests, our study commenced with a nickel surface as the initial model system. Unfortunately, we there was not enough time to extend the investigation to a ZnO surface, even though it is known to also possess magnetic dipoles. Considering the magnetic properties of ZnO is thus a promising path for future research and exploring the interactions between ZnO magnetic dipoles and chiral molecules could open up a new dimension of the research in terms of both fundamental knowledge and novel applications.

References

- [1] Y. Liu, J. Yang, P. Zhang, C. Liu, W. Wang, W. Liu, *J. Mater. Chem.* **2011**, *22*, 512.
- [2] L. He, X. Sun, X. Nan, T. Wang, P. Bai, *AIP Adv.* **2019**, *9*, 125026.
- [3] M. M. Rahman, A. J. S. Ahammad, J.-H. Jin, S. J. Ahn, J.-J. Lee, *Sensors* **2010**, *10*, 4855.
- [4] K. Jindal, M. Tomar, V. Gupta, *Analyst* **2013**, *138*, 4353.
- [5] G. Applerot, A. Lipovsky, R. Dror, N. Perkas, Y. Nitzan, R. Lubart, A. Gedanken, *Adv. Funct. Mater.* **2009**, *19*, 842.
- [6] P. T. S. Kumar, S. Abhilash, K. Manzoor, S. V. Nair, H. Tamura, R. Jayakumar, *Carbohydr. Polym.* **2010**, *3*, 761.
- [7] L. Zhang, Y. Jiang, Y. Ding, N. Daskalakis, L. Jeuken, M. Povey, A. J. O'Neill, D. W. York, *J. Nanoparticle Res.* **2010**, *12*, 1625.
- [8] M. Li, L. Zhu, D. Lin, *Environ. Sci. Technol.* **2011**, *45*, 1977.
- [9] R. Yu, C. Pan, Z. L. Wang, *Energy Environ. Sci.* **2013**, *6*, 494.
- [10] A. G. Cuevas, K. Balangcod, T. Balangcod, A. Jasmin, *Procedia Eng.* **2013**, *68*, 537.
- [11] P. T. S. Kumar, V.-K. Lakshmanan, T. V. Anilkumar, C. Ramya, P. Reshmi, A. G. Unnikrishnan, S. V. Nair, R. Jayakumar, *ACS Appl. Mater. Interfaces* **2012**, *4*, 2618.
- [12] Q. Yuan, S. Hein, R. D. K. Misra, *Acta Biomater.* **2010**, *6*, 2732.
- [13] A.-J. Cai, Y.-L. Wang, S.-T. Xing, L.-Q. Du, Z.-C. Ma, *Ceram. Int.* **2013**, *39*, 605.
- [14] R. de la Rica, H. Matsui, *Angew. Chem. Int. Ed.* **2008**, *47*, 5415.
- [15] Q. Wu, X. Chen, P. Zhang, Y. Han, X. Chen, Y. Yan, S. Li, *Cryst. Growth Des.* **2008**, *8*, 3010.
- [16] P. Gers^{TEL}, P. Lipowsky, O. Durupthy, R. C. Hoffmann, P. Bellina, J. Bill, F. Aldinger, *J. Ceram. Soc. Jpn.* **2006**, *114*, 911.
- [17] S. H. Kim, T. Y. Olson, J. H. Satcher, T. Y.-J. Han, *Microporous Mesoporous Mater.* **2012**, *151*, 64.
- [18] A.-J. Cai, Y.-L. Wang, S.-T. Xing, Z.-C. Ma, *Ceram. Int.* **2012**, *38*, 5265.

- [19] M. Z. Hussein, W. H. W. N. Azmin, M. Mustafa, A. H. Yahaya, *J. Inorg. Biochem.* **2009**, *103*, 1145.
- [20] H. Zhou, T. Fan, D. Zhang, *Microporous Mesoporous Mater.* **2007**, *100*, 322.
- [21] *Bioconjug. Chem.* **2016**, *27*, 1999.
- [22] Z. Huang, D. Yan, M. Yang, X. Liao, Y. Kang, G. Yin, Y. Yao, B. Hao, *J. Colloid Interface Sci.* **2008**, *325*, 356.
- [23] M. Umetsu, M. Mizuta, K. Tsumoto, S. Ohara, S. Takami, H. Watanabe, I. Kumagai, T. Adschiri, *Adv. Mater.* **2005**, *17*, 2571.
- [24] H. F. Greer, W. Zhou, M.-H. Liu, Y.-H. Tseng, C.-Y. Mou, *CrystEngComm* **2012**, *14*, 1247.
- [25] D. Rothenstein, B. Claasen, B. Omiecienski, P. Lammel, J. Bill, *J. Am. Chem. Soc.* **2012**, *134*, 12547.
- [26] M.-K. Liang, O. Deschaume, S. V. Patwardhan, C. C. Perry, *J. Mater. Chem.* **2010**, *21*, 80.
- [27] M. J. Limo, R. Ramasamy, C. C. Perry, *Chem. Mater.* **2015**, *27*, 1950.
- [28] T. Xie, S. Song, K. Schwenke, M. Singh, L. E. Gonzalez, E. Del Gado, J. Hahn, *Langmuir* **2015**, *31*, 10493.
- [29] G. Nawrocki, M. Cieplak, *Phys. Chem. Chem. Phys.* **2013**, *15*, 13628.
- [30] M. Muthukumar, *J. Chem. Phys.* **2009**, *130*, 161101.
- [31] V. Shewale, P. Joshi, S. Mukhopadhyay, M. Deshpande, R. Pandey, S. Hussain, S. P. Karna, *J. Phys. Chem. C* **2011**, *115*, 10426.
- [32] S. grosse Holthaus, S. Köppen, T. Frauenheim, L. C. Ciacchi, *J. Chem. Phys.* **2014**, *140*, 234707.
- [33] F. Buonocore, C. Arcangeli, F. Gala, G. Zollo, M. Celino, *J. Phys. Chem. B* **2015**, *119*, 11791.
- [34] S. Piscopo, E. R. Brown, *Small* **2018**, *14*, 1703403.
- [35] M. Bardhan, G. Mandal, T. Ganguly, *J. Appl. Phys.* **2009**, *106*, 034701.
- [36] S. Chakraborti, P. Joshi, D. Chakravarty, V. Shanker, Z. A. Ansari, S. P. Singh, P. Chakrabarti, *Langmuir* **2012**, *28*, 11142.

- [37] A. Bhogale, N. Patel, P. Sarpotdar, J. Mariam, P. M. Dongre, A. Miotello, D. C. Kothari, *Colloids Surf. B Biointerfaces* **2013**, *102*, 257.
- [38] B. P. Roques, M. C. Fournié-Zaluski, E. Soroça, J. M. Lecomte, B. Malfroy, C. Llorens, J.-C. Schwartz, *Nature* **1980**, *288*, 286.
- [39] P. Tejedor-Real, J. A. Mico, R. Maldonado, B. P. Roques, J. Gibert-Rahola, *Pharmacol. Biochem. Behav.* **1995**, *52*, 145.
- [40] H. Nam, R. Chandra, T. C. Francis, C. Dias, J. F. Cheer, M. K. Lobo, *Neuropsychopharmacology* **2019**, *44*, 1876.
- [41] X. Yang, Y. Rojanasakul, L. Wang, J. Y. Ma, J. K. Ma, *Pharm. Res.* **1998**, *15*, 1480.
- [42] U. Eriksson, J. Hassel, E. Lüllau, L. Häggström, *J. Biotechnol.* **2005**, *119*, 76.
- [43] G. Tiraboschi, N. Jullian, V. Thery, S. Antonczak, M.-C. Fournie-Zaluski, B. P. Roques, *Protein Eng. Des. Sel.* **1999**, *12*, 141.
- [44] P. Zipfel, C. Rochais, K. Baranger, S. Rivera, P. Dallemagne, *J. Med. Chem.* **2020**, *63*, 10705.
- [45] S. C. Abrahams, J. L. Bernstein, *Acta Crystallogr. Sect. B* **1969**, *25*, 1233.
- [46] A. Janotti, C. G. V. de Walle, *Rep. Prog. Phys.* **2009**, *72*, 126501.
- [47] D. Segets, J. Gradl, R. K. Taylor, V. Vassilev, W. Peukert, *ACS Nano* **2009**, *3*, 1703.
- [48] R. Yan, D. Gargas, P. Yang, *Nat. Photonics* **2009**, *3*, 569.
- [49] C. F. Klingshirn, A. Waag, A. Hoffmann, J. Geurts, *Zinc Oxide: From Fundamental Properties Towards Novel Applications*, Springer-Verlag, Berlin Heidelberg, **2010**.
- [50] Ü. Özgür, Ya. I. Alivov, C. Liu, A. Teke, M. A. Reshchikov, S. Doğan, V. Avrutin, S.-J. Cho, H. Morkoç, *J. Appl. Phys.* **2005**, *98*, 041301.
- [51] J. Cembrero, A. Elmanouni, B. Hartiti, M. Mollar, B. Marí, *Thin Solid Films* **2004**, *451–452*, 198.
- [52] M. T. Noman, N. Amor, M. Petru, *Crit. Rev. Solid State Mater. Sci.* **2021**, *0*, 1.
- [53] C. Wöll, *Prog. Surf. Sci.* **2007**, *82*, 55.
- [54] H. van Hove, R. Leysen, *Phys. Status Solidi A* **1972**, *9*, 361.

- [55] J. D. Levine, A. Willis, W. R. Bottoms, P. Mark, *Surf. Sci.* **1972**, 29, 144.
- [56] A. R. Lubinsky, C. B. Duke, S. C. Chang, B. W. Lee, P. Mark, *J. Vac. Sci. Technol.* **1976**, 13, 189.
- [57] C. B. Duke, A. R. Lubinsky, S. C. Chang, B. W. Lee, P. Mark, *Phys. Rev. B* **1977**, 15, 4865.
- [58] C. B. Duke, R. J. Meyer, A. Paton, P. Mark, *Phys. Rev. B* **1978**, 18, 4225.
- [59] Y. Wang, B. Meyer, X. Yin, M. Kunat, D. Langenberg, F. Traeger, A. Birkner, Ch. Wöll, *Phys. Rev. Lett.* **2005**, 95, 266104.
- [60] B. Meyer, D. Marx, O. Dulub, U. Diebold, M. Kunat, D. Langenberg, C. Wöll, *Angew. Chem. Int. Ed.* **2004**, 43, 6641.
- [61] Y. Yan, M. M. Al-Jassim, *Phys. Rev. B* **2005**, 72, 235406.
- [62] A. Wander, N. M. Harrison, *Surf. Sci.* **2000**, 457, L342.
- [63] O. Dulub, L. A. Boatner, U. Diebold, *Surf. Sci.* **2002**, 519, 201.
- [64] U. Diebold, L. V. Koplitz, O. Dulub, *Appl. Surf. Sci.* **2004**, 237, 336.
- [65] G. Heiland, H. Ibach, *Solid State Commun.* **1966**, 4, 353.
- [66] P. W. Tasker, *J. Phys. C Solid State Phys.* **1979**, 12, 4977.
- [67] A. Wander, F. Schedin, P. Steadman, A. Norris, R. McGrath, T. S. Turner, G. Thornton, N. M. Harrison, *Phys. Rev. Lett.* **2001**, 86, 3811.
- [68] S.-C. Chang, P. Mark, *Surf. Sci.* **1974**, 46, 293.
- [69] H. Moormann, D. Kohl, G. Heiland, *Surf. Sci.* **1980**, 100, 302.
- [70] D. Mora-Fonz, T. Lazauskas, M. R. Farrow, C. R. A. Catlow, S. M. Woodley, A. A. Sokol, *Chem. Mater.* **2017**, 29, 5306.
- [71] G. Thornton, S. Crook, Z. Chang, *Surf. Sci.* **1998**, 415, 122.
- [72] S. Crook, H. Dhariwal, G. Thornton, *Surf. Sci.* **1997**, 382, 19.
- [73] Y. Wang, M. Muhler, C. Wöll, *Phys. Chem. Chem. Phys.* **2006**, 8, 1521.
- [74] Y. Wang, R. Kováčik, B. Meyer, K. Kotsis, D. Stodt, V. Staemmler, H. Qiu, F. Traeger, D. Langenberg, M. Muhler, C. Wöll, *Angew. Chem. Int. Ed.* **2007**, 46, 5624.
- [75] G. Zwicker, K. Jacobi, *Surf. Sci.* **1983**, 131, 179.

- [76] Th. Becker, St. Hövel, M. Kunat, Ch. Boas, U. Burghaus, Ch. Wöll, *Surf. Sci.* **2001**, 486, L502.
- [77] V. Staemmler, K. Fink, B. Meyer, D. Marx, M. Kunat, S. Gil Girol, U. Burghaus, Ch. Wöll, *Phys. Rev. Lett.* **2003**, 90, 106102.
- [78] K. Fink, *Phys. Chem. Chem. Phys.* **2006**, 8, 1482.
- [79] R. Davis, J. F. Walsh, C. A. Muryn, G. Thornton, V. R. Dhanak, K. C. Prince, *Surf. Sci.* **1993**, 298, L196.
- [80] M. Fyta, *Computational Approaches in Physics*, Morgan & Claypool Publishers, **2016**.
- [81] J. Tersoff, *Phys. Rev. B* **1988**, 37, 6991.
- [82] D. W. Brenner, *Phys. Rev. B* **1990**, 42, 9458.
- [83] M. Z. Bazant, E. Kaxiras, J. F. Justo, *MRS Proc.* **1997**, 491, 339.
- [84] A. C. T. van Duin, S. Dasgupta, F. Lorant, W. A. Goddard, *J. Phys. Chem. A* **2001**, 105, 9396.
- [85] A. (viaf)92694743 Szabó, N. S. Ostlund, *Modern Quantum Chemistry : Introduction to Advanced Electronic Structure Theory*, Mineola (N.Y.) : Dover Publications, **1996**.
- [86] D. R. Hartree, *Math. Proc. Camb. Philos. Soc.* **1928**, 24, 89.
- [87] V. Fock, *Z. Für Phys.* **1930**, 61, 126.
- [88] P. Hohenberg, W. Kohn, *Phys. Rev.* **1964**, 136, B864.
- [89] D. Porezag, Th. Frauenheim, Th. Köhler, G. Seifert, R. Kaschner, *Phys. Rev. B* **1995**, 51, 12947.
- [90] G. Seifert, D. Porezag, Th. Frauenheim, *Int. J. Quantum Chem.* **1996**, 58, 185.
- [91] M. Elstner, D. Porezag, G. Jungnickel, J. Elsner, M. Haugk, Th. Frauenheim, S. Suhai, G. Seifert, *Phys. Rev. B* **1998**, 58, 7260.
- [92] T. Frauenheim, G. Seifert, M. Elstner, T. Niehaus, C. Köhler, M. Amkreutz, M. Sternberg, Z. Hajnal, A. D. Carlo, S. Suhai, *J. Phys. Condens. Matter* **2002**, 14, 3015.
- [93] M. Elstner, G. Seifert, *Philos. Trans. R. Soc. Math. Phys. Eng. Sci.* **2014**, 372, 20120483.
- [94] G. Seifert, J.-O. Joswig, *WIREs Comput. Mol. Sci.* **2012**, 2, 456.
- [95] M. Gaus, M. Elstner, *Extension and Parametrization of an Approximate Density Functional Method for Organic and Biomolecules*, KIT-Bibliothek, **2011**.

- [96] P. H. Hünenberger, in *Adv. Comput. Simul. Approaches Soft Matter Sci. I* (Eds: C. Dr. Holm, K. Prof. Dr. Kremer), Springer Berlin Heidelberg, Berlin, Heidelberg, **2005**, pp. 105–149.
- [97] G. J. Martyna, D. J. Tobias, M. L. Klein, *J. Chem. Phys.* **1994**, *101*, 4177.
- [98] R. W. Hamming, R. W. Hamming, *Numerical Methods for Scientists and Engineers*, Dover, **1986**.
- [99] L. Verlet, *Phys. Rev.* **1967**, *159*, 98.
- [100] W. F. Van Gunsteren, H. J. C. Berendsen, *Mol. Simul.* **1988**, *1*, 173.
- [101] W. C. Swope, H. C. Andersen, P. H. Berens, K. R. Wilson, *J. Chem. Phys.* **1982**, *76*, 637.
- [102] L. G. Ferreira, M. Marques, L. K. Teles, *Phys. Rev. B* **2008**, *78*, 125116.
- [103] L. G. Ferreira, M. Marques, L. K. Teles, *AIP Adv.* **2011**, *1*, 032119.
- [104] A. Janotti, C. G. Van de Walle, *Phys. Rev. B* **2007**, *76*, 165202.
- [105] A. Kohan, G. Ceder, D. Morgan, C. G. Van de Walle, *Phys. Rev. B - Condens. Matter Mater. Phys.* **2000**, *61*, 15019.
- [106] J. Wang, R. Chen, L. Xiang, S. Komarneni, *Ceram. Int.* **2018**, *44*, 7357.
- [107] X. Yin, Y. Wang, R. Jacobs, Y. Shi, I. Szlufarska, D. Morgan, X. Wang, *Nano Lett.* **2019**, *19*, 7085.
- [108] S. Wang, X. Shi, J. Li, *RSC Adv.* **2016**, *6*, 107865.
- [109] E. A. Alkahtani, A. E. Merad, M. R. Boufatah, A. Benosman, *Optik* **2017**, *128*, 274.
- [110] M. Buryi, Z. Remeš, V. Babin, S. Chertopalov, K. Děcká, F. Dominec, J. Mičová, N. Neykova, *Materials* **2022**, *15*, 2261.
- [111] M. Gerosa, C. E. Bottani, C. D. Valentin, G. Onida, G. Pacchioni, *J. Phys. Condens. Matter* **2017**, *30*, 044003.
- [112] I. N. Yakovkin, P. A. Dowben, *Surf. Rev. Lett.* **2007**, *14*, 481.
- [113] L. Hedin, B. I. Lundqvist, *J. Phys. C Solid State Phys.* **1971**, *4*, 2064.
- [114] F. Tran, P. Blaha, *Phys. Rev. Lett.* **2009**, *102*, 226401.
- [115] J. P. Perdew, *Int. J. Quantum Chem.* **1985**, *28*, 497.

- [116]S. Große Holthaus, S. Köppen, T. Frauenheim, L. Colombi Ciacchi, *J. Chem. Theory Comput.* **2012**, 8, 4517.
- [117]M. Y. Sengul, C. A. Randall, A. C. T. van Duin, *ACS Appl. Mater. Interfaces* **2018**, 10, 37717.
- [118]N. H. Moreira, G. Dolgonos, B. Aradi, A. L. da Rosa, T. Frauenheim, *J. Chem. Theory Comput.* **2009**, 5, 605.
- [119]A. Calzolari, M. Bazzani, A. Catellani, *Surf. Sci.* **2013**, 607, 181.
- [120]X. Zhang, Y. Xia, T. He, *Mater. Chem. Phys.* **2012**, 137, 622.
- [121]Z. Zhou, F. Zhang, J. Wang, X. Zhang, W. Xu, R. Wu, L. Liao, X. Wang, J. Wei, *Mater. Sci. Eng. C* **2019**, 103, 109818.
- [122]J. Chen, R. E. Ruther, Y. Tan, L. M. Bishop, R. J. Hamers, *Langmuir* **2012**, 28, 10437.
- [123]R. Kar, S. Pal, *Int. J. Quantum Chem.* **2010**, 110, 1642.
- [124]H. Hu, C. Kang, Z. Xiong, Y. Cui, L. Chen, *Mater. Today Commun.* **2023**, 36, 106789.
- [125]S. Ghosh, S. Mishra, E. Avigad, B. P. Bloom, L. T. Baczewski, S. Yochelis, Y. Paltiel, R. Naaman, D. H. Waldeck, *J. Phys. Chem. Lett.* **2020**, 11, 1550.
- [126]K. Banerjee-Ghosh, O. B. Dor, F. Tassinari, E. Capua, S. Yochelis, A. Capua, S.-H. Yang, S. S. P. Parkin, S. Sarkar, L. Kronik, L. T. Baczewski, R. Naaman, Y. Paltiel, *Science* **2018**, 360, 1331.

APPENDIX

A. Atomic force microscopy and further computational data

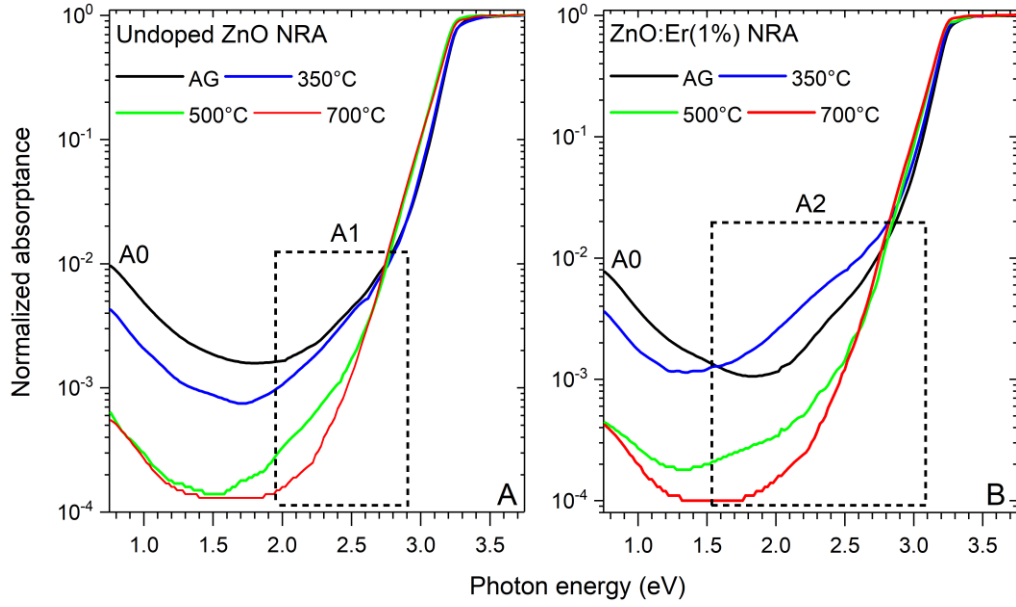


Figure A1. Absorbance of the undoped ZnO **a**) and ZnO:Er(1%) **b**) NRA, as grown and annealed in air at the temperatures indicated in the legends. A1,2 and FE stress specific bands.

Table A1. RMS roughness, thickness, and force threshold for BSA layers deposited on ZnO surfaces obtained from AFM measurements. RMS roughness of BSA molecule, averaged height of BSA molecule, and averaged binding energy for five amino acids from calculations.

Sample	RMS roughness (Å)	Thickness of BSA (Å)	Force threshold (nN)	RMS roughness in FF (Å)	Average height of in FF (Å)	Average binding energy (eV)
polar Zn-face (0001)	5.5 ± 1.5	20.5 ± 2.2	40 ± 5	15.4	45.7	-1.86
polar O-face (000 $\bar{1}$)	14.6 ± 2.5	27.0 ± 1.3	60 ± 5	26.4	103.0	-0.05
non-polar (10 $\bar{1}$ 0)	8.4 ± 2.1	18.9 ± 2.2	80 ± 10	20.4	53.3	-2.86
non-polar (11 $\bar{2}$ 0)	19.1 ± 4.2	15.4 ± 3.7	10 ± 5	20.1	52.9	-1.70

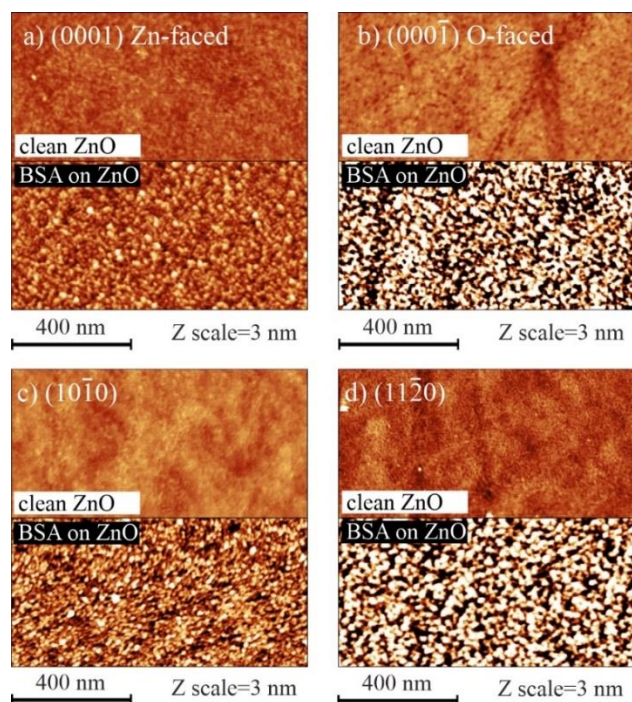


Figure A2. AFM Topography measurement of clean ZnO samples and BSA layers deposited on corresponding a) (0001), b) (000 $\bar{1}$), c) (10 $\bar{1}$ 0) and d) (11 $\bar{2}$ 0) ZnO surfaces.

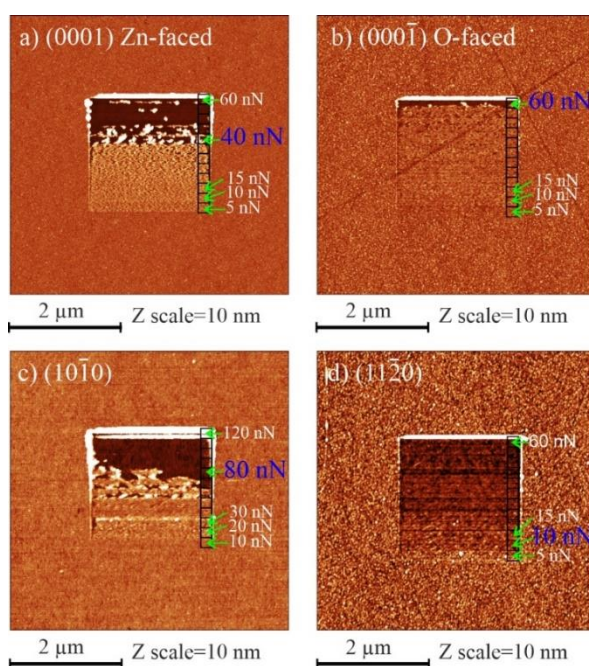


Figure A3. AFM nanoshaving experiments performed on BSA layers deposited on ZnO samples to measure the threshold of BSA layer removal from (a) (0001), (b) (000 $\bar{1}$), (c) (10 $\bar{1}$ 0) and (d) (11 $\bar{2}$ 0) ZnO surfaces.

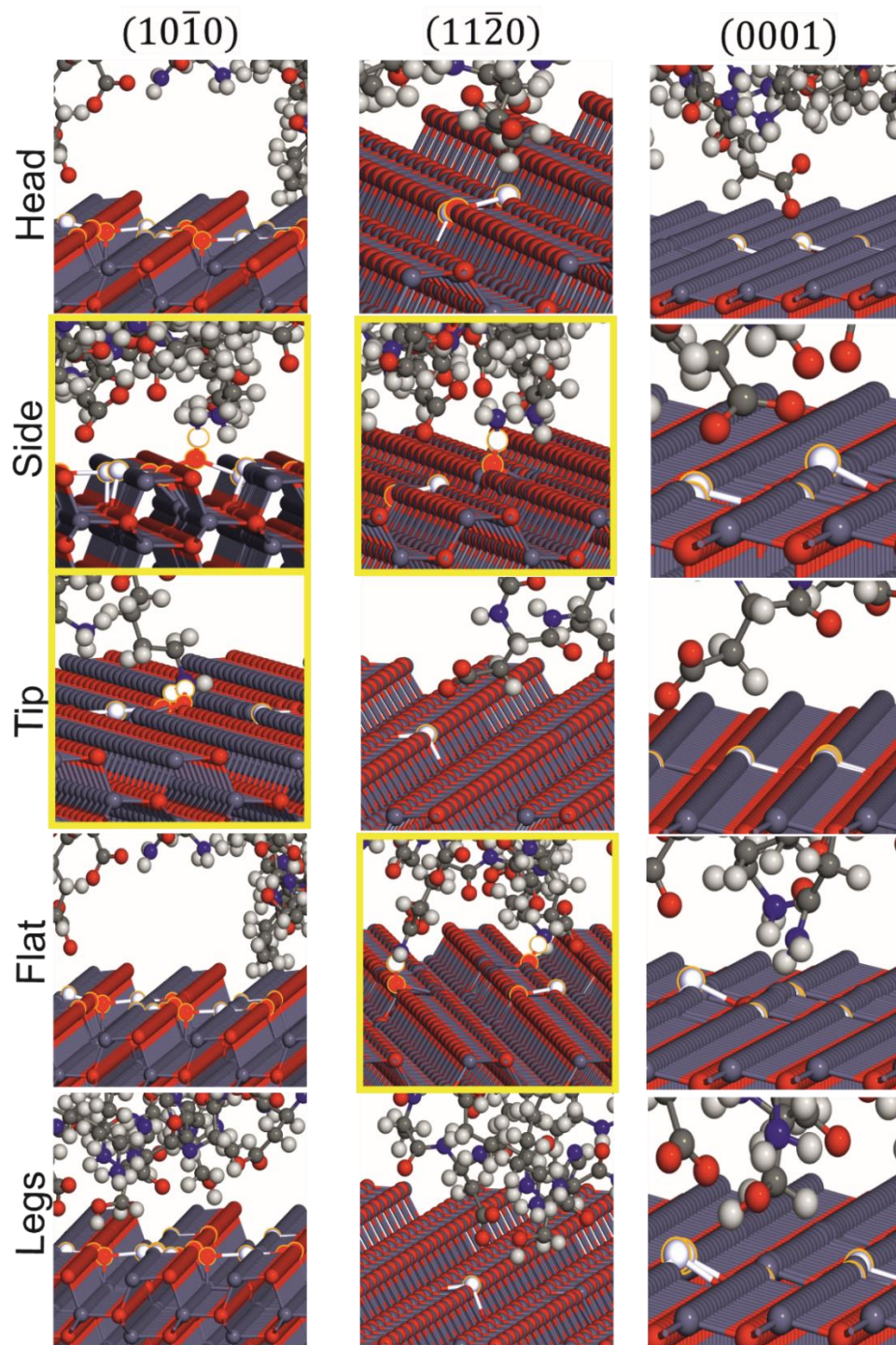
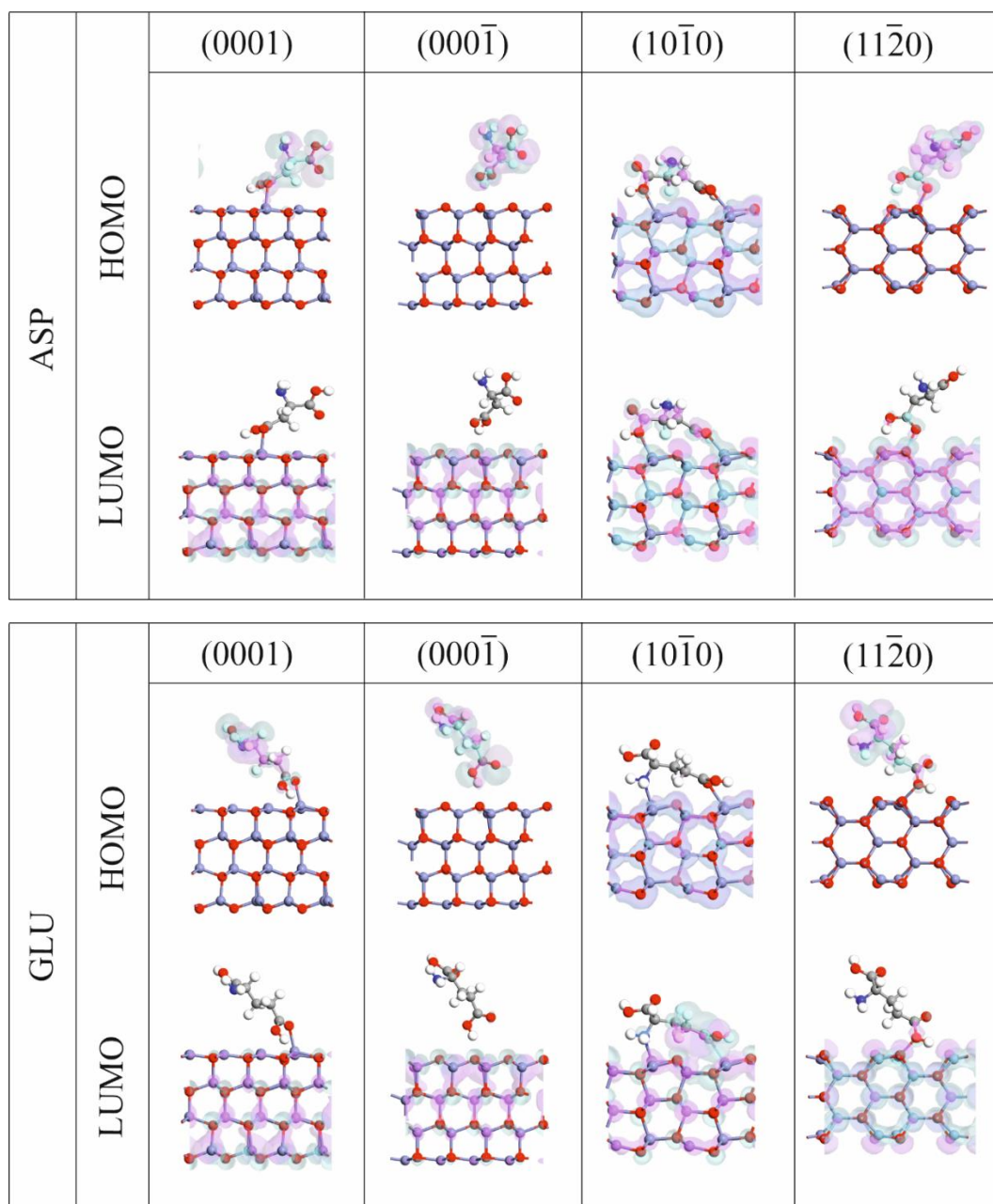
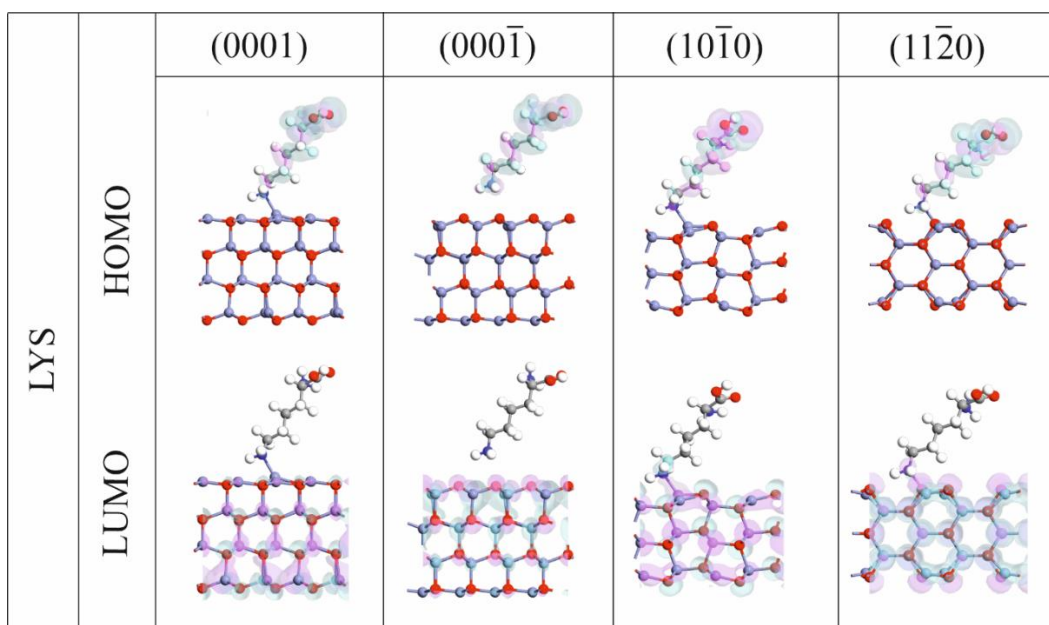
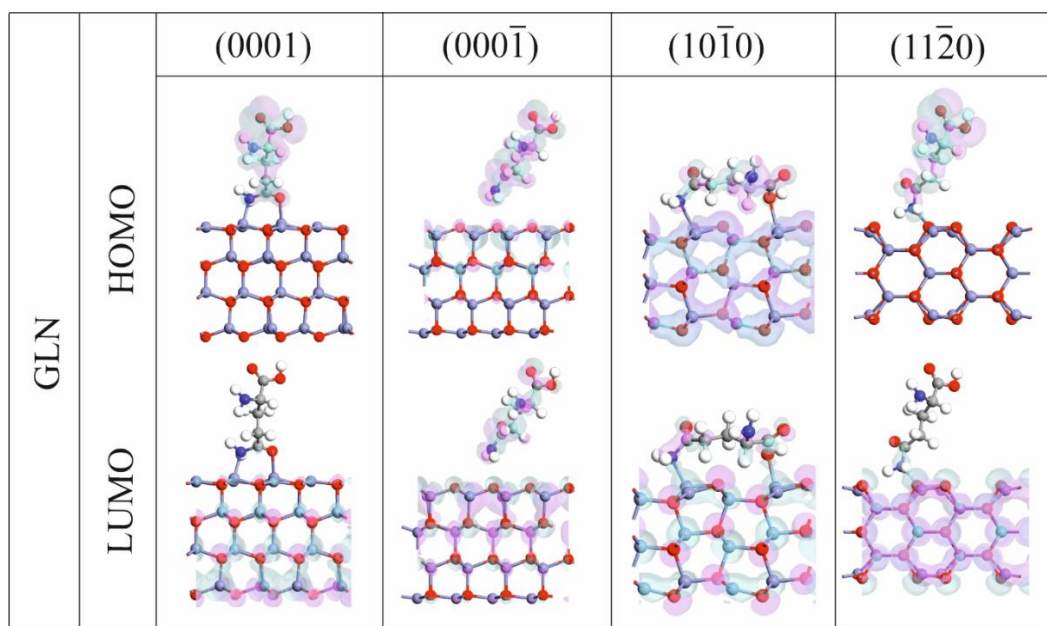


Figure A4. Magnified images of BSA-ZnO interaction sites for different orientations of BSA over $(10\bar{1}0)$, $(11\bar{2}0)$, and (0001) ZnO planes. The structures are results of force field simulations. Yellow frames denote the configurations in which chemical bonding happens in the calculations. Note, the O-faced surface repelled the BSA in all orientations, so no interactions observed in force field calculations.





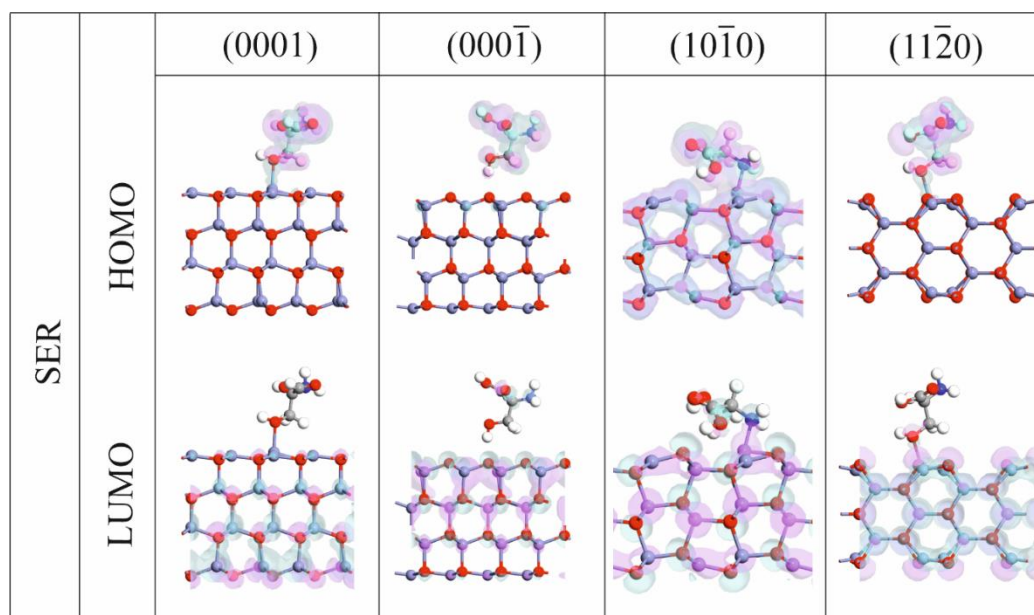


Figure A5. All configurations of chemisorption of amino acids on ZnO surfaces and their HOMO-LUMO distributions.

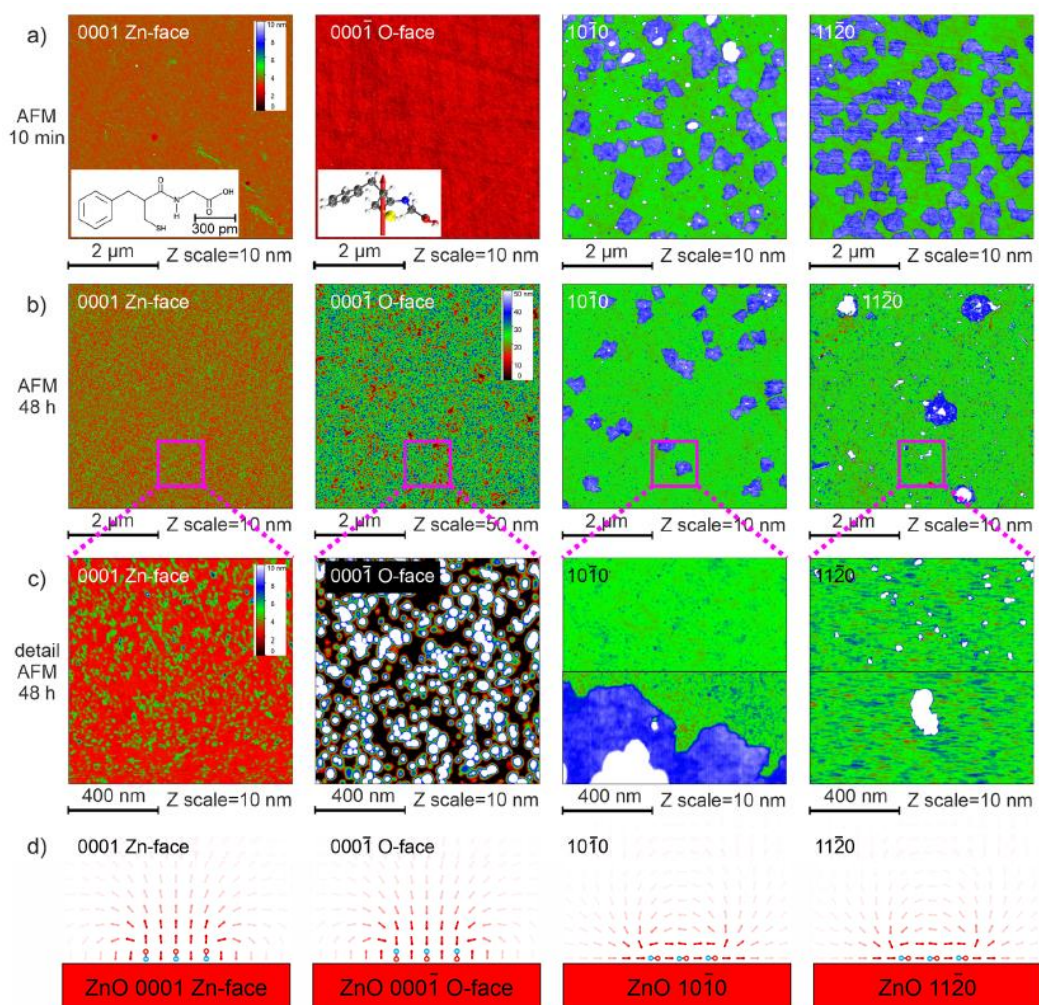


Figure A6. *a)* Overview AFM morphology of thiorphan self-assembled layers after 10 min adsorption in ethanol on different ZnO facets. (*a*,inset) Chemical structure of thiorphan molecule and dipole moment of individual thiorphan molecule. *b)* Overview AFM morphology of thiorphan self-assembled layers after 48 h adsorption in ethanol on different ZnO facets. *c)* Detailed AFM morphology of thiorphan self-assembled layers after 48h adsorption on different ZnO facets. *d)* Schematic model of thiorphan self-assembled layers, surface dipole orientation with electric field. Stronger electric field is shown with darker arrows.

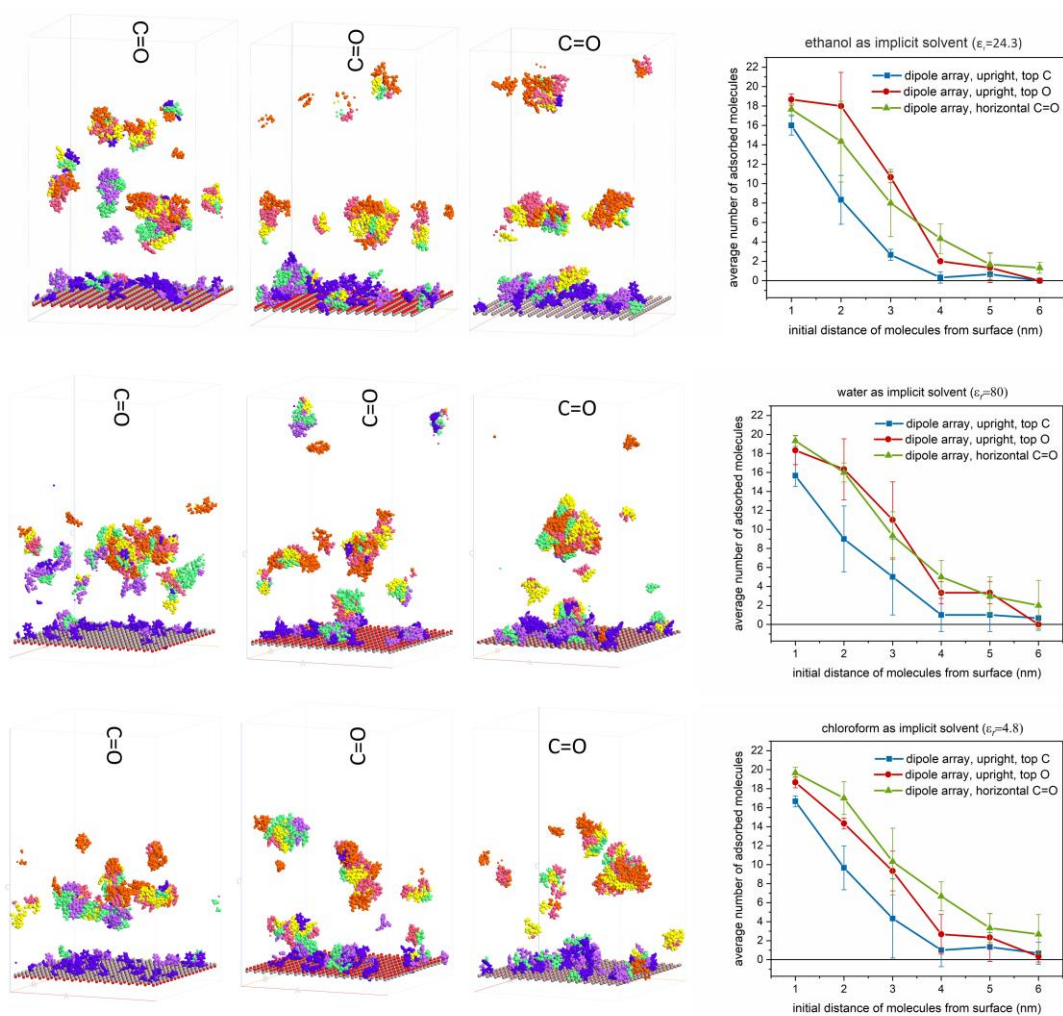


Figure A7. Final stages of adsorption process on C-top, O-top, and horizontally oriented C=O dipole array in **a)** ethanol, **b)** water, and **c)** chloroform respectively.

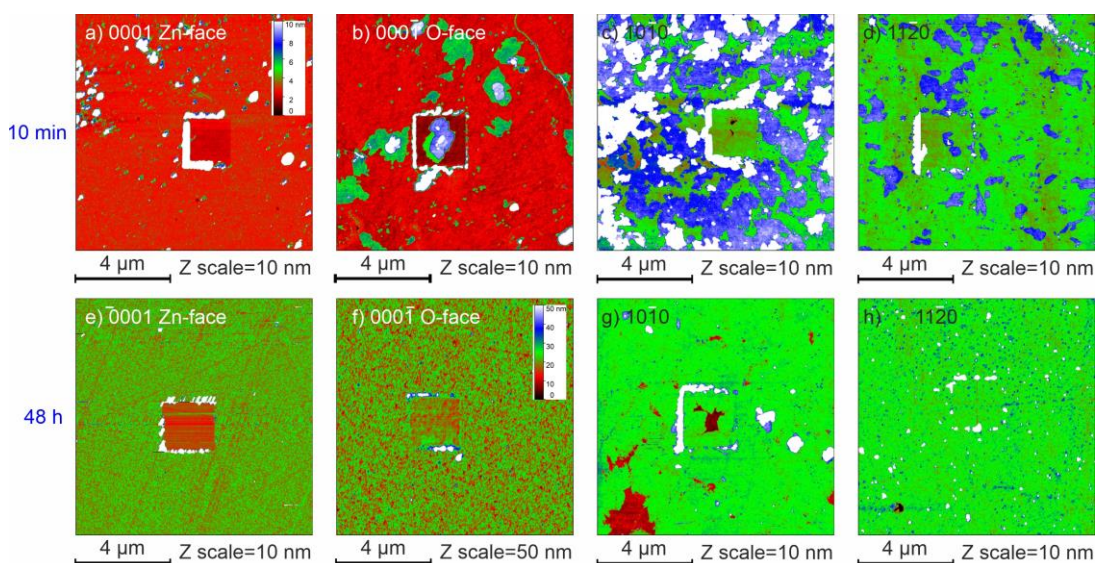


Figure A8. PFQNM AFM morphology after nanoshaving experiments for thiorphan adsorption **a-d)** after 10 min and **e-h)** after 48 h adsorption on different ZnO facets. Contact mode nanoshaving experiments were performed with stiff cantilever (Tap300, 40 N/m). First, $2 \times 2 \mu\text{m}^2$ area was scanned in contact mode with high load force 2400 nN. Then, $10 \times 10 \mu\text{m}^2$ area was scanned in PFQNM mode to observed the result on contact mode nanoshaving. Note that during nanoshaving experiments the AFM cantilever was not able to penetrate some of thiorphan layers.

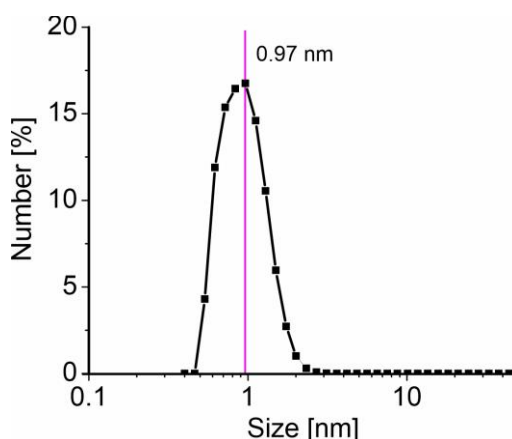


Figure A9. Number size distribution measured by DLS method on thiorphan solution in ethanol (concentration = 1 mg/ml). The result shows presence of individual molecules only (peak maximum is at the size 0.97 nm that is approximately equal to the size of one molecule) and absence of thiorphan aggregates in ethanol solution.

B. Own contribution of the author

In all publications, the author conceived and performed all the calculations presented in the publications as well as further calculations of the analysed properties based on the performed theoretical calculations. The author created all the figures and tables related to the theoretical results presented in the publications and supplementary information. He also contributed to the design of computational experiments including selection of theoretical methods and to the discussion and interpretation of the results. The author wrote all the texts in the publications where he is the first author and contributed with texts and revisions to the other publications.

C. List of co-authored publications

Publications in impacted journals:

1. M. BURYI, Z. REMEŠ, F. HÁJEK, K. KULDOVÁ, V. BABIN, K. DĚCKÁ, L. LANDOVÁ, H. HEMATIAN, B. REZEK. Peculiarities related to Er doping of ZnO nanorods simultaneously grown as particles and vertically arranged arrays. *Journal of Physical Chemistry C*, 2023, 127(45), 22177–22189. ISSN 1932-7447. DOI [10.1021/acs.jpcc.3c05471](https://doi.org/10.1021/acs.jpcc.3c05471). **Q1**
2. E. UKRAINTSEV*, H. HEMATIAN*, B. REZEK. Polarization controlled formation of thiorphan nanodots and nanoislands by surface dipoles on ZnO facets. *Langmuir*, 2023, 39(5), 1764-1774. ISSN 0743-7463. DOI [10.1021/acs.langmuir.2c02393](https://doi.org/10.1021/acs.langmuir.2c02393). **Q1**
(*shared the first authorship, both contributed equally)
3. H. HEMATIAN, E. UKRAINTSEV, and B. REZEK. Strong Structural and Electronic Binding of Bovine Serum Albumin to ZnO via Specific Amino Acid Residues and Zinc Atoms. *ChemPhysChem*, 2022, 23(2), 25-33. ISSN 1439-4235. DOI [10.1002/cphc.202100639](https://doi.org/10.1002/cphc.202100639). **Q2**
4. B. REZEK., H. HEMATIAN, J. JÍRA, D. RUTHERFORD, J. KULIČEK, E. UKRAINTSEV, Z. REMEŠ. Microscopic Study of Bovine Serum Albumin Adsorption on Zinc Oxide (0001) Surface. *Physica Status Solidi A*, 2021, 218(6), 2000558, 6 pages. ISSN 1862-6300. DOI [10.1002/pssa.202000558](https://doi.org/10.1002/pssa.202000558). **Q2**

Publications in conference proceedings:

5. H. HEMATIAN and B. REZEK. Study of bovine serum albumin interaction with zinc oxide surfaces by force field simulations. In: *IOP Conference Series: Materials Science and Engineering, Volume 1050, Development of Materials Science in Research and Education (DMSRE30 2020) 7th-11th September 2020, Pavlov, Czech Republic*. Pavlov, 2020-09-07/2020-09-11. Bristol: IOP Publishing Ltd, 2021. ISSN 1757-899X. DOI [10.1088/1757-899X/1050/1/012006](https://doi.org/10.1088/1757-899X/1050/1/012006).

D. Conference presentations

1. E. UKRAINTSEV, H. HEMATIAN, and B. REZEK. AFM-in-SEM analyses of thiorphan assembly on ZnO polar and nonpolar facets. Nanocon 2022, Brno, Czech Republic, October 2022.
2. H. HEMATIAN, E. UKRAINTSEV, and B. REZEK. Computational study of thiorphan molecule interaction with zinc oxide low index facets. Nanocon 2022, Brno, Czech Republic, October 2022; **oral presentation**
3. H. HEMATIAN, E. UKRAINTSEV, and B. REZEK. Adsorption of bovine serum albumin and amino acid residues on ZnO single-crystal facets: simulations and microscopy. Nanocon 2021, Brno, Czech Republic, October 2021; **oral presentation, best lecture award**
4. H. HEMATIAN and B. REZEK. Study of bovine serum albumin interaction with zinc oxide surfaces by force field simulations. DMSRE30 2020, Pavlov, Czech Republic, September 2020.

E. Awards and honours

1. Awarded the “**Best Lecture** for the Young scientist” prize in Nanocon 2021, Brno, October 2021 (more info: <https://www.nanocon.eu/en/about-the-conference-history-proceedings-gallery/2021/>)
2. Paper (doi: 10.1021/acs.langmuir.2c02393) was selected for the **cover page** in Langmuir journal by its editors.
3. Paper (doi: [10.1002/cphc.202100639](https://doi.org/10.1002/cphc.202100639)) was selected as the **Feature Article** by Chem. Phys. Chem. journal editors, including a graphical presentation as the **cover page** art.
4. Paper (doi: [10.1002/pssa.202000558](https://doi.org/10.1002/pssa.202000558)) was selected for the **cover page** in Physica Status Solidi A journal by its editors.
5. Awarded the "Student Grant Competition" **grant** of Czech Technical University in Prague, 2021-2023.
6. Completed a funded internship at **Max Planck Institute of Microstructure Physics**, Halle, Germany, under direct supervision of **prof. Stuart Parkin**, Jan. 2023-Jul. 2023.

F. Publications reprints

List of the enclosed publications:

1. Hematian, H.; Rezek, B. Study of Bovine Serum Albumin Interaction with Zinc Oxide Surfaces by Force Field Simulations. IOP Conference Series: Materials Science and Engineering 2021, 1050, 012006. <https://doi.org/10.1088/1757-899x/1050/1/012006>.
2. Rezek, B.; Hematian, H.; Jíra, J.; Rutherford, D.; Kuliček, J.; Ukraintsev, E.; Remeš, Z. Microscopic Study of Bovine Serum Albumin Adsorption on Zinc Oxide (0001) Surface. *Physica Status Solidi (A)* 2021, 218 (6), 2000558. <https://doi.org/10.1002/pssa.202000558>.
3. Hematian, H.; Ukraintsev, E.; Rezek, B. Strong Structural and Electronic Binding of Bovine Serum Albumin to ZnO via Specific Amino Acid Residues and Zinc Atoms. *ChemPhysChem* 2022, 23 (2), e202100639. <https://doi.org/10.1002/cphc.202100639>.
4. Ukraintsev, E.; Hematian, H.; Rezek, B. Polarization Controlled Assembly of Ultrathin Thiorphan Nanostructures on ZnO Surface Facets. *Langmuir* 2023, 39 (5), 1764–1774. <https://doi.org/10.1021/acs.langmuir.2c02393>.
5. Buryi, M.; Remeš, Z.; Hájek, F.; Kuldová, K.; Babin, V.; Děcká, K.; Hematian, H.; Landová, L.; Neykova, N.; Horynová, E.; Rezek, B. Peculiarities Related to Er Doping of ZnO Nanorods Simultaneously Grown as Particles and Vertically Arranged Arrays. *J. Phys. Chem. C* 2023, 127 (45), 22177–22189. <https://doi.org/10.1021/acs.jpcc.3c05471>.
6. Cover picture of *physica status solidi (a)* journal, volume 218, issue 6, March 2021.
7. Cover picture of *ChemPhysChem* journal, volume 23, issue 2, January 19, 2022.
8. Cover picture of *Langmuir* journal, volume 39, issue 5, February 7, 2023.

Study of bovine serum albumin interaction with zinc oxide surfaces by force field simulations

H Hematian and B Rezek

Faculty of Electrical Engineering, Czech Technical University in Prague, Technická 2, 16227 Prague, Czech Republic

hemathad@fel.cvut.cz

Abstract. We studied the interactions of bovine serum albumin (BSA) molecule with ZnO surfaces by force field simulations. The different orientations of BSA over the two main nonpolar wurtzite ZnO surfaces ($10\bar{1}0$) and ($11\bar{2}0$) have been investigated. These surfaces contain both Zn and O atoms. We compare the results also with polar Zn-face (0001) surface. The results demonstrate tendency of BSA molecule for being adsorbed on the ZnO surface in specific orientations. This happens either by bonding between a hydrogen atom of BSA molecule to an oxygen atom of the ZnO surface or by physical attraction inducing ZnO atoms displacement in some cases.

1. Introduction

Serum albumin (SA) is the most plentiful protein in blood plasma and has been investigated intensively for its numerous vital functions such as maintaining the oncotic pressure, transporting drugs as well as contribution in functionality of the immune system. The interactions of SA with a wide range of nanomaterials have been the subject of many investigations [1,2]. The adsorption of SA on diamond as one of the most popular materials in biomedicine and electronics has been already investigated [3–6]. Besides diamond, zinc oxide (ZnO) as a wide and direct band-gap semiconductor with well-known optical properties, low level of toxicity and great biocompatibility possesses luminescence property that can be extremely useful in various biomedical and pharmaceutical applications [7]. The interactions of ZnO with a range of biomolecules and proteins have been reported by multiple experimental studies [8,9]. In [8], an *in vitro* toxicological investigation supported by theoretical modelling has shown multilayer adsorption of lactate dehydrogenase (LDH) on ZnO nanomaterials. Strong interaction of adenosine triphosphate (ATP) with ZnO nanostructures through chelate formations has also been demonstrated by Raman spectroscopy, XRD, and electron microscopy in [9]. In addition, using UV–vis absorption, fluorescence, synchronous fluorescence, and Raman spectroscopy to study of ZnO nanoparticles covalently and non-covalently coated by bovine serum albumin (BSA) has shown that the binding between ZnO nanoparticles and BSA decreases the cytotoxicity of ZnO nanoparticles [10]. Despite availability of large amount of experimental data conducive to perceiving the essence of ZnO-proteins interactions, fine aspects behind the interactions still need to be studied theoretically to understand the details of the phenomena on atomic scale.

However, the main challenge in computational study of the systems constituting nanomaterials and complex molecules such as albumin is the huge number of the atoms in the system which can make the calculations extremely costly if a proper approach is not adopted. One possible approach to cope



Content from this work may be used under the terms of the [Creative Commons Attribution 3.0 licence](https://creativecommons.org/licenses/by/3.0/). Any further distribution of this work must maintain attribution to the author(s) and the title of the work, journal citation and DOI.

with large systems is selecting more computationally efficient methods, which are still sufficiently accurate, over more costly ones with higher levels of accuracy (such as DFT and *ab initio* methods). Another complementary way can be considering a reasonable simplification in the system under study, such as fixing or excluding some non-interacting atoms in computations.

In this study, we aimed to elucidate the interaction of a BSA molecule with ZnO surfaces on atomic scale. Force field simulations have been carried out under some simplifying assumptions to overcome the computational limitations imposed by the huge size of the system. The interactions between BSA and ZnO for nonpolar and polar surfaces of ZnO have been compared.

2. Method

The adsorption of BSA on ZnO nonpolar surfaces which contain both Zn and O atoms has been investigated by implementing force field method in QuantumATK software which enables the possibility of dealing with the huge number of atoms in our system. The results have also been compared to polar Zn-face (0001) surface. HP system with a Core i5 8th generation processor and 8 GB RAM was used to perform the computations.

The system under the study consists of a BSA molecule and ZnO slab that are available from the RCSB Protein Data Bank website and QuantumATK software database respectively. Since hydrogen atoms are generally not observed in X-ray crystal structures, BSA structure taken from the Protein Data Bank lacks hydrogen atoms. Mol Probioty has been employed to add hydrogen atoms to the molecule. Some approximations were also considered to provide the feasibility of using predefined force field potential sets as there are no sets of force fields defined for all types of atoms in BSA+ZnO system. Sulphur atoms have been excluded from the structure of BSA molecule to enable ReaxFF potential for force field simulations. This seems a reasonable simplification as sulphur atoms in BSA are not situated at or near the locations where the interaction of the molecule with ZnO occurs. To deduct the volume and duration of the calculations, different orientations of BSA molecule have been manually adjusted over ZnO surfaces in the distance range of 3-20 Å. The optimization trajectory and energy of the system then have been observed to discuss the interactions of the BSA molecule with ZnO planes.

3. Results and discussion

The simulations have been carried out for different orientations of BSA over nonpolar and polar ZnO planes. Figure 1 depicts five non-equivalent configurations used for forcefield simulations which are named based on the orientation of BSA molecule versus ZnO surface: Head, Side, Flat, Legs, and Tip. The distance between the nearest atom of BSA molecule and the surface of ZnO slab is set manually at around 3 Å for all configurations. The simulations have also been performed for the distance of 20 Å where there was no interaction between BSA molecule and ZnO surface detected regardless of the orientation of BSA.

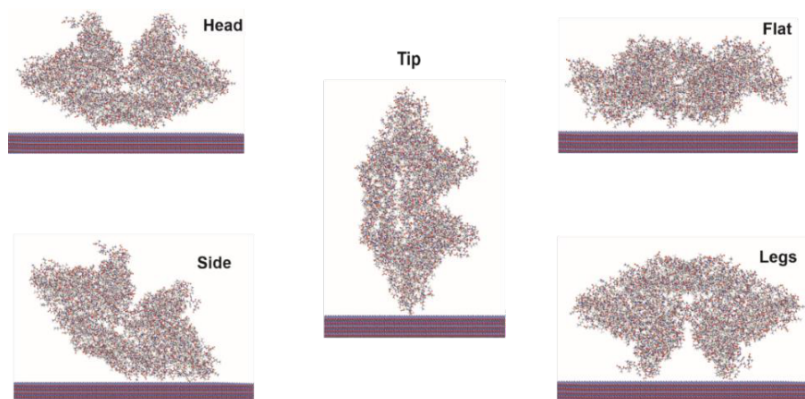


Figure 1. Different orientations of BSA molecule versus ZnO.

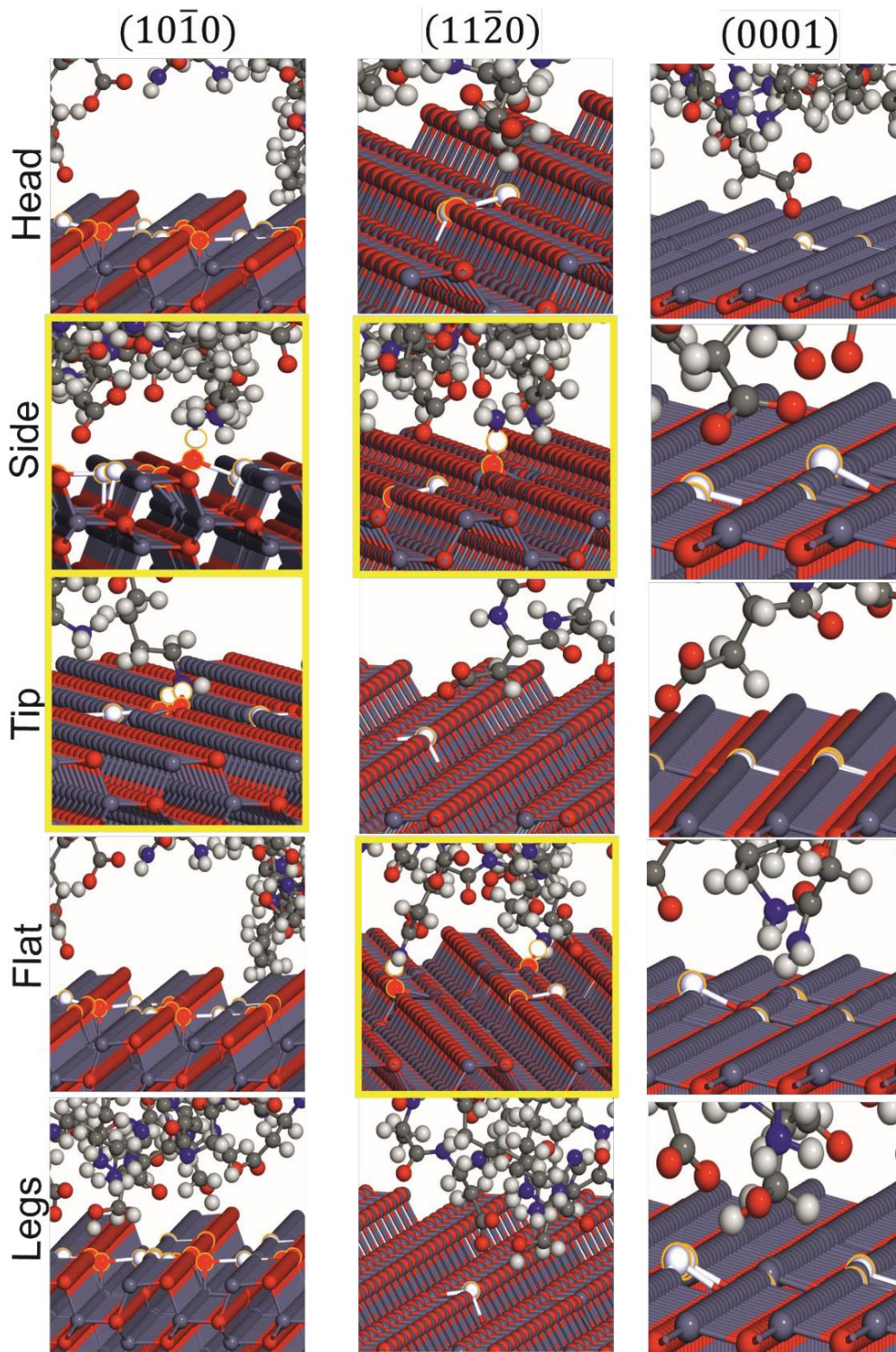


Figure 2. Magnified images of BSA-ZnO interaction sites for different orientations of BSA over $(10\bar{1}0)$, $(11\bar{2}0)$, and (0001) ZnO planes. The structures are results of force field simulations. Yellow frames denote the configurations in which chemical bonding happens in the calculations.

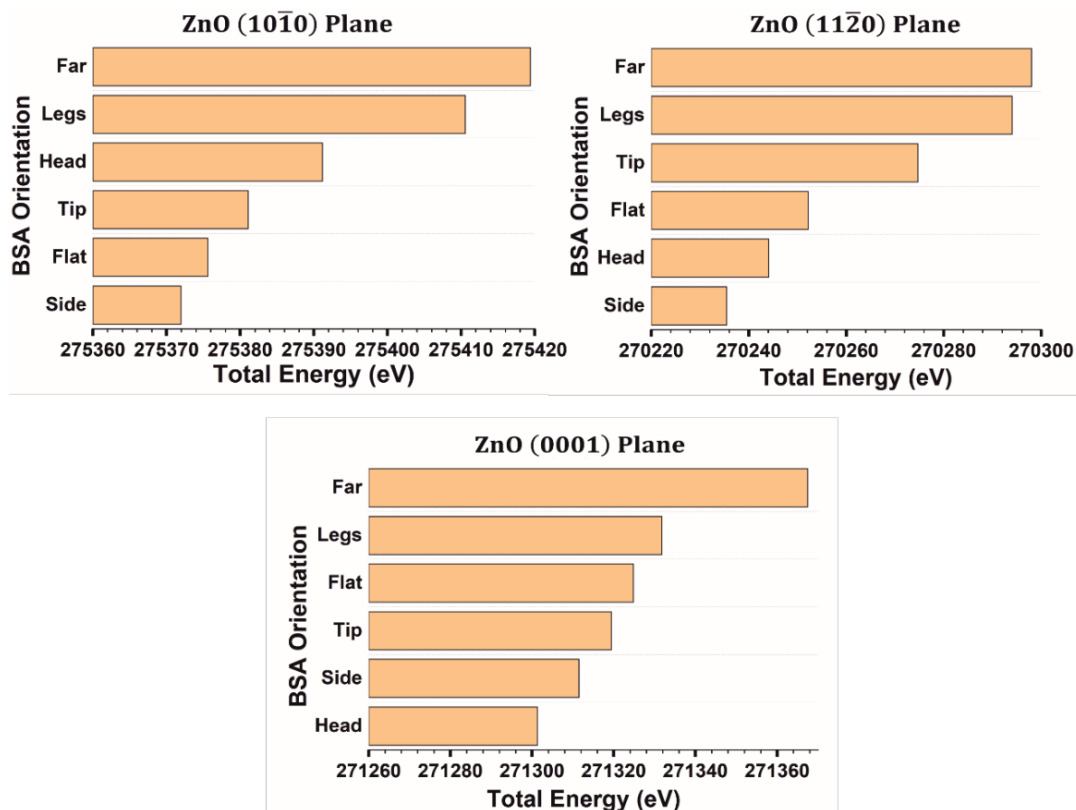


Figure 3. Total energies of BSA+ZnO($10\bar{1}0$), BSA+ZnO($11\bar{2}0$), and BSA+ZnO(0001) systems for different orientations of BSA.

Figure 2 summarizes the results of forcefield simulations for BSA molecule over ZnO non-polar and polar planes ($(10\bar{1}0)$, $(11\bar{2}0)$, and (0001)). Magnified images of the interaction sites between BSA molecule and ZnO planes are illustrated for different orientations of BSA. In all cases, the proximity of BSA molecule to ZnO surface has culminated in mutual attraction, followed by re-arrangement of surface atoms on ZnO slab. In addition to these displacements, chemical bonding of atoms from BSA molecule with atoms on ZnO surface can also be seen at interaction sites in Side and Tip orientations over $(10\bar{1}0)$ plane, as well as Side and Flat orientations over $(11\bar{2}0)$ plane. In these cases, which are highlighted by yellow frames in figure 2, chemical bonding happens between hydrogen atoms of BSA molecule and surface oxygen atoms of ZnO. For (0001) surface, no chemical bonding has been observed since it contains only Zn atoms compared to nonpolar surfaces which include both Zn and O atoms. It must be mentioned here that more accurate electron-based calculations such as DFT have to be employed to investigate the chemical bonding phenomena and to validate the observed chemical bonds. Nevertheless, the results obtained from the current force field simulations will be helpful for selection of relevant parts of the system for more expensive calculations. Validating the chemical bonding phenomena observed in force field simulations by employing DFT method is going to be done as the next phase of the current study.

To compare different orientations of BSA and determine the most likely one over each ZnO plane, total energy of the system is displayed via bar-graphs in figure 3. Since orientation of BSA molecule is the only varying aspect and other characteristics of the systems remain completely unaffected, total energy of the systems can be observed to deduce the favourable position. According to the total energy graphs in figure 3, tendency of BSA molecule for being adsorbed on ZnO surfaces is noticeably different for different orientations. The head orientation has the lowest energy in the BSA+ZnO(0001) system and thus it is the most likely orientation over ZnO (0001) surface. The side orientation has

been observed as the most favourable for BSA+ZnO(10 $\bar{1}$ 0) and BSA+ZnO(11 $\bar{2}$ 0) systems. It is also worth mentioning that mechanism of interactions is not identical in the most favourable positions over different planes and it depends on the different groups of atoms from the BSA molecule and type of the ZnO plane. Atoms are differently re-arranged, and the adsorption might occur through either physisorption or chemisorption.

4. Conclusion

We employed forcefield simulations to investigate the interactions of BSA molecule with ZnO nonpolar and polar surfaces. The total energy indicates that BSA molecule is likely to adsorb in different orientation on different types of ZnO surfaces. The way how BSA molecule interacts with ZnO surfaces depends on the type of ZnO surface as well as the orientation of the BSA molecule. The computational results demonstrate that the vicinity of BSA molecule with ZnO surfaces results in rearrangement of atoms on ZnO surfaces that lowers the total energy and gives rise to physical binding. Furthermore, in several configurations, chemical bonding between BSA atoms and ZnO surface has also been observed which needs to be validated by more accurate (but more costly) electron-based simulation methods in further studies. This may have important implications for interaction of ZnO with biological environment as well as impact its optical and electronic properties.

Acknowledgements

The work was supported by the Czech Science Foundation (GACR) project 19-02858J.

References

- [1] Anand K, Rajamanikandan R, Selva Sharma A, Ilanchelian M, Khan F I, Tiloke C, Katari N K, Boomi P, Balakumar C, Saravanan M, Palanisamy S, Ramesh M, Lai D and Chuturgoon A A 2020 Human serum albumin interaction in silico and anticancer evaluation of pine-gold nanoparticles *Process Biochemistry* **89** 98–109
- [2] Wang Y and Ni Y 2013 New insight into protein–nanomaterial interactions with UV-visible spectroscopy and chemometrics: human serum albumin and silver nanoparticles *Analyst* **139** 416–24
- [3] Rezek B, Michalíková L, Ukraintsev E, Kromka A and Kalbacova M 2009 Micro-pattern guided adhesion of osteoblasts on diamond surfaces *Sensors (Basel)* **9** 3549–62
- [4] Rezek B, Ukraintsev E, Krátká M, Taylor A, Fendrych F and Mandys V 2014 Epithelial cell morphology and adhesion on diamond films deposited and chemically modified by plasma processes *Biointerphases* **9** 031012
- [5] Kozak H, Artemenko A, Ukraintsev E, Choukourov A, Rezek B and Kromka A 2019 Infrared absorption spectroscopy of albumin binding with amine-containing plasma polymer coatings on nanoporous diamond surfaces *Langmuir* **35** 13844–52
- [6] Ukraintsev E, Rezek B, Kromka A, Broz A and Kalbacova M 2009 Long-term adsorption of fetal bovine serum on H/O-terminated diamond studied in situ by atomic force microscopy *physica status solidi (b)* **246** 2832–5
- [7] Kalpana V N and Devi Rajeswari V 2018 A review on green synthesis, biomedical applications, and toxicity studies of ZnO NPs *Bioinorganic Chemistry and Applications* **2018** e3569758
- [8] Da Silva E, Kembouche Y, Tegner U, Baun A and Jensen K A 2019 Interaction of biologically relevant proteins with ZnO nanomaterials: A confounding factor for in vitro toxicity endpoints *Toxicology in Vitro* **56** 41–51
- [9] Bhaumik A, Shearin A M, Delong R, Wanekaya A and Ghosh K 2014 Probing the interaction at the nano–bio interface using raman spectroscopy: ZnO nanoparticles and adenosine triphosphate biomolecules *J. Phys. Chem. C* **118** 18631–9
- [10] Žūkienė R and Snitka V 2015 Zinc oxide nanoparticle and bovine serum albumin interaction and nanoparticles influence on cytotoxicity in vitro *Colloids and Surfaces B: Biointerphases* **135** 316–23

Microscopic Study of Bovine Serum Albumin Adsorption on Zinc Oxide (0001) Surface

Bohuslav Rezek,* Hadi Hematian, Jaroslav Jíra, David Rutherford, Jaroslav Kuliček, Egor Ukraintsev, and Zdeněk Remeš

Properties and functions of various ZnO materials are intensively investigated in biological systems for diagnostics, therapy, health risks assessment as well as bactericidal and decontamination purposes. Herein, the interface between ZnO and biological environment is studied by characterizing adsorption of bovine serum albumin (BSA) and fetal bovine serum (FBS) using atomic force microscopy with CF₄-treated tips. Similar molecular morphologies (thickness around 2 nm) yet different binding forces to ZnO (10–25 nN) are observed. These observations are corroborated by atomic scale simulations of BSA on (0001) ZnO surface using force-field method and showing rearrangements of Zn surface atoms. Such binding may have an impact also on other properties of ZnO–BSA complex.

1. Introduction

Zinc oxide (ZnO) is a semiconductor material that can be prepared in various forms and sizes and it is commonly available commercially. It is well known as a material for transparent conductive electrodes and light-emitting^[2] and gas-sensor devices^[3] as well for its photocatalytic^[4] and bactericidal properties,^[5] in particular in nanoparticle form. ZnO nanomaterials can be prepared by various methods, from magnetron sputtering,^[6] wet chemical synthesis on substrates^[1,7] and in solutions^[8] to green eco-friendly approaches.^[9] Because of biocompatibility and antibacterial properties, ZnO is often used in exploratory as well as well-established biomedical research and applications.^[10] Application of beneficial physicochemical properties of ZnO nanostructures for the detection of wide range of biological compounds was highlighted.^[11] The hybrid inorganic/organic nanoparticles, including core-shell, Janus, dumbbells and others, offer new multifunctionality due to the synergy

between the involved components.^[12] Tuning combined magnetic and antibacterial properties of ZnO nanopowders was also reported.^[13]

One of the key factors affecting the material interaction with biological environment is the protein adsorption on its surface. The proteins can control and even pattern the cell adhesion on surfaces^[14] and affect electronic response of the biosensors.^[15] Interaction with proteins is the basis of a nanoparticle bioreactivity.^[16] It gives rise to the formation of dynamic nanoparticle–protein corona that may influence cellular uptake, inflammation, accumulation, degradation, and clearance of the nanoparticles. It can influence (positively

or negatively) toxicity of nanoparticles^[17–19] and generally induce conformational and compositional changes in adsorbed protein molecules which may affect the overall bioreactivity of nanoparticles.^[18]


In recent years, biointerface research that focuses on bacteria–surface interactions has been primarily driven by the goals of killing bacteria (antimicrobial) and fouling prevention (antifouling).^[20] Nevertheless, there is a potential to create biointerfaces with features that can manipulate and dictate the behavior of bacteria rather than killing or deterring them.^[21] For instance, ZnO hedgehog-like structures were used for controlled cell cultivation.^[8]

The mutual interaction of ZnO nanomaterials and biological environment can manifest itself in various ways and can be very specific for particular material and its surface modification.^[8] The surface, shape, size, and doping effects of ZnO provided opportunities for various gas sensors^[3] or biosensors.^[11] Free carrier concentration in ZnO can be significantly increased and photoluminescence altered by hydrogen plasma treatment.^[22] Optoelectronic properties of ZnO can also be influenced by adsorbed proteins. A study of bovine serum albumin (BSA) interacting with ZnO nanoparticles in aqueous medium or as a film on quartz substrates showed quenching of the fluorescence intensity of BSA in the presence of ZnO,^[19,23] presumably due to energy transfer from the excited BSA to ZnO in the ZnO–BSA complex.^[23]

Yet understanding actual processes behind observed biological and electronic effects is still debated. One reason is complexity in terms of ZnO fabrication parameters, resulting structural, chemical, and electronic properties as well as the effect of biological environment, where the nanomaterials can significantly change the size, shape, and zeta potential.

Prof. B. Rezek, H. Hematian, Dr. J. Jíra, Dr. D. Rutherford, Dr. J. Kuliček
Faculty of Electrical Engineering
Czech Technical University in Prague
Technická 2, Prague 6 16627, Czech Republic
E-mail: rezekboh@fel.cvut.cz

Dr. E. Ukraintsev, Dr. Z. Remeš
Institute of Physics
Czech Academy of Sciences
Cukrovarnická 10, Prague 6 16200, Czech Republic

 The ORCID identification number(s) for the author(s) of this article can be found under <https://doi.org/10.1002/pssa.202000558>.

DOI: 10.1002/pssa.202000558

Therefore, in this work, we aim to contribute to deeper understanding of the ZnO biointerface and its interaction with microorganisms such as cells and bacteria. We study adsorption of biomolecules from BSA and fetal bovine serum (FBS) solutions on the ZnO surface by microscopic methods and complement the study by theoretical computing. Similar molecular morphologies yet different binding forces of the biomolecules on ZnO are observed. We propose that the surface dipole and rearrangement of surface atoms are responsible rather than hydrophobic property of the polar ZnO surface. We not only discuss similarities but also specific differences on ZnO compared to other materials.

2. Results and Discussion

Figure 1 shows an optical photograph of the used ZnO substrate with typical yellow tint, Raman spectra of the ZnO substrate before and after adsorption of biomolecules, and contact-angle measurements using deionized water. The Raman spectra shows typical bands corresponding to C plane of bulk ZnO.^[24] Fingerprint of BSA could not be detected, most likely due to very small thickness of the adsorbed layer as shown by atomic force microscopy (AFM) measurements. Spectroscopy of such thin layers of biomolecules is extremely challenging. We tried also Fourier-transform infrared spectroscopy (FTIR) using SAGA (Specular Apertured Grazing Angle) accessory and mercury cadmium telluride (MCT) detector cooled to 77 K. In comparison

to blank ZnO, there was no difference in the spectra. The Raman or FTIR spectroscopy measurements of BSA or FBS monolayers directly on our ZnO samples were not sensitive enough. One could use ZnO attenuated total reflection (ATR) crystals or Au mirrors including a nanostructured diamond coating that can enable down to monolayer sensitivity to biomolecules,^[25,26] however, such measurements could not be directly correlated with our samples. Yet we detected protein presence on ZnO using AFM force–distance spectroscopy as shown later.

The contact angle on pristine ZnO surface was 100°, thus clearly hydrophobic. The contact angle of the ZnO with adsorbed biomolecules decreased to about 70°. This is a typical value for BSA layer adsorbed on both hydrophobic and hydrophilic surfaces.^[27] It is well known that biomolecules and in particular proteins interact quite strongly with hydrophobic surfaces. That often occurs via hydrophobic–hydrophobic bonding of the protein core with the surface, which can even lead to a change in protein morphology and denaturation.^[14,25,26] Note that also water interacts with hydrophobic surfaces, resulting in a thicker layer assuming different (more 3D like) structure compared with water on hydrophilic surfaces.^[28]

Figure 2 shows AFM morphology of ZnO surface before and after FBS or BSA adsorption. Characteristic structural features were resolved for both FBS and BSA, which are known also from their adsorption on other materials such as diamond.^[14] The feature size is 8–10 nm laterally as determined from autocorrelation function of the images. It is considerably smaller than 44 nm found on pristine ZnO. On the other hand, root mean square

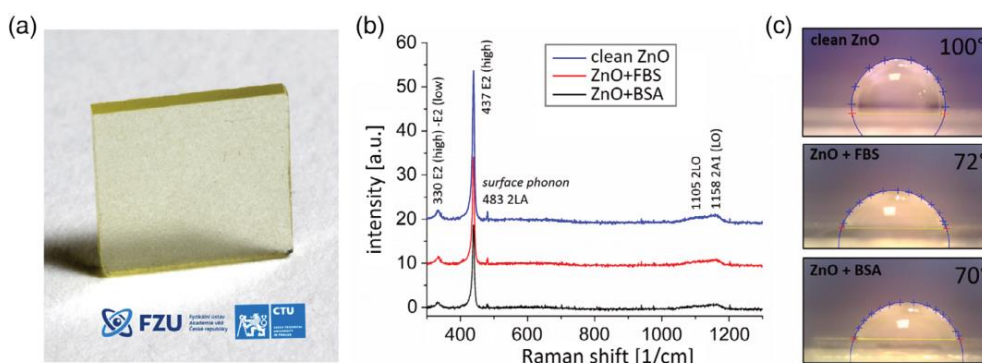


Figure 1. a) Photograph of the used ZnO substrate. b) Raman spectra with indicated major bands and c) water contact angle measurements of the ZnO substrate before and after adsorption of biomolecules.

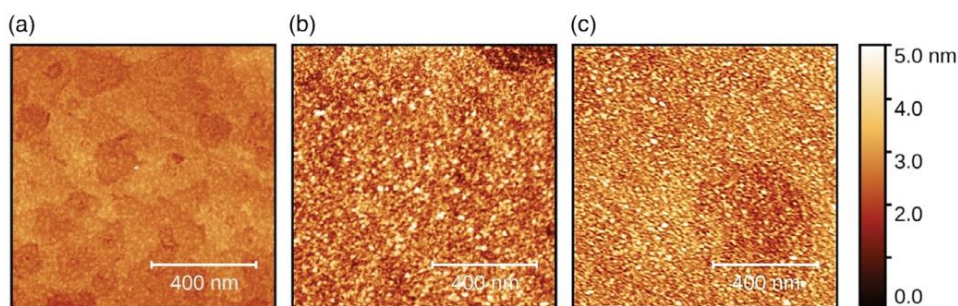


Figure 2. AFM surface morphology of a) pristine ZnO substrate, b) ZnO after FBS adsorption, c) ZnO after BSA adsorption. All images $1 \times 1 \mu\text{m}^2$, height color scale 5 nm.

(RMS) surface roughness is the highest for ZnO + FBS (0.7 nm), whereas pristine ZnO shows only 0.3 nm. The increase in roughness and decrease in lateral feature size is thus clearly due to molecules adsorbed on the surface from FBS or BSA solution.

We used the AFM nanoshaving method to determine thickness and characterize adhesion strength of the biomolecules adsorbed on ZnO. The results are shown in Figure 3. Using the height profiles as well as area statistics across a fully nanoshaved region, determined thickness of FBS was 1.9 ± 0.2 nm and thickness of BSA was 2.0 ± 0.3 nm. The values are comparable, indicating similar arrangement of the molecules on the surface. On the other hand, we found that BSA layer is more strongly attached to ZnO compared to FBS layer as shown also in Figure 3. Force of 10 ± 5 nN was sufficient to disturb and start removing FBS layer from ZnO; however, at least 25 ± 5 nN were needed for BSA layer. All the structural and adhesion data are summarized in Table 1.

Prior AFM nanoshaving experiment with BSA adsorbed on diamond surfaces showed that the thickness of BSA layer is 4.0 ± 1.7 nm on hydrogenated diamond surface, whereas it is only 1.8 ± 1.1 nm on oxidized diamond surface.^[26] RMS surface roughness is also comparable (0.7–0.9 nm). However, the force required to remove the BSA from H-diamond surface was 10 ± 5 nN and from O-diamond surface it was 20 ± 5 nN. Relatively small nanoshaving forces, compared to 40–50 nN for covalently grafted DNA^[29] or polypyrrole^[30] on diamond, suggested that BSA is physisorbed on the diamond surfaces and no covalent attachment is formed. Similar conclusion can

Table 1. Surface roughness, lateral feature size, layer thickness, and threshold nanoshaving force for pristine ZnO, ZnO + FBS, and ZnO + BSA samples.

Sample	RMS surface roughness [nm]	Lateral features Lx [nm]	Adsorbed layer thickness [nm]	Nanoshaving force [nN]
ZnO	0.3	44	–	–
ZnO + FBS	0.7	10	1.9 ± 0.2	10 ± 5
ZnO + BSA	0.5	8	2.0 ± 0.3	25 ± 5

be drawn here for BSA on ZnO. Still the difference in nanoshaving forces indicates different arrangement and different interaction of BSA with hydrogenated or oxidized diamond surfaces as corroborated also by infrared spectroscopy.^[26] Oxidized (100) diamond surface exhibits stronger surface dipole than hydrogenated surface and it is hydrophilic.^[31] In that sense, polar hydrophobic Zn-face (0001) surface of ZnO thus seems to interact similarly with BSA as the polar hydrophilic oxidized diamond surface.

Because the size of BSA is typically $4 \times 4 \times 14$ nm³ in solution, the small layer thickness (2 nm) indicates that in both cases BSA is laying on the surface. Similar arrangement has been indicated by AFM measurements of BSA adsorbed on diamond surfaces^[26] as well as from surface plasmon resonance (SPR) spectroscopy on gold surfaces where BSA was immobilized by mercaptoundecanoic acid.^[32] The small thickness of 2 nm,

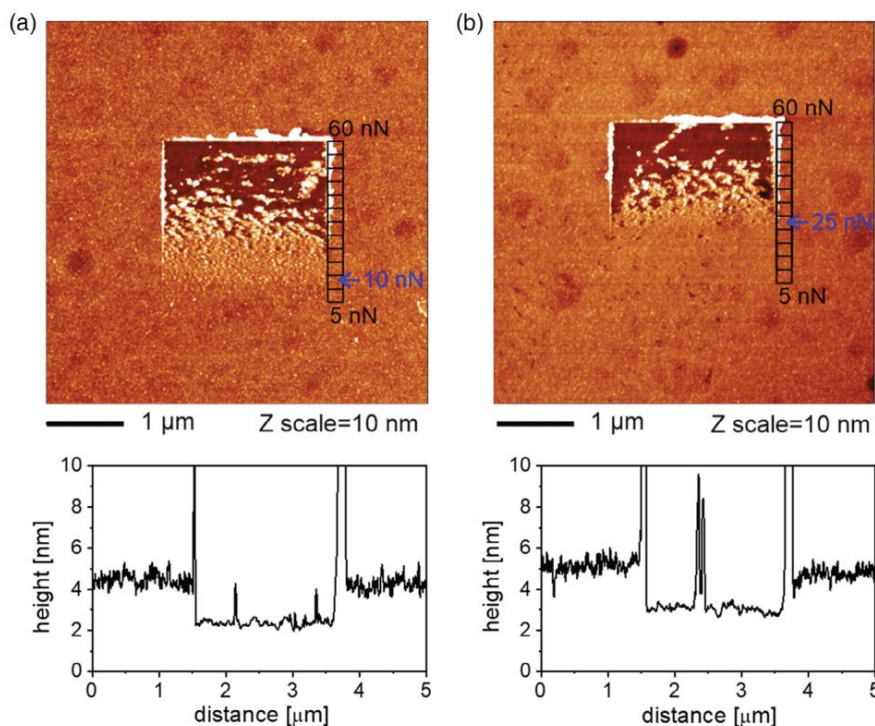


Figure 3. AFM surface morphology after the nanoshaving process on ZnO after a) FBS adsorption, b) BSA adsorption. Blue arrow indicates the threshold nanoshaving force where molecules start to be removed from the surface. Both images 5×5 μm², height color scale 10 nm. Line profiles indicating the molecular layer thickness are shown below the images.

compared to 6 nm observed by the SPR for BSA on gold,^[32] also suggests that BSA is in addition significantly collapsed (denatured) as found for proteins on hydrophobic surfaces.^[14] Also Raman spectra of BSA in the presence of ZnO nanoparticles indicated decreased α -helix content, increased unstructured folding and β -sheet content in BSA molecule.^[19] The FBS and BSA molecules were deposited from solution of neutral pH, i.e., the same as the contact-angle measurements, and would thus experience hydrophobic ZnO surface. However, surface morphology of BSA on both O-diamond and ZnO suggests globular (native) shape of BSA molecules or clusters. Thus, the likely explanation is that BSA molecules are compressed by the AFM tip during morphology measurement,^[29] not the hydrophobic or hydrophilic interaction.

This is then also the case for FBS layer thickness. The nanoshaving force threshold for FBS removal from ZnO is clearly lower than for BSA though, including the error bar range. Interestingly, it is again similar to the nanoshaving forces found for FBS on H-diamond (5 nN) or O-diamond (10 nN) surfaces, respectively.^[33] Thus, polar Zn-face (0001) surface of ZnO thus seems to interact as the oxidized diamond surface also with FBS. However, the ZnO surface is clearly hydrophobic (100°). Thus, it must be the surface dipole rather than hydrophobic interaction that controls the adhesion of FBS and BSA on the polar ZnO surface.

Further analysis of biomolecular adhesion on ZnO was performed by AFM force–distance spectroscopy. **Figure 4** shows typical force–distance curves obtained on pristine ZnO, ZnO with adsorbed FBS layer, and ZnO with adsorbed BSA layer. One main adhesion peak as well as additional adhesion events were detected on the BSA and FBS layers. The control experiments performed on pristine ZnO showed only the main adhesion peak. Thus, the main adhesion peak close to 0 nm distance is solely due to the interaction between the tip and the ZnO substrate. The additional adhesion events on ZnO with adsorbed BSA or FBS can be then attributed to typical stretching characteristics of proteins.^[34] Practically, all the stretching events were single worm-like chain (WLC) events. This indicates the stretching of individual BSA molecule with a clear single rupture event. In experiments with monocrystalline diamond (MCD), there were several WLC events during one approach–retraction cycle.^[34]

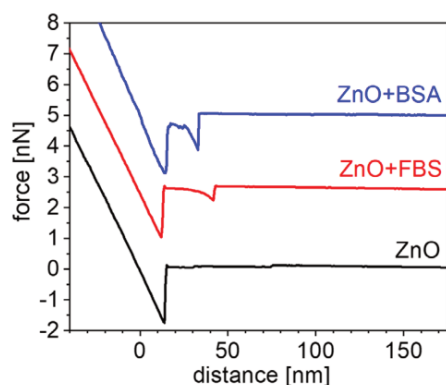


Figure 4. AFM force–distance curves obtained on pristine ZnO, ZnO with adsorbed FBS layer, and ZnO with adsorbed BSA layer.

It suggests different way of BSA molecules attachment to ZnO compared to H/O-MCD. Note also stronger adhesion forces during stretching events on BSA on ZnO compared with FBS on ZnO. It corroborates stronger adhesion forces of BSA adsorbed directly on ZnO compared with absorption from FBS, which were detected during the nanoshaving experiments (see Figure 3).

We performed atomic-scale computing of the ZnO biointerface with BSA to support understanding of the aforementioned effects and differences in structure and adhesion. **Figure 5** shows representative computational results of BSA adsorption on ZnO (0001) Zn-face. The images show various BSA orientations studied, where BSA is in 3 Å vicinity of the surface. They are named according to appearance: legs, flat, side, tip, head. For far distance (20 Å), BSA and ZnO behave just as standalone materials and there is no interaction for any orientation. For assessing favorable BSA orientation on ZnO, we compared total energies. Total energy from force-field simulations is not directly related to thermodynamic quantities such as free energy and cannot be compared between various molecules. However, in our case, we always have the same system, only in different orientations. The total energy can be thus taken as an indicator of favorable position. The data are shown in the bar graph in Figure 5. From the comparison, the “head” orientation seems the most likely. Surface roughness and lateral feature size (about half of the molecule length) seem well correlated with this orientation, too.

Additional subtle effect has been also observed at the ZnO–BSA interface: close vicinity of BSA gives rise to rearrangement of Zn surface atoms of ZnO. This effect is illustrated by the zoom-in image below the “head” BSA in Figure 5. The displaced Zn atoms are depicted lighter with yellow circles around them. Similar displacements were observed in other cases, too.

The force-field simulations thus suggest possible explanation for higher adhesion of BSA when adsorbed from pristine BSA solution. In this case, BSA comes in direct contact with ZnO and the aforementioned interactions bind it more strongly to the ZnO surface. When ZnO is exposed to FBS, various other components can adsorb to ZnO faster, prior to BSA component. This would cause spacing and screening BSA molecules from direct contact with ZnO and thereby prohibit the direct, stronger interaction. Similarly, this binding mechanism could also explain stronger adhesion of BSA than FBS on diamond.^[26,33] BSA interaction with ZnO (or diamond) could be thus controlled by used solution, i.e., BSA should be preadsorbed at first alone if stronger binding and generally stronger interaction with ZnO is required. The structural and binding differences may also have an effect on other properties of ZnO (such as optical, electronic, or microbiological), in particular for ZnO in nanomaterial form where surface-to-volume ratio is high.

3. Conclusion

We used the AFM nanoshaving method to determine thickness and characterize adhesion strength of the biomolecules adsorbed on ZnO from BSA and FBS solutions. The thickness and feature size were comparable (about 2 nm height and 10 nm lateral size), indicating similar arrangement of the molecules on the surface. However, we found that the BSA layer was more strongly

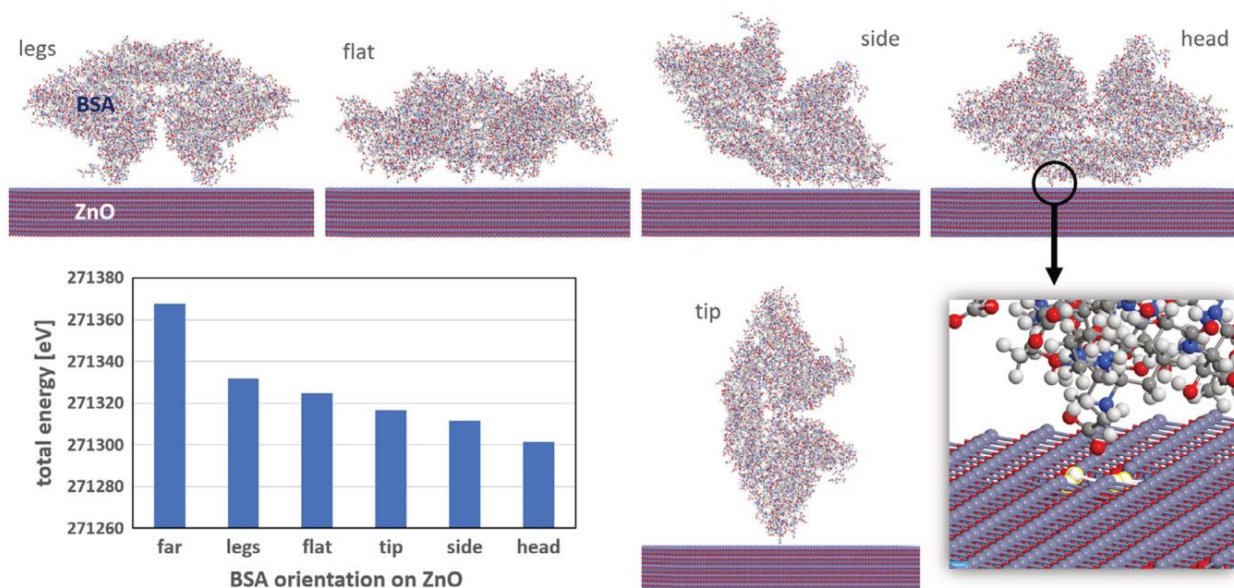


Figure 5. Representative computational results of BSA adsorption on ZnO (0001) Zn-face surface for different BSA orientations. Bar graph shows total energies of particular orientations. Detailed image for the “head” orientation shows Zn atom displacement due to ZnO–BSA interaction. Atom color coding: Zn—violet, O—red, C—gray, H—white, N—blue.

attached to ZnO when adsorbed alone from solution, not as a part of FBS. The force-field simulations suggested possible explanation for higher adhesion of BSA to ZnO. They showed that when BSA comes into direct contact with ZnO, surface atom rearrangement can occur. This assertion is corroborated by the detected difference in nanoshaving forces (25 nN for BSA, 10 nN for FBS) sample. They were similar to forces found for BSA or FBS physisorbed on oxidized (hydrophilic) diamond surfaces. By comparison with BSA on diamond surfaces, we suggested that it is the surface dipole rather than hydrophobic interaction that controls the adhesion of FBS and BSA on the polar ZnO surface. The aforementioned way of binding may have an impact also on other properties of ZnO–BSA complex such as electronic and optical properties or microbiological interactions. These effects are under ongoing investigation.

4. Experimental Section

ZnO samples were Zn-face single-side polished (0001) monocrystalline plates obtained from MSE supplies, USA (C plane $\langle 0001 \rangle \pm 0.5$ deg, 99.99% purity, lattice parameters $a = 3.252$ Å, $c = 5.313$ Å, hydrothermal growth). The plate size was $5 \times 5 \times 0.5$ mm³. We used the monocrystalline ZnO plates to enable a good microscopic resolution of biomolecules on the surface and also more straightforward correlation with computational study.

For studying ZnO biointerface properties, we applied BSA as a distinct protein molecule with various biological function including effects on cell-surface adhesion^[14] and FBS as a complex growth medium supplementing cell cultures that among many other components contains also BSA as the major component (45–50 mg mL⁻¹). Fresh 30 mg mL⁻¹ solutions of FBS and BSA in fresh deionized water were prepared using freshly opened boxes with FBS (as ice) and BSA (as powder). Droplets of the biomolecular solutions (20 µL) were then deposited on clean ZnO substrates for 10 min, rinsed with deionized water, and dried with nitrogen.

AFM was used to study morphology and adhesion of FBS and BSA on the ZnO plates. New CF₄ plasma-treated Multi75Al cantilevers were used in PFQNM mode on ICON AFM (Bruker) to characterize morphology at multiple spots on the sample. The scan parameters were 1×1 µm², 1024×1024 px, 0.1 Hz, gain 2, setpoint force 3 nN. We used CF₄-treated AFM cantilevers to minimize tip contamination by biomolecules during morphology analysis.^[35] Same Multi75Al cantilevers were used on Ntegra AFM (NT-MDT) for nanoshaving of FBS and BSA molecules from ZnO by contact mode AFM, similar to prior experiments on diamond surfaces.^[33] The force threshold for removal of molecules was identified by step-wise increase in the contact force setpoint (from 5 to 60 nN). The resulting morphology of the molecular layer was characterized in tapping mode regime. AFM force spectroscopy measurements on adsorbed biomolecules were performed using soft ultrasharp SLN-B cantilevers ($k = 0.12$ N m⁻¹, tip radius 2 nm, Bruker) in the Ntegra AFM (NT-MDT). The amount of stretching events was smaller and events were shorter compared with measurements of FBS and BSA layers deposited on H₂O-MCD.^[34] Therefore, longer approach and retraction times (10 s for both) and slightly smaller retraction distance (≈ 250 nm) were used for the experiments on ZnO.

Water contact angles were measured by the See System E (Advex instruments) using 3 mL droplet of deionized water. Raman measurements were performed in the Alpha 300 RAS (WITec) Raman spectrometer using 532 nm laser with 10 mW intensity, 1800 L mm⁻¹ grating, and 100× objective. We performed bracketing of the focal plane position. The highest signal was obtained for the focal plane positioned 2–5 µm below the surface. This occurs because the whole focus volume is actually inside the ZnO bulk. Thus, the signal is at maximum but only little sensitive to surface. Therefore, manual focusing was performed on each sample, with the highest possible sharpness of minor surface defects, i.e., the focal plane was placed directly on the surface. In this case, the signal was approximately twice smaller than the maximum signal. We collected 300 spectra in one point (each spectrum for 2 s) that were subsequently combined into one spectrum to obtain data with high signal-to-noise ratio. Several spikes were removed from the spectra manually.

The adsorption of biomolecules on ZnO was studied also by theoretical computing. We used force-field method in QuantumATK software that can

cope with high number of atoms in our system. The computing tasks were performed using the following hardware: HP system with a Core i5 8th generation processor and 8 GB RAM. The structure of ZnO plate and of the BSA molecule were taken from the software library and the RCSB Protein Data Bank, respectively. BSA model was additionally complemented by hydrogen atoms using Mol Probiy. To enable force-field calculations, we made several approximations as the set of force fields containing all types of atoms in ZnO + BSA system is not available. Sulfur atoms have been neglected in the BSA structure and ReaxFF potential set was implemented for force-field simulations. Unlike in other studies of proteins interacting with ZnO,^[36] for the investigated orientations, the sulfur atoms in BSA are not in a close vicinity to the ZnO surface. Thus, we assumed that sulfur atoms can be neglected from the computations. Furthermore, to make the calculations faster, we set the BSA and ZnO distance and orientation manually. Several nonequivalent orientations of the BSA versus ZnO were used and the mutual distances were set in the range 3–20 Å (defined as the distance between the nearest ZnO and BSA atoms). The structural changes and total energy of the system were then evaluated.

Acknowledgements

Dr. Petra Matunová is kindly acknowledged for fruitful discussions about computational simulations. The presented work has been financially supported by the project GACR 19-02858J. The authors also acknowledge use of CzechNanoLab Research Infrastructure supported by MEYS CR (LM2018110).

Conflict of Interest

The authors declare no conflict of interest.

Data Availability Statement

Research data are not shared.

Keywords

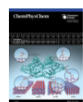
adhesions, albumin, atomic force microscopy, force fields, zinc oxide

Received: September 2, 2020

Revised: January 4, 2021

Published online: January 26, 2021

- [1] S. Rani, P. Suri, P. K. Shishodia, R. M. Mehra, *Sol. Energy Mater. Sol. Cells* **2008**, *92*, 1639.
- [2] D. C. Look, B. Clafin, *Phys. Status Solidi B* **2004**, *241*, 624.
- [3] M. Davydova, A. Laposa, J. Smarhak, A. Kromka, N. Neykova, J. Nahlik, J. Kroutil, J. Drahokoupil, J. Voves, *Beilstein J. Nanotechnol.* **2018**, *9*, 22.
- [4] C. B. Ong, L. Y. Ng, A. W. Mohammad, *Renewable Sustainable Energy Rev.* **2018**, *81*, 536.
- [5] A. Sirelkhatim, S. Mahmud, A. Seeni, N. H. M. Kaus, L. C. Ann, S. K. M. Bakhori, H. Hasan, D. Mohamad, *Nano-Micro Lett.* **2015**, *7*, 219.
- [6] C.-F. Yu, S.-J. Sun, H.-S. Hsu, *Phys. Lett. A* **2015**, *379*, 211.
- [7] Y. Natsume, H. Sakata, *Thin Solid Films* **2000**, *372*, 30.
- [8] N. Neykova, A. Brož, Z. Remeš, K. Hruška, M. Kalbáčová, A. Kromka, M. Vaněček, *Appl. Surf. Sci.* **2012**, *258*, 3485.
- [9] H. Agarwal, S. Venkat Kumar, S. Rajeshkumar, *Resour.-Effic. Technol.* **2017**, *3*, 406.
- [10] P. K. Mishra, H. Mishra, A. Ekielski, S. Talegaonkar, B. Vaidya, *Drug Discov. Today* **2017**, *22*, 1825.
- [11] A. Tereshchenko, M. Bechelany, R. Viter, V. Khranovskyy, V. Smyntyna, N. Starodub, R. Yakimova, *Sens. Actuators, B* **2016**, *229*, 664.
- [12] R. Jelinek, *Nanoparticles*, De Gruyter, Berlin/Boston **2015**.
- [13] K. Ravichandran, K. Karthika, B. Sakthivel, N. Jabena Begum, S. Snega, K. Swaminathan, V. Senthamilselvi, *J. Magn. Magn. Mater.* **2014**, *358–359*, 50.
- [14] B. Rezek, L. Michalíková, E. Ukraintsev, A. Kromka, M. Kalbacova, *Sensors* **2009**, *9*, 3549.
- [15] B. Rezek, M. Krátká, A. Kromka, M. Kalbacova, *Biosens. Bioelectron.* **2010**, *26*, 1307.
- [16] S. R. Saptarshi, A. Duschl, A. L. Lopata, *J. Nanobiotechnol.* **2013**, *11*, 26.
- [17] A. Panáček, L. Kvítek, M. Smékalová, R. Večeřová, M. Kolář, M. Röderová, F. Dyčka, M. Šebela, R. Prucek, O. Tomanec, R. Zbořil, *Nat. Nanotechnol.* **2018**, *13*, 65.
- [18] I. Machova, M. Hubalek, T. Belinova, A. Fucikova, S. Stehlik, B. Rezek, M. H. Kalbacova, *Carbon* **2020**, *162*, 650.
- [19] R. Žūkienė, V. Snitka, *Colloids Surf. B* **2015**, *135*, 316.
- [20] J. H. Park, T. N. Sut, J. A. Jackman, A. R. Ferhan, B. K. Yoon, N.-J. Cho, *Phys. Chem. Chem. Phys.* **2017**, *19*, 8854.
- [21] T. B. Donadt, R. Yang, *ACS Biomater. Sci. Eng.* **2020**, *6*, 182.
- [22] Y.-Y. Chang, J. Stuchlík, N. Neykova, J. Souček, Z. Remeš, *J. Electron. Eng.* **2017**, *68*, 70.
- [23] C. Hansda, P. Maiti, T. Singha, M. Pal, S. A. Hussain, S. Paul, P. K. Paul, *J. Phys. Chem. Solids* **2018**, *121*, 110.
- [24] E. Nowak, M. Szybowicz, A. Stachowiak, W. Koczorowski, D. Schulz, K. Paprocki, K. Fabisiak, S. Los, *Appl. Phys. A* **2020**, *126*, 552.
- [25] H. Kozak, O. Babchenko, A. Artemenko, E. Ukraintsev, Z. Remes, B. Rezek, A. Kromka, *Langmuir* **2014**, *30*, 2054.
- [26] H. Kozak, A. Artemenko, E. Ukraintsev, A. Choukourov, B. Rezek, A. Kromka, *Langmuir* **2019**, *35*, 13844.
- [27] B. Sweryda-Krawiec, H. Devaraj, G. Jacob, J. J. Hickman, *Langmuir* **2004**, *20*, 2054.
- [28] S. Stehlik, T. Glatzel, V. Pichot, R. Pawlak, E. Meyer, D. Spitzer, B. Rezek, *Diamond Relat. Mater.* **2016**, *63*, 97.
- [29] B. Rezek, D. Shin, H. Uetsuka, C. E. Nebel, *Phys. Status Solidi A* **2007**, *204*, 2888.
- [30] B. Rezek, J. Čermák, A. Kromka, M. Ledinský, P. Hubík, J. J. Mareš, A. Purkrt, V. Cimrová, A. Fejfar, J. Kočka, *Nanoscale Res. Lett.* **2011**, *6*, 238.
- [31] F. Maier, J. Ristein, L. Ley, *Phys. Rev. B* **2001**, *64*, 165411.
- [32] E. Buzavaite-Verteliene, I. Plikusiene, T. Tolenis, A. Valavicius, J. Anulyte, A. Ramanavicius, Z. Balevicius, *Opt. Express* **2020**, *28*, 29033.
- [33] E. Ukraintsev, B. Rezek, A. Kromka, A. Broz, M. Kalbacova, *Phys. Status Solidi B* **2009**, *246*, 2832.
- [34] B. Rezek, E. Ukraintsev, L. Michalíková, A. Kromka, J. Zemek, M. Kalbacova, *Diamond Relat. Mater.* **2009**, *18*, 918.
- [35] B. Rezek, E. Ukraintsev, M. Krátká, A. Taylor, F. Fendrych, V. Mandys, *Biointerphases* **2014**, *9*, 031012.
- [36] A. Tereshchenko, V. Fedorenko, V. Smyntyna, I. Konup, A. Konup, M. Eriksson, R. Yakimova, A. Ramanavicius, S. Balme, M. Bechelany, *Biosens. Bioelectron.* **2017**, *92*, 763.



Strong Structural and Electronic Binding of Bovine Serum Albumin to ZnO via Specific Amino Acid Residues and Zinc Atoms

Hadi Hematian,^{*,[a]} Egor Ukraintsev,^[b] and Bohuslav Rezek^[a]

ZnO biointerfaces with serum albumin have attracted noticeable attention due to the increasing interest in developing ZnO-based materials for biomedical applications. ZnO surface morphology and chemistry are expected to play a critical role on the structural, optical, and electronic properties of albumin-ZnO complexes. Yet there are still large gaps in the understanding of these biological interfaces. Herein we comprehensively elucidate the interactions at such interfaces by using atomic force microscopy and nanoshaving experiments to determine roughness, thickness, and adhesion properties of BSA layers adsorbed on the most typical polar and non-polar ZnO single-crystal facets. These experiments are corroborated by force field (FF) and density-functional tight-binding (DFTB) calculations on ZnO-BSA interfaces. We show that BSA adsorbs

on all the studied ZnO surfaces while interactions of BSA with ZnO are found to be considerably affected by the atomic surface structure of ZnO. BSA layers on the (000 $\bar{1}$) surface have the highest roughness and thickness, hinting at a specific upright BSA arrangement. BSA layers on (10 $\bar{1}$ 0) surface have the strongest binding, which is well correlated with DFTB simulations showing atomic rearrangement and bonding between specific amino acids (AAs) and ZnO. Besides the structural properties, the ZnO interaction with these AAs also controls the charge transfer and HOMO-LUMO energy positions in the BSA-ZnO complexes. This ZnO facet-specific protein binding and related structural and electronic effects can be useful for improving the design and functionality of ZnO-based materials and devices.

1. Introduction

Zinc oxide (ZnO) is a direct bandgap semiconductor that gained a great importance in optical, electrical, optoelectronic, and biomedical research and applications. ZnO has been synthesized and used in nanorod, nanowire, and two-dimensional (2D) forms in a variety of applications such as photonic devices, lasers, and photovoltaics.^[1–5] The four (0001), (000 $\bar{1}$), (10 $\bar{1}$ 0), and (11 $\bar{2}$ 0) surfaces depicted in Figure 1a are the dominant facets of the surface morphology of a wurtzite ZnO crystal. The Zn-faced (0001) and the O-faced (000 $\bar{1}$) surfaces are polar, while the (10 $\bar{1}$ 0) and (11 $\bar{2}$ 0) surfaces are considered non-polar.

Beyond its traditional applications, the interest in implementing ZnO beneficial properties (bactericidal activity, high biocompatibility, etc.) for biological applications, ranging from drug delivery^[6–8] and biosensing^[9–11] to tissue regeneration,^[12] has been rapidly growing during the last decades. ZnO nanostructures are currently widely used for rapid and superior

bacteria killing,^[13] anti-diabetic activity, biocompatibility with RBCs and bactericidal biological applications,^[14] degradation of tetracycline antibiotic,^[15] and humidity,^[16] acetone^[17–19] and electrochemical sensors.^[20] ZnO nanowire protein sensors enhanced by the piezotronic effect,^[21] ZnO films synthesized using spray pyrolysis with antibacterial activity,^[22] flexible and microporous chitosan hydrogel/nano ZnO composite bandages for wound dressing,^[23] and a new generation of chitosan-encapsulated ZnO quantum dots for drug delivery,^[24] are only some examples of successful implementation of ZnO materials for biological purposes. Besides, regarding the increasingly widespread use of ZnO materials in other biological applications such as cosmetic and consumer products, food additives, and medical textiles,^[25–27] it is crucial to study the behaviour of protein-ZnO interfaces on different ZnO crystallographic planes. The study of protein-ZnO interfaces would be also intriguing from optoelectronic point of view due to possibly modified electrical and optical properties.

For instance, a multi-method experimental study of surface chemistry and optical properties of ZnO nanoparticles in interaction with L-Cysteine has demonstrated a significant effect on the photoluminescent properties.^[28] Interactions of ZnO surfaces with various biomolecules and proteins have been subject to several experimental studies. For instance, multiple experimental studies investigated the interactions between ZnO surfaces and peptides for ZnO morphology modification.^[29–31] Several computational efforts also employed molecular dynamic,^[32] density functional theory,^[33] and density-functional tight-binding theory^[34] to study the binding between some AAs and ZnO surfaces. To our best knowledge, only a few

[a] H. Hematian, Prof. B. Rezek
Department of Physics, Faculty of Electrical Engineering
CTU in Prague
Technická 2

166 27 Prague 6, Czech Republic
E-mail: hemathad@fel.cvut.cz

[b] Dr. E. Ukraintsev
Institute of Physics
Czech Academy of Sciences
Cukrovarnická 10
162 00 Prague 6, Czech Republic

Supporting information for this article is available on the WWW under <https://doi.org/10.1002/cphc.202100639>

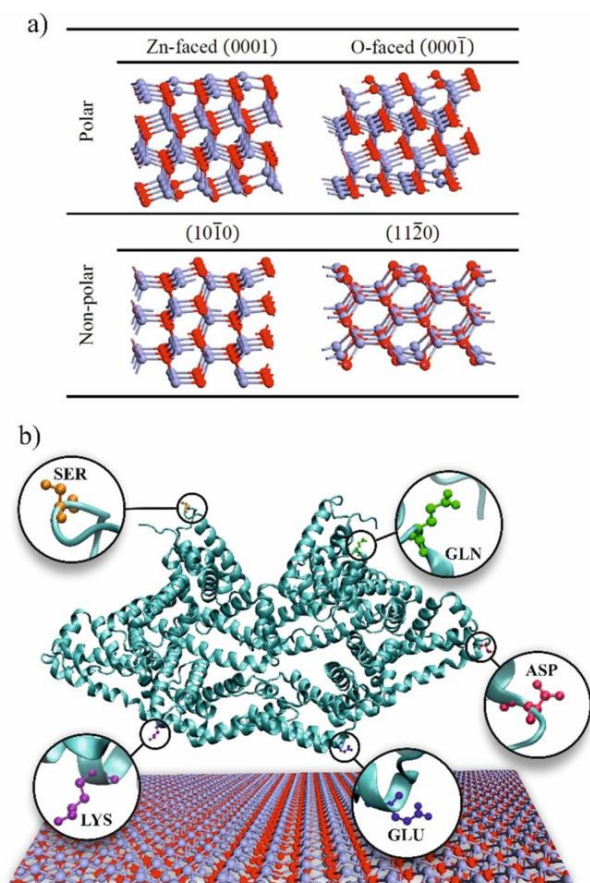


Figure 1. a) ZnO polar and non-polar surfaces, b) BSA amino acid residues selected based on FF calculations.

of these studies compare the adsorption of AAs on different ZnO surfaces, and none of them studied the electronic properties of the complexes.

Amongst the wide range of proteins, the interactions of ZnO materials with serum albumin as the most abundant plasma protein in mammals' blood have been studied in a limited number of studies, and in most cases, merely experimentally.^[35–38] Bardhan et al. showed that static quenching of BSA results in a ground-state complex between ZnO nanoparticles and BSA.^[36] Study of the interaction between polyethyleneimine-functionalized ZnO nanoparticles with core size of 3–7 nm and BSA proved static and single type of protein quenching.^[37] Interactions of 7.5 nm ZnO nanoparticles with BSA were investigated at different temperatures, indicating a decrease in binding sites with the increase of temperature.^[38] Our recent studies theoretically examined the different orientations of the BSA on two ZnO non-polar and Zn-faced polar surfaces.^[39,40] A more detailed inspection of the FF calculation results in these studies reveals that the interactions between BSA and ZnO surfaces in different orientations are mainly about the interactions between specific amino acid residues (ASP, GLU, GLN, LYS, and SER displayed in Figure 1b) with the atoms on ZnO surfaces.

Despite the valuable findings from the previous research mainly focused on probing the adsorption of BSA on different ZnO materials, it is still unclear how the BSA adsorbs and binds on ZnO surfaces. Here we conduct a comprehensive, systematic study on the adsorption process of BSA on various ZnO surfaces by atomic force microscopy (AFM) with molecular resolution as well as by force field (FF) and density-functional tight-binding (DFTB) calculations. Although, there is some research available on BSA adsorption on ZnO nanoparticles using other simulation methods such as molecular docking,^[41,42] to the best of our knowledge, this is the first combined study on adsorption of BSA on various ZnO surfaces. ZnO atomic surface structure and chemistry are observed to have a pronounced effect on interactions at BSA-ZnO interfaces. ZnO crystal orientation is shown to substantially affect the structural properties of the BSA-ZnO interfaces, such as roughness, thickness, and adhesion strength of adsorbed BSA layers. We propose that specific BSA arrangement and interactions of its specific AAs with different ZnO surfaces are responsible for this effect. We show that these interactions also control charge transfer and HOMO-LUMO energy positions in the BSA-ZnO complexes. This ZnO facet-specific protein binding and related structural and electronic effects can be useful for explaining many experimental data reported already in the literature as well as for improving design and function of ZnO-based materials and devices such as in biosensing.^[43]

2. Material and Methods

2.1. Samples Preparation

ZnO substrates were polar Zn-faced single-side polished (0001), polar O-face single-side polished (000 $\bar{1}$), non-polar (10 $\bar{1}$ 0), and non-polar (11 $\bar{2}$ 0) monocrystalline 5×5×0.5 mm³ plates from MSE supplies, USA (C plane (0001) ± 0.5°, 99.99% purity, lattice parameters a = 3.252 Å, c = 5.313 Å).

BSA is a globular protein with typical size 4×4×14 nm³.^[44] BSA (Sigma-Aldrich) solution with specific concentration (30 mg ml⁻¹) was freshly made using DI water. Two droplets (20 μl) were deposited on four ZnO samples for 10 minutes. The ZnO samples were rinsed with DI water and dried with nitrogen.

2.2. AFM Measurements

Scanning electron microscopy is often used in the literature to characterize the morphology of BSA on ZnO and other surfaces, but it does not provide true height information. The SEM contrast is also electronic, not directly structural, and cannot provide mechanical information. Some structural arrangement of molecules could be resolved also by ellipsometry, however again only indirectly and without spatial resolution. Further methods are Raman and infrared optical spectroscopies, where molecular structure and binding may be resolved from various vibrations, yet again also indirectly. Therefore, we employed

AFM to analyze the surface morphology, thickness and adhesion of BSA molecules adsorbed on ZnO.

The topography measurements were performed on ICON AFM (Bruker) in PFQNM mode using a new CF₄ plasma-treated Multi75Al cantilever (BudgetSensors).^[45] Topography measurements were performed with the following parameters: scan size 1×1 μm², image resolution 1024×1024 px², scanning speed 0.1 Hz, gain 10, dz=30 nm, Z-scale=2 μm, force threshold=2–5 nN. Results were analyzed using Gwyddion software.

Thickness measurements were performed on ICON AFM using Tap300 cantilevers (nominal force constant 40 N/m) (BudgetSensors) in contact mode (2×2 μm²) and PFQNM mode (6×6 μm² cropped to 4×4 μm²).

To analyze not only the topography but also the adhesion of the BSA molecules, we employed nanoshaving experiments. They have been previously well proven in studies of DNA molecules grafted on diamond,^[46] BSA molecules adsorbed on plasma polymer coating,^[47] on diamond^[48] and on ZnO (0001) surface.^[39] Hereby, we perform them on the BSA to analyze the layer thickness and adhesion properties of BSA layers on various ZnO surfaces. Nanoshaving experiments were performed on Ntegra AFM (NT-MDT) using CF₄ plasma-treated Multi75Al cantilever (nominal force constant 3 N/m) in contact mode (2×2 μm²) and tapping mode (5×5 μm² overscan). The applied force for scratching the BSA layers on the surfaces was varied from 5 nN to 60 nN, and 10 nN to 120 nN. Thickness was determined by averaged line profile on several images. Error bars are standard deviation values.

2.3. Force Field Calculations

In FF calculations, molecules are simply defined as a set of atoms that is held together by simple elastic harmonic forces. FF replaces true potential with a simplified model and its parameters. Thanks to this simple way of modelling, FF method enables the possibility of coping with large systems with huge number of atoms, such as our BSA-ZnO systems.

FF calculations were performed to determine the most likely orientation of BSA over different ZnO surfaces. We used same FF methodology as in our recently published papers.^[39,40] Briefly, the systems under the study consist of BSA molecules and ZnO slabs that are available from the RCSB Protein Data Bank (pdb ID of 4F5S) and QuantumATK software database respectively.

Different orientations of BSA molecule are adjusted over ZnO surfaces in vacuum in the distance range of 3–20 Å. The optimization trajectory and total energy of the system then have been observed to determine the most favourable orientation of the BSA molecule on various ZnO planes.

The 200×200 px² mesh (20×20 nm², 1 Å step) was constructed for each BSA molecule, adhered to one of four ZnO surfaces. The position of the highest atom in each point of the mesh was determined,^[49] and used to define the average BSA molecule height above ZnO surface and RMS roughness of individual BSA molecule, presented in Table 1.

2.4. DFTB Calculations

The density-functional tight-binding (DFTB) method is a fast and efficient quantum mechanical simulation method using a second-order expansion of the Kohn-Sham total energy in density functional theory with respect to charge density fluctuations.^[50] Compared to FF calculations, DFTB calculations are much more precise on atomic scale and provide reasonably reliable information about electronic properties of the system. To verify and understand the results of our study in the FF and AFM sections, we carried out DFTB calculations for some selected segments of our large BSA-ZnO systems. DFTB calculations are done for various ZnO surfaces and specific AAs selected based on the interacting sites of BSA with ZnO surfaces in FF calculations. The directions of AAs are also selected based on their exposure on ZnO surfaces in FF calculations.

The DFTB calculations, therefore, were carried out for 20 structures: five amino acids selected based on force field calculation results over four ZnO surfaces. A self-consistent tight-binding model based on the Slater-Koster model using *znorg-0-1* parameter set, which has been built for calculations on Zn bulk, ZnO bulk, ZnO surfaces, and ZnO interactions with organic molecules,^[51] has been implemented. The ZnO surfaces have been prepared by cleaving the ZnO bulk in four orientations of interest with the cell dimensions of 10×10×30 Å³. The surfaces and the molecules were allowed to relax to the minimum energy separately before running the final optimization process for molecule-on-surface systems. The molecules were then adjusted on the surfaces in the similar orientations they showed favourable in FF simulations and the whole structures were allowed to relax to the stable config-

Table 1. RMS roughness, thickness, and force threshold for BSA layers deposited on ZnO surfaces defined by AFM measurements. RMS roughness of BSA molecule, averaged height of BSA molecule, and averaged binding energy for five amino acids, determined by calculations.

Sample		RMS roughness of BSA layer in AFM [Å]	Thickness of BSA layer in AFM [Å]	Force threshold in nano-shaving [nN]	RMS roughness of BSA molecule in FF [Å]	Average height of BSA molecule in FF [Å]	Average binding energy of AAs [eV]
polar Zn-faced	(0001)	5.5 ± 1.5	20.5 ± 2.2	40 ± 5	15.4	45.7	−1.86
polar O-faced	(000 $\bar{1}$)	14.6 ± 2.5	27.0 ± 1.3	60 ± 5	26.4	103.0	−0.05
non-polar	(10 $\bar{1}$ 0)	8.4 ± 2.1	18.9 ± 2.2	80 ± 10	20.4	53.3	−2.86
non-polar	(11 $\bar{2}$ 0)	19.1 ± 4.2	15.4 ± 3.7	10 ± 5	20.1	52.9	−1.70

urations with criteria of force tolerance of 0.01 eV/Å and stress error tolerance of 0.001 eV/Å³. Following boundary conditions have been considered in the simulations: periodic in A and B directions, Neumann under the slab, and Dirichlet above the slab. Note that under physiological conditions, amino acids are negatively charged. The AAs models employed here are the models which remain stable during the optimization and relaxation process in the DFTB calculations. Other models of these amino acids were also tried but failed to stay stable, they collapsed during the optimization process. Nevertheless, we verified the results by implementing water as implicit solvent (see further below).

The final relaxed ZnO polar and non-polar surfaces are illustrated in Figure 1a. The relaxation process was relatively straightforward for two non-polar surfaces, comprising cleaving the bulk in defined directions and allowing the surfaces to relax. In contrast, doing the same process for polar surfaces would culminate in instability due to the establishment of an internal dipole moment. Even though ZnO polar surfaces appear unstable and thus theoretically unfeasible, they have been proved to exist and their stability has been subject to many studies.^[52] Several explanations have been proposed for their stability, such as surface vacancies and surface functional groups.^[53] This study used surface zinc and oxygen vacancies offered in^[54] to stabilize ZnO polar surfaces for further calculations.

For the 20 structures following characteristics have been calculated and discussed: post-contact optimized systems, the binding energy between the adsorbed amino acids and ZnO surfaces, charge transfer between the adsorbed amino acids and ZnO surfaces, and HOMO-LUMO energy levels for the post-contact structures.

3. Results

3.1. Roughness, Thickness, and Adhesion of BSA on ZnO Analyzed by AFM

AFM topography images of clean ZnO samples and BSA layers, deposited on corresponding ZnO samples, are shown in Figure 2. ZnO samples are flat and do not contain spherical particles, while BSA layers have densely packed spherical particles, individual or aggregated BSA molecules. The results are comparable with topography images of BSA molecules deposited on diamond.^[47] Averaged RMS roughness values from several experiments and corresponding standard error values as error bars are summarized in Table 1. The highest roughness of BSA molecules was measured on (11 $\bar{2}$ 0) and (000 $\bar{1}$) surfaces with the values of 19.1 ± 4.2 Å and 14.6 ± 2.5 Å, respectively. The roughness of adsorbed BSA molecules on (0001) and (10 $\bar{1}$ 0) planes are similar and considerably lower than on the other two surfaces (5.5 ± 1.5 Å and 8.4 ± 2.1 Å).

The results of thickness determination for BSA layers, deposited on ZnO samples are shown in the Supplementary Information in Figure S1. Averaged thickness values from several experiments and corresponding standard deviation

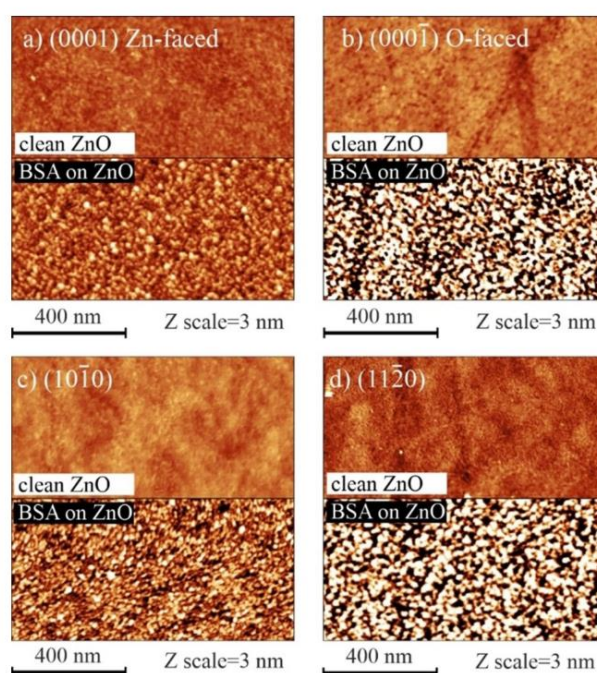


Figure 2. Topography measurement of clean ZnO samples and BSA layers deposited on corresponding; a) (0001), b) (000 $\bar{1}$), c) (10 $\bar{1}$ 0) and d) (11 $\bar{2}$ 0) ZnO surfaces.

values as error bars are summarized in Table 1. BSA layer adsorbed on O-faced (000 $\bar{1}$) polar surface has the highest thickness (27.0 ± 1.3 Å). The BSA layers thickness values for (0001), (10 $\bar{1}$ 0), and (11 $\bar{2}$ 0) surfaces are 20.5 ± 2.2 Å, 18.9 ± 2.2 Å, and 15.4 ± 3.7 Å, respectively. Since BSA molecule size is 4 × 4 × 14 nm³, the most probable explanation of the observed thickness values is the complete monolayer coverage BSA molecules with different orientations and configuration. Similar result was obtained on BSA^[47] and Fetal Bovine Serum^[44,55] layers adsorbed on H/O-terminated diamond. It was suggested that hydrophobic and hydrophilic parts of BSA molecule have different configuration on hydrophobic and hydrophilic surfaces.^[44]

Figure 3 shows the results of nanoshaving experiments. The results are also summarized in Table 1. BSA molecules were removed from (0001), (000 $\bar{1}$), (10 $\bar{1}$ 0) and (11 $\bar{2}$ 0) surfaces by forces of 40 ± 5 nN, 60 ± 5 nN, 80 ± 10 nN, and 10 ± 5 nN, respectively. These values suggest the possibility of covalent bonding of BSA molecules to the surfaces. They are also comparable with the results of nanoshaving experiments for BSA molecules deposited on diamond (5 nN–10 nN).^[48] In addition, BSA layer peel-off can be apparently observed at the threshold force on (0001), (000 $\bar{1}$), (10 $\bar{1}$ 0) surfaces. On the (11 $\bar{2}$ 0) surface, strong compression and clear edge can be seen at the threshold force (10 nN), but no layer peel-off is detected up to the force of 1200 nN.

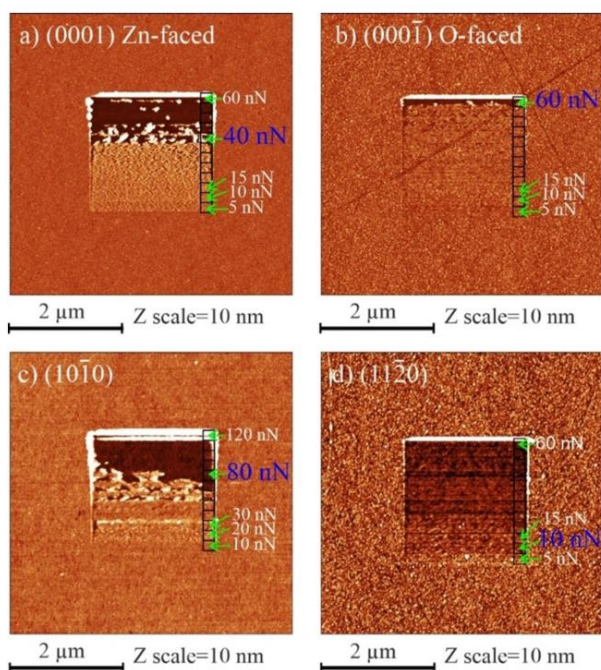


Figure 3. Nanoshaving experiments performed on BSA layers deposited on ZnO samples to measure the threshold of BSA layer removal from: a) (0001), b) (000 $\bar{1}$), c) (10 $\bar{1}$ 0) and d) (11 $\bar{2}$ 0) ZnO surfaces.

3.2. Force Field Calculations

Figure 4 shows the most stable orientations of BSA over four ZnO surfaces based on the total energies of the systems. The data for non-polar and polar Zn-faced surfaces were taken from,^[40] and the same type of calculations was done and added for the polar O-faced plane.

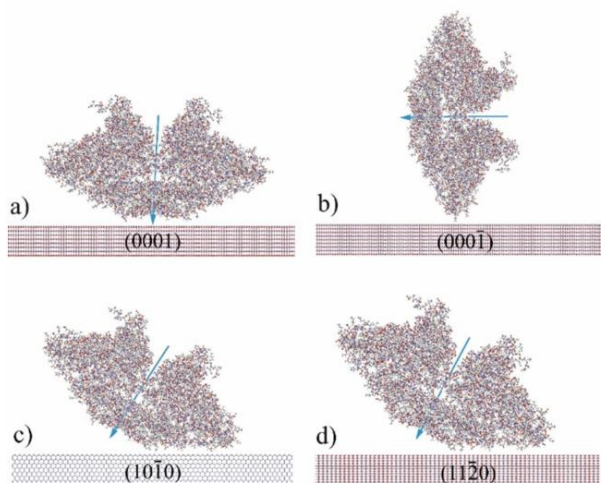


Figure 4. Energetically the most stable orientations of BSA on ZnO a) (0001), b) (000 $\bar{1}$), c) (10 $\bar{1}$ 0) and d) (11 $\bar{2}$ 0) surfaces. Blue arrow represents the dipole moment of BSA.

In the force field simulation, the BSA molecule is inherently implemented as a collection of atoms. Thus, we keep the same representation in the Figure 4, exactly as imported from the simulation environment.

The alignment of BSA dipole moment against the surface can be used as a reference for comparing the orientation of the molecule on different surfaces. It is displayed as the blue arrow. One can see that the dipole moment vector of BSA is almost perpendicular to the (0001) surface while for (000 $\bar{1}$) facet it is parallel to the surface. For two non-polar facets, it keeps almost the same orientation against the surfaces.

The orientation preference of BSA on ZnO surfaces results in different RMS roughness and averaged height of the adsorbed molecule. The calculated averaged height, and RMS roughness data are summarized in Table 1. One can see that the values for RMS roughness and averaged height range from 15.4 Å to 26.4 Å and 45.7 Å to 103.0 Å, respectively. Both the highest RMS roughness and average height of BSA are observed on (000 $\bar{1}$) facet. It is most likely because of the specific upright orientation of the BSA molecule on this surface that may lead to a close packing and mutual tight binding of the molecules.

3.3. DFTB Calculations

Figure 5 shows different configurations of chemisorption of AAs on four ZnO surfaces. One can see that amino acids have been chemisorbed vertically or horizontally on non-polar and polar Zn-faced surfaces through either one or two oxygen-zinc and nitrogen-zinc bonds. The same depicts for all structures can be found in Figure S2. For Zn-faced (0001), (10 $\bar{1}$ 0) and (11 $\bar{2}$ 0) surfaces, DFTB calculations confirm the formation of the covalent bonds between the amino acids and ZnO surfaces. Through the optimization process, the amino acids approached and made bonds with the surfaces without noticeable deviation from the initially set alignments. The exception is for (10 $\bar{1}$ 0) systems in which most amino acids deviated considerably from their commencing orientations and lay on the surface, which probably cannot be the case when one considers the amino acids connected to the BSA. On the other hand, the surface repelled the amino acids on the O-faced (000 $\bar{1}$) polar surface, and the systems relaxed for the distance between the surface and the molecule in the range 2–3 Å.

DFTB simulations are done for different single amino acids on different ZnO surfaces. We believe that this is reasonable since in each interaction site in our FF calculations, one specific amino acid is in interaction with the surface. Single amino acids are generally freer to move and can adopt different orientations compared to AAs bound in BSA. Some observed orientations of amino acids in DFTB calculations may thus be not structurally likely for the whole BSA. We also did not consider bridge-like adsorption configurations^[56,57] in our work. Yet both FF calculations of the whole BSA molecule and DFTB calculations with individual AAs agree well on the way of bonding to different ZnO facets. Note that in the DFTB simulations above we employed the ideal ZnO surfaces. In reality, ZnO exhibits several non-ideal features such as surface and subsurface defects

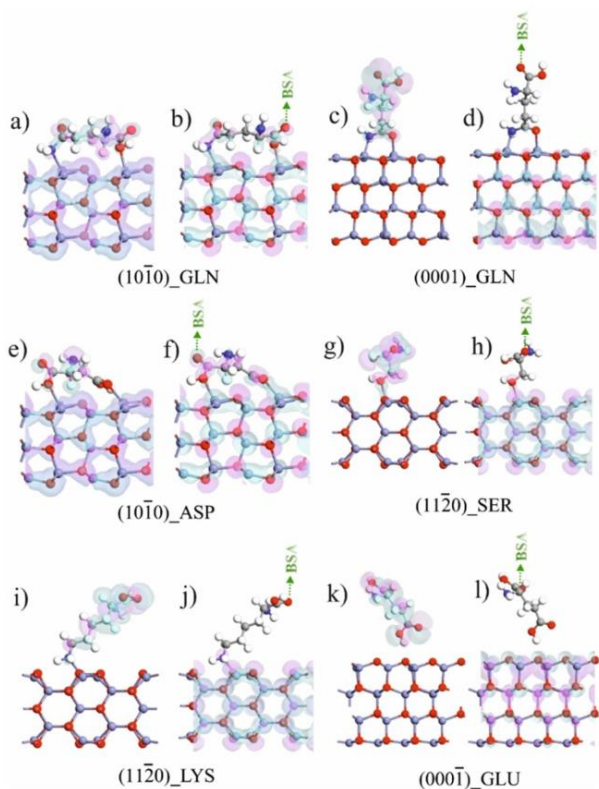


Figure 5. Different configurations of chemisorption of amino acids on ZnO surfaces and HOMO-LUMO distributions. Standing double O–Zn and N–Zn bonds a) HOMO and b) LUMO, lying double O–Zn and N–Zn bonds c) HOMO and d) LUMO, double O–Zn bonds e) HOMO and f) LUMO, single O–Zn bond g) HOMO and h) LUMO, single N–Zn bond i) HOMO and j) LUMO, and no bonds k) HOMO and l) LUMO.

including oxygen vacancies, passivation effects by hydrogen atoms and surface chemistry such as hydroxylation. Investigating such features represent a large and computationally demanding work. It could be the subject of further study where the present fundamental study would provide useful foundation and benchmark for comparison. It is also worth mentioning that in our DFTB simulations we tried to use the implicit solvent model in few cases such as (11 $\bar{2}$ 0)_{GLN} system (see Figure S3 in the Supplementary Information). No qualitative differences were observed in the structures and properties with and without the implicit solvent while the calculations were several times more costly with the solvent. Therefore, the present study as a whole was conducted without the solvent.

In addition to the optimized AA-ZnO configurations, Figure 5 displays also HOMO and LUMO orbitals for the representative structures. All the computed structures are presented in the Supplementary Information in Figure S2. Spatially separated HOMO-LUMO levels were observed for all complexes related to (11 $\bar{2}$ 0) and (0001) surfaces, but for the (10 $\bar{1}$ 0) surface, HOMO-LUMO separation only occurred for LYS. For the O-faced surface, the HOMO-LUMO separation was seen for all amino acids except GLN. It is also worth mentioning that HOMO is placed on the amino acid for most of the structures with spatially

separated HOMO-LUMO, while LUMO is placed on the ZnO slab. The observed spatial separation of the HOMO and LUMO can affect the separation of excitons and charge carrier transport, which could be highly interesting for sensing applications and optoelectronics.

Figure 6 presents HOMO-LUMO energetic levels for all structures, including amino acids, ZnO slabs, and all post-contact structures. The values of HOMO-LUMO energy gaps for all systems are listed in Table S1. The HOMO-LUMO gaps for ZnO slabs are 2.91 eV, 2.77 eV, 3.72 eV, and 3.96 eV for (0001), (000 $\bar{1}$), (10 $\bar{1}$ 0), and (11 $\bar{2}$ 0) respectively. Compared to the gap in bulk ZnO (3.37 eV^[58]), the HOMO-LUMO gaps in (10 $\bar{1}$ 0) and (11 $\bar{2}$ 0) slabs are higher probably because of the well-known electron confinement phenomenon that occurs in finite slabs. However, in (0001) and (000 $\bar{1}$) slabs, the gaps are lower than the bulk gap, probably because of the vacancies imposed on these surfaces for the aforementioned stabilization purposes. For amino acids, the calculated HOMO-LUMO gaps are in the range 5.55–5.87 eV. After the optimization process, the calculated HOMO-LUMO gaps for almost all (10 $\bar{1}$ 0), (11 $\bar{2}$ 0), (0001) systems decreased to the range between 1.72 eV and 3.65 eV. The exceptions are ASP, GLN and SER over (10 $\bar{1}$ 0) surface, in which a slight increase was detected. For O-faced surface structures, HOMO-LUMO gaps decreased drastically in the AA-ZnO complexes, indicating a semi-metallic behavior that may again be interesting for some applications.

Figure 7 shows the calculated values for binding energy and charge transfer for all the structures. Binding energy (E_b) represents the energy preference of the related interaction. It can be understood as the difference in the total energies of the relaxed structures after and before contact. In this work, it is calculated according to the Equation 1:

$$E_b = E_{sm}^t - E_s^t - E_m^t \quad (1)$$

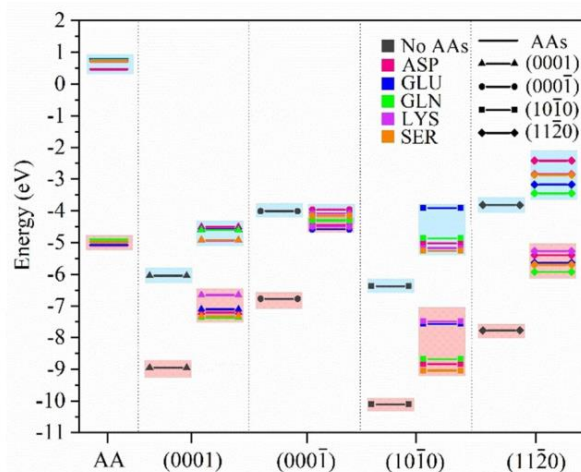


Figure 6. HOMO-LUMO levels for all structures, including amino acids, ZnO slabs, and all post-contact structures. (HOMOs in red and LUMOs in blue boxes)

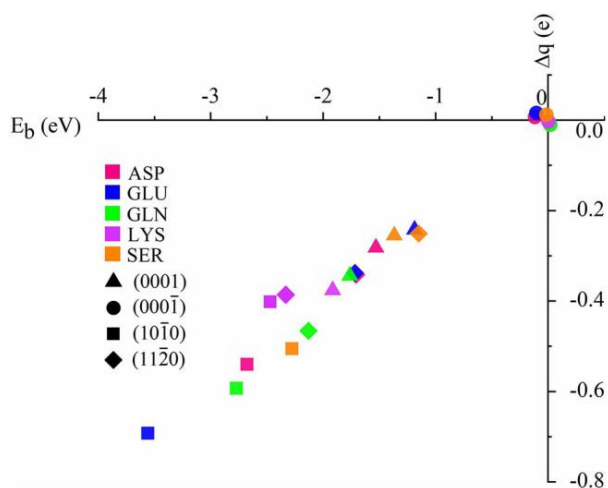


Figure 7. Binding energy and charge transfer for all post-contact structures.

where E_{sm}^t corresponds to the total energy of the structure, including molecule adsorbed on the slab surface while E_s^t and E_m^t stands for the total energies of the solo slab and solo molecule, respectively. Charge transfer between the molecules and zinc oxide surfaces was studied by calculating the atomic charge on the intrinsic and adsorbed systems using a Mulliken charge analysis.^[59]

The striking result is the clear linear correlation of binding energy with the charge transfer in the AA-ZnO complexes. To our best knowledge, such trend has not been observed before yet it is in a clear agreement with other computational and AFM results. It may explain various reported photoluminescence results and opens prospects for tuning the optical and electronic properties of ZnO in biological environments.^[60–63] The binding energies are overall negative and, therefore, exothermic (thermodynamically favorable) for all amino acids adsorbed on non-polar and Zn-faced polar surfaces, suggesting they are likely to form in real systems spontaneously. Spontaneous interactions between ZnO nanoparticles and BSA have been already reported experimentally^[36] and it is thus supported by our simulation results. The exception is for the O-faced surface, in which the binding energies are close to zero. An apparent surface morphology dependency is observed. Generally, non-polar surfaces compared to polar surfaces show higher values for both binding energy and charge transfer. Therefore, the tendency of amino acids to be adsorbed on these surfaces seems to be higher. To be more specific, (10 $\bar{1}0$) surface is likely to make the most potent binding with amino acids. In contrast, the O-faced (000 $\bar{1}$) surface with negligible values for both binding energy and charge transfer had the weakest interactions with ZnO surfaces.

4. Discussion

Figure 8a illustrates the comparison between BSA layer thickness defined by AFM and averaged height of BSA molecule

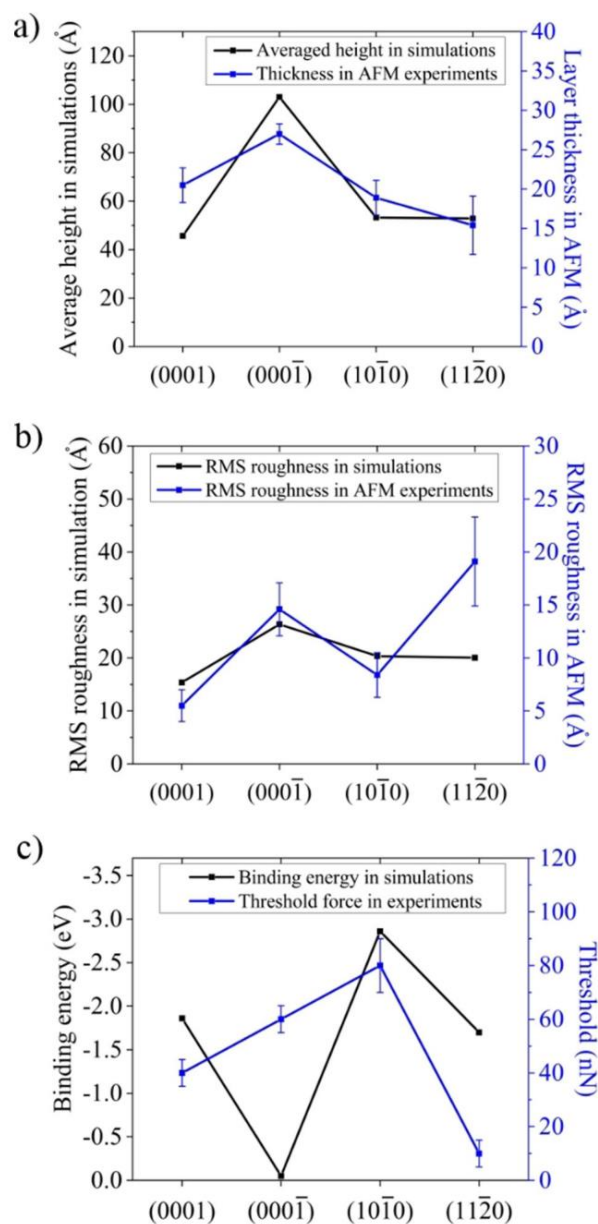


Figure 8. a) Comparison between BSA layer thickness defined by AFM and averaged height of BSA molecule obtained by force field simulations, b) comparison between RMS roughness of BSA layer obtained by AFM and FF simulations, c) comparison between force threshold required to remove BSA layer from ZnO surfaces by AFM tip and binding energy.

obtained in simulation. Figure 8b compares the RMS roughness of the BSA layer obtained by AFM and FF simulations. Both dependencies show good agreement between experimental and theoretical results. We consider only the relative difference between different ZnO surfaces in experiments and computing. Two to three times observed differences in absolute values for experiment and computing could be due to the deformation of molecules by AFM tip. Figure 8c shows the comparison between the force threshold required to remove the BSA layer

from ZnO surfaces by AFM tip, and binding energy, averaged values for five amino acids, obtained by DFTB simulations.

The first key finding is the high thickness of the BSA layer on the polar O-faced (000 $\bar{1}$) ZnO surface. This is clearly explained by FF and DFTB simulations showing that the BSA molecule adopts a vertical orientation on polar O-faced (000 $\bar{1}$) plane while its AAs are repelled from the surface. On the other hand, lower values of BSA layer thickness on the other three surfaces might be because the BSA molecules are attracted to all other ZnO surfaces with more horizontal orientations. RMS roughness values of BSA layers measured in AFM also correspond well to RMS roughness values of BSA molecules defined by FF simulations. The only discrepancy is the non-polar (11 $\bar{2}$ 0) facet. The reason could be the slightly higher aggregation of BSA molecules on non-polar (11 $\bar{2}$ 0) ZnO surface compared to the other three ZnO surfaces.

The second key point is the high force threshold required to remove the BSA layer from the non-polar (10 $\bar{1}$ 0) ZnO surface, clearly explained by DFTB simulations indicating high binding energies and covalent bonds to Zn surface atoms for all five amino acids on non-polar (10 $\bar{1}$ 0) ZnO surface. Covalent bonds between organic molecules and (10 $\bar{1}$ 0) ZnO surface are not unprecedented. Potent Zn–S covalent bonds are already reported experimentally for octadecanethiols on (10 $\bar{1}$ 0) ZnO surface.^[64] Our results indicate that spontaneous formation of covalent bonds between organic molecules and ZnO is far more general effect. Extensively more adhesion of proteins on (10 $\bar{1}$ 0) than other ZnO surfaces has also been reported in another AFM study of ZnO surfaces^[65] which can be appropriately justified with our DFTB calculation. The force threshold is lower for the other three surfaces because BSA molecules have lower binding energy to all other ZnO surfaces. The only discrepancy here is the O-faced (000 $\bar{1}$) surface for which the BSA removal force cannot be explained based on the binding energy. This could be because the main part of the removal force on (000 $\bar{1}$) surface is the force needed to penetrate the mutually tightly bound BSA layer (as discussed above) rather than to break the binding between BSA molecules and the ZnO surface.

5. Conclusions

The adsorption of BSA on various ZnO surfaces has been studied experimentally and theoretically. We employed AFM topography measurements and nanoshaving method to determine the roughness, thickness, and adhesion strength of BSA on four dominant low-index ZnO surface facets. FF and DFTB calculations were also carried out to study the physics behind the interactions on atomic and electronic level. BSA layers were formed on all the studied ZnO facets. AFM measurements and FF calculations are in a good agreement showing higher roughness and layer thickness for the (000 $\bar{1}$) surface due to BSA particular upright orientation preference on this surface. The nanoshaving experiments indicate the strongest binding of BSA to the (10 $\bar{1}$ 0) plane. This is corroborated by the DFTB simulations that show the most potent binding of BSA AAs on the (10 $\bar{1}$ 0) facet. DFTB simulations also reveal that the

interaction between BSA AAs and ZnO surfaces affects the electronic properties of the complexes, such as charge transfer, that has linear dependence on the binding energy, and HOMO–LUMO energy levels and spatial localization (including spatial separation in many cases). The results of this study are thus highly relevant for designing ZnO-based materials and for understanding their function in various applications ranging from biomedicine and biosensing to optoelectronics.

Supporting Information

Supporting Information is available from the Wiley Online Library or from the author.

Acknowledgements

Funding: The work has been supported by the projects GACR 19-02858J, SGS21/158/OHK4/3T/13, CAAS (CZ.02.1.01/0.0/0.0/16_019/0000778), and CzechNanoLab Research Infrastructure supported by MEYS CR (LM2018110).

Conflict of Interest

The authors declare no conflict of interest.

Keywords: bovine serum albumin · ZnO · atomic force microscopy · nanoshaving · density-functional tight-binding

- [1] R. Yan, D. Gargas, P. Yang, *Nat. Photonics* **2009**, *3*, 569.
- [2] C. F. Klingshirn, A. Waag, A. Hoffmann, J. Geurts, *Zinc Oxide: From Fundamental Properties Towards Novel Applications*, Springer-Verlag, Berlin Heidelberg, **2010**.
- [3] Ü. Özgür, Y. I. Alivov, C. Liu, A. Teke, M. A. Reshchikov, S. Doğan, V. Avrutin, S.-J. Cho, H. Morkoç, *J. Appl. Phys.* **2005**, *98*, 041301.
- [4] J. Cembrero, A. Elmanouni, B. Hartiti, M. Mollar, B. Mari, *Thin Solid Films* **2004**, *451–452*, 198.
- [5] M. T. Noman, N. Amor, M. Petru, *Crit. Rev. Solid State Mater. Sci.* **2021**, *0*, 1.
- [6] F. Muhammad, M. Guo, Y. Guo, W. Qi, F. Qu, F. Sun, H. Zhao, G. Zhu, *J. Mater. Chem.* **2011**, *21*, 13406.
- [7] Y. Liu, J. Yang, P. Zhang, C. Liu, W. Wang, W. Liu, *J. Mater. Chem.* **2011**, *22*, 512.
- [8] H. Qiu, B. Cui, G. Li, J. Yang, H. Peng, Y. Wang, N. Li, R. Gao, Z. Chang, Y. Wang, *J. Phys. Chem. C* **2014**, *22*, 14929.
- [9] M. M. Rahman, A. J. S. Ahammad, J.-H. Jin, S. J. Ahn, J.-J. Lee, *Sensors* **2010**, *10*, 4855.
- [10] E. Topoglidis, C. J. Campbell, A. E. G. Cass, J. R. Durrant, *Langmuir* **2001**, *17*, 7899.
- [11] K. Jindal, M. Tomar, V. Gupta, *Analyst* **2013**, *138*, 4353.
- [12] G. Applerot, A. Lipovsky, R. Dror, N. Perkas, Y. Nitzan, R. Lubart, A. Gedanken, *Adv. Funct. Mater.* **2009**, *19*, 842.
- [13] Y. Xiang, C. Mao, X. Liu, Z. Cui, D. Jing, X. Yang, Y. Liang, Z. Li, S. Zhu, Y. Zheng, K. W. K. Yeung, D. Zheng, X. Wang, S. Wu, *Small* **2019**, *15*, 1900322.
- [14] W. Muhammad, N. Ullah, M. Haroon, B. H. Abbasi, *RSC Adv.* **2019**, *9*, 29541.
- [15] R. D. C. Soltani, M. Mashayekhi, M. Naderi, G. Boczkaj, S. Jorfi, M. Safari, *Ultrason. Sonochem.* **2019**, *55*, 117.
- [16] S. Yu, H. Zhang, C. Chen, C. Lin, *Sens. Actuators B* **2019**, *287*, 526.

- [17] J. E. Lee, C. K. Lim, H. J. Park, H. Song, S.-Y. Choi, D.-S. Lee, *ACS Appl. Mater. Interfaces* **2020**, *12*, 35688.
- [18] R. Yoo, A. T. Güntner, Y. Park, H. J. Rim, H.-S. Lee, W. Lee, *Sens. Actuators B* **2019**, *283*, 107.
- [19] P. Wang, T. Dong, C. Jia, P. Yang, *Sens. Actuators B* **2019**, *288*, 1.
- [20] N. P. Shetti, S. D. Bukkittgar, K. R. Reddy, C. V. Reddy, T. M. Aminabhavi, *Biosens. Bioelectron.* **2019**, *141*, 111417.
- [21] R. Yu, C. Pan, Z. L. Wang, *Energy Environ. Sci.* **2013**, *6*, 494.
- [22] A. G. Cuevas, K. Balangcod, T. Balangcod, A. Jasmin, *Procedia Eng.* **2013**, *68*, 537.
- [23] P. T. S. Kumar, V.-K. Lakshmanan, T. V. Anilkumar, C. Ramya, P. Reshmi, A. G. Unnikrishnan, S. V. Nair, R. Jayakumar, *ACS Appl. Mater. Interfaces* **2012**, *4*, 2618.
- [24] Q. Yuan, S. Hein, R. D. K. Misra, *Acta Biomater.* **2010**, *6*, 2732.
- [25] Y. H. Mohammed, A. Holmes, I. N. Haridass, W. Y. Sanchez, H. Studier, J. E. Grice, H. A. E. Benson, M. S. Roberts, *J. Invest. Dermatol.* **2019**, *139*, 308.
- [26] P. J. P. Espitia, N. de F. F. Soares, J. S. dos R. Coimbra, N. J. de Andrade, R. S. Cruz, E. A. A. Medeiros, *Food Bioprocess Technol.* **2012**, *5*, 1447.
- [27] P. Petkova, A. Francesko, I. Perelshtein, A. Gedanken, T. Tzanov, *Ultrason. Sonochem.* **2016**, *29*, 244.
- [28] A. Sandmann, A. Kompch, V. Mackert, C. H. Liebscher, M. Winterer, *Langmuir* **2015**, *31*, 5701.
- [29] D. Rothenstein, B. Claasen, B. Omiecienski, P. Lammel, J. Bill, *J. Am. Chem. Soc.* **2012**, *134*, 12547.
- [30] M.-K. Liang, O. Deschaume, S. V. Patwardhan, C. C. Perry, *J. Mater. Chem.* **2010**, *21*, 80.
- [31] M. J. Limo, R. Ramasamy, C. C. Perry, *Chem. Mater.* **2015**, *27*, 1950.
- [32] G. Nawrocki, M. Cieplak, *Phys. Chem. Chem. Phys.* **2013**, *15*, 13628.
- [33] Y. K. Gao, F. Traeger, O. Shekhah, H. Idriss, C. Wöll, *J. Colloid Interface Sci.* **2009**, *338*, 16.
- [34] S. grosse Holthaus, S. Köppen, T. Frauenheim, L. C. Ciacchi, *J. Chem. Phys.* **2014**, *140*, 234707.
- [35] S. Piscopo, E. R. Brown, *Small* **2018**, *14*, 1703403.
- [36] M. Bardhan, G. Mandal, T. Ganguly, *J. Appl. Phys.* **2009**, *106*, 034701.
- [37] S. Chakraborti, P. Joshi, D. Chakravarty, V. Shanker, Z. A. Ansari, S. P. Singh, P. Chakrabarti, *Langmuir* **2012**, *28*, 11142.
- [38] A. Bhogale, N. Patel, P. Sarpotdar, J. Mariam, P. M. Dongre, A. Miotello, D. C. Kothari, *Colloids Surf. B* **2013**, *102*, 257.
- [39] B. Rezek, H. Hematian, J. Jira, D. Rutherford, J. Kuliček, E. Ukraintsev, Z. Remeš, *Phys. Status Solidi A* **2021**, *218*, 2000558.
- [40] H. Hematian, B. Rezek, *Iop. Conf. Ser. Mater. Sci. Eng.* **2021**, *1050*, 012006.
- [41] K. Giannousi, G. Geromichalos, D. Kakolyri, S. Mourdikoudis, C. Dendrinou-Samara, *ACS Chem. Neurosci.* **2020**, *11*, 436.
- [42] A. R. Prasad, S. M. Basheer, I. R. Gupta, K. K. Elyas, A. Joseph, *Mater. Chem. Phys.* **2020**, *240*, 122115.
- [43] V. Myndrul, E. Coy, M. Bechelany, I. Iatsunskiy, *Mater. Sci. Eng. C* **2021**, *118*, 111401.
- [44] B. Rezek, E. Ukraintsev, L. Michalíková, A. Kromka, J. Zemek, M. Kalbacova, *Diamond Relat. Mater.* **2009**, *18*, 918.
- [45] B. Rezek, E. Ukraintsev, M. Krátká, A. Taylor, F. Fendrych, V. Mandys, *Biointerphases* **2014**, *9*, 031012.
- [46] B. Rezek, D. Shin, T. Nakamura, C. E. Nebel, *ACS Publ.* **2006**, *128*, 3884.
- [47] H. Kozak, A. Artemenko, E. Ukraintsev, A. Choukourov, B. Rezek, A. Kromka, *Langmuir* **2019**, *35*, 13844.
- [48] B. Rezek, E. Ukraintsev, A. Kromka, M. Ledinský, A. Brož, L. Nosková, H. Hartmannová, M. Kalbacova, *Diamond Relat. Mater.* **2010**, *19*, 153.
- [49] E. Ukraintsev, V. Houska, J. Vacek, I. Starý, G. I. Stará, B. Rezek, **2020**, pp. 561–567.
- [50] M. Elstner, D. Porezag, G. Jungnickel, J. Elsner, M. Haugk, Th. Frauenheim, S. Suhai, G. Seifert, *Phys. Rev. B* **1998**, *58*, 7260.
- [51] N. H. Moreira, G. Dolgonos, B. Aradi, A. L. da Rosa, T. Frauenheim, *J. Chem. Theory Comput.* **2009**, *5*, 605.
- [52] A. Wander, F. Schedin, P. Steadman, A. Norris, R. McGrath, T. S. Turner, G. Thornton, N. M. Harrison, *Phys. Rev. Lett.* **2001**, *86*, 3811.
- [53] D. Mora-Fonz, T. Lazauskas, M. R. Farrow, C. R. A. Catlow, S. M. Woodley, A. A. Sokol, *Chem. Mater.* **2017**, *29*, 5306.
- [54] A. Calzolari, M. Bazzani, A. Catellani, *Surf. Sci.* **2013**, *607*, 181.
- [55] B. Rezek, E. Ukraintsev, A. Kromka, *Nanoscale Res. Lett.* **2011**, *6*, 337.
- [56] J.-J. Feng, G. Zhao, J.-J. Xu, H.-Y. Chen, *Anal. Biochem.* **2005**, *342*, 280.
- [57] X. Yan, L. Lin, S. Li, W. Wang, B. Chen, S. Jiang, S. Liu, X. Ma, X. Yu, *Chem. Eng. J.* **2020**, *395*, 125171.
- [58] P. Yang, H. Yan, S. Mao, R. Russo, J. Johnson, R. Saykally, N. Morris, J. Pham, R. He, H.-J. Choi, *Adv. Funct. Mater.* **2002**, *12*, 323.
- [59] L. Wu, L. Zhang, L. Shen, *Appl. Surf. Sci.* **2018**, *447*, 22.
- [60] X. Zhang, Y. Xia, T. He, *Mater. Chem. Phys.* **2012**, *137*, 622.
- [61] Z. Zhou, F. Zhang, J. Wang, X. Zhang, W. Xu, R. Wu, L. Liao, X. Wang, J. Wei, *Mater. Sci. Eng. C* **2019**, *103*, 109818.
- [62] M. Gharagozlou, S. Naghibi, *Mater. Res. Bull.* **2016**, *84*, 71.
- [63] M. Singh, X. Zhuo, D. S. Choi, L. E. Gonzalez, J. Wang, J. Hahm, *Nanoscale* **2015**, *7*, 18813.
- [64] J. Chen, R. E. Ruther, Y. Tan, L. M. Bishop, R. J. Hamers, *Langmuir* **2012**, *28*, 10437.
- [65] T. Xie, S. Song, K. Schwenke, M. Singh, L. E. Gonzalez, E. Del Gado, J. Hahm, *Langmuir* **2015**, *31*, 10493.

Manuscript received: September 1, 2021
Revised manuscript received: October 24, 2021
Accepted manuscript online: November 10, 2021
Version of record online: November 23, 2021

Polarization Controlled Assembly of Ultrathin Thiorphan Nanostructures on ZnO Surface Facets

Egor Ukraintsev,^{*,†} Hadi Hematian,[†] and Bohuslav Rezek

Cite This: *Langmuir* 2023, 39, 1764–1774

Read Online

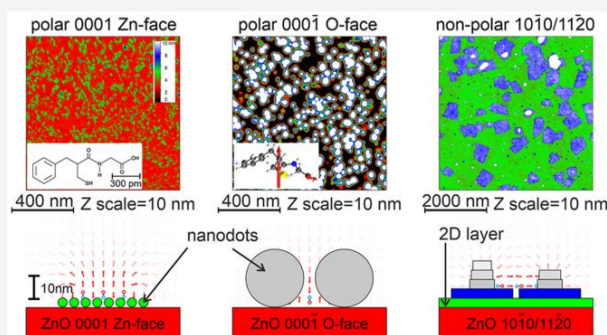
ACCESS |

Metrics & More

Article Recommendations

Supporting Information

ABSTRACT: Despite the importance of thiorphan as a small molecule with vital biological roles, its interactions with zinc oxide (ZnO) nanomaterials that are prospective in drug delivery and theranostic applications have not yet been sufficiently explored. Here the impact of surface polarity of different ZnO facets on thiorphan adsorption is studied both experimentally by atomic force microscopy (AFM) and angle resolved X-ray photoelectron spectroscopy (XPS) and theoretically by force field molecular dynamics (FFMD) and density functional tight binding simulations (DFTB). Polar ZnO surfaces cause the formation of thiorphan nanodots, where the size of the nanodots depends on the direction of dipoles: small (4 nm) nanodots are formed on Zn-face ZnO, while large (25 nm) nanodots are formed on O-face ZnO. Nonpolar ZnO surfaces cause self-assembly into layered nanoislands with characteristic 4 nm layer thickness, which subsequently merge into rigid nanolayers. The self-assembly is shown to be controlled solely by the effect of surface dipole electric field orientation and magnitude, whereas effects of surface chemistry or solution are negligible. The results thus also show a way for controlling the assembly of thiorphan and other molecular nanomaterials for diverse applications.



1. INTRODUCTION

Thiorphan ((DL-3-mercapto-2-benzylpropanoyl)-glycine) is a small bioactive molecule, which was first introduced in 1980¹ and currently has many possible applications in medicine. For instance, thiorphan protects the enkephalins from the action of enkephalinase *in vitro* in nanomolar concentrations and *in vivo* after either intracerebroventricular or systemic administration. In addition, thiorphan itself displays antinociceptive activity which is blocked by naloxone, an antagonist of opiate receptors,¹ it is an active metabolite enkephalinase inhibitor that has strong affinity for membrane metallo-endopeptidase,^{2–4} it has the ability to block the degradation of the luteinizing hormone-releasing hormone,⁵ and it potentiates the natriuretic activity of atrial natriuretic peptide ANP(99-126) by inhibiting its degradation.⁶ Mostly, thiorphan is used as a selective inhibitor of neutral endopeptidase^{5,7,8} and of metalloproteinase.⁹ Neutral endopeptidase 24.11 (NEP; EC.3.4.24.11, neprilysin) is a zinc-ectoenzyme involved in the metabolism of some important regulatory peptides in both the central nervous system and the periphery.¹⁰ The zinc atom in NEP and both the thiol group and benzene ring in thiorphan play crucial roles in molecular interactions and forming tertiary structures.¹⁰ Zinc, sulfur, and nitrogen atoms are important in the processes, in which biomolecules act as inhibitors of matrix metalloproteinases.^{11–13}

In spite of its practical importance, thiorphan adsorption on surfaces (including surfaces with zinc atoms) has not been

studied yet. Zinc oxide (ZnO) and other metal oxide nanomaterials represent a versatile platforms for biomedical applications and therapeutic intervention.^{14–18} ZnO nanostructures are widely used for drug delivery and theranostic applications.¹⁹ For instance, ZnO is used for the treatment of various types of cancer diseases²⁰ and ZnO nanoparticles are utilized in bioimaging because of their high stability and inherent photoluminescence properties.²¹ The ZnO surface structure as well as photoluminescence can be modified by hydrogen plasma.²² ZnO exhibits also a high adsorption capability and selectivity for photocatalytic dye removal²³ and wastewater treatment in general.²⁴

In addition to microscopic and spectroscopic methods, a more profound understanding of adsorption and interaction of molecules on surfaces benefits from computational simulations using methods such as density functional tight binding (DFTB)²⁵ and force field molecular dynamics simulations (FFMD).²⁶ Even though implementing DFTB and FFMD for large protein molecules such as albumin (BSA) is too costly,

Received: September 1, 2022

Revised: January 3, 2023

Published: January 19, 2023



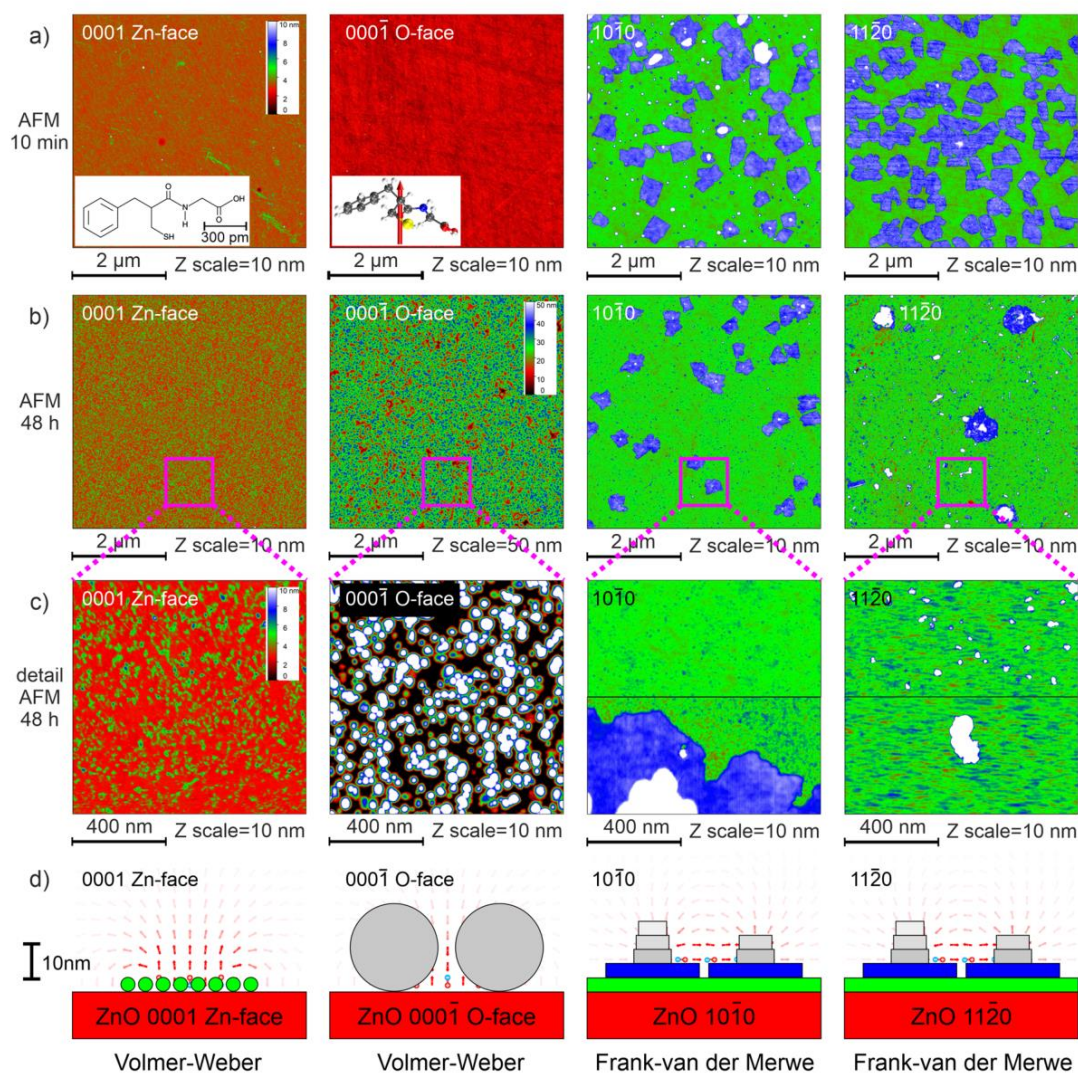


Figure 1. (a) Overview AFM morphology of thiorphan self-assembled layers after 10 min adsorption in ethanol on different ZnO facets. (a, inset) Chemical structure of thiorphan molecule and dipole moment of individual thiorphan molecule. (b) Overview AFM morphology of thiorphan self-assembled layers after 48 h adsorption in ethanol on different ZnO facets. (c) Detailed AFM morphology of thiorphan self-assembled layers after 48 h adsorption on different ZnO facets. (d) Schematic model of thiorphan self-assembled layers, surface dipole orientation with electric field, and possible adsorption modes on different ZnO facets. Stronger electric field is shown with darker arrows. Background ZnO substrate has red color. Single 4 nm thick thiorphan layer grown on ZnO substrate has green color. Double 8 nm thick thiorphan layer has blue color.

amino acids (AAs) are sufficiently small molecules, adsorption and interaction of which can be simulated economically using these simulation techniques.^{27,28} On ZnO, AAs were found to form covalent Zn–N and Zn–O bonds with three ZnO surfaces (0001), (10 $\bar{1}$ 0) and (11 $\bar{2}$ 0)) and to be repelled from O-face ZnO.²⁷ Thiorphan is also a small molecule; therefore, its adsorption and assembly can be simulated using DFTB and FFMD methods. It has sulfur and nitrogen atoms and thus formation of Zn–N¹¹ and Zn–S bonds^{12,13} can be expected.

A review²⁹ critically investigated to what extent self-assembly can be directed, enhanced, or controlled by either changing the energy or entropy landscapes, using templates or applying external fields. It was demonstrated that external field³⁰ and solvent with different polarity³¹ can influence the resulting self-assembled structures for a specific material and substrate.

Thus, in this work, four different ZnO surfaces (two polar and two nonpolar) are used as model substrates for studying

the interaction with thiorphan. Atomic force microscopy (AFM) experiments and angle resolved X-ray photoelectron spectroscopy (XPS) are used to characterize the adsorption and assembly of thiorphan on different ZnO facets, showing the formation of different thiorphan nanostructures on those ZnO surfaces. The AFM experiments also suggest that surface dipole orientation plays a dominant role in the different types of thiorphan adsorption on ZnO surfaces and theoretical simulations corroborate the experimental findings. In the simulations, ZnO interactions with thiorphan molecules are investigated from two aspects: surface chemistry and surface polarity. To investigate the surface chemistry (the interactions between surface atoms and thiorphan atoms), we applied DFTB as a reliable electronic simulation method which can model the formation of covalent bonds. The effects of surface polarity are studied by FFMD simulations. Different self-assembled molecular nanostructures can thus arise from the

same molecules due to different local electric fields, in the present case created inherently by the ZnO surface dipoles of various magnitudes and orientations without any significant influence from other external factors.

2. RESULTS AND DISCUSSION

2.1. Atomic Force Microscopy. Figure 1 shows the result of adsorption experiments and the formation of thiorphan nanodots and nanoislands on different ZnO facets at the macroscale; image size is $5 \times 5 \mu\text{m}^2$. Here we define nanodots as three-dimensional objects whereas nanoislands are objects composed of two-dimensional-like layers. Figure S1 in the Supporting Information illustrates the same images in three-dimensional (3D) view. The chemical structure of a thiorphan molecule is also presented in Figure 1a as an inset. The dipole moment of individual thiorphan molecule is presented also in the Figure 1a inset and in Figure S1e.

In Figure 1a, one can see the initial stage of the adsorption process of thiorphan on ZnO. After 10 min of thiorphan deposition from ethanol solution, ZnO samples were cleaned with water, dried using nitrogen flow, and studied by AFM. After 10 min of adsorption, the sample coverage is non-homogeneous and some parts of the surfaces are uncovered. The most representative topography features are presented in Figure 1a. Figure 1a shows small nanodots (red-green color), usually with 4 nm and smaller height, on the Zn-face surface. The O-face ZnO surface looks clean at this stage. On the other hand, thick nanoislands (green color) with a thickness of ~ 4 nm can be observed on the nonpolar surfaces in Figure 1a. On top of those islands, more ~ 4 nm nanoislands are formed (double layers have blue color and triple layers have white color). The thickness of those layers varies in a very narrow range of 3.4–3.6 nm (as shown in Figure S2).

The lowest visible layer (ZnO surface or thiorphan layer in some cases) is shown in red color. Contact mode nanoshaving experiments,^{32,33} performed with a stiff cantilever (Tap300, 40 N/m) and high load force (2400 nN), were not able to penetrate through some of the thiorphan layers (Figure S3); therefore, we cannot prove the absence or presence of thiorphan layers below the lowest visible layer using AFM.

After 48 h of thiorphan deposition on ZnO samples, the coverage of ZnO samples is much more homogeneous than that after 10 min adsorption. Practically all studied spots have similar morphology in different spots (Figure 1b). The Zn-face ZnO facet has a larger amount of small nanodots with a height of 4 nm or smaller. The O-face ZnO facet is homogeneously covered with large nanodots with heights up to 25 nm. After 48 h thiorphan deposition on the (10 $\bar{1}$ 0) ZnO facet, only 2–3 layers could be identified. Even a stiff AFM tip could not penetrate the bottom layer. Thus, based on AFM data, it is not possible to tell whether 10 previously found layers (Figure S2a) were grown to ~ 40 nm thick layers or thiorphan molecules from top layers migrate and homogeneously fill the bottom ~ 4 –8 nm thick layers. After 48 h thiorphan deposition on the (11 $\bar{2}$ 0) ZnO facet, 2–3 layers could be identified in many places, while in some places up to 9 layers could be identified (Figure S2b).

Figures 1, S1, and S2 show different large-scale structures formed from thiorphan on different ZnO facets. In order to understand the adsorption process in detail, fine topography AFM images were obtained on all samples after 48 h deposition. Figure 1c shows small nanodots (height 4 nm or smaller), formed on the Zn-face ZnO facet, and large nanodots

(height ~ 25 nm), formed on the O-face ZnO facet. On the other hand, the 4 nm thick nanoislands are observed on the (10 $\bar{1}$ 0) and (11 $\bar{2}$ 0) ZnO facets. On both the (10 $\bar{1}$ 0) and (11 $\bar{2}$ 0) ZnO samples, there are many ~ 50 nm wide small nanoislands as well as ~ 2000 nm wide large multilayer nanoislands. Zoom pictures were selected in a way to be the most informative, and they could be from different areas of the surfaces.

Based on the presented AFM results, the schematic model of thiorphan self-assembled layer formation on different ZnO facets is suggested in Figure 1d. Figure 1d shows small nanodots, large nanodots, and a continuous thiorphan layer with several nanoislands on the Zn-face, O-face, and nonpolar surfaces, respectively. Figure 1d is an outcome of all our results and discussion. We put the model to Figure 1d rather than as a separate figure to be easily correlated with structural topographies. The growth models were selected mainly based on AFM data.

Based on the morphology and growth scheme, we attribute the formation of both small and large nanodots on polar ZnO facets to the Volmer–Weber growth model.³⁴ The formation of several layers of nanoislands on (10 $\bar{1}$ 0) and (11 $\bar{2}$ 0) ZnO facets can be described by the Frank–van der Merwe growth model.³⁵ In this case, the minimal building block is a single thiorphan molecule (consisting from 32 atoms) and not the single C atom as for example in homoepitaxial graphene growth.³⁶ Figure 1 shows that the thickness of a single thiorphan layer is self-limited to 4 nm. The length of the thiorphan molecule is only 1 nm; thus, the 4 nm thickness does not correspond to a thiorphan monolayer in the common definition of this term. Yet it indicates some specific arrangement that leads to a tight and rigid layer-like thiorphan assembly. Note also that such layers can be stacked on each other as shown by the topographies of the nanoislands.

One possible reason for the different assembly of thiorphan molecules on different ZnO facets is the impact of the ZnO surface dipole on thiorphan molecules during their adsorption. Figure 1d shows the direction and magnitude of the electric field, created by three differently oriented dipoles. Electric field lines were simulated using the direction of a dipole moment of ZnO surface and positive/negative charges of Zn and O atoms.³⁷ The direction of the ZnO dipole moment is taken from ref 38. As one can see, the magnitude of the electric field decreases rapidly for nonpolar surfaces compared to polar surfaces (for details, see part 2.3).

We observed formation of different structures on different ZnO facets. Generally speaking, the ZnO surface can influence thiorphan adsorption due to the presence of Zn and O atoms on the surface or due to the presence of dipoles on the ZnO surface. Both possibilities will be considered in the next parts. To consider the impact of Zn and O atoms on the surface the adsorption of one thiorphan molecule on different ZnO facets was modeled using DFTB simulations (part 2.2). To run DFTB simulations, we have to cancel ZnO dipole moments to have stable polar surfaces. Therefore, results of DFTB simulations may differ from reality. To consider the impact of dipoles, the adsorption of thiorphan molecules on C=O dipoles with different dipole orientations was modeled using FFMD simulations (part 2.3). The simulation result shows that the interaction of surface dipoles with thiorphan molecules can explain the experimental AFM results with high precision.

2.2. Density Functional Tight Binding simulations. ZnO interactions with thiorphan molecules were investigated

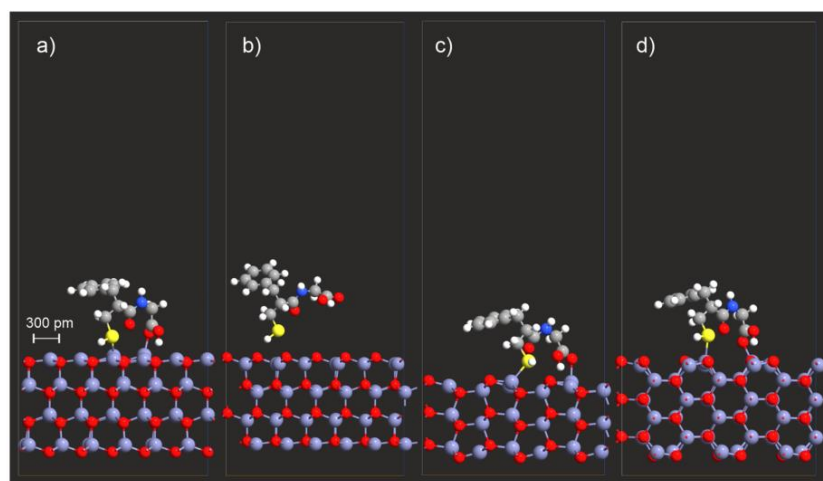


Figure 2. Final stages of DFTB simulations for one thiorphan molecule adsorption process on (a) (0001), (b) (000 $\bar{1}$), (c) (10 $\bar{1}$ 0) and (d) (11 $\bar{2}$ 0)ZnO facets.

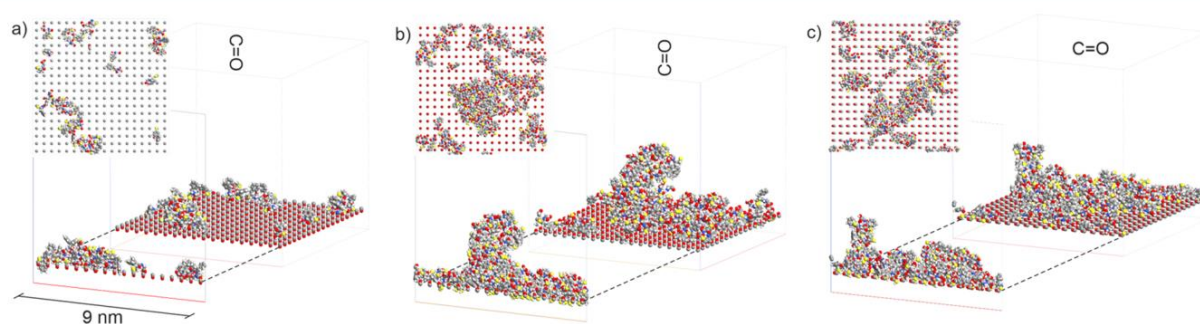


Figure 3. Final stage of FFMD simulations for 10 \times 20 thiorphan molecules adsorption process on (a) C-top, (b) O-top, and (c) horizontally oriented C=O dipole layers.

from two aspects in the simulations: (i) surface chemistry and (ii) surface polarity. To investigate the surface chemistry (the interactions between surface atoms and thiorphan atoms), we applied DFTB as a reliable electronic simulation method which can model the formation of covalent bonds. However, we had to exclude the polarity of the ZnO slabs to make their structure stable in DFTB, as usually done in the literature.³⁹ Since we are modeling the surface chemistry effects of adsorbed molecules, the long-range dipole interactions can be reasonably neglected. The results of DFTB simulations can be thus attributed to the effects of surface chemistry with a good confidence.

Figure 2 shows the result of DFTB simulations with one thiorphan molecule, placed into vacuum above four different ZnO facets. Covalent bonding between the S atom in the thiorphan molecule and the Zn atom in the ZnO slab was observed in the case of the (0001), (10 $\bar{1}$ 0), and (11 $\bar{2}$ 0) ZnO facets. Repelling of the thiorphan molecule from the O-face (000 $\bar{1}$) ZnO facet was observed.

This behavior is very similar to the adsorption of amino acids on different ZnO facets.²⁷ In those simulations, covalent bonding between N and/or O atoms in amino acids and the Zn atom in the ZnO slab was observed in case of the (0001), (10 $\bar{1}$ 0), and (11 $\bar{2}$ 0)ZnO surfaces. Repelling of amino acids was observed from the O-face (000 $\bar{1}$) ZnO facet.²⁷ This behavior in DFTB simulations (repulsion from O-face surface and adhesion to other surfaces) was experimentally corroborated by nanoshaving experiments.²⁷ Thus, despite surface polarity

exclusion, we consider the binding information from DFTB as reliable also for the case of thiorphan.

To investigate adsorption and possible aggregation of thiorphan molecules as an ensemble, the behavior of many molecules should be simulated. However, DFTB simulations are computationally costly and the necessity to compensate the dipole moment leads to loss of interaction. FFMD simulations were thus used to speed up the calculations and make a more realistic analysis.

2.3. Force Field Molecular Dynamics Simulations.

In order to define the behavior of thiorphan molecules, the adsorption of thiorphan molecules on different dipole facets was studied by the FFMD method. The adsorption kinetics of thiorphan on different dipoles was studied by a method in which new portions of molecules arrive after the previous portion has its time to interact with the surface. This method is described in detail in section 3.6. To speed up simulations instead of individual ethanol molecules we used implicit solvent with $\epsilon = 24.3$.⁴⁰

Figure 3a–c shows the FFMD computational results of adsorption for the C-top dipole (mimicking Zn-face ZnO), O-top dipole (mimicking O-face ZnO), and horizontally oriented C=O dipole (mimicking nonpolar ZnO facets), respectively. For each set of simulations, the final 3D image, side view, and top view are shown. Rotatable 3D objects are provided in Figure S4.

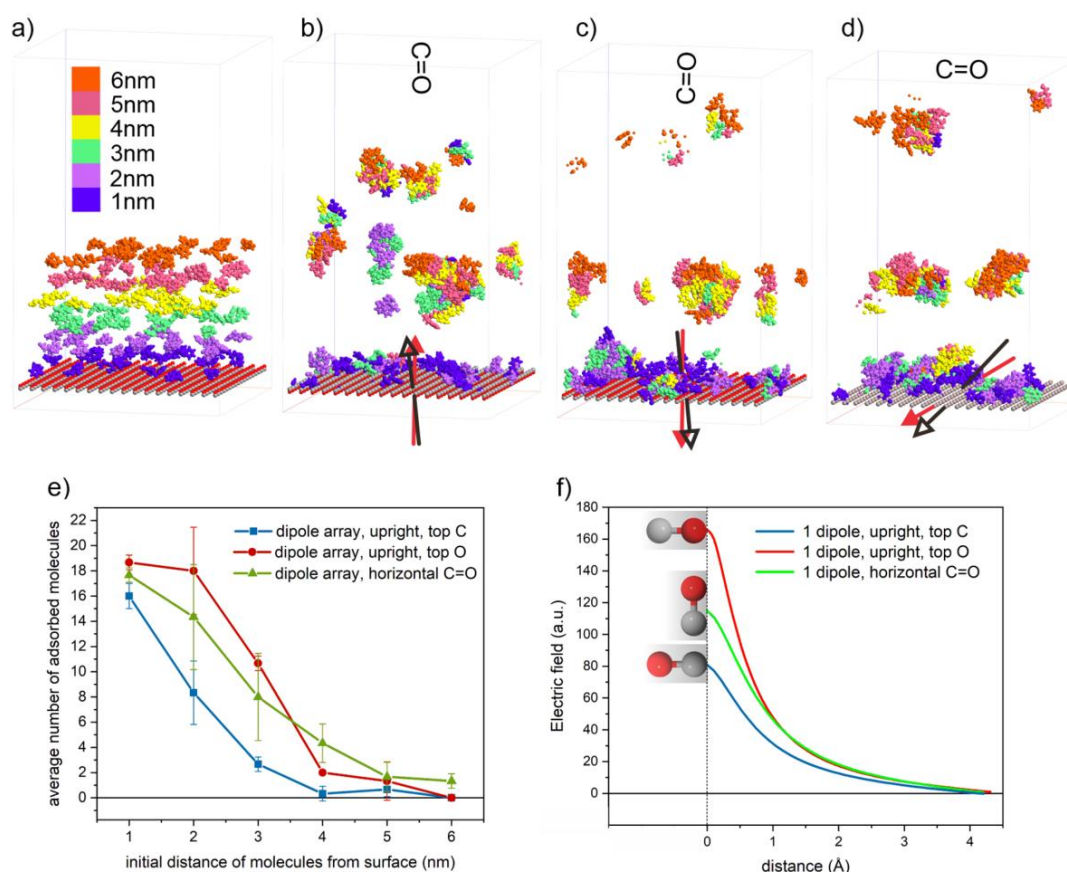


Figure 4. (a) Initial stage of adsorption process of six layers, consisting of 20 thiorphan molecules each. Final stage of adsorption process on (b) C-top, (c) O-top, and (d) horizontally oriented C=O dipole array, respectively. Total surface dipoles and total dipoles of the adsorbed molecules are shown using red and black arrows, respectively. (e) Dependences of the average number of adsorbed molecules vs initial distance of molecules from dipole array surface. (f) Dependences of the electric field vs distance from single dipole. Electrostatic potential for single dipole was calculated by DFT (GGA, PBE).

The number of adsorbed molecules is the smallest for the C-top dipole. About 50%, 10%, and 30% of total adsorbed molecules were adsorbed as individual molecules on C-top, O-top, and horizontally oriented dipoles, respectively. In addition, aggregates that were formed on the nonpolar surface were mostly smaller, i.e., consisted of less molecules rather than the ones for the O-top surface. Therefore, we can say that single adsorption (and small aggregates) happens on the nonpolar surface more than it does on the O-top surface. This result is in line with experimental AFM results (Figure 1) and with simulation results (Figure 4), too.

To address the reason behind the formation nanodots with different sizes on polar surfaces and the formation of 4 nm thick nanoislands on nonpolar surfaces, six layers with 1 nm thickness were filled with 6×20 thiorphan molecules and placed above three different dipole layers. The results of FFMD simulations are shown in Figure 4. Figure 4a shows the initial placement of thiorphan molecules. Molecules with different initial heights are marked with different colors. Figure 4b–d shows the results of adsorption for the C-top, O-top dipole, and horizontally oriented C=O dipole, respectively. Those simulations were performed three times. Figure 4e summarizes the results of FFMD simulations and shows the probability of adsorption for molecules, placed at a certain height above the surface. In all cases, the larger distance from

the surface causes a smaller probability of adsorption. Analysis of these data reveal a distance at which the probability of adsorption is 50%. The height values are 1.74, 3.08, and 2.65 nm for the C-top dipole, O-top dipole, and horizontally oriented C=O dipole, respectively.

In Figure 4, one can also see the total dipole of the surfaces and adsorbed molecules calculated and visualized by VMD. It is important to note that the total dipoles of the adsorbed molecules were calculated separately and independently from the surface dipole arrays, merely based on the orientation and arrangement of the molecules on each surface. The arrangement and orientation of the molecules on each surface are in a way that the total dipole of the adsorbed molecules aligns along the corresponding surface total dipole. Figure 4 confirms that the molecule orientation and adsorption process is governed by electric field lines and not by polarization (that would turn it in the opposite direction).

Figure 4f shows the dependences of the electric field magnitude vs distance from a single dipole. It proves that the reason for such adsorption behavior is solely the impact of electric field created by ZnO dipoles. Such data correlate well with the results of experiments. On average, a thiorphan molecule should approach a twice closer distance to the C-top dipole (represents Zn-face ZnO facet) than to all other dipoles. Thus, the smallest coverage can be expected for the C-top

dipole surface (Figures 3a and 4b) and for the Zn-face ZnO facet (Figure 1) due to the interaction of the molecule with the surface dipole. This result clearly shows that thiorphan molecules behave differently depending on the surface dipole orientation.

The orientation of the dipole on the different ZnO surfaces is not identical. The surface dipole in the ZnO crystal is in the [0001] direction, from the O-face facet to Zn-face facet.³⁸ This results in pointing up and pointing down surface dipoles on Zn-face and O-face surfaces, respectively. In FFMD simulations, we modeled these orientations by using C=O dipole arrays. Depending on the orientation of the ZnO dipole, thiorphan adsorption can be explained by the Volmer–Weber³⁴ or Frank–van der Merwe³⁵ growth model.

The results of similar MD simulations with two other solvents, namely, water ($\epsilon \approx 80$) and chloroform ($\epsilon = 4.8$), are shown in Figure S5. Chloroform has the lowest ϵ value for all solvents, in which thiorphan can be dissolved. Water has a higher ϵ value than any solvent, in which thiorphan can be dissolved. As one can see, the surface polarity dependent adsorption behavior is observed for these two solvents, too. This behavior is the same in all three solvents, indicating negligible influence of the solvent on adsorption behavior.

2.4. DLS Measurements. The result of DLS measurements for thiorphan solution in ethanol ($c = 1$ mg/mL) is shown in Figure S6. The number size distribution shows the presence of only individual molecules (peak maximum is at size 0.97 nm that is approximately equal to the size of one molecule) and absence of thiorphan aggregates in the ethanol solution.

2.5. XPS Measurements. Ordering of the thiorphan molecules on the ZnO surface was analyzed by angular resolved XPS measurements. The results are shown in Figure 5. Figure 5a shows the wide XPS spectra at 0° angle, obtained on the Zn-face, O-face, (10 $\bar{1}$ 0) and (11 $\bar{2}$ 0) ZnO facets after 48 h thiorphan adsorption. The analysis of all peaks at different angles reveals that major changes happen in O 1s region. Twenty high resolution spectra of the O 1s region with corresponding deconvolution of all peaks are shown in Figures 5b and S7. The peak around 532 eV is attributed to the combined C–O/C=O peak from thiorphan, and the peak around 530 eV corresponds to the Zn–O peak from the ZnO surface (and also possible Zn–O covalent bond between the ZnO surface and thiorphan).⁴¹

The ratios between intensities of the C–O/C=O and Zn–O peaks for all 4 samples and 5 different angles are shown in Figure 5c. Such analysis was used earlier to deduce the orientation of TFAAD molecules on diamond surface.⁴² Here a similar approach was used. On the Zn-face and (10 $\bar{1}$ 0) samples, the ratio rapidly increases with the angle, indicating high ordering of thiorphan molecules within the small nanodots or thiorphan layers. On the other hand, on the O-face and (11 $\bar{2}$ 0) ZnO samples, the ratio is less dependent on the angle, and therefore, thiorphan molecules are oriented more randomly.

The different dependency of angle resolved XPS spectra on otherwise both nonpolar (10 $\bar{1}$ 0) and (11 $\bar{2}$ 0) ZnO surfaces is most likely due to the different magnitude of the lateral dipole that is obvious from the different surface atomic structure in Figure 2. The stronger the lateral dipole, the more effective the alignment of thiorphan dipole along it would be, and thus the more effective the orientation of thiorphan in the layers. As shown already on polar surfaces in Figure 4, it is not only the

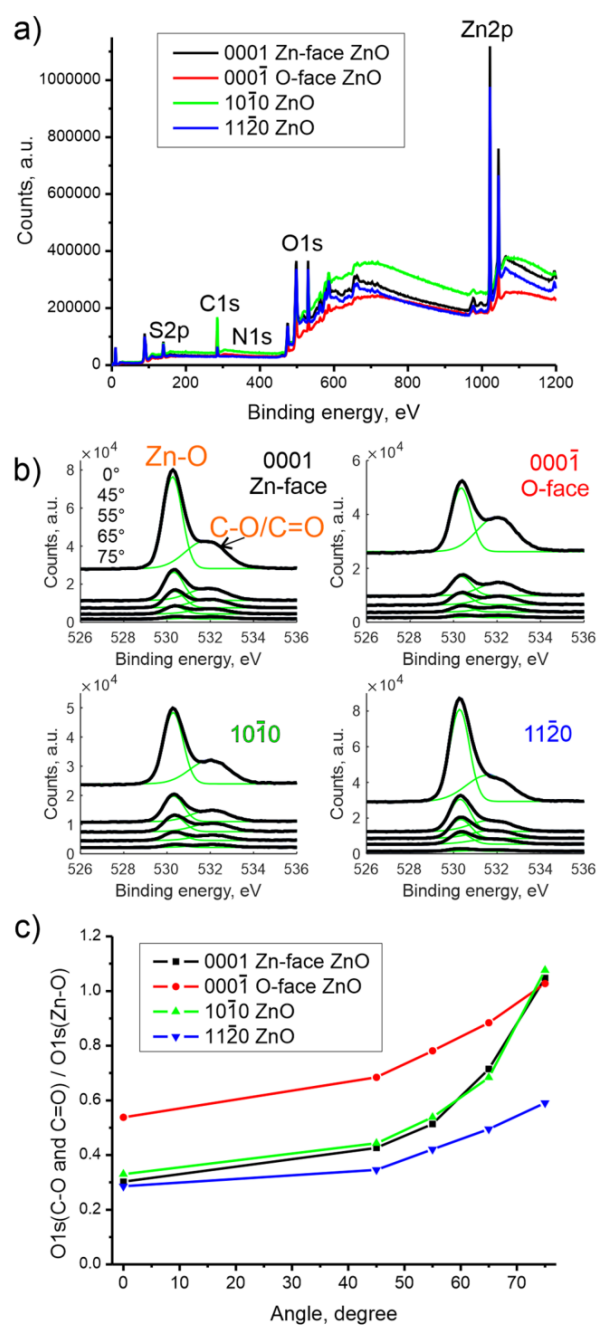


Figure 5. (a) Wide XPS spectra at 0° angle, obtained on Zn-face, O-face, (10 $\bar{1}$ 0) and (11 $\bar{2}$ 0) ZnO facets after 48 h thiorphan adsorption. (b) Twenty high resolution spectra of the O 1s region with corresponding deconvolution of all peaks. (c) The ratio values between intensities of C–O/C=O and Zn–O peaks for all 4 facets and 5 different angles.

orientation of the dipole (up or down) but also its magnitude that control the thiorphan adsorption.

XPS was also used to elucidate formation of covalent bond between the ZnO surface and thiorphan. Based on DFTB simulations, one can expect the formation of Zn–S and Zn–O bonds (Figure 2) but not the formation of Zn–N, Zn–C bonds or any bond between the O atom from ZnO and the thiorphan molecule. Confirmation of the presence of thiorphan

can be done, for example, by observation of C–S and C–N–C bonds. These expectations are analyzed in the following. The position of the expected thiolate (Zn–S) bond in S $2p_{1/2}$ region is 162 eV.⁴³ The position of the expected thiol (C–S–H) bond in thiorphan in the S $2p_{1/2}$ region is 164 eV.⁴⁴ Thus, one can expect to observe two peaks in the S $2p_{1/2}$ region. Deconvoluted spectra in the S $2p_{1/2}$ region are shown in Figure S8. In spite of low signal intensities, two broad peaks at ~159 eV and at ~169 eV were indeed identified. The peak at ~159 eV is probably related to Zn–S bonds between the ZnO substrate and thiorphan molecules, while the peak at ~169 eV is probably related to C–S bonds in thiorphan. We are aware of the fact that the shift from expected 162 eV to ~159 eV and broadening of this peak may be due to a reason other than the formation of a covalent bond between thiorphan molecules and ZnO. However, since we do not expect any other covalent bond, we think that the presence of the broad peak at ~159 eV may indicate the presence of Zn–S covalent bonds between ZnO and thiorphan on all 4 samples. A Zn–S bond should be present also in the Zn $2p_{3/2}$ peak. Unfortunately, the position of the expected Zn–S bond between ZnO and thiorphan in the Zn $2p_{3/2}$ region is the same as the position of the expected Zn–O bond (1022 eV); thus, it is not possible to reliably corroborate the presence of the Zn–S bond in the Zn $2p_{3/2}$ region.

In the N 1s region, the Zn–N signal is expected to be at 395 eV⁴⁵ and the C–N–C signal from thiorphan is expected to be at ~400 eV.⁴⁶ Deconvoluted spectra, presented in Figure S9, show a weak peak at ~400 eV, proving the presence of thiorphan molecules. The presence of Zn–N bonds was not detected by XPS in the N 1s region. A possible Zn–N peak and expected Zn–O peak have similar binding energies in the Zn $2p_{3/2}$ region⁴⁷ (1020.3 and 1022.7 eV respectively); therefore, for analysis, it was assumed that the Zn–N shoulder peak has a 2.4 eV smaller binding energy than the strong Zn–O peak does. The shoulder peak, if present, have negligible intensity, as shown in deconvoluted spectra in Figure S10, so Zn–N bonds were also not detected by XPS in Zn $2p_{3/2}$ region. The missing Zn–N bond is in agreement with DFTB results (Figure 2).

Interestingly, during XPS measurements, a higher charging was observed on polar ZnO samples compared to nonpolar ZnO samples. This indicates higher conductivity of layered thiorphan nanoislands compared to nanodots on ZnO.

2.6. Discussion. In this work, we demonstrated how surface dipoles (and induced electric field) with different directions and magnitudes can affect the adsorption of thiorphan molecules on ZnO surfaces and cause the formation of nanodots or nanoislands. A similar kind of effect has been induced by a magnetic field with poles oriented either parallel or perpendicular to the substrate surface, which causes patterning of microcrystalline/amorphous silicon growth by influencing gas molecular precursors during the chemical vapor deposition process.⁴⁸ As the DLS measurements (Figure S16) prove the absence of thiorphan aggregates in ethanol solution, the vicinity of the surface is a major reason for thiorphan aggregation. A similar effect was observed earlier for lysozyme molecules.⁴⁹

On the Zn-face surface, as shown in Figure 1d, the presence of surface dipoles pointing up creates an electric field with electric field lines pointing up. In the FFMD simulations in Figure 4b and e, it corresponds to the weakest field intensity. Accordingly, only few thiorphan molecules from a close surface

vicinity (0–1.74 nm) tend to adsorb on the C-top surface which mimics the polarity of the Zn-face ZnO surface. Therefore, the coverage of thiorphan molecules in FFMD simulations is low and scattered on this surface (50% of the molecules adsorbed individually). This is in agreement with the formation of small nanodots (<4 nm) observed on the Zn-face ZnO facet by AFM experiments in Figure 1. Such nucleation of small nanodots on Zn-face ZnO facet can be described by the Volmer–Weber growth model.

On the other hand, on the O-face surface in Figure 1d, the presence of surface dipoles pointing down creates an electric field with electric field lines pointing down. In the FFMD simulations in Figure 4c and e, it corresponds to the strongest field intensity. Accordingly, a larger amount of thiorphan molecules from a farther distance (0–3.08 nm) tends to adsorb on the O-top surface which represents the O-face ZnO surface. Therefore, the coverage of thiorphan molecules in FFMD simulations is high and most of the molecules adsorb in the form of large aggregations. These observations from simulations correlate well with the AFM experiments in Figure 1 in which large nanodots (~25 nm) are observed on the O-face ZnO facet after 48 h deposition. The formation of such large nanodots on the O-face ZnO facet can be described by the Volmer–Weber growth model, too.

On the nonpolar surfaces, as shown in Figure 1d, the presence of horizontally oriented surface dipoles creates an electric field with electric field lines aligned horizontally. In the FFMD simulations in Figure 4d and e, it still corresponds to a decaying electrical field in the perpendicular direction from the surface with an intensity that is between the upward and downward oriented dipoles. Therefore, the coverage of thiorphan molecules is relatively high in FFMD simulations on the horizontal C=O dipoles surface which mimics the polarity of ZnO nonpolar surfaces. It is also noteworthy that more molecules tend to adsorb individually (30%) on the horizontal C=O dipoles surface, compared to the O-top surface (10%). Opposite to aggregation, the individually adsorbed molecules can join each other to form layers. The laterally oriented electric dipole can thus explain the formation of the first 4 nm thick layer and subsequent formation of larger nanoislands on (10 $\bar{1}$ 0) and (11 $\bar{2}$ 0) ZnO facets as observed by AFM in Figure 1. Although at the moment we do not have a specific explanation for why subsequent thiorphan layers are formed and why they have the same thickness as the first layer. The process on nonpolar ZnO facets can be generally described by the Frank–van der Merwe growth model.

Figure 1a shows the O-face ZnO surface after 10 min of thiorphan adsorption. Note that in a few places on O-face ZnO we observed also some nanodots or nanoislands (e.g., as shown in Figure S3b) after 10 min adsorption. We attribute it to some local contamination on the O-face ZnO surface (as possible atomic defects or hydroxylation would be present everywhere on the surface). We performed a 3 h long adsorption on the O-face ZnO surface and observed densely packed small nanodots with heights of 2–7 nm. Thus, the process of thiorphan adsorption on the O-face ZnO surface takes a longer time than it does on the other surfaces. The reason could be the absence of covalent bonding between thiorphan and the O-face ZnO surface (Figure 2b).

The inability of the AFM tip even with a high load (2400 nN) to penetrate and completely remove thiorphan nanoislands and large nanodots shows that the thiorphan structures are quite rigid (Figure S3). This may indicate strong

intermolecular interactions between the molecules within the nanoislands and large nanodots. Based on DLS measurements (Figure S16), thiorphan molecules do not aggregate in solution; however, according to MD simulations, the bigger aggregations and clusters of thiorphan molecules have been observed on the O-face ZnO surface compared to the other surfaces. Thus, even in spite of the absence of covalent bonds between thiorphan molecules and O-face ZnO (Figure 2b), mutual interactions of molecules are stronger on this surface compared to other surfaces, leading to the formation of large nanodots and to the inability of the AFM tip to remove nanoislands and large nanodots from O-face ZnO (Figure S3b and f). On the other hand, the formation of covalent bonds between thiorphan molecules and Zn-face ZnO surface (Figure 2a) together with the formation of only small nanodots (Figure 1a) and weak aggregation (Figure 4b) does not create sufficiently strong interactions and allow the AFM tip to remove small nanodots (Figure S3e).

The orientation of the electric field on nonpolar surfaces, which is lateral, applies lateral forces to the molecules (see the dipole direction in Figure 4d) and thus can spread the molecules more uniformly on the nonpolar surfaces. This can aid the formation of more uniform layers all over the surface compared to the nanodots on the polar surfaces with vertical dipoles (see the dipole directions in Figure 4b and c). Moreover, simulations show that a large amount of molecules are adsorbed on the surface individually, not as aggregates. These individually placed molecules can then more easily merge to form layers.

Figure S2 shows that the thickness of each layer within nanoislands is 3.4–3.6 nm. Therefore, the thiorphan layer can be considered as a new example of an ultrathin nanostructured nanomaterial⁵⁰ and thus open a new field of research for such molecular materials.

3. EXPERIMENTAL SECTION

3.1. Sample Preparation. ZnO substrates were polar Zn-face single-side polished (0001), polar O-face single-side polished (0001), and nonpolar (1010) and nonpolar (1120) monocrystalline $5 \times 5 \times 0.5$ mm³ plates from MSE supplies, USA (C plane $\langle 0001 \rangle \pm 0.5^\circ$, 99.99% purity, lattice parameters $a = 3.252$ Å, $c = 5.313$ Å).

Thiorphan (Alchemica s.r.o.) was dissolved in ethanol to a concentration of 1 mg/mL. Each sample was placed into an eppendorf tube cover, placed upside-down. Then 200 μ L of thiorphan in ethanol solution was added to each cover, and the eppendorf tube was closed. After 10 min or after 48 h deposition, the ZnO samples were rinsed with ethanol and DI water and dried with nitrogen.

3.2. AFM Measurements. To analyze the surface morphology of the adhered thiorphan molecules, we performed topography measurements by AFM. The topography measurements were performed on an ICON atomic force microscope (Bruker) in PFQNM mode using untreated Multi75Al cantilevers (BudgetSensors). Topography measurements were performed with the following parameters: scan size 1×1 μ m², image resolution 1024×1024 px², scanning speed 0.1 Hz, gain 1.5, $dz = 20$ nm, Z-scale = 1 μ m, force threshold = 1 nN and scan size 10×10 μ m², image resolution 2048×2048 px², scanning speed 0.1 Hz, gain 10, $dz = 20$ nm, Z-scale = 2 μ m, force threshold = 1 nN. Results were analyzed using Gwyddion software.⁵¹

3.3. DLS Measurements. DLS measurements were performed using 1 mL of 1 mg/mL thiorphan (refractive index = 1.593) in ethanol solution (refractive index = 1.3614), filled into a narrow cuvette on a Zetasizer Nano ZS instrument (Malvern).

3.4. XPS Measurements. XPS measurements were performed by using an Axis Supra spectrometer (Kratos Analytical) equipped with a monochromatic Al K α X-ray source (power 225 W). For the standard electron emission angle of 0° (perpendicular to the surface), spectra

were collected from an area of 700×300 μ m². The base pressure during analyses was 2×10^{-8} Torr. Survey spectra were collected using an analyzer pass energy of 80 eV, and high resolution spectra of individual peaks were collected using a pass energy of 20 eV. Samples were fixed on Cu conductive tape, and spectra were acquired without using a charge neutralization system; however, due to the lower conductivity of the samples, a small shift of spectra (approximately 0.5 eV) toward higher binding energies has been observed. Therefore, this shift was compensated during data processing, by setting the main C 1s component (C–C bonds) to an energy of 284.8 eV.

3.5. DFTB Simulations. DFTB simulations, a fast and efficient quantum mechanical simulation method, have been carried out for 4 structures: single thiorphan molecule over four ZnO surfaces. A self-consistent tight-binding model based on the Slater–Koster model using the *znorg-0-1* parameter set, which has been built for simulations on Zn bulk, ZnO bulk, ZnO surfaces, and ZnO interactions with organic molecules,⁵² has been implemented. The ZnO surfaces have been prepared by cleaving the ZnO bulk in four orientations of interest with the settings that ensure the slabs can host thiorphan molecules with no interaction between adjacent slabs and between the surfaces at the top and bottom of the slab. The polar surfaces were cleaved by surface lattice definition vectors of 4 and 6 times in the A and B directions, respectively, resulting in a slab of $13.1 \times 17 \times 40$ Å³. The nonpolar surfaces were cleaved by surface lattice definition vectors of 3 times in both directions, providing a slab of $9.8 \times 16 \times 40$ Å³. The surfaces and the molecules were allowed to relax to the minimum energy separately before running the final optimization process for molecule-on-surface systems. The relaxation process was relatively straightforward for two nonpolar surfaces, comprising cleaving the bulk in defined directions and allowing the surfaces to relax. In contrast, doing the same process for polar surfaces would culminate in instability due to the establishment of an internal dipole moment. Even though ZnO polar surfaces appear unstable and thus theoretically unfeasible, they have been proved to exist and their stability has been subject to many studies.⁵³ Several explanations have been proposed for their stability, such as surface vacancies and surface functional groups.³⁸ This study used surface zinc and oxygen vacancies offered in ref 39 to cancel the internal dipole and stabilize ZnO polar surfaces for further simulations. The molecules were then adjusted on the surfaces and the whole structures were allowed to relax to the stable configurations with criteria of force tolerance of 0.01 eV/Å and stress error tolerance of 0.001 eV/Å³. The following boundary conditions have been considered in the simulations: periodic in A and B directions, Neumann under the slab, and Dirichlet above the slab.

3.6. Classical Force Field Molecular Dynamics Simulations. NPT molecular dynamics simulations were used in this study to investigate the effects of surface polarity on adsorption of thiorphan molecules on different ZnO surfaces. Similar to our recent publications,^{27,28} the ReaxFF empirical force field method was used for optimizing the systems to the lowest energy (0.05 eV/Ang) prior to molecular dynamics simulations. The same force field was employed to describe the interactions between atoms in all molecular dynamics simulations too. Reliability of ReaxFF potential for describing interactions between ZnO surfaces with biomolecules has been shown in multiple research such as ref.⁵⁴

To investigate the polarity effects, we used well-known C=O dipoles to mimic the ZnO polar and nonpolar surface polarity. Dipole surfaces were constructed with 324 C=O dipoles with the same orientation, fixed next to each other with 0.5 nm distance in a $9 \times 9 \times 9$ nm³ cell. The orientation of the C=O dipoles was changed to mimic the ZnO polar and nonpolar surface dipoles. C=O dipoles with the carbon atoms at the top and C=O dipoles with the oxygen atoms at the top represent the ZnO polar (0001) and (0001) surfaces, respectively. Ten layers of 20 randomly distributed thiorphan molecules then were exposed to the three dipole surfaces in a layer-by-layer process. Enough time was given to each layer to develop changes upon each dipole surface. We found 1–2 million steps with 0.1–0.5 fs settings as optimal for the molecular dynamics simulations. A shorter time did not cover the complete development of the

systems, while a longer one did not show any further useful changes. The adsorbed thiorphan molecules then were fixed, and the remaining floating molecules in the solution were removed from the system prior to doing the same process for the next layer.

We also did multilayer simulations for three C=O dipole surfaces to study the effects of layer distance on the adsorption of thiorphan molecules. The same above-mentioned dipole surfaces were used in a $9 \times 9 \times 15 \text{ nm}^3$ cell along with 6 layers of 20 randomly distributed thiorphan molecules (120 molecules) in 6 layers with distances between 1 and 6 nm. The simulation settings are the same as mentioned in the former paragraph. All the molecular dynamics simulations in this work were done with periodic boundary conditions and at ambient conditions.

4. CONCLUSIONS

The adsorption of thiorphan, a small bioactive molecule, on various ZnO surfaces with different surface polarities was studied experimentally by AFM and theoretically by DFTB and classical MD. AFM high resolution topography measurements and the contact mode nanoshaving method were employed to study the morphology and adhesion strength of thiorphan on four low-index ZnO surface facets. Experiments show that polar surfaces cause the formation of thiorphan nanodots while size of nanodots depends on the direction of the dipole moment. Small (4 nm) nanodots are formed on the Zn-face ZnO facet, whereas large (25 nm) nanodots are formed on the O-face ZnO facet. Nonpolar surfaces cause the formation of layered nanoislands, which later merge into complete layers with characteristic 4 nm thickness. Nanoshaving AFM experiments in contact mode with a rather high load (2400 nN) were not able to penetrate thiorphan layers, and thus, they assemble into rigid ultrathin layers.

Covalent bonding of individual thiorphan molecules to all ZnO facets, except the O-face ZnO, was theoretically observed by DFTB. FFMD was also carried out for the C-top dipole (mimicking Zn-face ZnO), O-top dipole (mimicking O-face ZnO), and horizontally oriented C=O dipole (mimicking nonpolar ZnO facets) to study the physics behind the thiorphan–ZnO interactions. FFMD explains experimentally observed results solely by impact of the surface dipoles orientation and electric field magnitude. The characteristic distance, at which the thiorphan molecule has a 50% chance to adhere, is the lowest (1.74 nm) for the C-top dipole layer, mimicking the Zn-face ZnO facet (i.e., the surface with upright dipole and minimal thiorphan coverage) and is the highest (3.08 nm) for the O-top dipole layer, mimicking the O-face ZnO facet (i.e., the surface with downward dipole and maximum thiorphan coverage).

The XPS data corroborated the AFM experiments and MD simulations. Angle resolved XPS measurements showed a specific angle dependence of XPS peak intensities from thiorphan molecules adsorbed on ZnO surfaces, which evidenced the ordering of thiorphan molecules within the layers, and the possible presence of covalent bonds between ZnO and thiorphan molecules.

According to the results of this work, different ZnO surfaces can be good candidates for different applications based on the desired purpose. For instance, the O-face ZnO surface can be the most useful for biosensing, biointerfaces, or drug delivery when the purpose is maximizing the amount of engaged molecules but without affecting the chemistry of the sensor surface and the structure of the molecule. On the other hand, the (1010) ZnO surface may be the best choice when oriented molecules with oriented dipoles and maximum chemical

interactions with the sensor surface are necessary to enhance the sensor response.

The controlled self-assembly of thiorphan molecules by ZnO surface dipole orientation and magnitude can be a rather general effect applicable also for other molecules and surfaces. Moreover, the well-defined self-limited nanometer thicknesses of the observed dense molecular layers can be considered as an example of the formation of novel ultrathin nanostructured two-dimensional (2D) molecular nanomaterials. Thereby, the present study can open a new field of research for such materials.

■ ASSOCIATED CONTENT

Supporting Information

The Supporting Information is available free of charge at <https://pubs.acs.org/doi/10.1021/acs.langmuir.2c02393>.

3D visualization of AFM morphology of thiorphan nanodots and nanoislands; dipole moment of individual thiorphan molecule; AFM morphology of thiorphan layers after 10 min and 48 h adsorption; results of nanoshaving experiments; rotatable 3D objects of final stage of FF simulations; final stages of adsorption process on C-top, O-top, and horizontally oriented C=O dipole arrays; results of DLS measurements; deconvoluted O 1s, S 2p, N 1s, and Zn 2p angle resolved XPS spectra (DOCX)

■ AUTHOR INFORMATION

Corresponding Author

Egor Ukraintsev – Faculty of Electrical Engineering, Czech Technical University in Prague, Prague 6 166 27, Czech Republic; orcid.org/0000-0002-9768-5119; Phone: +420 773 453 637; Email: ukraiego@fel.cvut.cz

Authors

Hadi Hematian – Faculty of Electrical Engineering, Czech Technical University in Prague, Prague 6 166 27, Czech Republic

Bohuslav Rezek – Faculty of Electrical Engineering, Czech Technical University in Prague, Prague 6 166 27, Czech Republic; orcid.org/0000-0002-0378-4598

Complete contact information is available at: <https://pubs.acs.org/10.1021/acs.langmuir.2c02393>

Author Contributions

[†]E.U. and H.H. contributed equally. This manuscript was written with contributions from all authors. All authors have given approval to the final version of the manuscript.

Funding

This research was supported by the MEYS project “Centre of Advanced Applied Sciences” CZ.02.1.01/0.0/0.0/16_019/0000778 and student’s CTU project SGS21/158/OHK4/3T/13. We acknowledge the use of CzechNanoLab Research Infrastructure supported by MEYS CR (LM2018110).

Notes

The authors declare no competing financial interest.

■ ACKNOWLEDGMENTS

We acknowledge Rayisa Yatskiv for kindly providing DLS measurements. We acknowledge Josef Polčák (CEITEC, Czech Republic) for XPS measurements.

■ ABBREVIATIONS

AAs, amino acids; AFM, atomic force microscopy; BSA, bovine serum albumin; DFT, density functional theory; DFTB, density functional tight binding; FFMD, force field molecular dynamics simulations; MD, molecular dynamics simulations; NEP, neutral endopeptidase; NPs, nanoparticles; XPS, X-ray photoelectron spectroscopy

■ REFERENCES

- (1) Roques, B. P.; Fournié-Zaluski, M. C.; Soroca, E.; Lecomte, J. M.; Malfroy, B.; Llorens, C.; Schwartz, J. C. The Enkephalinase Inhibitor Thiorphan Shows Antinociceptive Activity in Mice. *Nature* **1980**, *288* (5788), 286–288.
- (2) Tejedor-Real, P.; Mico, J. A.; Maldonado, R.; Roques, B. P.; Gibert-Rahola, J. Implication of Endogenous Opioid System in the Learned Helplessness Model of Depression. *Pharmacol., Biochem. Behav.* **1995**, *52* (1), 145–152.
- (3) Nam, H.; Chandra, R.; Francis, T. C.; Dias, C.; Cheer, J. F.; Lobo, M. K. Reduced Nucleus Accumbens Enkephalins Underlie Vulnerability to Social Defeat Stress. *Neuropsychopharmacol. Off. Publ. Am. Coll. Neuropsychopharmacol.* **2019**, *44* (11), 1876–1885.
- (4) Jia, M.-R.; Wei, T.; Xu, W.-F. The Analgesic Activity of Bestatin as a Potent APN Inhibitor. *Front. Neurosci.* **2010**, *4*, 50.
- (5) Yang, X.; Rojanasakul, Y.; Wang, L.; Ma, J. Y. C.; Ma, J. K. H. Enzymatic Degradation of Luteinizing Hormone Releasing Hormone (LHRH)/[D-Ala⁶]-LHRH in Lung Pneumocytes. *Pharm. Res.* **1998**, *15* (9), 1480–1484.
- (6) Trapani, A. J.; Smits, G. J.; McGraw, D. E.; Spear, K. L.; Koepke, J. P.; Olins, G. M.; Blaine, E. H. Thiorphan, an Inhibitor of Endopeptidase 24.11, Potentiates the Natriuretic Activity of Atrial Natriuretic Peptide. *J. Cardiovasc. Pharmacol.* **1989**, *14* (3), 419–424.
- (7) Reche, I.; Ruiz-Gayo, M.; Fuentes, J. A. Inhibition of Opioid-Degrading Enzymes Potentiates Δ^9 -Tetrahydrocannabinol-Induced Antinociception in Mice. *Neuropharmacology* **1998**, *37* (2), 215–222.
- (8) Amantini, C.; Mosca, M.; Lucciarini, R.; Perfumi, M. C.; Santoni, G. Thiorphan-Induced Survival and Proliferation of Rat Thymocytes by Activation of Akt/Survivin Pathway and Inhibition of Caspase-3 Activity. *J. Pharmacol. Exp. Ther.* **2008**, *327* (1), 215–225.
- (9) Eriksson, U.; Hassel, J.; Lüllau, E.; Häggström, L. Metalloproteinase Activity Is the Sole Factor Responsible for the Growth-Promoting Effect of Conditioned Medium in Trichoplusia Ni Insect Cell Cultures. *J. Biotechnol.* **2005**, *119* (1), 76–86.
- (10) Tiraboschi, G.; Jullian, N.; Thery, V.; Antonczak, S.; Fournie-Zaluski, M.-C.; Roques, B. P. A Three-Dimensional Construction of the Active Site (Region 507–749) of Human Neutral Endopeptidase (EC.3.4.24.11). *Protein Eng. Des. Sel.* **1999**, *12* (2), 141–149.
- (11) Puerta, D. T.; Lewis, J. A.; Cohen, S. M. New Beginnings for Matrix Metalloproteinase Inhibitors: Identification of High-Affinity Zinc-Binding Groups. *J. Am. Chem. Soc.* **2004**, *126* (27), 8388–8389.
- (12) Tu, G.; Xu, W.; Huang, H.; Li, S. Progress in the Development of Matrix Metalloproteinase Inhibitors. *Curr. Med. Chem.* **2008**, *15* (14), 1388–1395.
- (13) Zipfel, P.; Rochais, C.; Baranger, K.; Rivera, S.; Dallemagne, P. Matrix Metalloproteinases as New Targets in Alzheimer's Disease: Opportunities and Challenges. *J. Med. Chem.* **2020**, *63* (19), 10705–10725.
- (14) Rasmussen, J. W.; Martinez, E.; Louka, P.; Wingett, D. G. Zinc Oxide Nanoparticles for Selective Destruction of Tumor Cells and Potential for Drug Delivery Applications. *Expert Opin. Drug Delivery* **2010**, *7* (9), 1063–1077.
- (15) Xia, T.; Kovoichich, M.; Liong, M.; Mädler, L.; Gilbert, B.; Shi, H.; Yeh, J. I.; Zink, J. I.; Nel, A. E. Comparison of the Mechanism of Toxicity of Zinc Oxide and Cerium Oxide Nanoparticles Based on Dissolution and Oxidative Stress Properties. *ACS Nano* **2008**, *2* (10), 2121–2134.
- (16) Li, Y.; Zhang, W.; Niu, J.; Chen, Y. Mechanism of Photogenerated Reactive Oxygen Species and Correlation with the Antibacterial Properties of Engineered Metal-Oxide Nanoparticles. *ACS Nano* **2012**, *6* (6), 5164–5173.
- (17) Eixenberger, J. E.; Anders, C. B.; Wada, K.; Reddy, K. M.; Brown, R. J.; Moreno-Ramirez, J.; Weltner, A. E.; Karthik, C.; Tenne, D. A.; Fologea, D.; Wingett, D. G. Defect Engineering of ZnO Nanoparticles for Bioimaging Applications. *ACS Appl. Mater. Interfaces* **2019**, *11* (28), 24933–24944.
- (18) Ma, W.; Du, H.; Zhang, M.; Mori, J.; Ren, X.; Wang, H.; Zhang, X. One-Step Synthesis of Tunable Zinc-Based Nanohybrids as an Ultrasensitive DNA Signal Amplification Platform. *ACS Appl. Mater. Interfaces* **2020**, *12* (2), 2983–2990.
- (19) Martínez-Carmona, M.; Gun'ko, Y.; Vallet-Regí, M. ZnO Nanostructures for Drug Delivery and Theranostic Applications. *Nanomaterials* **2018**, *8* (4), 268.
- (20) Singh, T. A.; Das, J.; Sil, P. C. Zinc Oxide Nanoparticles: A Comprehensive Review on Its Synthesis, Anticancer and Drug Delivery Applications as Well as Health Risks. *Adv. Colloid Interface Sci.* **2020**, *286*, 102317.
- (21) Sahoo, R. K.; Rani, S.; Kumar, V.; Gupta, U. Zinc Oxide Nanoparticles for Bioimaging and Drug Delivery. In *Nanostructured Zinc Oxide*; Elsevier, 2021; pp 483–509. DOI: 10.1016/B978-0-12-818900-9.00021-8.
- (22) Remes, Z.; Artemenko, A.; Ukraintsev, E.; Sharma, D. K.; Buryi, M.; Kromka, A.; Potocky, S.; Szabo, O.; Kulicek, J.; Rezek, B.; Poruba, A.; Micova, J.; Shu Hsu, H. Changes of Morphological, Optical, and Electrical Properties Induced by Hydrogen Plasma on (0001) ZnO Surface. *Phys. Status Solidi A* **2022**, *219*, 2100427.
- (23) Zhang, F.; Chen, X.; Wu, F.; Ji, Y. High Adsorption Capability and Selectivity of ZnO Nanoparticles for Dye Removal. *Colloids Surf. Physicochem. Eng. Asp.* **2016**, *509*, 474–483.
- (24) Elfeky, A. S.; Youssef, H. F.; Elzarez, A. S. Adsorption of Dye from Wastewater onto ZnO Nanoparticles-Loaded Zeolite: Kinetic, Thermodynamic and Isotherm Studies. *Z. Für Phys. Chem.* **2020**, *234* (2), 255–278.
- (25) Elstner, M.; Porezag, D.; Jungnickel, G.; Elsner, J.; Haugk, M.; Frauenheim, Th.; Suhai, S.; Seifert, G. Self-Consistent-Charge Density-Functional Tight-Binding Method for Simulations of Complex Materials Properties. *Phys. Rev. B* **1998**, *58* (11), 7260–7268.
- (26) González, M. A. Force Fields and Molecular Dynamics Simulations. *Éc. Thématique Société Fr. Neutron.* **2011**, *12*, 169–200.
- (27) Hematian, H.; Ukraintsev, E.; Rezek, B. Strong Structural and Electronic Binding of Bovine Serum Albumin to ZnO via Specific Amino Acid Residues and Zinc Atoms. *ChemPhysChem* **2022**, DOI: 10.1002/cphc.202100639.
- (28) Rezek, B.; Hematian, H.; Jira, J.; Rutherford, D.; Kuliček, J.; Ukraintsev, E.; Remeš, Z. Microscopic Study of Bovine Serum Albumin Adsorption on Zinc Oxide (0001) Surface. *Phys. Status Solidi A* **2021**, *218* (6), 2000558.
- (29) Grzelczak, M.; Vermant, J.; Furst, E. M.; Liz-Marzán, L. M. Directed Self-Assembly of Nanoparticles. *ACS Nano* **2010**, *4* (7), 3591–3605.
- (30) Tan, S.; Shi, H.; Du, X.; Wang, K.; Xu, H.; Wan, J.; Deng, K.; Zeng, Q.; Liu, Y. Electric Field Controlled Superlubricity of Fullerene-Based Host–Guest Assembly. *Nano Res.* **2022**, DOI: 10.1007/s12274-022-4641-7.
- (31) Xi, Y.; Wolf, C. M.; Pozzo, L. D. Self-Assembly of Donor-Acceptor Conjugated Polymers Induced by Miscible ‘Poor’ Solvents. *Soft Matter* **2019**, *15* (8), 1799–1812.
- (32) Rezek, B.; Ukraintsev, E.; Kromka, A.; Ledinský, M.; Brož, A.; Nosková, L.; Hartmannová, H.; Kalbacova, M. Assembly of Osteoblastic Cell Micro-Arrays on Diamond Guided by Protein Pre-Adsorption. *Diam. Relat. Mater.* **2010**, *19* (2–3), 153–157.
- (33) Kozak, H.; Artemenko, A.; Ukraintsev, E.; Choukourov, A.; Rezek, B.; Kromka, A. Infrared Absorption Spectroscopy of Albumin Binding with Amine-Containing Plasma Polymer Coatings on Nanoporous Diamond Surfaces. *Langmuir* **2019**, *35* (43), 13844–13852.

- (34) Bauer, E. Phänomenologische Theorie Der Kristallabscheidung an Oberflächen. I. *Z. Für Krist.* **1958**, *110* (1–6), 372–394.
- (35) Frank, F. C.; van der Merwe, J. H. One-Dimensional Dislocations. I. Static Theory. *Proc. R. Soc. London Ser. Math. Phys. Sci.* **1949**, *198* (1053), 205–216.
- (36) Wang, H.; Wang, G.; Bao, P.; Shao, Z.; Zhang, X.; Yang, S.; Zhu, W.; Deng, B. Lateral Homoepitaxial Growth of Graphene. *CrystEngComm* **2014**, *16* (13), 2593.
- (37) https://phet.colorado.edu/sims/html/charges-and-fields/latest/charges-and-fields_en.html (accessed 08-09-2022).
- (38) Mora-Fonz, D.; Lazauskas, T.; Farrow, M. R.; Catlow, C. R. A.; Woodley, S. M.; Sokol, A. A. Why Are Polar Surfaces of ZnO Stable? *Chem. Mater.* **2017**, *29* (12), 5306–5320.
- (39) Calzolari, A.; Bazzani, M.; Catellani, A. Dipolar and Charge Transfer Effects on the Atomic Stabilization of ZnO Polar Surfaces. *Surf. Sci.* **2013**, *607*, 181–186.
- (40) Kar, R.; Pal, S. Effect of Solvents Having Different Dielectric Constants on Reactivity: A Conceptual DFT Approach. *Int. J. Quantum Chem.* **2010**, *110* (9), 1642–1647.
- (41) <http://sites.cardiff.ac.uk/Xpsaccess/Reference/Oxygen/> (accessed 18-11-2022).
- (42) Hamers, R. J.; Butler, J. E.; Lasseter, T.; Nichols, B. M.; Russell, J. N.; Tse, K.-Y.; Yang, W. Molecular and Biomolecular Monolayers on Diamond as an Interface to Biology. *Diam. Relat. Mater.* **2005**, *14* (3–7), 661–668.
- (43) Liu, W.-L.; Chen, W.-J.; Hsieh, S.-H.; Yu, J.-H. Growth Behavior of Nanocrystalline ZnS Thin Films for Solar Cell Using CBD Technique. *Procedia Eng.* **2012**, *36*, 46–53.
- (44) <http://www.xpsfitting.com/2014/04/Organic-Sulphur.Html> (accessed 18-11-2022).
- (45) Haider, M. B. XPS Depth Profile Analysis of Zn₃N₂ Thin Films Grown at Different N₂/Ar Gas Flow Rates by RF Magnetron Sputtering. *Nanoscale Res. Lett.* **2017**, *12* (1), 5.
- (46) Wu, J.; Wang, W.; Wang, Z. Porphin-Based Carbon Dots for “Turn Off-On” Phosphate Sensing and Cell Imaging. *Nanomaterials* **2020**, *10* (2), 326.
- (47) Gangil, S.; Nakamura, A.; Yamamoto, K.; Ohashi, T.; Temmyo, J. Fabrication and EL Emission of ZnO-Based Heterojunction Light-Emitting Devices. *J. Korean Phys. Soc.* **2008**, *53* (1), 212–217.
- (48) Fejfar, A.; Stuchlík, J.; Mates, T.; Ledinský, M.; Honda, S.; Kočka, J. Patterning of Hydrogenated Microcrystalline Silicon Growth by Magnetic Field. *Appl. Phys. Lett.* **2005**, *87* (1), 011901.
- (49) Ukraintsev, E. V.; Kiselev, G. A.; Kudrinskii, A. A.; Lisichkin, G. V.; Yaminskii, I. V. Formation of Lysozyme Fibrils on a Solid Support. *Polym. Sci. Ser. B* **2007**, *49* (1–2), 6–9.
- (50) Tan, C.; Cao, X.; Wu, X.-J.; He, Q.; Yang, J.; Zhang, X.; Chen, J.; Zhao, W.; Han, S.; Nam, G.-H.; Sindoro, M.; Zhang, H. Recent Advances in Ultrathin Two-Dimensional Nanomaterials. *Chem. Rev.* **2017**, *117* (9), 6225–6331.
- (51) <http://gwyddion.net/> (accessed 08-09-2022).
- (52) Moreira, N. H.; Dolgonos, G.; Aradi, B.; da Rosa, A. L.; Frauenheim, T. Toward an Accurate Density-Functional Tight-Binding Description of Zinc-Containing Compounds. *J. Chem. Theory Comput.* **2009**, *5* (3), 605–614.
- (53) Wander, A.; Schedin, F.; Steadman, P.; Norris, A.; McGrath, R.; Turner, T. S.; Thornton, G.; Harrison, N. M. Stability of Polar Oxide Surfaces. *Phys. Rev. Lett.* **2001**, *86* (17), 3811–3814.
- (54) Sengul, M. Y.; Randall, C. A.; van Duin, A. C. T. ReaxFF Molecular Dynamics Study on the Influence of Temperature on Adsorption, Desorption, and Decomposition at the Acetic Acid/Water/ZnO(1010) Interface Enabling Cold Sintering. *ACS Appl. Mater. Interfaces* **2018**, *10* (43), 37717–37724.

NOTE ADDED AFTER ASAP PUBLICATION

This paper was published on January 19, 2023 with an incorrect file type for the Supporting Information. The file was replaced and the article reposted on January 19, 2023.

Recommended by ACS

Time-Dependent Pinning of Nanoblisters Confined by Two-Dimensional Sheets. Part 1: Scaling Law and Hydrostatic Pressure

Chengfu Ma, Jiaru Chu, *et al.*

JANUARY 03, 2023
LANGMUIR

READ 

Heterogeneous Fe-Doped NiCoP–MoO₃ Efficient Electrocatalysts for Overall Water Splitting

Fengye Guo, Qin Zhong, *et al.*

JANUARY 10, 2023
LANGMUIR

READ 

Janus Fabric with Asymmetric Wettability for Switchable Emulsion Separation and Controllable Droplets with Low Friction

Deke Li, Zhiguang Guo, *et al.*

JANUARY 10, 2023
LANGMUIR

READ 

Universal Langmuir and Fractal Analysis of High-Resolution Adsorption Isotherms of Argon and Nitrogen on Macroporous Silica

Trevor C. Brown, Christopher M. Fellows, *et al.*

JANUARY 23, 2023
LANGMUIR

READ 

Get More Suggestions >

Peculiarities Related to Er Doping of ZnO Nanorods Simultaneously Grown as Particles and Vertically Arranged Arrays

Maksym Buryi,* Zdeněk Remeš, František Hájek, Karla Kuldová, Vladimír Babin, Kateřina Děcká, Hadi Hematian, Lucie Landová, Neda Neykova, Eva Horynová, and Bohuslav Rezek

Cite This: *J. Phys. Chem. C* 2023, 127, 22177–22189

Read Online

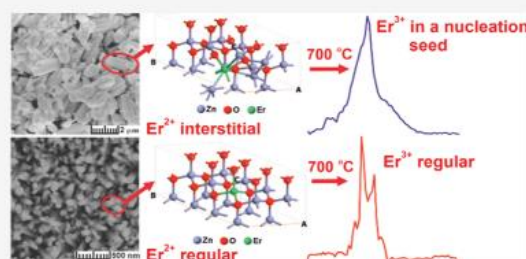
ACCESS |

Metrics & More

Article Recommendations

Supporting Information

ABSTRACT: A unique set of undoped and Er-doped ZnO nanorods that are grown by a hydrothermal method under exactly the same conditions in the form of 2D nanoarrays on the SiO₂/ZnO substrate or in a free-standing form on random nucleation seeds in solution were investigated. Their optoelectronic properties are characterized by photo-, radio-, and cathodoluminescence in correlation with scanning electron microscopy, energy-dispersive X-ray spectroscopy, electron paramagnetic resonance spectroscopy, resonance Raman spectroscopy, and theoretical computing by using density functional theory. We demonstrate that erbium is incorporated at a regular zinc site in the 2D arrays and as additional nucleation seeds in the free-standing nanorods. The deposited nanorods contain a larger number of shallow donors (by about 2 orders of magnitude) and a larger number of free carriers (by about 1 order of magnitude) as compared to the free-standing ones. It is related to the fact that the nanorods grow about 1 order of magnitude larger and in polycrystalline bunches on the random seeds in solution compared to the deposited arrays. Doping by Er slows the excitonic emission from 465 to 522 ps.



1. INTRODUCTION

ZnO is a multifunctional material that is applied in various fields of science and industry, and it is especially grown at the micro- and nanoscale. In particular, it is used in photo- and electrocatalysis, sensing, and Li-ion batteries.^{1–6} Moreover, ZnO nanoparticles and ZnO-based nanocomposites are applied in the waste solidification/stabilization.^{7,8} Besides, ZnO nano- and microwires have the potential to be applied in future ultracompact near-infrared electronic and optoelectronic devices or systems.⁹ ZnO-based alloys lead to intrinsic large bandgaps and, as a result, large exciton binding energy (see ref 10 and the references therein). In addition, they can be implemented in photodetectors and, more importantly, nanomedicine,¹¹ e.g., for drug delivery¹² or wound scaffolding.¹³ Moreover, Er-doped ZnO nanoparticles are suitable for the nanocomposite heterostructures' creation, for example, with CdS for upconversion applications.¹⁴ ZnO:Er nanorods find application in optical thermometry,¹⁵ while ZnO:Er nanoparticles covered with polyethylene glycol are suitable for cell imaging.¹⁶ ZnO:Er nanoparticles exhibit antimicrobial activity.¹⁷ Zinc oxide is also known for its scintillating abilities. For example, ZnO:Cu was used in cathodoluminescence screens,¹⁸ while ZnO:Ga is also considered for use in alpha particle scintillation screens.¹⁹ Recently, the nanostructures of ZnO were considered as eligible candidates for the ultrafast scintillating detector in the time-of-flight positron emission tomography.²⁰ They can also be combined with other materials

for this purpose. As an example, the MoS₂(CdS)/ZnO nanocomposite nanowires can be mentioned.^{14,21}

The cheapest ZnO-based nanostructures in most cases are hexagonal (wurtzite)²² free-standing (NRF), hedgehog-like or deposited arrays of nanorods/nanocolumns/nanowires (NRA) grown by the hydrothermal method.^{23–25} The corresponding luminescence spectra are complex, composed of the ultrafast (the decay time is hundreds of picoseconds) exciton (ultraviolet, UV) emission band peaking at about 380 nm^{24,26,27} and red, zinc vacancy-related bands (peaking at about 680 nm).^{25,28} The luminescence, scintillation, and morphology properties can be modified by doping ZnO nanorods with erbium and/or post growth treatments (annealing in air at elevated temperatures, hydrogen or oxygen plasma treatment), as has been demonstrated in the recent works.^{23–25,28,29} Note that Er leads to the improved photovoltaic (charge carrier transport) properties,²⁹ important for the exciton luminescence as well. Plasma hydrogenation as well as annealing in air at 350 °C significantly improves the intensity of the UV band.^{28,29} Oxygen plasma has the opposite

Received: August 13, 2023
Revised: October 8, 2023
Accepted: October 11, 2023
Published: November 1, 2023



effect.^{28,29} The typical Er³⁺ 1.54 μm luminescence becomes visible in the ZnO nanorods only after the annealing in air at 700–800 °C as experimentally found in the previous works.^{25,28}

Density functional theory (DFT) has already been successfully used to study structural, electronic, and optical properties of a wide range of semiconductors.³⁰ However, it suffers from underestimating the bandgap energy of most semiconductor oxides such as zinc oxide. Many theoretical approximation methods, such as DFT + U, are commonly used to solve this problem.³¹ Erbium-doped ZnO systems have also been the subject of limited theoretical studies that employed diverse methods including DFT + U DFT + U.^{32,33} Still, compared to the well-known local-density approximations (LDA) or generalized gradient approximations (GGA), these methods are computationally expensive. Besides, only a few possible scenarios of Er doping have been investigated in these studies.

The incorporation of erbium and its charge state in the ZnO host are still not known, especially taking into account the commonly known variety of ZnO forms. The influence of Er on the absorption properties of ZnO nanopowder is, to the best of our knowledge, not known either. Moreover, there is still a general lack of information about the influence of ZnO morphology and growth rate governed by erbium on the free carrier concentration and luminescence properties of the ZnO structures.

The aim of the present work is thus to combine experimental techniques and DFT calculations to reveal the peculiarities of the erbium incorporation into the ZnO host having the morphology of the nanorods, free-standing and deposited onto a quartz substrate, grown under the same conditions. Moreover, the influence of the nanorod morphology and growth rate on the luminescence and scintillation properties as well as on the free carrier concentration will be disclosed.

The DFT-1/2 method was implemented to comprehensively study the effects of Er doping in different possible sites along with varying kinds of defects on ZnO's electronic and optical properties. DFT-1/2 is based on a fast and efficient semiempirical approach to correcting the self-interaction error in local and semilocal exchange–correlation density functionals for extended systems, similar in spirit to the DFT + U method.³⁴

Considering the variety of applications where erbium doping of ZnO nanoparticles is used, the above-mentioned points must be clarified to gain the improvement and optimization of ZnO structures and to push them to the theoretically predicted limits.

2. EXPERIMENTAL SECTION

2.1. Preparation of Deposited and Free-Standing ZnO:Er Nanorods. First, thin films of ZnO were deposited on a commercially available 1 in. fused silica glass substrate by pulsed laser deposition (PLD). The substrate was placed into a holder heated to 100 °C and rotated at 5 rpm for uniform deposition of the layer through the whole sample. After the chamber was pumped and reached a pressure of 10–4 Pa, oxygen was introduced with a process pressure of 10 Pa. After that, a KrF ($\lambda = 248$ nm) excimer laser COMPex 50 was used for target ablation. The pulse energy was set to 120 mJ, the number of pulses to 50,000, and the repetition rate to 30 Hz. A cooling step of introducing oxygen with pressure 105 Pa followed after deposition. Thereafter, undoped and Er-doped

ZnO nanorods were grown on the ZnO seeding layers prepared by the PLD method in an aqua solution containing 25 mmol/L hexamethylene tetramine and 25 mmol/L mixture of zinc nitrate hexahydrate and erbium nitrate pentahydrate with the content of erbium source 0 and 1 mol % at 90 °C for 3 h. Subsequently, the substrate was removed from the solution, rinsed with deionized water, and dried with nitrogen. Additionally, the other two samples, undoped and 1 mol % Er doped ZnO, were grown at 90 °C for 30 min from the solution. The reaction mixtures in both cases of growth (3 h and 30 min) were cooled, and free-standing nanorods were isolated, rinsed with deionized water, and dried at 60 °C for 3 h. The grown samples were annealed in air for 15 min at 350 °C for characterization by various techniques mentioned in the sub Section 2.2 below. For electron paramagnetic resonance (EPR) measurements, all the samples were normalized on weight to compare the spectral intensities.

2.2. Experimental Techniques and Calculation Methods. The size and morphology of ZnO NRs has been checked by scanning electron microscopy (SEM) using a MAIA3, TESCAN electron microscope with the in-beam SE detector placed in objective lens and the electron beam energy of 5 keV. X-ray diffraction (XRD) on powder samples was performed using a RigakuMiniFlex 600. XRD patterns were compared with the relevant records in the ICDD PDF-2 database (version 2013). The angular range was 10–80°, with a step of 0.02° and a scanning speed of 2°/min.

Cathodoluminescence (CL) and energy-dispersive X-ray spectroscopy (EDX) measurements were performed on an FEI XL30 ESEM. EDX mapping was carried out with a 30 kV acceleration voltage. A CL home-built setup consists of a single-grating monochromator with a spectral resolution of 10 nm, Hamamatsu H7711-13 photomultiplier tube for CL images, and AvaSpec ULS2048LTEC spectrometer for spectra recording. For the spectra acquisition, the sample area of 23 \times 15 μm was scanned.

The photoluminescence (PL) spectra in the UV–visible range were excited by the 340 nm pulsed UV LED with a narrow bandpass optical filter and recorded with 2 nm spectral resolution using a spectrally calibrated double grating monochromator SPEX 1672, long-pass filters, and a cooled multialkali photomultiplier.

Another part of the photoluminescence data was obtained by LabRAM HR Evolution equipped by a high power (HP) He–Cd excitation laser ($\lambda = 325$ nm), objective 74CG, and with a 2 μm laser spot diameter.

Infrared (IR) PL spectra were measured with 8 nm resolution using spectrally calibrated dispersive monochromator HORIBA H20-IR, N.A. 0.5 fused silica objective, InGaAs photodiode detector, and 980 nm excitation provided by a pulsed laser diode. To have better resolution, some of the IR PL spectra were also measured using a Nicolet iS50 FTIR spectrometer (Thermo Fisher Scientific) equipped with FT-Raman module with the 1064 nm laser and InGaAs photodiode detector.

The radioluminescence (RL) and thermally stimulated luminescence (TSL) were measured using the HORIBA Jobin-Yvon 5000 M spectrometer with a Janis liquid nitrogen cryostat and TBX-04 (IBH) photomultiplier operating in the 200–800 nm spectral range. The spectral resolution of the monochromator was 8 nm. All of the spectra were corrected for experimental distortions caused by the setup. The samples were irradiated with a Seifert X-ray tube operated at 40 kV

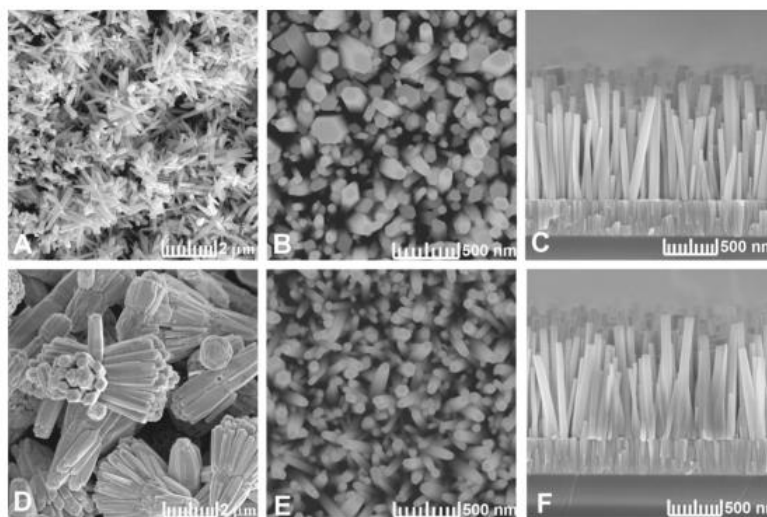


Figure 1. SEM images of the free-standing undoped ZnO (A) and ZnO:Er(1%) (D) nano- and microrods grown separately with the growth time 30 min and undoped ZnO (B (top view),C (side view)) and ZnO:Er(1%) (E (top view),F (side view)) nanorods deposited on a quartz substrate.

with a tungsten target. The RL spectra were measured at 300 and 77 K.

Ultrafast decays under pulsing X-ray excitation were measured using a picosecond (ps) X-ray tube N5084 (Hamamatsu, 40 kV). The X-ray tube is driven by a picosecond light pulser equipped with a laser diode with a repetition rate up to 1 MHz. The signal was detected by a hybrid picosecond photon detector and Fluorohub unit (HORIBA Scientific). The setup instrumental response function, fwhm, is about 76 ps. The spectrally unresolved luminescence decay curves were detected from the surface excited by X-rays.

EPR measurements were performed with a commercial Bruker EMXplus spectrometer in the X-band (9.4 GHz) within the 4–296 K temperature range using an Oxford Instruments ESR900 cryostat. The sensitivity of the EPR spectrometer is 10^{12} spins/G. The EPR intensity was recalculated to 1 mg of a sample.

The surface chemical composition was studied by XPS. For analysis, the powder samples were pressed in pellets and fixed by Cu tape on the sample holder. The spectra were acquired with the Axis Supra XPS electron spectrometer (Kratos Analytical Ltd., UK) equipped with a monochromated Al $K\alpha$ X-ray source (1486.6 eV) and hemispherical energy analyzer. CasaXPS software using the Shirley background was used for processing measured XPS spectra. The Ag $L\alpha$ X-ray source (2984.2 eV) was used.

The annealing in air was done in a quartz tube for 15 min for each set of samples, within the modular vertical tube furnace Tersid Carbolite with the possibility to elevate the temperature up to 1000 °C.

We performed density functional theory calculations to investigate the impacts of doped erbium atoms in the ZnO lattice on atomic and electronic scales. All the structures have been optimized using the DFT method, GGA exchange–correlation, and the PBE functional. Afterward, the structures' electronic and optical properties were calculated using the DFT-1/2 method and the same exchange–correlation and functional. By creation of an atomic self-energy potential that cancels the electron–hole self-interaction energy, the DFT-1/2 technique corrects the DFT self-interaction error. This

potential is determined for atomic sites in the system and is defined as the difference between the neutral atom's potential and a charged ion's potential after removing a fraction of the atom's charge. The sum of these atomic potentials is the overall self-energy potential. The DFT Hamiltonian with added DFT-1/2 self-energy potential has been found to considerably enhance band gaps for various semiconducting and insulating systems.³⁴

We used a supercell of the Wurtzite structure with a total of 32 atoms inside. The supercells were allowed to relax to the minimum energy with periodic boundary conditions and criteria of force tolerance of 0.01 eV/Å and stress error tolerance of 0.001 eV/Å³. All the optimized systems used to perform the calculations can be seen in Figure S1 in [Supporting Information](#). There are one or two erbium atoms in different possible sites in the ZnO structure in each system. In some cases, various possible defects (substitutional and interstitial) have also been introduced into the erbium-doped ZnO system.

3. RESULTS AND DISCUSSION

3.1. Materials Structure and Phase Analyses. The SEM images of the undoped ZnO and ZnO:Er (1%) NRF samples are shown in Figure S2 in the [Supporting Information](#). Each NRF sample demonstrates variation of the rods size, and the samples in general exhibit the tendency to grow larger when Er is doped as it has also been shown earlier.²⁵ In the undoped sample, a single rod width varies within the approximately 200–400 nm range, whereas the length is about 1–2 μm (Figure S2A in [Supporting Information](#)). The ZnO rods doped with 1 at. % of Er are larger, of the microscale, about 0.5–1 μm in circumference and longer than 2 μm (Figure S2B in the [Supporting Information](#)). Besides, there are the structures referred to as “hedge-hog” composed of the microrods²⁵ (indicated by a white circle in Figure S2B in [Supporting Information](#)). These characteristics are known from previous work.²⁵ However, there is another interesting effect: the coalescence of the single microrods into the larger ones, as shown by the arrow in Figure S2B in [Supporting Information](#). This indicates the polycrystalline structure of the single ZnO microrod in the case of the ZnO:Er(1%) NRF sample. To

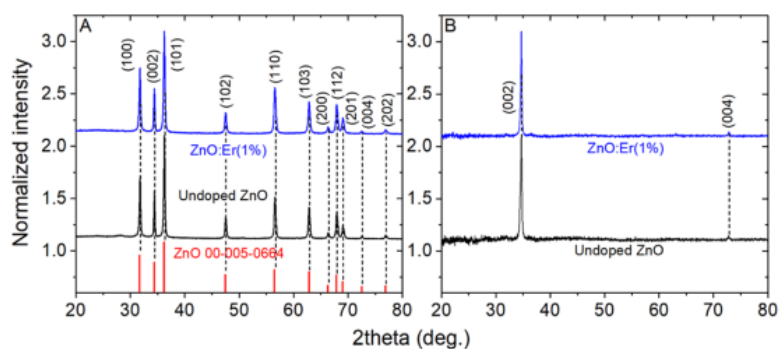


Figure 2. (A) XRD patterns of undoped ZnO and ZnO:Er(1%) NRF prepared by hydrothermal growth. The reflections are designated in accordance with wurtzite ZnO phase (PDF database record 00-005-0664). (B) XRD patterns of the undoped ZnO and ZnO:Er(1%) NRA prepared by hydrothermal growth.

prove this, the free-standing (FS) undoped ZnO and ZnO:Er(1%) samples were grown for 30 min each (typically, for NRA and NRF samples it was 3 h, see [Experimental Section](#) and²⁵). The corresponding SEM images are shown in [Figure 1A,D](#). As one can see, the undoped ZnO FS sample is composed of hexagonal nanorods of about the same size, i.e., 200 nm thick and about 2 μ m long. The situation is completely different in the case of the ZnO:Er(1%) FS sample. There, the structures are mostly composed of groups of rods growing from one nucleation seed ([Figure 1D](#)). All of these led to the conclusion that erbium or erbium-based structures create nucleation seeds for ZnO rod growth, supporting fast growth of the ZnO rods ([Figure 1A,D](#)).

SEM images of the top and side views of the undoped ZnO and ZnO:Er(1%) arrays of nanorods deposited on a quartz substrate (NRA) grown under the same conditions as the NRF ones discussed above are shown in [Figure 1B,C,E,F](#). The rods are hexagonal prisms. The averaged single nanorod size varies within the 20–100 nm in diameter with the length of about 500–800 nm in both samples. Er doping has some effect on the nanorod size—they are, on average, thinner and more or less homogeneous in size in the ZnO:Er(1%) NRA sample as compared to the undoped ZnO NRA.

XRD patterns of the undoped ZnO and ZnO:Er(1%) NRF samples are plotted in [Figure 2A](#). By comparing with the PDF database record #00-005-0664, the samples are single-phase hexagonal Wurtzite ZnO. No traces of other phases were detected.

The lattice parameters and the size of the NRF crystallites were calculated. They are listed in [Table 1](#). The lattice

Table 1. Lattice Parameters of the Undoped ZnO and ZnO:Er (1%) NRF Samples

Sample	<i>a</i> (Å)	<i>c</i> (Å)	size (nm)
ZnO undoped	3.2510 ± 0.0003	5.2080 ± 0.0006	105 ± 35
ZnO:Er(1%)	3.252 ± 0.0005	5.2090 ± 0.0011	64 ± 12

constants listed in [Table 1](#) are approximately the same in both NRF samples. This can likely be explained by the localization of Er mostly outside the ZnO host. This is in good agreement with the erbium nucleation seeds, as stated above. This can be a kind of amorphous phase as previously reported for the ZnO:Er(1%) NRF after plasma hydrogenation.²⁸ This is also consistent with EPR measurements proving Er³⁺ existence in the nonoriented system earlier²⁵ (see also below).

The average crystallite size is about 1.5 times larger in the undoped ZnO NRF as compared to the ZnO:Er (1%) NRF, as can be seen in [Table 1](#). Interestingly, the size of the ZnO rods is much larger than 60–100 nm in the undoped ZnO and ZnO:Er(1%) samples, as can be seen in SEM images shown in [Figures 1A,D](#) and [S2](#) in the [Supporting Information](#). This supports the conclusion about the polycrystalline origin of the NRF rods ([Figure 1A,D](#)) mentioned above. Even undoped ZnO NRF sample is polycrystalline—the nucleation seeds in this case are expected to be the remnants of the not fully dissolved precursors.

According to XRD, the structure of undoped ZnO and ZnO:Er(1%) NRA is hexagonal wurtzite. Based on the observed pattern [the dominating (002) peak in [Figure 2B](#)] the majority of crystallites are oriented along the *c*-axis perpendicular to the substrate. The (002) peak exhibits no shift upon the Er doping level. No stresses in the *c* direction in the undoped ZnO and ZnO:Er(1%) sample can thus be expected. Therefore, the incorporation of Er into the ZnO host in this case is expected to be very small.

3.2. Optical Absorption Properties. Absorbance was measured to study the optical absorption properties and possible defect states in the nanorods structures. The absorbance spectra measured in the NRA samples are shown in [Figure 3A](#).

Besides the absorption edge, the spectra are composed of two broad band contributions. The first one appeared within the 1.9–2.9 eV range (A1 band, observed in undoped ZnO

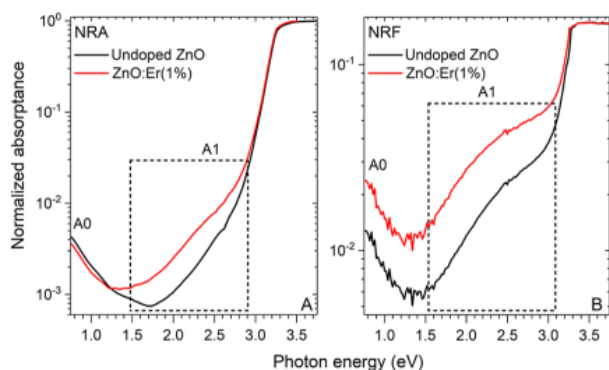


Figure 3. (A) Absorbance spectra of the undoped ZnO and ZnO:Er(1%) NRA; (B) undoped ZnO and ZnO:Er(1%) NRF. A0,1 stress specific bands.

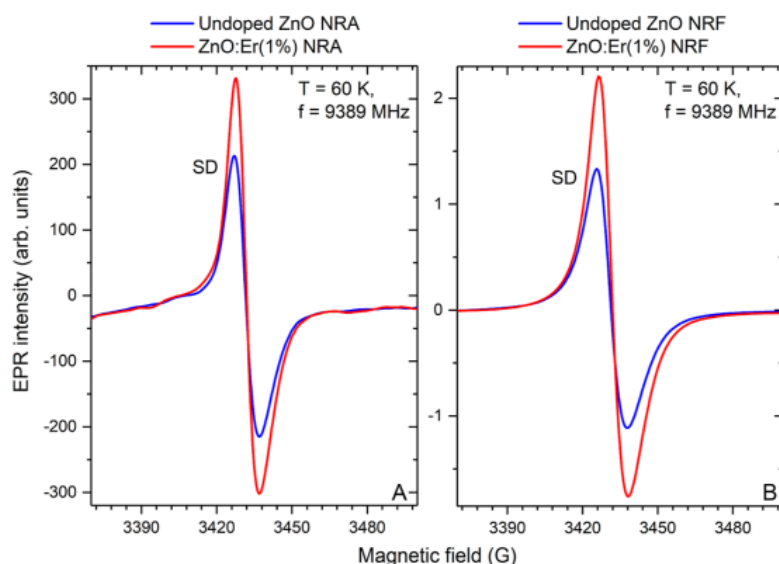


Figure 4. EPR spectra of the shallow donor (SD) signal measured at $T = 60$ K in undoped ZnO and ZnO:Er(1%) NRA (A) and NRF (B) samples.

NRA, see Figure 3A). The A1 band is strongly overlapped with the absorption edge. It is very weak in the undoped ZnO NRA sample. This band is expected to originate from the number of defects, and therefore, erbium is expected to activate defects inside the ZnO host. Some of them can have the same origin in both undoped ZnO and ZnO:Er(1%) NRA samples (e.g., zinc vacancy^{25,28}). The second contribution has a maximum below 0.75 eV (A0 in Figure 3A). It was observed in both undoped and erbium doped NRA as well. The A0 band may originate from the defects as well as free electrons' absorption.³⁵ It is almost unchanged upon Er doping in the ZnO NRA samples (Figure 3A). The same may be suitable for the A0 band in the ZnO NRF samples (Figure 3B). The A1 band is very well visible in the undoped ZnO NRF and has even larger intensity in the ZnO:Er(1%) NRF (Figure 3B). This is the same trend upon Er doping, as discussed for the ZnO NRA samples above. Therefore, indeed, erbium has an influence on the defect states in ZnO. To have a better insight into this problem, the DFT calculations have been made and are shown further below.

3.3. EPR Measurements. The clearest indication of the donor properties of ZnO is the shallow donor (SD) EPR signal as its measurement is straightforward, requiring no wiring, i.e., no losses. It can be seen as the contribution at the g factor $g = 1.954$ in the EPR spectra of the undoped ZnO and ZnO:Er(1%) NRA and NRF shown in Figure 4, respectively. Its origin is $Zn^{+} + D$ ($D = H, Al$ or Ga) center (see, e.g., recent works^{23,25,28,29} and the references therein). It is not excluded that Zn^{+} here could be interstitial (Zn_i).²⁵ The SD signal was increased by about 1.5 times in the ZnO:Er(1%) NRA and NRF compared to the undoped ZnO NRA and NRF (Figure 4). Note that EPR intensity is directly proportional to the concentration of paramagnetic particles.³⁶ Therefore, the raised SD EPR intensity indicates the increased content of shallow donors, i.e., Zn^{+} as the paramagnetic part of the SD.

This also indicates the improvement of the n-type conductivity of the ZnO, i.e., one may expect Er^{3+} to serve as a donor as well. Therefore, erbium presence in both ZnO NRF and NRA hosts can be expected. There is another interesting observation. The intensity of the SD signal in the NRA nanorods is, in general, about 2 orders of magnitude

stronger as compared to the NRF ones. This points to the better conduction properties in the NRA as compared to NRF.

The EPR signal at the g factor ≈ 11.54 (corresponds to the resonance magnetic field 581 G) has been measured only for the ZnO:Er(1%) NRF, as shown in Figure S3 in the Supporting Information. The $g \approx 11.54$ resonance line of ZnO:Er(1%) NRF has the glass-like line shape, as has also been reported in the previous works (see, e.g., refs 37 and 38). It has previously been attributed to Er^{3+} ($4f^{11}$) in the free-standing ZnO:Er microrods.^{25,28} The glass-like shape of the signal is in good agreement with the SEM and XRD findings above; i.e., erbium nucleation seeds should have nonoriented, not regular character in the ZnO NRF. No Er^{3+} signals were detected in the ZnO:Er(1%) NRA.

It is noteworthy that the resonances located in the described spectral region of the Er^{3+} $g \approx 11.54$ (about 580 G, Figure S3 in Supporting Information) have been proven to originate from Er^{2+} in the CeO_2 nanoparticles and other nanomaterials, including ZnSe isostructural with ZnO.^{39–41} Moreover, the assumption about Er^{2+} existence in ZnO has previously been made for the Er doped free-standing ZnO rods.⁴² To check whether, in principle, erbium can be in the Er^{2+} ($4f^{12}$) or Er^{3+} state as well as its possible position in the ZnO samples, DFT calculations were carried out.

EPR intensity is directly proportional to the paramagnetic particle concentration (e.g., Er^{3+} or Er^{2+} , see refs 36 and 39). Therefore, by measuring the Er^{3+} EPR signal of the “glass-shape” in the ZnO:Er(1%) NRF, it was possible to determine real erbium content there as being about $0.4 \pm 0.2\%$, which is in agreement with the previous work.²⁵ However, there was no EPR signals in the ZnO:Er(1%) NRA. Considering the EPR spectrometer sensitivity reaching about 10^{12} spins (see Experimental Section) and the signal-to-noise ratio, practically, the concentration of spins, which could be reliably detected, is about tens of ppm.⁴³ Therefore, one may expect the Er concentration to be lower than that in the NRF sample. Due to the same reason, the Er^{3+} to Er^{2+} concentration ratio cannot be derived in the NRA samples. In the NRF samples, the “glass-like” very broad EPR spectrum does not allow for the separation of contributions of Er^{3+} and Er^{2+} .

3.4. Resonance Raman Measurements. EPR intensity of the shallow donor signal was higher in the NRA as compared with the NRF samples (see Figure 4). To explain this the equilibrium, carrier concentration should be measured. Hall measurements are not possible (the samples are polycrystalline rods), and, therefore, the estimation of free carriers was carried out based on the resonance Raman measurements and the peak shape complex calculation procedure, as described in detail in refs 44–46 (see Figure S4 in Supporting Information). The A1(2LO) Raman peak has been used to avoid the distortion of the peak width by the impurity-broadening contribution. Moreover, the peak is plotted in energy scale divided by a factor of 2 to avoid confusion. The obtained results are listed in Table 2.

Table 2. Parameters for Calculation of the Raman Peak Shapes

sample	n (10^{16} cm^{-3})	Γ (cm^{-1})	γ (cm^{-1})
ZnO:Er(1%) NRF	2	24	500
undoped ZnO NRF	2	24	500
ZnO:Er(1%) NRA	15	12	1000
undoped ZnO NRA	15	12	1000

The obtained parameters were carrier concentration n , phonon damping constant Γ , and plasmon damping constant γ . Other parameters needed for the model were taken from ref 44. It is observed that the NRA samples have higher concentrations of equilibrium free charge carriers. The NRA samples grown on the nucleation layer are densely packed arrays with a surface to volume ratio much larger than in the case of NRF (the single NRA ZnO rod is much smaller than the single NRF ZnO rod, as can be seen in Figure 1). Moreover, the surface of the ZnO NRF rods appears to be etched, more irregular as compared to the ZnO NRA rods, leading to the larger number of defects participating at the charge trapping processes. In addition, this agrees with higher SD EPR intensity in NRA samples as compared to NRF (Figure 4), indicating a larger number of shallow donors there. All these factors influence the charge carrier concentration measured in the NRA and NRF rods.

3.5. DFT Calculations. To understand the optical absorption properties and the creation of defects native for ZnO structures (zinc and oxygen vacancies) as well as erbium incorporation, the crystal structure, band structure, and absorption coefficient spectrum were calculated by using DFT for the 14 different models. The models include the following ZnO structures: (i) defects-free (pristine); (ii) containing only one single Er ion at the regular Zn site (Er_{Zn}); (iii) containing two adjacent Er_{Zn} ions; (iv) containing two Er_{Zn} ions separated by Zn ions; (v) containing a single Er_{Zn} ion neighboring with zinc vacancy (V_{Zn}); (vi) containing a single Er_{Zn} ion separated by the Zn ion from V_{Zn} ; (vii) containing a single Er_{Zn} ion in the close vicinity of an oxygen

vacancy (V_{O}); (viii) containing a single Er_{Zn} ion in the close vicinity of a Zn_i ; (ix) containing a single interstitial erbium ion (Er_i); (x) containing single Er_i next to V_{Zn} ; (xi) containing single Er_i next to V_{O} ; (xii) containing only V_{Zn} ; (xiii) containing only V_{O} ; (xiv) containing both V_{Zn} and V_{O} . They are shown in Figure S1 in the Supporting Information. Comparing these models, one can infer that ZnO preserves its crystalline structure for all erbium-doped systems with substitutional erbium defects [models (i–viii)]. In contrast, the interstitial erbium dopant agitates the ZnO crystal, resulting in an amorphous structure around the doping agent. This is in good agreement with the previous work dedicated to the hydrogen and oxygen plasma treatment of free-standing ZnO:Er nano- and microrods²⁸ where the presence of amorphous phase was detected in the hydrogen plasma treated ZnO:Er(1%) sample. Moreover, this is in good agreement with EPR measurements showing Er^{3+} glass-like spectrum existence (see Figure S3 in the Supporting Information). However, interestingly, as soon as the V_{Zn} appears in the close vicinity to the Er_i [model (x)], the erbium ion moves and fills in the zinc vacancy during the optimization process. The final relaxed system again exhibits a crystalline structure.

Based on the analysis of the band structures calculated for the models (i–xiv), as shown in Figure S1 in the Supporting Information, several important conclusions can be derived: (1) as expected, the Fermi level of the pristine ZnO is situated at 0, i.e., in the middle of the bandgap; (2) erbium-doped systems generally have much more condensed bands, especially valence bands; (3) 4f orbitals of erbium ions are localized close to the Fermi level; the Fermi level appears in the conduction band close to its bottom (Er is a donor contributing to n-type conductivity); (5) V_{Zn} has an opposite effect and pushes the system toward a p-type semiconductor; (6) the other important point is that while zinc vacancy results in the p-type behavior in the band structure, the oxygen vacancy does not cause any n-type behavior, but it is a potential source of compensation in the p-type ZnO.

The valence configuration of an erbium atom is $6s^2 4f^{12}$ with 14 valence electrons. Surprisingly, the Bader charge analysis gives the result of almost 12 valence electrons (see Table 3) in all models (see Figure S1 in the Supporting Information).

This indicates that by incorporation into the ZnO host, an erbium atom provides two electrons to create bonds, becoming Er^{2+} , even when it is interstitial. Therefore, the observed erbium spectrum in Figure S3 in Supporting Information should originate at least partly (tiny amount) from Er^{2+} , as also discussed in Section 3.3 dedicated to EPR measurements.

For all of the models, the absorption spectra were calculated (Figure S1 in Supporting Information). By qualitatively and tentatively (considering only the shape) comparing them with the experimentally obtained absorbance spectra in Figure 3, one may infer that the theoretically predicted model (xii) and models ii–vii, ix, and x are the closest to the experimentally

Table 3. Summary of the Results From Bader Charge Analysis

model	(ii)	(iii)	(iv)	(v)	(vi)	(vii)	(viii)	(ix)	(x)	(xi)	
Erbium ^a ions	Er1	12.00	12.02	12.02	11.59	11.75	12.01	12.04	11.98	12.00	11.98
	Er2		11.97	12.02							

^aNumber of calculated valence electrons after the optimization for erbium atoms in the erbium-doped structures [models (ii–xi)], see also Figure S1 in Supporting Information.

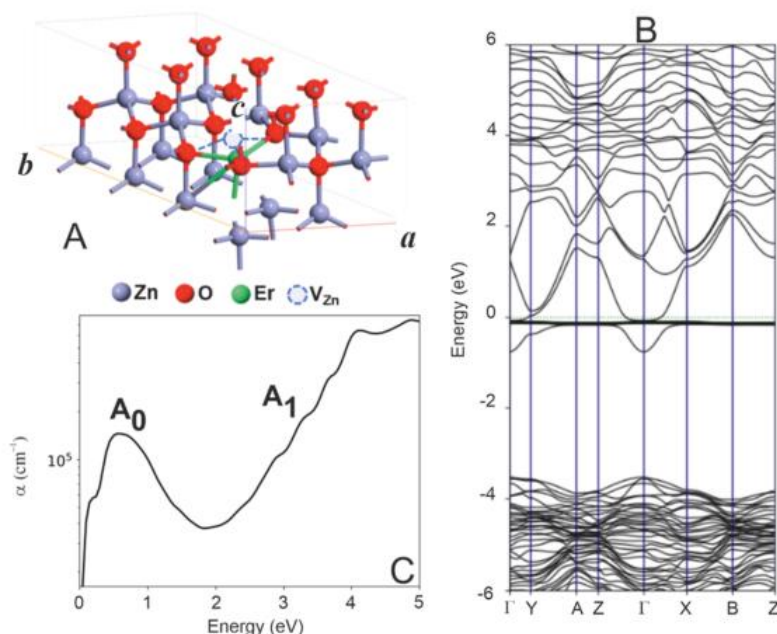


Figure 5. Model (x) of the ZnO structure doped with erbium atoms. Native defect like zinc vacancy was considered. (A) Computational unit cell of a ZnO structure with defects. (B) Band structure. (C) Absorption coefficient. A0,1 bands are indicated.

observed absorbance of the undoped ZnO and ZnO:Er(1%) NRA, NRF (Figure 3). The fragment of crystalline structure, bandgap structure, and absorption spectra corresponding to model (x) are shown in Figure 5. They exhibit one relatively broad band peaking at about 0.75 eV and the other band strongly overlapped with the absorption edge covering the about 1–2 eV range (starting from approximately 1.5–1.8 eV) of visible light. The position of the first band correlates very well with the position of the experimentally observed A0 band (Figures 3, 5). Note that the calculated absorption band with the maximum at about 0.75 eV is present in the calculated absorption spectra of the ZnO structures containing only zinc vacancy [model (xii)] as well as in the ZnO structures containing only Er^{2+} in different positions [model (ii–iv, ix)] and in the ZnO structures containing Er^{2+} and V_{Zn} [models (v, vi)] or V_{O} [model (vii)]. Along with the discussion above, this leads to the conclusion that the 0.75 eV band origin is the absorption on free electrons [see the conclusion points (1–6)] as well as the experimental A0 band.

The position of the second calculated band [models (ii–vii, ix, x, and xii)] is in good agreement with the localization of the experimental A1 band (Figures 3, 5). This led to the conclusion that, in principle, Er^{2+} may substitute for the regular Zn with and without V_{Zn} or V_{O} in the local surroundings or be interstitial in the ZnO host. The Er^{3+} EPR glass-like spectrum was observed only in the ZnO NRF sample, and no Er^{3+} EPR spectrum was detected in the ZnO NRA (see Figure S3 in Supporting Information). However, the influence of Er on shallow donors was found out. Therefore, based on the presented calculations, one may conclude that indeed, ZnO NRF rods grow on erbium-related seeds (where erbium is Er^{3+}), whereas a tiny amount of erbium is incorporated in the ZnO host as Er^{2+} . In the case of ZnO NRA, erbium is only Er^{2+} . It is the source of electrons, $\text{Er}^{2+} \rightarrow \text{Er}^{3+} + e^-$ in this case. Therefore, the A1 band increases in the Er containing ZnO NRA and NRF samples (Figure 3).

3.6. Erbium Spectrum in Infrared Photoluminescence. It is known that the Er^{3+} spectrum is very well visible after the annealing in air at relatively high annealing temperatures of the ZnO nano- or microrods.^{25,28} The normalized infrared IR PL spectra of the ZnO:Er(1%) NRA and NRF, measured after annealing in air at 700 °C and the IR PL spectrum of Er_2O_3 , for comparison, are shown in Figure 6.

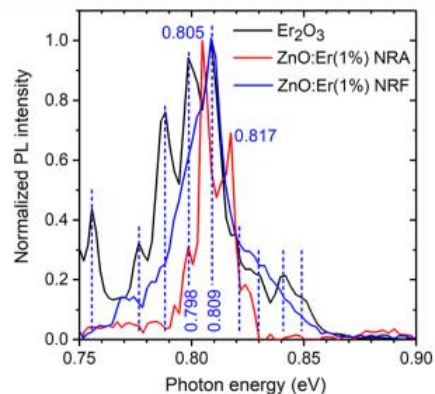


Figure 6. Normalized ${}^4\text{I}_{13/2} \rightarrow {}^4\text{I}_{15/2}$ Er^{3+} optical transition measured in the ZnO:Er(1%) NRA and NRF samples annealed in air at 700 °C as well as in the as grown Er_2O_3 powder at room temperature. The transitions between the Stark levels in the spectrum of Er_2O_3 are marked by dashed vertical lines.

The absolute intensity of the Er^{3+} transition (Figure 6) is several orders of magnitude stronger in the ZnO:Er(1%) NRF as compared with the ZnO:Er(1%) NRA sample. Moreover, the Er^{3+} spectrum measured in the ZnO:Er(1%) NRF is approximately the same as reported in the previous work²⁵—the transitions between the Stark levels^{25,47,48} are strongly overlapped and unresolved. Only one can be unambiguously resolved at 0.809 eV. This points to a rather glass-like

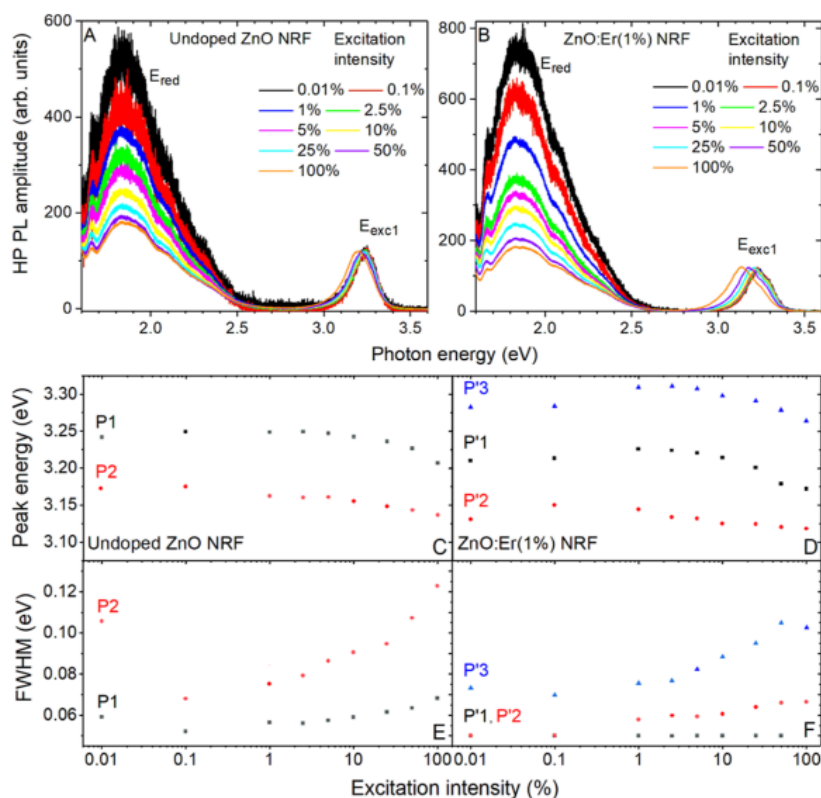


Figure 7. HP PL spectra measured under 3.82 eV (325 nm) laser excitation with different intensities (given in the legends as the weight fractions in % of the full amplification) in the undoped ZnO NRF (A) and ZnO:Er(1%) NRF (B) samples. Dependence of the P1–3 peak energy and fwhm on the HP laser excitation intensity (as the weight fraction in % of the full intensity $2.5 \text{ kW/cm}^2 = 100\%$) for the undoped ZnO NRF (C,E) and ZnO:Er(1%) NRF (D,F) samples.

spectrum, i.e., amorphous. This is in good agreement with EPR measurements (Figure S3 in Supporting Information). Since this spectrum differs from the IR PL spectrum of Er_2O_3 (Figure 6), one may expect indeed Er-like nucleation seeds existence. These are not metal Er clusters; otherwise, they should not be detectable in EPR, but considering hydrothermal growth, they should appear as $\text{Er}_x\text{O}_y\text{H}_z$ compounds. Annealing in air at $700 \text{ }^\circ\text{C}$ changes Er^{3+} oxygen surrounding, and therefore, the spectrum becomes visible. However, the Er^{3+} spectrum measured in ZnO:Er(1%) NRA is different. It is characterized by features that are different from those of the Er^{3+} spectrum of Er_2O_3 . At least three Stark transitions at 0.798, 0.805, and 0.817 eV could be detected there pointing to rather crystalline feature. This is a sign of the Er^{3+} existence in the ZnO host at the regular Zn site. Considering DFT calculations above, the Er^{2+} at the Zn^{2+} site becomes Er^{3+} after annealing and, therefore, the IR PL spectrum appears visible (Figure 6). This spectrum cannot be observed in the ZnO NRF sample, as it is hidden in the background of the amorphous spectrum.

Taking into account the typical Er^{3+} IR PL spectrum measured in the NRA sample after the annealing in air at $700 \text{ }^\circ\text{C}$ (Figure 6) to have clearly visible Stark transitions indicating its crystalline origin and having no other evidence of the other Er^{3+} IR PL spectrum, one may expect the probability of the regular substitution to be much higher as compared to the interstitial in the NRA. Therefore, considering the $\text{Er}_x\text{O}_y\text{H}_z$ -like structures to appear as a kind of small particle seeds for the ZnO growth, one may expect Er incorporation into the ZnO

structure at the ZnO/cluster interface rather as the regular substitution in the NRF as well. The “glass-like” Er^{3+} IR PL spectrum thus originates from the $\text{Er}_x\text{O}_y\text{H}_z$ -like structures dominating over the Er_{Zn} one.

3.7. UV and Visible Photoluminescence Characterization. To improve the optical density and to study in detail the luminescence properties of the ZnO NRA and NRF samples, high power (HP) laser irradiation was used for excitation. The corresponding PL spectra were measured at different laser power. They are shown for the NRF samples in Figure 7A,B. As one can see, the E_{exc1} emission shifts toward lower energies upon the increased excitation intensity there: from about 3.22 eV (384 nm) at low excitation intensity to 3.14 eV (395 nm) at high excitation intensity. This behavior was not observed in the NRA samples at all.

To study the redshift of the E_{exc1} band, it was decomposed into two (P1,2 in the undoped ZnO NRF) or three [P'1–3 in the ZnO:Er(1%) NRF] components using pseudo-Voigt functions. The experimental and fitting spectra are shown in Figure S5 in Supporting Information for the undoped ZnO NRF and in Figure S6 in Supporting Information for the ZnO:Er(1%) NRF. The dependences of thus determined P1,2 and P'1–3 spectral positions (energies) and full widths at half maxima (fwhm) on the weight fraction of the laser power full amplification are shown in Figure 7C–F.

The redshift and increase of the fwhm of the P1,2 and P'2,3 components of the E_{exc1} upon the excitation intensity can clearly be observed for the undoped ZnO and ZnO:Er(1%) NRF samples (Figure 7C–F). The fwhm of the P'1

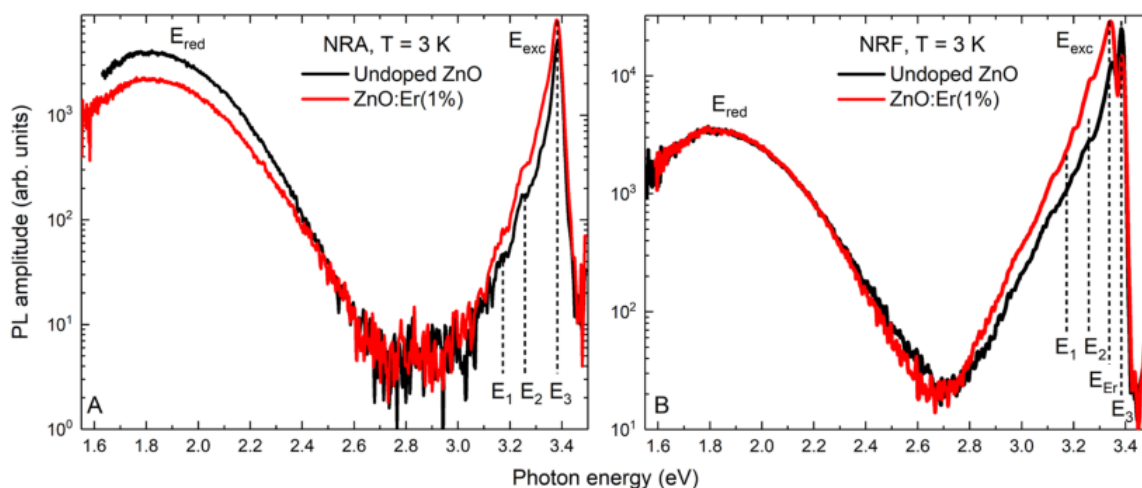


Figure 8. (A) PL spectra measured in undoped ZnO and ZnO:Er(1%) NRA. (B) PL spectra measured in the undoped ZnO and ZnO:Er(1%) NRF. E_{red} , E_{exc} , E_{1-3} , and E_{Er} indicate the specific emission bands.

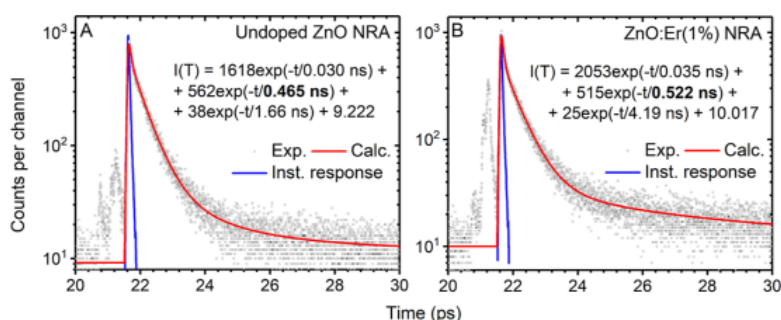


Figure 9. Experimental RL decay curves of undoped ZnO NRA (A) and ZnO:Er(1%) NRA (B) measured with X-ray excitation at room temperature are shown along with the fitting curves (the expressions are also given).

component remains constant upon excitation intensity (Figure 7F). It should be noted that the fwhm is initially large (at 0.01% of full intensity) for all the P_{1,2} and P'₁₋₃ peaks and, therefore, the fitted peak energies were determined with some error. By comparing the spectral positions for the P_{1,2} (Figure 7C) and P'_{1,2} (Figure 7E) peaks, as well as the characters of their dependences on the excitation intensity, one may conclude that they are quite similar. This allowed us to infer that P₁ = P'₁ and P₂ = P'₂ in both undoped and Er doped ZnO NRF samples. However, the fwhm's of the P'_{1,2} peaks exhibit a less pronounced rate of changes as compared to the P_{1,2} ones (Figure 7E,F). This indicates the influence of the erbium donor levels on the excitons, i.e., the density of the exciton states is larger in the erbium doped NRF samples. Moreover, the P'₃ component is unique, observed only in the Er doped NRF sample. Considering the previous study on the ZnO:Er(2–30%) microrods⁴⁹ where the existence of the Er-bound exciton was confirmed, one may expect the P'₃ band to originate from the Er-bound exciton as well.

The defect-related red band (E_r) peaking at 1.86 eV had the tendency to drop upon the increased laser intensity. This is the well-known saturation effect. No shift was observed.

To prove the multicomponent origin of the PL in Er doped ZnO, the low power PL was measured at 3 K in undoped and Er doped ZnO NRA and NRF. The corresponding spectra are shown in Figure 8. The spectra, in general, were composed of two bands: the defect-related red band (E_{red}) peaking at 1.86

eV and the multicomponent exciton band (E_{exc} with the maximum at 3.37 eV in both the NRA and NRF samples). Erbium causes the decrease of the E_{red} by about twice in the undoped ZnO NRA as compared to the ZnO:Er(1%) NRA. At the same time, the almost doubled increase of the E_{exc} was detected in the ZnO:Er(1%) NRA as compared to the undoped ZnO NRA. All these confirm the influence of Er and thus its incorporation into the ZnO host as discussed above, however to the very little extent since the E_{exc} shape remains classical and does not differ for the ZnO:Er(1%) NRA as compared to the undoped ZnO NRA (Figure 8A). Only three contributions creating this band were revealed: $E_{1,2}$ (peaking at 3.17 and 3.26 eV, respectively) are LO phonon replicas, whereas the E_3 (peaking at 3.37 eV) was related to free excitons.⁵⁰

The situation is different in the ZnO NRF samples (Figure 8B). There, the E_{red} band intensity remains unchanged upon Er doping. The E_{exc} band is more complex as compared to that of the NRA sample. There are also E_{1-3} contributions as well as the fourth, the new one, marked as E_{Er} (peaking at 3.34 eV) in Figure 8B. This contribution being weak in the undoped ZnO NRF sample becomes more than twice as strong in the ZnO:Er(1%) NRF sample. The influence of erbium can again be concluded, probably even the Er-related exciton creation. This is in good agreement with the HP PL measurements (Figure 7). Moreover, the E_3 band becomes about twice as weak in the PL spectrum of the ZnO:Er(1%) NRF compared

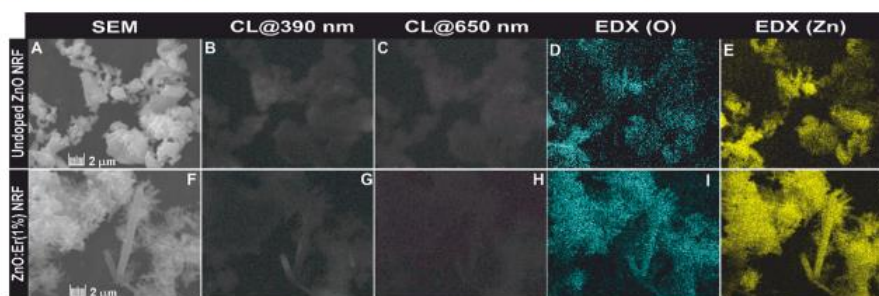


Figure 10. Images in contrast of secondary electrons (A,F), CL at 390 nm (3.19 eV) (B,G), CL at 650 nm (1.91 eV) (C,H), and EDX maps of O (D,I) and Zn (E,J) of the undoped ZnO NRF sample and of the ZnO:Er(1%) NRF sample.

to the undoped ZnO NRF sample. Considering the increase of the E_{Er} and decrease of the E_3 , one may expect energy transfer between these free excitons with participation of E_t levels inside the bandgap of ZnO. Taking into account calculations mentioned above, one may conclude that erbium indeed exists in the ZnO host as Er^{2+} .

3.8. Ultrafast Kinetics. In order to determine the influence of Er on the timing characteristics, the RL decay kinetics was measured for the undoped ZnO and ZnO:Er(1%) NRA (the decay kinetics could not be reliably measured for the NRF samples due to a very low signal). The corresponding decay curves are shown in Figure 9. The experimental decay curves have been fitted using the multiexponential expression (convolved with the instrumental response function)

$$I(t) = \sum_{i=1}^3 A_i \exp(-t/\tau_i) + I_0 \quad (1)$$

where A_i and τ_i are the amplitude and decay time of the i -th component, respectively; I_0 is background. The fit parameters can be found in Figure 9 as well.

Three exponentials were revealed for both undoped ZnO and ZnO:Er(1%) NRA samples. The component with a decay time τ_1 about 30 ps with the largest contribution is irrelevant since it appears as the tail of the excitation pulse (also demonstrated in Figure 9). Meaningful components are (i) $\tau_2 = 465$ ps ($A_2 = 562$), $\tau_3 = 1.66$ ns ($A_3 = 38$) in the decay curves of undoped ZnO NRA and (ii) $\tau_2 = 522$ ps ($A_2 = 515$), $\tau_3 = 4.19$ ns ($A_3 = 25$) in the decay curves of ZnO:Er(1%) NRA. Note that τ_2 components are typical for ZnO nanoparticles.^{23,51} The third component may originate from the unfiltered tail of some other emission.

Considering the fact that Er presence causes the creation of the Er-bound exciton as reported in the previous work,⁴⁹ one may expect the slowed exciton emission to be due to erbium presence itself and not to the defects. Note also that the P'3 component (see Figures 7 and S6 in Supporting Information) discussed in Section 3.7 is unique, observed only in the Er doped samples.

3.9. Cathodoluminescence and EDX. To map the spatial luminescence properties of the ZnO NRA and NRF samples and to address the distribution of excitonic and defect-related emission centers, CL correlated to EDX and SEM was measured. By analogy with PL, the CL spectra were composed of excitonic (3.25 eV in NRA and 3.19 eV in NRF) and red bands (1.91 eV in NRA and NRF). The difference in the spectral positions of the excitonic emission is typical for the hydrothermally grown ZnO nanorods.⁵²

Correlated CL, SEM, and EDX mapping of both undoped and Er doped ZnO NRA samples are approximately the same, indicating the homogeneous distribution of light extracted from the ZnO nanorods (both 3.25 and 1.91 eV). Moreover, EDX mapping reveals a similar distribution of Zn and O. Erbium concentration was below the detection abilities.

Correlated CL (for 3.19 and 1.91 eV) and SEM and EDX mappings of the undoped ZnO NRF sample are shown in Figure 10A–E.

According to the CL image obtained for the 3.25 eV emission, larger rods emit brighter. There must be nonradiative transitions on the surface of smaller rods, stronger than in the case of the larger ones, degrading the excitonic luminescence there. Larger rods have a higher volume/surface ratio, so they are relatively less affected by the surface recombination. Interestingly, the CL image obtained for 1.91 eV reveals no tendencies related to the size of the rods. The defect states responsible for the red luminescence (zinc vacancies) seem to be distributed homogeneously over the rods of different sizes in this case. There is no clear correlation between the Zn and O concentrations and the size of the rods according to EDX mapping as well. Correlated SEM image and CL and EDX mapping of the ZnO:Er(1%) NRF sample are shown in Figure 10F–J. Again, as in the case of the undoped ZnO NRF, the CL at 3.25 and 1.91 eV are not strictly correlated. Larger rods emit brighter at 3.25 eV. EDX maps of both Zn and O are not in a good correlation with the CL image at 3.25 eV. It might be quite surprising since EDX intensity is connected to excited volume of ZnO. However, in the images (Figure 10), one may find that high CL intensity comes primarily from larger microrods, while the clusters of nanorods do not contribute to CL intensity as much. The same phenomenon was observed for the undoped ZnO NRF mentioned above. This suggests that the nonradiative recombination in the case of ZnO nano/micro rods is governed by surface recombination. The CL image obtained for the 1.91 eV reveals no tendencies related to the size of the rods as mentioned above for the undoped ZnO NRF sample.

EDX measurements positively confirmed the presence of Er in the ZnO:Er(1%) NRF sample, but its signal was too weak to perform mapping (see the EDX spectrum in Figure S7 in the Supporting Information).

The emission spectra of the NRF samples exhibit strong dependence on excitation intensity in CL [shown in an example of the ZnO:Er(1%) NRF in Figure S8 in the Supporting Information]. This is in good agreement with high power PL measurements under the 3.82 eV (325 nm) laser excitation discussed above.

4. CONCLUSIONS

Undoped and Er doped (1 wt %) ZnO nanorods were simultaneously grown as a thin film of vertically aligned arrays deposited on a fused silica glass substrate (NRA) and free-standing ones in the powder form (NRF). The nanorods grew thin (about 50 nm thick) and to large extent homogeneous in the NRA form, whereas they were about 1 order of magnitude larger in the form of NRF. In average, each of the NRA nanorods was single crystalline particle, whereas in the case of NRF, the nanorods appeared as agglomeration of single crystalline particles into the larger polycrystalline ones. Er incorporation was pronounced in the NRF system as compared to the NRA. To the best of our knowledge, there are no works reporting unambiguously on the incorporation of Er and its charge state. Therefore, presently, in our detailed investigation, a broad scale of the experimental techniques like scanning electron microscopy, X-ray diffraction, radioluminescence, photoluminescence, scintillation (including ultrafast timing), electron paramagnetic resonance, and photothermal deflection spectroscopies as well as first-principles calculations were used to meet this goal. Based on the rigorous and correlated analysis of the data, we disclose, for the first time in literature, the occurrence of Er^{2+} in the ZnO host, at the regular Zn site in the deposited nanorod arrays and mostly as nucleation seeds in the free-standing ones (incorporation as Er^{2+} is not excluded there as well). Moreover, erbium acts as a donor, creating energy states at the bottom of the conduction bands participating in excitonic emission. EPR measurements indicated the increased number of shallow donors in the NRA. This is in good correlation with the free carriers' concentration, about 1 order of magnitude larger in the NRA as compared to NRF. The timing of the excitonic emission is worsening upon Er doping in the NRA samples. The corresponding decay time was improved from 465 ps in undoped ZnO to 522 ps in the ZnO:Er(1%).

■ ASSOCIATED CONTENT

Supporting Information

The Supporting Information is available free of charge at <https://pubs.acs.org/doi/10.1021/acs.jpcc.3c05471>.

Atomistic models, electronic bandstructures, and absorption coefficients of ZnO structures doped with erbium atoms, SEM images, EPR spectrum, Raman peaks, HP PL spectra, EDX spectrum, and CL spectrum (PDF)

■ AUTHOR INFORMATION

Corresponding Author

Maksym Buryi – FZU—Institute of Physics of the Czech Academy of Sciences, Prague 162 00, Czechia; Faculty of Nuclear Sciences and Physical Engineering, Czech Technical University in Prague, Prague 115 19, Czechia; orcid.org/0000-0002-7529-255X; Email: buryi@fzu.cz

Authors

Zdeněk Remeš – FZU—Institute of Physics of the Czech Academy of Sciences, Prague 162 00, Czechia; orcid.org/0000-0002-3512-9256

František Hájek – FZU—Institute of Physics of the Czech Academy of Sciences, Prague 162 00, Czechia; Faculty of Nuclear Sciences and Physical Engineering, Czech Technical University in Prague, Prague 115 19, Czechia

Karla Kuldová – FZU—Institute of Physics of the Czech Academy of Sciences, Prague 162 00, Czechia

Vladimír Babin – FZU—Institute of Physics of the Czech Academy of Sciences, Prague 162 00, Czechia; orcid.org/0000-0003-3072-2242

Kateřina Děcká – FZU—Institute of Physics of the Czech Academy of Sciences, Prague 162 00, Czechia; Faculty of Nuclear Sciences and Physical Engineering, Czech Technical University in Prague, Prague 115 19, Czechia; orcid.org/0000-0002-2824-2381

Hadi Hematian – Faculty of Electrical Engineering, Czech Technical University in Prague, Prague 166 27, Czechia

Lucie Landová – FZU—Institute of Physics of the Czech Academy of Sciences, Prague 162 00, Czechia; Faculty of Electrical Engineering, Czech Technical University in Prague, Prague 166 27, Czechia

Neda Neykova – FZU—Institute of Physics of the Czech Academy of Sciences, Prague 162 00, Czechia; Faculty of Electrical Engineering, Czech Technical University in Prague, Prague 166 27, Czechia

Eva Horynová – Faculty of Electrical Engineering, Czech Technical University in Prague, Prague 166 27, Czechia

Bohuslav Rezek – Faculty of Electrical Engineering, Czech Technical University in Prague, Prague 166 27, Czechia; orcid.org/0000-0002-0378-4598

Complete contact information is available at: <https://pubs.acs.org/10.1021/acs.jpcc.3c05471>

Notes

The authors declare no competing financial interest.

■ ACKNOWLEDGMENTS

This work was supported by the Czech Science Foundation by the project no. 20-05497Y and by the student project SGS21/158/OHK4/3T/13. Z. R. acknowledges the support from the CAS-SAS Mobility Plus project SAV-23-13, CAS-SAS-2022-08 and MSTC Danube 8X23025.

■ REFERENCES

- (1) Chen, Y.; Su, L.; Jiang, M.; Fang, X. Switch Type PANI/ZnO Core-Shell Microwire Heterojunction for UV Photodetection. *J. Mater. Sci. Technol.* **2022**, *105*, 259–265.
- (2) Yan, J.; Fang, X.; Zhang, L.; Bando, Y.; Gautam, U. K.; Dierre, B.; Sekiguchi, T.; Golberg, D. Structure and Cathodoluminescence of Individual ZnS/ZnO Biaxial Nanobelt Heterostructures. *Nano Lett.* **2008**, *8* (9), 2794–2799.
- (3) You, D.; Xu, C.; Wang, X.; Wang, J.; Su, W.; Wang, R.; Chen, T.; Wang, R.; Shi, Z. A Core@Dual-Shell Nanorod Array with a Cascading Band Configuration for Enhanced Photocatalytic Properties and Anti-Photocorrosion. *J. Mater. Chem. A* **2020**, *8* (7), 3726–3734.
- (4) Zhou, Y.; Chen, G.; Sargent, E. H.; Zhuang, T.; Thang Dinh, C.; He, F. Freestanding Nano-Photoelectrode as a Highly Efficient and Visible-Light-Driven Photocatalyst for Water-Splitting. *J. Mater. Chem. A* **2017**, *5* (21), 10651–10657.
- (5) Barbillon, G.; Sandana, V. E.; Humbert, C.; Bélier, B.; Rogers, D. J.; Teherani, F. H.; Bove, P.; McClintock, R.; Razeghi, M. Study of Au Coated ZnO Nanoarrays for Surface Enhanced Raman Scattering Chemical Sensing. *J. Mater. Chem. C* **2017**, *5* (14), 3528–3535.
- (6) Feng, H.; Liang, L.; Wu, W.; Huang, Z.; Liu, Y. Architecting Epitaxial-Lattice-Mismatch-Free (LMF) Zinc Oxide/Bismuth Oxide Nano-Heterostructures for Efficient Photocatalysis. *J. Mater. Chem. C* **2020**, *8* (32), 11263–11273.
- (7) Garg, N.; White, C. E. Mechanism of Zinc Oxide Retardation in Alkali-Activated Materials: An in Situ X-Ray Pair Distribution

- Function Investigation. *J. Mater. Chem. A* **2017**, *5* (23), 11794–11804.
- (8) Chen, H.; Shen, K.; Chen, J.; Chen, X.; Li, Y. Hollow-ZIF-Templated Formation of a ZnO@C-N-Co Core-Shell Nanostructure for Highly Efficient Pollutant Photodegradation. *J. Mater. Chem. A* **2017**, *5* (20), 9937–9945.
- (9) He, G.-H.; Jiang, M.-M.; Dong, L.; Zhang, Z.-Z.; Li, B.-H.; Shan, C.-X.; Shen, D.-Z. Near-Infrared Light-Emitting Devices from Individual Heavily Ga-Doped ZnO Microwires. *J. Mater. Chem. C* **2017**, *5* (10), 2542–2551.
- (10) Xie, A.; Yang, D.; Li, X.; Zeng, H. Lattice Restraint Induced Ultra-Large Bandgap Widening of ZnO Nanoparticles. *J. Mater. Chem. C* **2019**, *7* (29), 8969–8974.
- (11) D'Agostino, D.; Di Giorgio, C.; Bobba, F.; Di Trollo, A.; Alippi, P.; Cucolo, A. M.; Amore Bonapasta, A. Effects of Cobalt Substitution on ZnO Surface Reactivity and Electronic Structure. *J. Mater. Chem. C* **2019**, *7* (27), 8364–8373.
- (12) Kapat, K.; Shubhra, Q. T. H.; Zhou, M.; Leeuwenburgh, S. Piezoelectric Nano-Biomaterials for Biomedicine and Tissue Regeneration. *Adv. Funct. Mater.* **2020**, *30* (44), 1909045.
- (13) Siebert, L.; Luna-Cerón, E.; García-Rivera, L. E.; Oh, J.; Jang, J.; Rosas-Gómez, D. A.; Pérez-Gómez, M. D.; Maschkowitz, G.; Fickenscher, H.; Ocegüera-Cuevas, D.; et al. Light-Controlled Growth Factors Release on Tetrapodal ZnO-Incorporated 3D-Printed Hydrogels for Developing Smart Wound Scaffold. *Adv. Funct. Mater.* **2021**, *31* (22), 2007555.
- (14) Lee, J.-W.; Cho, K.-H.; Yoon, J.-S.; Sung, Y.-M. Enhanced IR-Driven Photoelectrochemical Responses of CdSe/ZnO Heterostructures by up-Conversion UV/Visible Light Irradiation. *Nanoscale* **2020**, *12* (15), 8525–8535.
- (15) Senapati, S.; Nanda, K. K. Designing Dual Emissions via Co-Doping or Physical Mixing of Individually Doped ZnO and Their Implications in Optical Thermometry. *ACS Appl. Mater. Interfaces* **2017**, *9* (19), 16305–16312.
- (16) Chen, Y.; Xue, Q.; Luo, W.; Sun, Y.; Zhang, X.; Lu, D.; Qian, X.; Chen, C.-C.; Li, M.; Hang, T. Sol-Gel-Derived Biodegradable Er-Doped ZnO/Polyethylene Glycol Nanoparticles for Cell Imaging. *ACS Appl. Nano Mater.* **2022**, *5* (5), 7103–7112.
- (17) Sánchez-López, A. L.; Perfecto-Avalos, Y.; Sanchez-Martinez, A.; Ceballos-Sanchez, O.; Sepulveda-Villegas, M.; Rincón-Enriquez, G.; Rodríguez-González, V.; Garcia-Varela, R.; Lozano, L. M.; Eloyr Navarro-López, D.; et al. Influence of Erbium Doping on Zinc Oxide Nanoparticles: Structural, Optical and Antimicrobial Activity. *Appl. Surf. Sci.* **2022**, *575*, 151764.
- (18) Leiter, F.; Zhou, H.; Henecker, F.; Hofstaetter, A.; Hofmann, D. M.; Meyer, B. K. Magnetic Resonance Experiments on the Green Emission in Undoped ZnO Crystals. *Phys. B Condens. Matter* **2001**, *308–310*, 908–911.
- (19) Chen, J.-X.; Hao, S.-T.; Sun, Z.-X.; Zheng, P.; Tang, J.; Yang, Y.-L.; Zhang, S.-L.; Liu, X.-L.; Zhao, J.-T.; Li, Q.-L.; et al. Development of the ZnO:Ga Nanorod Arrays as an Alpha Particle Scintillation Screen for the Associated Particle Neutron Generator. *Appl. Phys. Lett.* **2022**, *120* (19), 193502.
- (20) Dujardin, C.; Auffray, E.; Bourret-Courchesne, E.; Dorenbos, P.; Lecoq, P.; Nikl, M.; Vasil'ev, A. N.; Yoshikawa, A.; Zhu, R.-Y. Needs, Trends, and Advances in Inorganic Scintillators. *IEEE Trans. Nucl. Sci.* **2018**, *65* (8), 1977–1997.
- (21) Jiang, C.-H.; Yao, C.-B.; Wang, Z.-M.; Wang, X.; Wang, L. Y. Heterostructure MoS₂@ZnO Nanowires: Preparation, Ultrafast Nonlinear Optical Behavior and Photoelectric Functional Application. *Appl. Surf. Sci.* **2022**, *599*, 153920.
- (22) Abrahams, S. C.; Bernstein, J. L. Remeasurement of the Structure of Hexagonal ZnO. *Acta Crystallogr., Sect. B: Struct. Sci.* **1969**, *25* (7), 1233–1236.
- (23) Buryi, M.; Remeš, Z.; Babin, V.; Novotný, M.; Vaněček, V.; Aubrechtová Dragounová, K.; Mičová, J.; Landová, L.; Kučerková, R.; More-Chevalier, J.; et al. Influence of Mo Doping on the Luminescence Properties and Defect States in ZnO Nanorods. Comparison with ZnO:Mo Thin Films. *Appl. Surf. Sci.* **2021**, *555*, 149679.
- (24) Buryi, M.; Babin, V.; Chang, Y.-Y.; Remeš, Z.; Mičová, J.; Šimek, D. Influence of Precursor Age on Defect States in ZnO Nanorods. *Appl. Surf. Sci.* **2020**, *525*, 146448.
- (25) Buryi, M.; Remeš, Z.; Babin, V.; Artemenko, A.; Vaněček, V.; Aubrechtová Dragounová, K.; Landová, L.; Kučerková, R.; Mičová, J. Transformation of Free-Standing ZnO Nanorods upon Er Doping. *Appl. Surf. Sci.* **2021**, *562*, 150217.
- (26) Neykova, N.; Chang, Y.-Y.; Buryi, M.; Davydova, M.; Kucerkova, R.; Šimek, D.; Remeš, Z.; Pop-Georgievski, O. Study of ZnO Nanorods Grown under UV Irradiation. *Appl. Surf. Sci.* **2019**, *472*, 105–111.
- (27) Mičová, J.; Buryi, M.; Šimek, D.; Drahokoupil, J.; Neykova, N.; Chang, Y.-Y.; Remeš, Z.; Pop-Georgievski, O.; Svoboda, J.; Im, C. Synthesis of Zinc Oxide Nanostructures and Comparison of Their Crystal Quality. *Appl. Surf. Sci.* **2018**, *461*, 190–195.
- (28) Buryi, M.; Remeš, Z.; Babin, V.; Artemenko, A.; Chertopalov, S.; Mičová, J. Cold Plasma Treatment of ZnO:Er Nano- and Microrods: The Effect on Luminescence and Defects Creation. *J. Alloys Compd.* **2022**, *895*, 162671.
- (29) Buryi, M.; Remeš, Z.; Babin, V.; Chertopalov, S.; Děcká, K.; Dominec, F.; Mičová, J.; Neykova, N. Free-Standing ZnO:Mo Nanorods Exposed to Hydrogen or Oxygen Plasma: Influence on the Intrinsic and Extrinsic Defect States. *Materials* **2022**, *15* (6), 2261.
- (30) Hautier, G.; Miglio, A.; Ceder, G.; Rignanese, G.-M.; Gonze, X. Identification and Design Principles of Low Hole Effective Mass P-Type Transparent Conducting Oxides. *Nat. Commun.* **2013**, *4* (1), 2292.
- (31) Yaakob, M. K.; Hussin, N. H.; Taib, M. F. M.; Kudin, T. I. T.; Hassan, O. H.; Ali, A. M. M.; Yahya, M. Z. A. First Principles LDA+U Calculations for ZnO Materials. *Integr. Ferroelectr.* **2014**, *155* (1), 15–22.
- (32) Wang, S.; Shi, X.; Li, J. Ferromagnetism Properties of Er-Doped ZnO: A GGA + U Study. *RSC Adv.* **2016**, *6* (109), 107865–107870.
- (33) Alkahtani, E. A.; Merad, A. E.; Boufatah, M. R.; Benosman, A. DFT Investigation of Structural, Electronic and Optical Properties of Pure and Er-Doped ZnO: Modified Becke-Johnson Exchange Potential. *Optik* **2017**, *128*, 274–280.
- (34) Ferreira, L. G.; Marques, M.; Teles, L. K. Slater Half-Occupation Technique Revisited: The LDA-1/2 and GGA-1/2 Approaches for Atomic Ionization Energies and Band Gaps in Semiconductors. *AIP Adv.* **2011**, *1* (3), 032119.
- (35) Ding, L.; Nicolay, S.; Steinhäuser, J.; Kroll, U.; Ballif, C. Relaxing the Conductivity/Transparency Trade-Off in MOCVD ZnO Thin Films by Hydrogen Plasma. *Adv. Funct. Mater.* **2013**, *23* (41), 5177–5182.
- (36) Abragam, A.; Bleaney, B. *Electron Paramagnetic Resonance of Transition Ions*; Oxford classic texts in the physical sciences; Oxford University Press: Oxford, 2012.
- (37) Mims, W. B.; Davis, J. L. The Local Symmetry of Ce³⁺, Nd³⁺, Er³⁺, and Yb³⁺ in Frozen Aqueous Solutions as Studied by EPR and the Linear Electric Field Effect. *J. Chem. Phys.* **1976**, *65* (8), 3266–3274.
- (38) Antuzevics, A. EPR Characterization of Erbium in Glasses and Glass Ceramics. *Low Temp. Phys.* **2020**, *46* (12), 1149–1153.
- (39) Rakhmatullin, R. M.; Aminov, L. K.; Kurkin, I. N.; Pöpl, A. EPR Evidence of Unusual Dopant Valency States in Nanocrystalline Er-Doped CeO₂. *Appl. Magn. Reson.* **2015**, *46* (7), 741–748.
- (40) Dziesiaty, J.; Müller, S.; Boyn, R.; Buhrow, T.; Klimakov, A.; Kreissl, J. Non-Cubic Er Centres in ZnSe Studied by Electron Paramagnetic Resonance and Optical Analysis. *J. Phys.: Condens. Matter* **1995**, *7* (22), 4271–4282.
- (41) MacDonald, M. R.; Bates, J. E.; Ziller, J. W.; Furche, F.; Evans, W. J. Completing the Series of + 2 Ions for the Lanthanide Elements: Synthesis of Molecular Complexes of Pr²⁺, Gd²⁺, Tb²⁺, and Lu²⁺. *J. Am. Chem. Soc.* **2013**, *135* (26), 9857–9868.
- (42) Buryi, M.; Remeš, Z.; Babin, V.; Vaněček, V.; Aubrechtová Dragounová, K.; Mičová, J.; Landová, L.; Kučerková, R. ZnO

Nanorods Alloyed with Mo/Er. The Effect of Post-Deposition Treatment on Defect States and Luminescence. *IOP Conf. Ser.: Mater. Sci. Eng.* **2021**, *1050* (1), 012002.

(43) Babin, V.; Buryi, M.; Chlan, V.; Fomichov, Y.; Kamada, K.; Laguta, V. V.; Nikl, M.; Pejchal, J.; Štěpánková, H.; Yoshikawa, A.; et al. Influence of Gallium Content on Ga³⁺ Position and Photo- and Thermally Stimulated Luminescence in Ce³⁺-Doped Multicomponent (Y,Lu)₃GaxAl₅XO₁₂ Garnets. *J. Lumin.* **2018**, *200*, 141–150.

(44) Cheng, A.-J.; Tzeng, Y.; Xu, H.; Alur, S.; Wang, Y.; Park, M.; Wu, T.; Shannon, C.; Kim, D.-J.; Wang, D. Raman Analysis of Longitudinal Optical Phonon-Plasmon Coupled Modes of Aligned ZnO Nanorods. *J. Appl. Phys.* **2009**, *105* (7), 073104.

(45) Mao, Z.; Fu, C.; Pan, X.; Chen, X.; He, H.; Wang, W.; Zeng, Y.; Ye, Z. Raman-Based Measurement of Carrier Concentration in n-Type ZnO Thin Films under Resonant Conditions. *Phys. Lett. A* **2020**, *384* (7), 126148.

(46) Fu, C.; Pan, X.; Chen, S.; Ye, Z. Raman Determination of Carrier Concentration in ZnO-Based Heterostructure Light-Emitting Diodes. *Opt. Lett.* **2019**, *44* (7), 1576.

(47) Michel, J.; Benton, J. L.; Ferrante, R. F.; Jacobson, D. C.; Eaglesham, D. J.; Fitzgerald, E. A.; Xie, Y.-H.; Poate, J. M.; Kimerling, L. C. Impurity Enhancement of the 1.54- μm Er³⁺ Luminescence in Silicon. *J. Appl. Phys.* **1991**, *70* (5), 2672–2678.

(48) Venkatramu, V.; León-Luis, S. F.; Rodríguez-Mendoza, U. R.; Monteseguro, V.; Manjón, F. J.; Lozano-Gorrín, A. D.; Valiente, R.; Navarro-Urrios, D.; Jayasankar, C. K.; Muñoz, A.; et al. Synthesis, Structure and Luminescence of Er³⁺-Doped Y₃Ga₅O₁₂ Nano-Garnets. *J. Mater. Chem.* **2012**, *22* (27), 13788.

(49) Buryi, M.; Neykova, N.; Ridzoňová, K.; Remeš, Z.; Děcká, K.; Hájek, F.; Artemenko, A.; Míčová, J.; Landová, L.; Jakubec, I. Peculiarities of Erbium Incorporation into ZnO Microrods at High Doping Level Leading to Upconversion and the Morphology Change. Influence on Excitonic as Well as Shallow Donor States. *Appl. Surf. Sci.* **2023**, *611*, 155651.

(50) Özgür, D. C.; Alivov, Y. I.; Liu, C.; Teke, A.; Reshchikov, M. A.; Doğan, S.; Avrutin, V.; Cho, S.-J.; Morkoç, H. A Comprehensive Review of ZnO Materials and Devices. *J. Appl. Phys.* **2005**, *98* (4), 041301.

(51) Procházková, L.; Vaněček, V.; Čuba, V.; Pjatkan, R.; Martínez-Turtos, R.; Jakubec, I.; Buryi, M.; Omelkov, S.; Auffray, E.; Lecoq, P.; et al. Core-Shell ZnO:Ga-SiO₂ Nanocrystals: Limiting Particle Agglomeration and Increasing Luminescence via Surface Defect Passivation. *RSC Adv.* **2019**, *9* (50), 28946–28952.

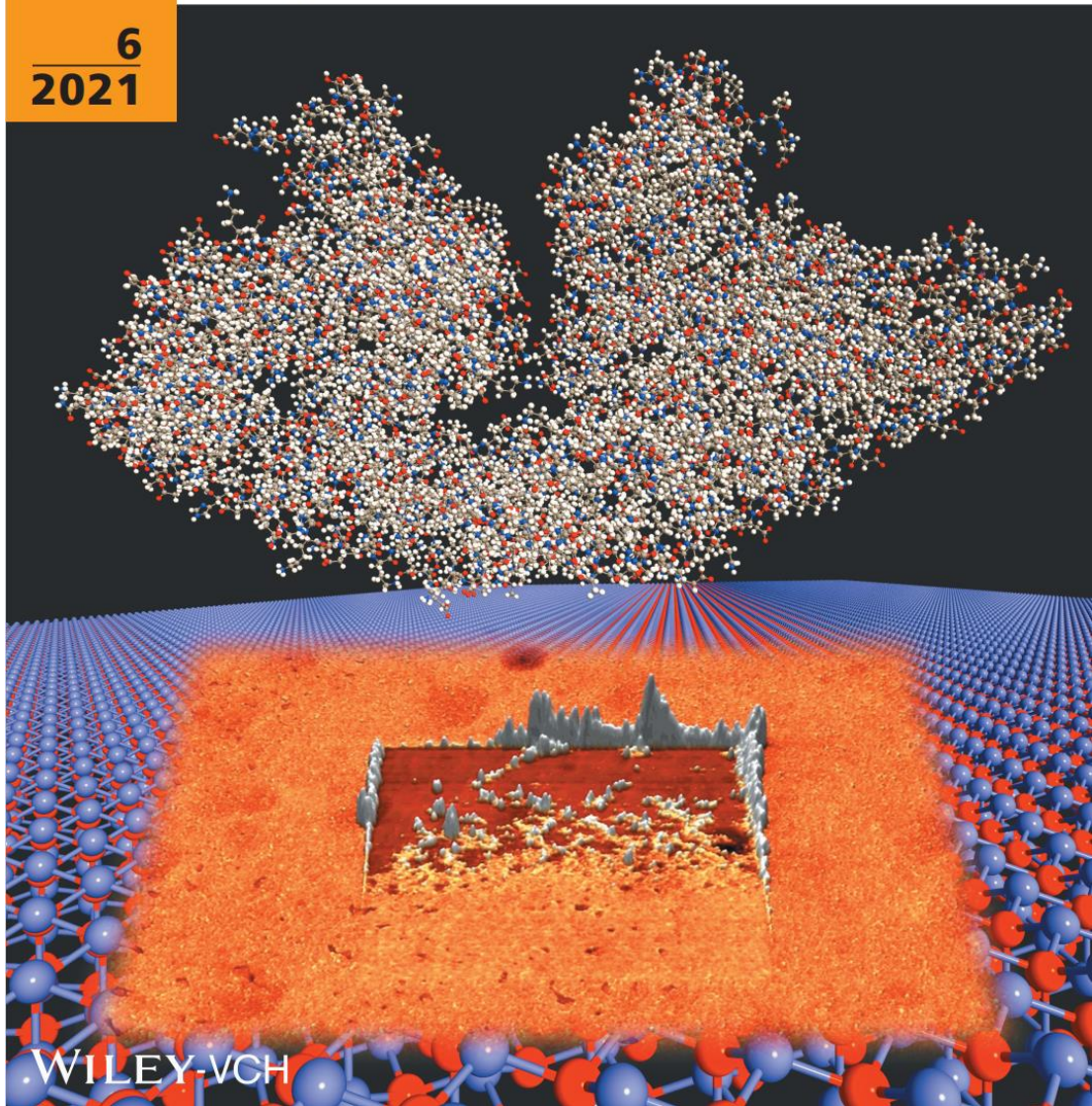
(52) Buryi, M.; Ridzoňová, K.; Neykova, N.; Landová, L.; Hájek, F.; Babin, V.; Děcká, K.; Sharma, R. K.; Pop-Georgievski, O. Effect of UV Irradiation on the Growth of ZnO:Er Nanorods and Their Intrinsic Defects. *Chemosensors* **2023**, *11* (3), 156.

ISSN 1862-6319
Phys. Status Solidi A
218 - No. 6 March 16
(2021)

physica **p** status **s** solidi **s**^a
www.pss-a.com

applications and materials science

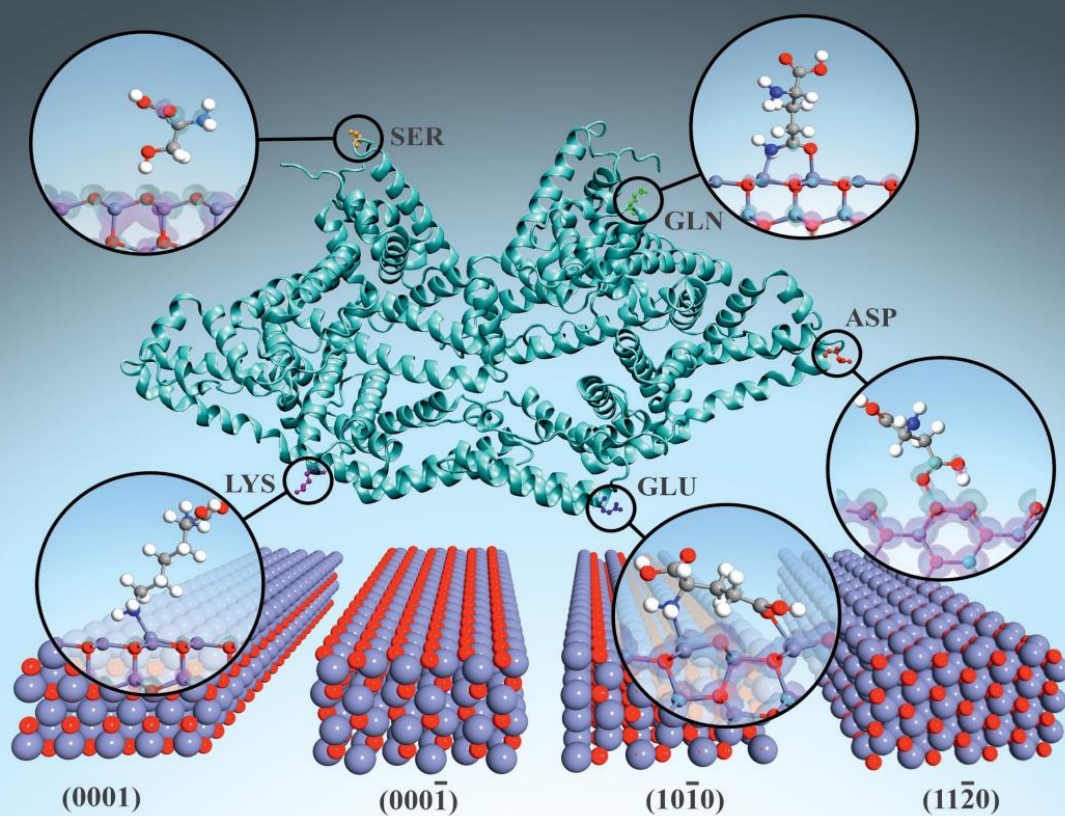
6
2021



Cover Feature:

Hadi Hematian and co-workers

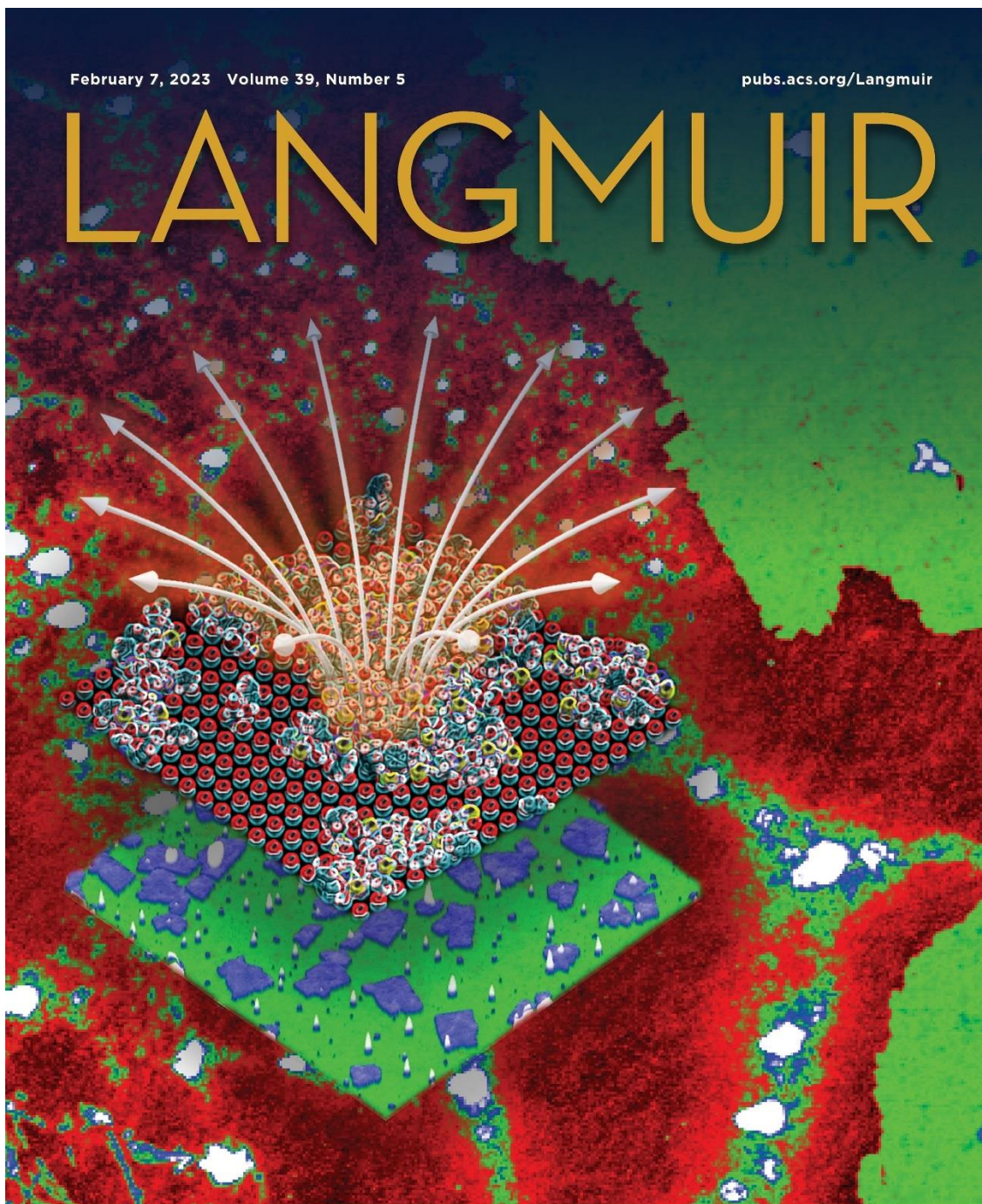
Strong Structural and Electronic Binding of Bovine Serum Albumin to ZnO via Specific Amino Acid Residues and Zinc Atoms



February 7, 2023 Volume 39, Number 5

pubs.acs.org/Langmuir

LANGMUIR



 ACS Publications
Most Trusted. Most Cited. Most Read.

www.acs.org